Doctoral theses at NTNU, 2017:231

Seniz Ucar

The Effects of Alginate Additives on Calcium Phosphate Mineralization

NTNU
Norwegian University of
Science and Technology

Doctoral thesis

Seniz Ucar

NTNU
Norwegian University of Science and Technology
Thesis for the Degree of
Philosophiae Doctor
Faculty of Natural Sciences
Department of Chemical Engineering

Doctoral theses at NTNU, 2017:231

NTNU

ISBN 978-82-326-2534-5 (printed ver.)
ISBN 978-82-326-2535-2 (electronic ver.)
ISSN 1503-8181

NTNU
Norwegian University of
Science and Technology

Seniz Ucar

The Effects of Alginate Additives on Calcium Phosphate Mineralization

Thesis for the Degree of Philosophiae Doctor

Trondheim, August 2017

Norwegian University of Science and Technology
Faculty of Natural Sciences
Department of Chemical Engineering

NTNU
Norwegian University of
Science and Technology

NTNU
Norwegian University of Science and Technology

Thesis for the Degree of Philosophiae Doctor

Faculty of Natural Sciences
Department of Chemical Engineering

ISBN 978-82-326-2534-5 (printed ver.)
ISBN 978-82-326-2535-2 (electronic ver.)
ISSN 1503-8181

Doctoral theses at NTNU, 2017:231

Printed by NTNU Grafisk senter

Abstract

Nature produces a variety of highly functional composite structures by the combination of organic and inorganic constituents and these composites stand as a central source of interest and inspiration for tissue engineering applications. In order to highlight the controlling mechanisms used by nature and employ these strategies to design efficient synthetic materials for clinical use, it is vital to study the interactions between organic and inorganic components. In this context, the purpose of this work has been to investigate the effects of alginate additives on different stages of calcium phosphate mineralization. The motivation for this study was founded on a model system composed of alginate hydrogel with calcium phosphate mineral content which has been comprehensively explored in our group as a potential scaffold material for bone tissue engineering applications. The intermolecular interactions of alginate with calcium phosphate minerals were investigated by using compositional variations of alginate in terms of block structure and molecular weight so that the operative interactions between the molecules and minerals could be assessed. The mineralization processes and regulatory roles of alginate additives were systematically studied by use of the complementary experimental techniques that combine monitoring of solution chemistry with material characterization. Detailed studies were conducted on brushite crystallization where the growth rates were determined quantitatively and the effects of alginate additives on growth mechanisms were investigated. By coupling of growth data and spontaneous precipitation experiments information on nucleation kinetics were also deduced. The kinetics of brushite transformation to hydroxyapatite in the presence of alginate was investigated in detail and the rate-determining reaction mechanisms were determined. Hydroxyapatite formation was also investigated via the amorphous calcium phosphate precursor. The course of reaction was studied in detail where the steps of hydroxyapatite formation and the operating mechanisms were discussed as well as the effects of varying alginate additives on these processes. The findings in this study may improve the understanding of the roles of additives with similar structure and functionality during mineralization such as other polysaccharides that are known to have regulatory roles in biomineral formation and contribute to the design of better controlled composite model structures.

Acknowledgements

Last four years I have spent in Norway as a PhD student has offered me great times beyond my expectations and I would like to express my gratitude to all the people who have been the key elements in this lucky ride.

First and foremost I want to express my sincere appreciation to my supervisor, Jens-Petter Andreassen, aka *The Boss*, for being the best supervisor ever, and for the great working environment he created effortlessly by his always-open door and encouraging attitude.

I am very thankful to my co-supervisor Pawel Sikorski, as well as Berit L. Strand, David C. Bassett and Sindre H. Bjørnøy. I had great pleasure working in the same project with these skillful people who have inspired me to aim for higher goals.

I want to thank all members of the Crystallization Group; Xiaoguang, Lijuan, Ina and Margrethe for their most valuable help and friendship. I hope we will keep planning sporty activities together and not do them in the future also. A great acknowledgement goes to my officemates, especially Georgios and Ricardo, who had always made my days in their special ways by sharing a morning coffee or a daily horoscope. I also want to remark my colleagues from the Department of Chemical Engineering with whom I enjoyed many lunch and cake breaks, and a welcoming working place.

The life outside work has been as rewarding where I got to collect many good friends along the way. I am most grateful to have the irreplaceable Turkish Gang, the party-beast Italians and my partners in crime Scandinavians; an exclusive collection of lovely people who have brighten up my time in Trondheim.

I have a huge family to express my appreciation. The one I have back at home has always been my strongest support and source of love and I am most grateful for it. My Norwegian family deserves a big thank you for making me a member of their circle and giving me a home, far away from mine but as sincere. Best saved for the last, I am deeply thankful to my roommates Beate Myrvang Inderhaug and Ella Bella the Princess who have become my core family in Trondheim. Your value to me is beyond words.

List of Papers

The following publications are included in this thesis:

(I) Nucleation and Growth of Brushite in the Presence of Alginate
Ucar, S., Bjørnøy, S.H., Bassett, D.C., Strand, B.L., Sikorski, P., Andreassen, J.P.
Crystal Growth and Design, 2015, 15, p 5397-5405.

Designed the study: SU, PS and JPA. Performed the experiments: SU. Analyzed the data: SU. Contributed materials or analysis: BLS. Wrote the paper: SU and DCB. All authors contributed in the discussion and revision of the paper.

(II) Transformation of Brushite to Hydroxyapatite and Effects of Alginate Additives
Ucar, S., Bjørnøy, S.H., Bassett, D.C., Strand, B.L., Sikorski, P., Andreassen, J.P.
Journal of Crystal Growth, 2016, 468, p 774-780.

Designed the study: SU and JPA. Performed the experiments: SU. Analyzed the data: SU. Contributed materials or analysis: BLS. Wrote the paper: SU. All authors contributed in the discussion and revision of the paper.

(III) Transformation of Amorphous Calcium Phosphate to Hydroxyapatite in the Presence of Alginate Additives
Ucar, S., Bjørnøy, S.H., Bassett, D.C., Strand, B.L., Sikorski, P., Andreassen, J.P.
submitted to Crystal Growth and Design

Designed the study: SU and JPA. Performed the experiments: SU. Analyzed the data: SU. Contributed materials or analysis: BLS. Wrote the paper: SU. All authors contributed in the discussion and revision of the paper.

Related publications:

(I) Controlled Mineralisation and Recrystallisation of Brushite within Alginate Hydrogels
Bjørnøy, S. H., Bassett, D. C., Ucar, S., Andreassen, J.P., Sikorski, P.

Biomedical Materials, 2016, 11, 015013.

(II) Gelling Kinetics and In Situ Mineralization of Alginate Hydrogels: A Correlative Spatiotemporal Characterization Toolbox
Bjørnøy, S. H., Mandaric, S., Bassett, D. C., Åslund, A. K. O., Ucar, S., Andreassen, J.P., Strand, B. L., Sikorski, P.

Acta Biomaterialia, 2016, 44, p243-253.

(III) A Correlative Spatiotemporal Microscale Study of Calcium Phosphate Formation and Transformation within an Alginate Hydrogel Matrix
Bjørnøy, S. H., Bassett, D. C., Ucar, S., Strand, B. L., Andreassen, J.P., Sikorski, P.

Acta Biomaterialia, 2016, 44, p254-266.

(IV) Letter to The Editor Re "Characterization Of Alginate-Brushite In-Situ Hydrogel Composites"
Bjørnøy, S. H., Bassett, D. C., Ucar, S., Andreassen, J.P., Sikorski, P.

Materials Science and Engineering C, 2017, 70, p930-931.

TABLE OF CONTENTS

PAPERS

SUPPLEMENTARY ATTACHMENTS

CHAPTER 1

INTRODUCTION

Formation of biological minerals *in vivo* (biomineralization) is a well regulated process that results in highly hierarchical and reproducible structures with superior biological and physical properties. During biomineralization, the course of mineral formation is often under efficient biological control and involve interactions with a high number of biological macromolecules.[1] By the inclusion of organic materials, a stunning diversity of structures with a range of properties and functionality are produced *in vivo* from the fundamental inorganic building blocks.[2] During this process, mineralization is modulated via the effects of biological molecules on nucleation, growth rates, resultant shape, size and spatial orientation of the crystals.[3]

The advanced functionality of natural hybrid structures with organic and inorganic constituents has led the attempts to unravel the mechanisms underlying their formation. In addition, the strategies used by nature have been an important source of inspiration for the design and development of biomaterials to be used as biological substitutes in case of need to restore, maintain or improve tissue function.[4] Much progress has been made in identifying the effects of organic constituents on mineral components and controlling strategies have been developed for designed synthetic systems in the light of this research. However, the operating mechanisms of matrix molecules throughout the different stages of mineralization are yet to be fully revealed. The study of mineral formation in biological systems comprises a high order of complexity, and thus, is a challenging task. While biological systems underlies the key inspiration for the design of synthetic structures, investigating mineralization in simple representative systems, where the number of variables can be controlled, is a proficient approach to gain an insight into *in vivo* processes. In this regard, the effects of particular groups of additives on mineral formation have been investigated such as proteins and polysaccharides which are in close relevance with the biological systems. It is now well established that the influence of the molecules is determined by their structural relationship with the forming mineral and their impact on the energy landscape of the mineralization reaction.[5] The properties of the molecules such as chemical structure, functionality and molecular weight are effective parameters in this interplay.

Among the natural composite structures, calcified tissues of mammals such as bone and teeth have been under the focus of extensive research for their obvious relevance to medical concerns. There is a significant interest in natural and synthetic bone-mimetic materials for clinical bone treatment.[6] Scaffold based tissue engineering strategies where synthetic functional materials are designed by inspiration from the nature offers promising alternatives to the current gold standard of using autografts (i.e. using one's own tissue for transplantation) for bone repair and regeneration.[7] To date, no synthetic material can surpass autografted bone in terms of clinical outcome, which although often very effective, suffers from a limited supply, extended surgical procedure and a risk of donor site infection and morbidity. Therefore the search for effective synthetic alternatives is well motivated. Scaffolds composed of organic and inorganic components and functionalized with genetic material or other biological factors are under constant development for this purpose. The highly hierarchical structure of natural bone is not easy to reproduce synthetically; however, as the formation mechanisms and the controlling strategies are revealed, the closer replicates with better functionality can be produced.

1.1 Aim of the Research

In relevance with the current focus on tissue engineering strategies for bone repair, this work is included within the project 'Mineralized, Hierarchical, Bioinspired Materials for Tissue Engineering' where the aim is to develop a model composite system composed of an alginate hydrogel matrix and calcium phosphate (CaP) mineral for bone tissue engineering applications. In this thesis, mineralization kinetics of calcium phosphates are studied and the effects of alginate additives on crystallization are investigated. The purpose of the fundamental crystallization studies is to understand and control mineral formation within the chosen biopolymer network. This feature can be employed afterwards to construct complex, highly hierarchical scaffolds with controlled properties such as mineralization potential and mechanical performance.

CaPs are the main mineral component in calcified tissues of mammals such as bone and teeth, hence, have been investigated in numerous studies in an attempt to elucidate the formation mechanism of those hard tissues. CaP precipitation is a complex process that depends on various parameters, mainly supersaturation, calcium and phosphate ion concentrations, pH, temperature, ionic strength and also time due to phase transformations.[8] Moreover, when present in the reaction medium, biological molecules and inorganic additives other than calcium and phosphate ions influence the crystallization process significantly. Consequently, considering the high number of variables, it is difficult to predict the exact mechanism of CaP formation in any given matrix.[9]

The role of macromolecules in controlling crystallization in *in vivo* and *in vitro* model systems has been at the center of comprehensive research and continues to be an advancing field. Exploring the governing mechanisms of polymers on mineral formation is necessary to better understand *in vivo* processes that can lead to the design of advanced composite materials with higher complexity and functionality to serve for the case specific applications of biomaterials and tissue engineering. The aim of this thesis is to provide valuable understanding to the literature on crystal-macromolecule interactions from an aspect of crystallization fundamentals.

1.2 Model Composite System

The experimental work in this thesis has its foundations on the questions arisen from the CaP-alginate composite model system that is designed as a building block of a scaffold material for bone tissue engineering applications.[10-12] The composite model system of mineralized alginate hydrogel is introduced below and the relevant findings on mineralization events are summarized.

Alginate hydrogels with CaP mineral content was prepared by double-diffusion method which allows the gelation of alginate and mineralization to occur simultaneously as illustrated in Figure 1.1. The 3-dimensional (3D) hydrogel beads were prepared by addition of the phosphate containing alginate solution into a high concentration calcium solution dropwise where the diffusion of ions resulted in the gelation of alginate simultaneously with the formation of CaP mineral phase within. The 2-dimensional (2D) counterparts of the same system were used for time-resolved microscopic investigations of the gelation and mineralization processes. For this purpose, a drop of phosphate containing alginate solution was placed between two microscope slides and the calcium solution was then introduced into the spacing between the slides to initiate the gelling and mineralization in the droplets.

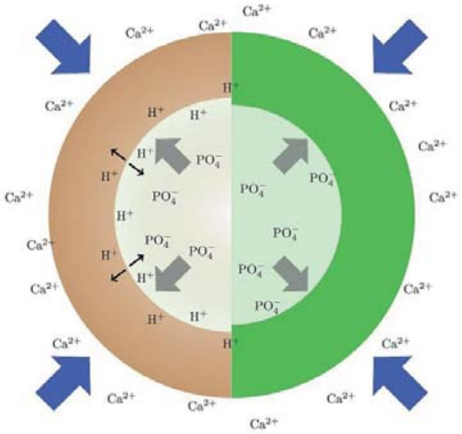

Figure 1.1. An illustration of the gelling and mineralizing system. After the alginate drop has entered the calcium solution, Ca^{2+} diffuses inwards (blue arrows), the PO4$^-$ ions diffuse outwards (grey arrows), gelling and mineralizing occurs as illustrated by a color difference in the figure. On the right, the green color indicates gelled alginate. On the left, the brown color illustrates mineral formation and the associated local release of H$^+$, their diffusion being indicated by black arrows. The mineral front trails slightly behind the gelling front.[10]

Brushite was chosen as the target CaP phase to be formed within hydrogels due to its high resorbability and thus reorganization ability. However, although reaction conditions were set to favor brushite precipitation, multiple CaP phases were observed in the hydrogel beads. It was shown that to fabricate hydrogels with pure brushite content seeding was necessary and without seeding different and multiple phases formed depending on the pH of the reaction medium.[10] As a result of the concentration gradient due to ion diffusion, hydrogel beads were heavily mineralized close to the edge and the mineral content decreased towards the center. In addition, amorphous calcium phosphate (ACP) was detected as the initial metastable phase in both unseeded and seeded precipitation that transformed into octacalcium phosphate (OCP) under unseeded precipitation and readily into brushite in the presence of the seeds (Figure 1.2).

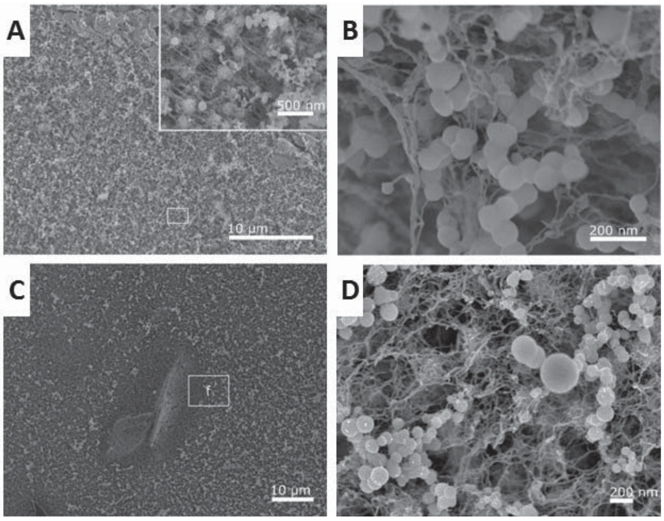

Figure 1.2. SEM images of the amorphous precursor phase that forms initially in both (A-B) unseeded and (C-D) seeded alginate hydrogels. ACP is highly unstable in the vicinity of the brushite seeds and readily transforms to brushite by a dissolution- reprecipitation reaction (C).[11]

When aged in their reaction medium or incubated in synthetic representative of physiological solutions (simulated body fluid, SBF), unseeded hydrogels showed formation of OCP and hydroxyapatite (HA) respectively; whereas brushite content of the seeded hydrogels showed transformation to HA. During incubation of seeded beads in SBF, it was observed that the transformation to HA was driven by both the dissolution of brushite seeds and the flux of SBF solution close to the edge of the beads whereas towards the center dissolution of brushite seeds were the primary source to provide the supersaturation to induce HA nucleation and growth.[11] In addition, both in the reaction medium and SBF solution, transformation of seeds to HA started on the edge of the hydrogels and continued inwards.

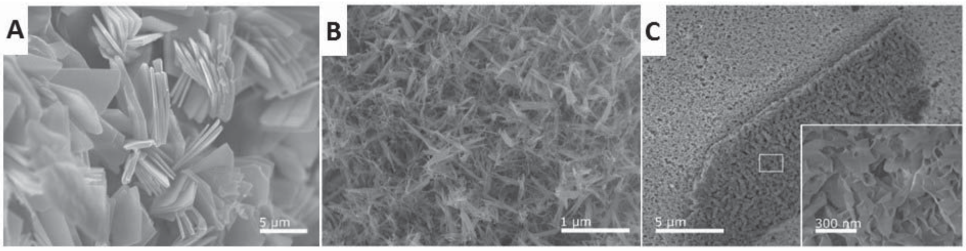

Figure 1.3. SEM images of the seeded alginate hydrogels after incubation in the calcium solution for (A) 1 h, (B) 24 h and (C) in SBF for 24. Large brushite plates are shown in (A) whereas after longer incubation in either gelling medium or SBF solution results in the transformation of brushite to HA (B-C).[11]

1.3 Organization of Work

The theoretical background and experimental details of this work are given in Chapter 2 and Chapter 3, respectively. Following in Chapter 4, findings are summarized and discussed. Chapter 5 presents the concluding remarks and an outlook regarding the matrix assisted mineralization studies. Three publications included in this thesis are attached. Two of the related publications which describe the alginate-CaP composite system are provided as supplementary attachments for the convenience of the reader.

Experimental studies in this thesis started with investigation of how alginate additives affect the nucleation and growth kinetics of brushite. Through screening the effects of alginate additives varying in functionality and molecular weight, it was aimed to have more insight on the intermolecular interactions between the chosen mineral and organic phase of the model system. In this part of the study, growth kinetics were studied by both batch and constant composition experiments according to their applicability. Growth mechanisms were discussed in detail with respect to supersaturation range and effects of additives on nucleation kinetics and morphology of the crystals were examined. The results are given in Paper I.

In the model system, transformation of brushite seeds into HA was observed upon aging in reaction medium or incubation in SBF which is a desirable property for a bone tissue engineering construct. In order to look into the details of this transformation reaction by highlighting the controlling mechanisms and investigating the effects of alginate additives, brushite transformation to HA was studied in aqueous alkaline medium through monitoring the supersaturation profiles. This method was chosen since it enables detailed kinetic analysis on the transformation reaction. The results of this work are given in Paper II.

Phase transformation studies brought up new questions on the nucleation events of HA such as the nucleation mechanism, possibility of an amorphous precursor and the role of alginate additives on nucleation. Therefore, the last part of this work focused on mechanisms controlling HA nucleation in the presence of alginate additives. For this purpose, solution chemistry was monitored to follow subsequent stages during HA formation and evolution of its formation was monitored by detailed characterization. Results are presented in Paper III.

CHAPTER 2

BACKGROUND

2.1 Biomineralization

According to its most recognized definition by Mann, biomineralization is the study of the formation, structure and properties of inorganic solids deposited in biological systems.[13] Mineral formation *in vivo* is a complex process that involves organic phases which regulate the nucleation, growth, morphology and organization of biogenic minerals that form the major inorganic solid component of hard tissues in many different organisms.[14] This intricate and well-regulated process results in composite materials with exceptional features which are often vastly different from the properties of the bulk inorganic material alone. The structural, mechanical, optical, and magnetic properties of these materials are exploited by the organisms for a variety of purposes and through active control mechanisms on mineral formation, their biophysical properties are optimized for specific functions.

The distinguishable properties of biomimetic materials include uniform particle size, well-defined compositions, preferential crystallographic orientation, high levels of spatial orientation and high orders of hierarchical assembly. The key control mechanisms directing the biomineralization process involve the regulation of chemistry, space, structure and morphology.[14] The fundamental factors of *chemical control* involve the solubility and supersaturation that in turn affect nucleation and growth rates. In biological systems the control of solubility and supersaturation are achieved by the regulation of ion transport, and further control is attained on nucleation and growth rates by molecular based promoters or inhibitors. The *spatial control* refers to restricting the mineralization process to specific boundary spaces which impacts on the size and shape of the mineral deposits such as formation of the nano-sized hydroxyapatite crystals within the collagen fibrous network in bone. The *structural control* is associated with interfacial molecular recognition by what structural alignment is governed as the matrix acts as an organic template. The general hypothesis relates this phenomenon to the reduction of interfacial energies via matching of charge, polarity, structure and stereochemistry that leads to controllable site-specific nucleation and crystallographic alignment of minerals. The *morphological control* gives the biominerals their complex and diverse structural forms via coupling of mineral growth and biological organization.

The comprehensive control mechanisms in natural biomineralization processes result in advanced materials with high functionality and site-specific features which offer valuable insight and inspiration for the synthetic materials chemistry.[15] Developing strategies by mimicking nature has been a valuable approach especially in the field of regenerative medicine where biomaterials play a pivotal role in the success of tissue engineering applications. Although the natural biomineralization processes offer a great source of inspiration to design advanced functional materials, such structures are difficult to reproduce synthetically in the laboratory due to the complex control processes. Detailed studies of the molecular interactions between the organic and inorganic phases are a significant aspect of biomineralization and can contribute to highlight the acting control mechanisms for a better understanding of *in vivo* processes and for enhanced *in vitro* model systems.

Among over 70 different biominerals found in nature, calcium carbonates and calcium phosphates are the most abundant and particularly well investigated ones. The calcium carbonate minerals of invertebrates, such as corals and sea urchin spines, have been well studied due to their accessibility and high degree of crystallographic control achieved in these biologically formed crystals. The calcium phosphate (CaP) minerals constitute a major portion of minerals found in living beings from unicellular organisms to vertebrates and have also been at focus for their remarkable structure and mechanical properties along with the more obvious reasons of medical issues. In human body, the main mineral component of the composite tissues of teeth and bone are composed of calcium phosphate apatites, and also a variety of other calcium phosphate phases (amorphous CaP, brushite, and octacalcium phosphate) may form as precursor phases or as a result of uncontrolled pathologic calcifications.[9] CaP minerals show high physicochemical and structural adaptability in accordance with their functionality which make them useful for a variety of biological uses and a great source of inspiration for the design of advanced materials.

2.2 Crystallization

Crystallization is a phase transition process during which matter is transformed from a high free energy, disordered, solvated state to a crystal phase characterized by the regular arrangement of its building units to a low free energy state.16 Crystallization from solution proceeds via establishment of supersaturation in the system, followed by spontaneous formation of the nuclei of the new phase, and the subsequent growth. Supersaturation is defined as the fundamental thermodynamic driving force for the crystallization to occur. In a supersaturated system, different pathways of thermodynamic and kinetic origins have been proposed on the progress of the nucleation and growth events and they are discussed further as classical and non-classical routes of crystallization. The classical theory of crystallization is presented in terms of its thermodynamic background and well-established quantitative expressions. A brief summary of several non-classical theories which envision alternative pathways for crystal formation are also given in this section.

2.2.1 Supersaturation

The fundamental driving force for crystallization is the difference between the chemical potential of a given substance in the solution (state 1) and in the solid phase (state 2).[16] This can be written as:

$$\Delta\mu = \mu_1 - \mu_2 \tag{2.1}$$

The chemical potential, μ, can be expressed in terms of the standard potential, μ_0, and the activity, α, as:

$$\mu = \mu_0 + RTlna \tag{2.2}$$

where T is the temperature and R is the universal gas constant. The activity of a solute is a measure of its effective concentration in solution and it is defined by means of the free concentration, c, of a chemical species and the activity coefficient, γ, as:

$$a = c.\gamma \tag{2.3}$$

By combining Equations 2.1 and 2.2, the driving force for the crystallization can be expressed as:

$$\Delta\mu = RTln\left(\frac{a}{a^*}\right) \tag{2.4}$$

where α is the activity of the chemical species and α* is the activity of the same compound in the equilibrium state. The activity ratio given in Equation 2.4 is defined as the supersaturation, S.

$$S = \left(\frac{a}{a^*}\right) \tag{2.5}$$

In other words, S is a measure of the tendency of a system to precipitate. The difference in the chemical potential must be larger than zero for the crystallization to occur which provides S > 1.

For electrolyte solutions, the mean ionic activity, a± should be used which is defined by means of the ionic activity product (IAP) of the lattice ions in solution, and υ is the number of moles of ions in 1 mole of electrolyte:

$$a_{\pm} = (IAP)^{\frac{1}{\upsilon}} \tag{2.6}$$

Based on Equation 2.6, the supersaturation for electrolyte solutions is defined as:

$$S = \left(\frac{IAP}{K_{sp}}\right)^{\frac{1}{\upsilon}} \tag{2.7}$$

where K_{sp} is the ionic activity product of the cations and anions at equilibrium state, that represents the solubility product for the corresponding compound.

It should be noted that the definition of supersaturation can vary between different studies although the point of origin for any defined concept is the chemical potential difference between two phases, or in other words the driving force for crystallization. Another common definition to represent the driving force is:

$$\sigma = ln\left(\frac{IAP}{K_{sp}}\right) \tag{2.8}$$

where σ is equal to Δμ/RT and can also be referred as supersaturation. However, in this study, σ is used to represent the relative supersaturation which is important when considering the kinetics of growth and defined as:

$$\sigma = S - 1 \tag{2.9}$$

Some other definitions for representing the driving force in a system are the supersaturation ratio, Ω; and the supersaturation index (SI) which is the commonly used form in thermodynamic calculation programs. They are defined as:

$$\Omega = \left(\frac{IAP}{K_{sp}}\right) \tag{2.10}$$

$$SI = \log\left(\frac{IAP}{K_{sp}}\right) \tag{2.11}$$

While it is possible to represent the driving force for crystallization and supersaturation in multiple ways, great caution should be taken to clearly present the employed terminology. Equation 2.7 is used to define supersaturation throughout this thesis and in published work.

2.2.2 Classical Theory of Crystallization

According to the classical crystallization model, a crystal forms via formation of a stable nucleus with a critical size where its bulk energy balances the energetic costs of creating a surface; and subsequently grows via monomer-by-monomer attachment of its building units, that can be atoms, molecules or ions. Details of classical route of crystallization are discussed below.

2.2.2.1 Classical Nucleation Theory

Classical nucleation theory (CNT) is based on the quantitative works of Volmer and Weber and has its foundation on the ideas of Gibbs.[17] According to CNT, in a supersaturated solution, the thermodynamic driving force induces formation of the solid phase to reach the equilibrium state. The formation of the solid phase starts with nucleation where nanoscale molecular clusters of the new phase appear.[18] The molecules repeatedly come together and part again until reaching a critical number that forms a stable cluster in solution which is referred as the nucleus. The process that describes the situation up to the point where particles reach critical size can be called the nucleation stage.[19] It should be noted, the structure of the assembly of ions or molecules which is called as the critical nucleus here can be a miniature crystal of perfect form, or a rather diffused body of molecules or solvated ions.

Nucleation can be classified as primary and secondary nucleation where primary nucleation processes represent all cases of nucleation in systems that do not contain the forming crystalline matter; and secondary nucleation occurs when parent crystals catalyze the formation of a new crystalline phase of the same substance. Primary nucleation can further be divided into homogenous and heterogeneous nucleation. Homogenous nucleation occurs spontaneously in the system whereas heterogeneous nucleation is induced by the presence of a solid surface that can be the surface wall of the vessel, a foreign particle or an impurity in the medium.

Homogeneous nucleation

According to CNT, the driving force for nucleation is the overall excess free energy, ΔG, which is the sum of the excess free energy of the metastable liquid phase in a supersaturated solution, ΔG_v, and the energy needed to create a new surface, ΔG_s (Equation 2.12).[16]

$$\Delta G = \Delta G_V + \Delta G_S \tag{2.12}$$

The overall free energy change to form a spherical nucleus with the radius r can be expressed as:

$$\Delta G = \frac{4}{3}\pi r^3 \Delta G_v + 4\pi r^2 \gamma \tag{2.13}$$

$$\Delta G_v = -\frac{k_B T lnS}{v} \tag{2.14}$$

where ΔG_v is the free energy change of transformation per unit volume, v, as defined in Equation 2.14, k_B is the Boltzmann constant and γ is the surface free energy of the solid-liquid interface.

The first term on the right hand side of Equation 2.12 expresses the fact that the solid is more stable than the supersaturated fluid. This term is negative and proportional to the volume of crystallite. The second term expresses the free energy cost of creating a solid-liquid interface. It is positive and proportional to the surface area of the crystallite. A stable nuclei can form only when the critical radius, r_c, is reached and slope of the ΔG curve attains a negative value (Figure 2.1).

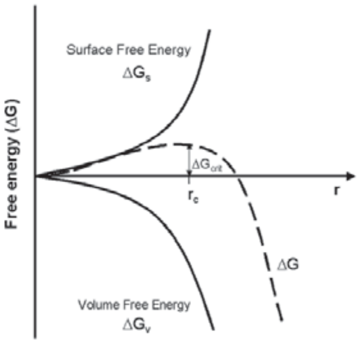

Figure 2.1. The change of free energy as a function of nucleus radius.[20]

The point where the first derivative of Equation 2.13 with respect to r equals to zero, represents ΔG_{crit} where r equals to r_c:

$$r_c = -\frac{2\gamma}{\Delta G_v} = \frac{2\gamma v}{k_B T lnS} \tag{2.15}$$

As Equation 2.15 illustrates, at constant temperature, size of the critical nuclei decreases with increasing supersaturation.

The nucleation rate, J, expresses the number of stable nuclei formed per unit time per unit volume and can be given in the form of the Arrhenius reaction rate equation:

$$J = Aexp\left[-\frac{\Delta G_{crit}}{k_B T}\right] = Aexp\left[\frac{16\pi\gamma^3 v^2}{3k_B^3 T^3 (\upsilon \ln S)^2}\right] \tag{2.16}$$

where υ is the number of ions, T is the temperature and S is the supersaturation. As can be seen from Equation 2.16, magnitude of the free energy barrier to nucleation with respect to the thermal energy, $k_B T$, is a critical factor determining the number of particles produced, and the rate of nucleation is efficiently influenced by temperature, supersaturation and interfacial tension. The pre-exponential factor, A, deals with the kinetic factors of nucleation and given as:

$$A = zf^* C_0 \tag{2.17}$$

The Zeldovich factor, z, corrects for the fraction of critical size nuclei that dissolve rather than grow; f* represents the attachment frequency of building units to nucleus and can be represented as the multiplication of incoming flux of monomers to the nucleus surface and the nucleus surface area; and C_0 gives the concentration of nucleation sites.[21,22]

Heterogeneous nucleation

Most of the primary nucleation events happen via heterogeneous pathway because it is difficult to achieve the energy barrier for homogeneous nucleation and to completely eliminate surfaces aiding for nucleation in a precipitating system.[20] The nucleation rate expression given in Equation 2.16 can also be used for the heterogeneous nucleation mechanism with the modifications for the reduced energy barrier for nucleation.[16] In case of foreign particles being present, the energy barrier for the onset of nucleation decreases in dependence with the contact angle between the crystalline deposit and the foreign solid surface as given:

$$\Delta G_{het} = \emptyset \Delta G_{hom} \tag{2.18}$$

$$\emptyset = \frac{(2+cos\theta)(1-cos\theta)^2}{4} \tag{2.19}$$

where θ is the contact angle between the heteronuclei and the crystalline deposit. The contact angle is a measure of the affinity between two surfaces and as it increases the interfacial energy between two surfaces decreases so that the impurity can act as a nucleation site. In the case of partial wetting where $0<\theta<180°$, the value of ø is lower than 1, which indicates lowered free energy barrier for heterogeneous nucleation. In the case of $\theta=180°$, indicating complete non-affinity between the heteronuclei and the crystalline phase (ø=1), the presence of the foreign nuclei do not affect the nucleation process (i.e. homogeneous nucleation).

Secondary nucleation

Secondary nucleation refers to the catalytic effect of the parent crystals present in the medium on the nucleation of new crystalline material. It is a complicated phenomenon that has not been fully understood yet.[23,24] The mechanisms of secondary nucleation is in general evaluated in two categories as originating from the parent crystal or from the concentrated liquid layer adjacent to the crystal surface.[23,25] The first mechanism suggests breeding of new nuclei from the parent crystals where the rate would be affected by the degree of supersaturation, agitation level, concentration of parent crystals and the hardness of the crystals. Based on the second mechanism, the high local concentration of the liquid near the crystal enhances the possibility of nucleation. The concentration gradient theory proposes that the solution is more structured in the presence of a crystal and this increases the local supersaturation of the fluid near the crystal.[24] According to the embryo coagulation secondary nucleation theory, the liquid layer adjacent to the crystal surface is rich in nuclei embryos because they are attracted to the seed crystals with van der Waals forces.[25] These theories suggest that removal of the concentrated layer into the solution by interaction of the crystal surface either with other solid objects like, stirrers, flow lines or other crystals (contact nucleation); or with the fluid (shear nucleation) results in production of secondary nuclei.

2.2.2.2 Determination of Induction Times

Between the establishment of supersaturation in a system and the appearance of first stable nuclei, a time period usually elapses depending on the level of supersaturation, state of agitation, viscosity of the solution, presence of impurities etc. The experimentally observable value of this time period is referred as induction time, t_{ind}, and it is a measure of the ability of a supersaturated solution to remain in this metastable state. Although induction time cannot be regarded as a fundamental property of a system, it has been shown to provide useful information about the nucleation rate and mechanism.

The rate of nucleation, J, in a system can be related to the induction time measurements by the following expression given;

$$J \approx \frac{N}{t_{ind}} \tag{2.20}$$

where N is the number of stable nuclei formed. When the appearance of the stable nuclei is responsible for bringing the solution out of the metastable equilibrium, and the experimental technique allows for counting N effectively, induction time can be given as[18];

$$t_{ind} = \frac{N}{JV} \tag{2.21}$$

where V is the solution volume.

In most applied cases, however, induction time measurements depend on monitoring of a certain variable in the system such as pH, turbidity, conductivity etc., until a detectable change occurs.[26] Yet, combining Equation 2.16 and 2.20, gives the relation between J and t_{ind} (Equation 2.22) which allows for deduction of information on nucleation mechanisms and interfacial energy (γ) as shown in Figure 2.2.

$$\ln t_{ind} \sim \frac{\gamma^3}{T^3(lns)^2} \tag{2.22}$$

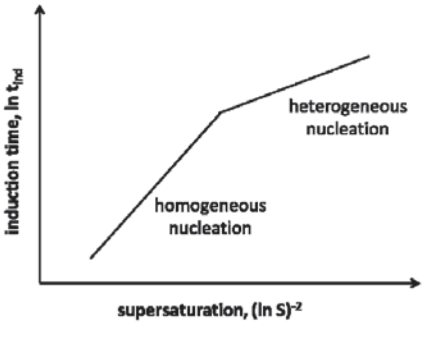

Figure 2.2. Logarithmic plot of induction period as a function of initial supersaturation. Change of slope indicates a transition between homogeneous and heterogeneous nucleation mechanisms. Note that slope of the lines relates to interfacial energy.[16]

In practice, the breakdown of the solution metastability is mostly due to progressive appearance of many nuclei and their overgrowth to macroscopically large sizes. Therefore, experimentally determined induction times can be considered as sum of the time lapse until formation of the stable nuclei and the time lag until the onset of a significant detectable change in the system by crystal growth.[27] Then, the induction time can be given as;

$$t_{ind} = \sqrt[4]{\frac{3\alpha_v}{\pi G^3 J}} \tag{2.23}$$

when nuclei grow as spheres with a time-independent growth rate, G, and α_v is the detectable volume (or mass) fraction of the new phase [28]. Hence, the use of Equation 2.23 is valid when the experimental method used detects the induction time based on the appearance of a certain volume (or mass) of many nucleating crystallites.

2.2.2.3 Ostwald's Rule of Stages

The classical theory of crystallization assumes formation of the thermodynamically most stable phase out of a supersaturated solution. However, it does not dictate that the unstable supersaturated system transforms directly into the most stable phase. According to the Ostwald's rule of stages, thermodynamically metastable phases associated with lower energy barriers of formation can initially appear in a supersaturated system as a coaction of thermodynamic and kinetic factors.[29] Given the sufficient time and the free energy of activation, they eventually transform into the more stable phase. A stepwise formation behavior as shown in Figure 2.3 would be particularly preferred in systems where the final stable phase has a high activation energy barrier for formation. In that case, a sequential precipitation pathway involving metastable intermediates with lower activation energies becomes favorable. Observation of amorphous phases prior to crystallization in many systems stands as an example of this rule where crystalline phases have high interfacial energies and large unit cell volumes.[30,31] In the last two decades appearance of dense liquid precursors in the early stages of nucleation has also been reported.[32,33] This phenomenon can also be interpreted in correlation with the Ostwald's rule as Thompson addressed in his book "On Growth and Form", first published in 1917, as; when a substance begins to form from a solution, it first undergoes a liquid phase separation which is accompanied by the smallest loss of free energy.[34]

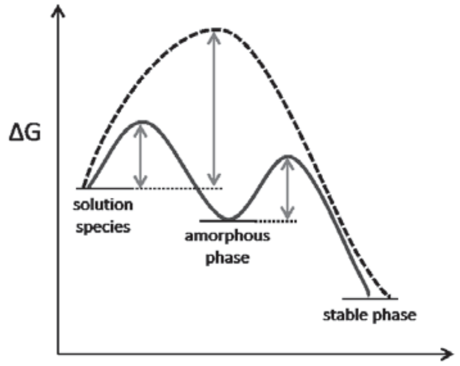

Figure 2.3. Reaction coordinate diagram demonstrates alternative pathways to lower Gibbs free energy; direct transformation to stable phase (dashed line) or transformation via metastable intermediates (solid line).

2.2.2.4 Classical Theory of Crystal Growth

According to the classical view, as the stable nuclei form in a supersaturated solution, subsequent growth occurs via continual addition of building units on the crystal surfaces and their incorporation into the lattice sites. The Kossel model given in Figure 2.4 illustrates the atomic processes occurring at a crystal surface.[35] The surface consists of flat regions named terraces which contain moving layers (steps) and steps can contain one or more kinks. The kink sites have the highest energy of binding, which makes them the favorable sites for ion incorporation, and growth rate (R) scales with the kink density. The classical model of crystal growth assumes that ions enter kink sites either directly from the solution or after adsorbing and diffusing through the terraces.[36]

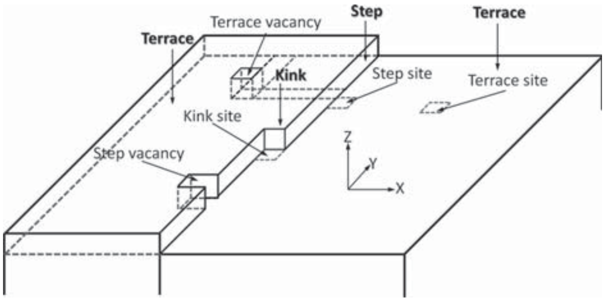

Figure 2.4. The graphical representation of the crystal surface according to the Kossel model.[35]

As the ions incorporate on the kink sites, steps propagate and this process continues until reaching crystal edges and completing the surface layer. At this point, new steps should be generated for the growth to continue. One way of doing this is to generate two-dimensional islands of molecules that require a critical size and overcoming the associated energy barrier. Therefore, sufficiently high supersaturation levels are required for polynuclear growth mechanism to be active.[37] This combination of two dimensional nucleation and lateral growth of the islands on the surface is termed as the 'birth and spread mechanism' and it shows strong dependence on the supersaturation level.[21] At sufficiently high supersaturation multiple 2D surface nuclei can form on a crystal surface and moreover polynucleation of new islands on existing islands can occur, results in high numbers of active sites.

Under low supersaturation, critical size for 2D nucleation is large and the probability of reaching it becomes low. However experimental observations showed, although slow, crystals continued to grow even at low supersaturation where 2D nucleation could not be accounted for growth. The screw dislocation (spiral growth) theory accounts for these observations by considering the fact that crystals are not perfect.[38] They contain dislocations in the crystal lattice that generate continues source of steps.[39] Both 2D nucleation and spiral growth theories have been observed experimentally with advanced microscopic techniques (Figure 2.5).

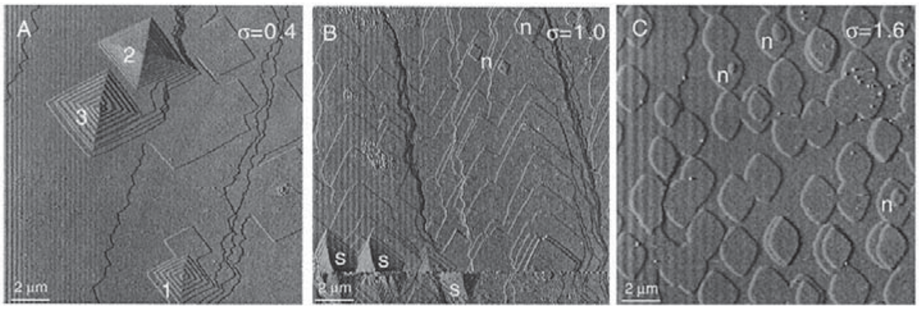

Figure 2.5. AFM images showing the change in growth mechanism of calcite crystals from spiral growth to 2D nucleation with increasing supersaturation; (A) spiral growth, (B) spiral growth and 2D nucleation, and (C) 2D nucleation. Note that σ is defined as given in Equation 2.9.[40]

Finally, under very high supersaturation levels, numerous active sites can be generated on the crystal surface which leads to rapid ion incorporation. In that case, the transport of ions from the bulk solution or their diffusion into the adsorption layer becomes the limiting and controlling factor on the growth rate.

The growth rate and mechanism of a crystal depends highly upon supersaturation, and it is possible to obtain different and multiple mechanisms dominating at different regions of the supersaturation range as discussed above. The growth rate, R, can be expressed as a function of relative supersaturation (σ) (Equation 2.9) and kinetic components:

$$R = k\sigma^g \tag{2.24}$$

where k is the growth rate constant and g is the apparent growth order, the value of which depends on the rate-determining mechanism and how it correlates with the supersaturation value.

In order to explain how different growth mechanisms correlate with the relative supersaturation, concentration gradients of mass transfer can be used by applying the assumption.[36]

$$\sigma = S - 1 = \left(\frac{a-a^*}{a^*}\right) \sim \left(\frac{c-c^*}{c^*}\right) \tag{2.25}$$

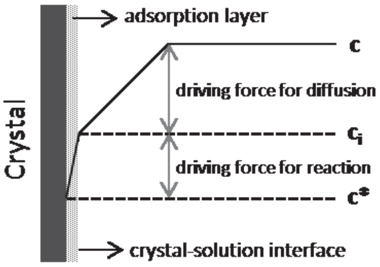

Figure 2.6. Concentration gradients of mass transfer between the bulk solution and crystal surface.[41]

Figure 2.6 shows the mass transfer from the bulk solution with concentration c, to the crystal surface with equilibrium concentration, c*. Surface reactions take place in the crystal-solution interface, denoted as the adsorption layer with concentration c_i. If the processes on the crystal surface is rapid (c_i~c*), the transport of ions from the bulk solution to the adsorption layer controls the growth process. The rate of this diffusion step is proportional to the concentration difference (c-c*) which consequently relates the growth rate to the relative supersaturation with a linear dependence (g=1).[36] When the transport from bulk to crystal surface is rapid (c_i~c), the growth rate is determined by the surface reactions including adsorption of growth units to the crystal surface and their incorporation into the lattice sites. Spiral growth appears when the growth units integrate in the kinks with a rate proportional to driving force. The kink density also varies proportionally with relative supersaturation which results in a parabolic dependence of growth rate on it. The assumptions leading to growth rates are similar for spiral growth and polynuclear growth with the difference in the source of steps.[40] Compared to spiral growth, kink density increases more strongly with increasing supersaturation for polynuclear growth and results in an exponential dependence in between.

As a result, in general the values of *g* and the corresponding growth mechanisms can be given as:

- $g = 1$; mass transport and diffusion-limited growth
- $g = 2$; screw dislocation growth
- $g > 2$; polynuclear growth (2D surface nucleation)

Figure 2.7 summarizes the dependence of growth mechanism and rate on supersaturation, by showing the possible mechanisms with increasing driving force and how they correlate with the growth rate. However it should be noted that it is rather common that the rate of a crystal growth would be controlled by multiple mechanisms. If they are acting on growth in parallel (eg. spiral growth and 2D nucleation), the faster one becomes the rate-determining mechanism and would be expressed more strongly in the rate equation. On the other hand if different growth mechanisms act consecutively (eg. bulk diffusion and spiral growth), the slower reaction determines the overall rate.

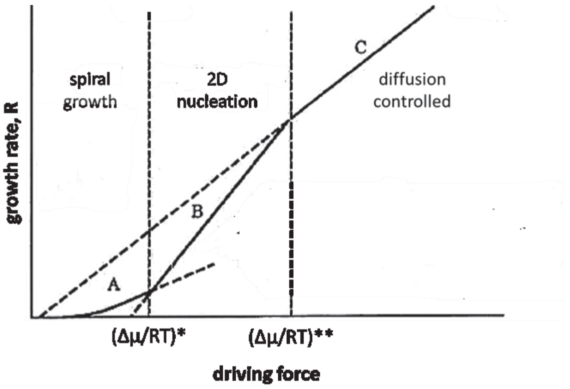

Figure 2.7. The growth rate versus driving force diagram showing the expected growth models with solid lines. Slope of the curves indicate the dependence of growth rate on the driving force with respect to associated mechanism.[19]

2.2.2.5 Determination of Growth Rates

The growth rate of minerals can be quantified in terms of face growth rates or overall growth rates with different experimental techniques. The single crystal growth techniques with microscopic measurements can be used for determination of individual face growth rates of a crystal for a fundamental assessment of the growth kinetics and mechanism of a mineral. On the other hand, the overall growth rates can be measured in terms of the total mass deposited per unit time per unit area of the crystal surface regardless of the contributions from individual faces.[16]

Quantification of overall growth rates can be made conveniently by monitoring the changes in solution supersaturation. Depending on the rate of growth and the concentration range of the experimental conditions batch (desupersaturation) or constant composition experiments can be used for growth rate determinations. In the batch experiments supersaturation is allowed to be continuously consumed by growth. Then, the growth rate can be determined by monitoring the consumption of supersaturation with respect to time in units of deposited mass (dM/dt) or concentration change of precursor ions (dC/dt) as given:

$$R = \frac{1}{A}\frac{dC}{dt} \tag{2.26}$$

where A is the surface area of the seeds. In order to obtain reliable data during desupersaturation, the changes in solution composition due to growth should be accurately detectable. Thus, batch experiments are not efficiently applicable for the kinetic studies of slow growing minerals at low supersaturation range. Data obtained by batch experiments cover a range of supersaturation which can evoke nucleation and growth of additional crystal phases or polymorphs, and different growth mechanisms with changing driving force. Therefore, the experimental conditions should be well-defined to prevent supersaturation consumption by any other process than the growth of the crystal of interest, and interpretation of the results to define the growth mechanism should be made with caution.

In the constant composition experiments initial conditions are maintained by the addition of titrant solutions to compensate for consumption of precursor ions, pH and ionic strength so that the supersaturation is kept constant at its initial value. The working principle of constant composition method lies in observing the concentration fluctuations of a variable due to growth, upon which addition of titrants is triggered by use of automated titration systems with high sensitivity. Thus, this method provides better accuracy, reproducibility and control over growth rate determinations at well-defined conditions and enhanced applicability for growth studies of slow growing minerals. Growth rates are calculated by relation to the rate of titrant addition:

$$R = \frac{1}{A}\frac{dV}{dt}C_{eff} \tag{2.27}$$

where the effective concentration (Ceff) denotes number of moles precipitated per liter of titrant addition and dV/dt is the titrant curve gradient. A drawback of constant composition method over batch experiments is the surplus experimental work it requires.

2.2.2.6 Crystal Dissolution

Compared to the well-established theories of crystal growth, dissolution has not been investigated in detail until the last two decades, and has usually been evaluated analogously to growth.[42] In this concept, the dissolution rates vary with the Gibbs free energy change. The first step is the formation of a pit analogous to 2D nucleation on the surface and when the pit reaches the critical size, spontaneous dissolution occurs. The rate of dissolution (R_d) is expressed as:

$$R_d = k\sigma_u \tag{2.28}$$

where σ_u represents the undersaturation and can be given as:

$$\sigma_u = 1 - S \tag{2.29}$$

According to Equation 2.28, dissolution rate is dependent only on variables that effect supersaturation, and temperature that is included in the rate constant. Therefore when the undersaturation is maintained, dissolution rate should be constant. However, experimental studies showed deviation from this linear relation and dissolution rates were observed to be decreasing over time.[43] Recently developed theories for crystal dissolution take into account the effect of particle size on the rate of dissolution to account for these deviations.[44-46]

According to classical theories analogous to formation of a 2D nucleus, the free energy change for the formation of a pit can be given as:

$$\Delta G = \frac{\pi r^2 h}{\mathrm{v}} kTlnS + 2\pi rh\gamma \tag{2.30}$$

where r is the radius and h is the depth of a pit, and v is the molecular volume. When the solution is undersaturated, the first term on the right hand side of the equation becomes negative and generates the driving force for spontaneous dissolution. The second term of the equation is positive due to increasing surface roughness and interfacial area between the solid and liquid. Therefore a critical radius, r_c, giving the maxima for the Gibbs free energy change can be formulated as:

$$r_c = \frac{\gamma \mathrm{v}}{|kTlnS|} \tag{2.31}$$

The recent theories supported by AFM studies presented that only the pits with a radius larger than r_c provide the active sites for dissolution.[46] As the radius of the pits come closer to r_c by the decreasing crystallite size, their contribution to dissolution is suppressed or even inhibited.

2.2.2.7 Phase Transformations

For a defined set of experimental conditions (eg. temperature, pressure, composition), the solid phase resulting in the minimum free energy in the system is thermodynamically the most stable one and all other phases appearing under the same conditions are metastable with respect to this phase. However, although they are metastable, those phases can still appear and exist in the system for relatively long periods of time (Ostwald Rule of Stages). Metastable phases (phase 1) are potentially capable of transforming to the stable phase (phase 2) and the driving force for this process, ΔG_{trs}, is minimization of the total free energy of the system.[47]

$$\Delta G_{trs} = G_2 - G_1 < 0 \tag{2.32}$$

Even if a system theoretically allows for phase transformation, it can be hindered by kinetic constraints. In such cases, transformation can be ensured if the particles of the stable phase are present in the system already. The transformation between solid structures can occur via internal rearrangement of molecules or atoms in the solid state (solid-solid transformation), or through dissolution and reprecipitation in the solvent-mediated environment. The kinetics of solvent-mediated transformation established by Cardew and Davey is discussed in detail below.[48]

For a structural solid-state transformation, during which the chemical formula is not altered (polymorphic transformation), local atomic movements can induce the change. On the other hand, if the transformation reaction results in a solid phase with a different chemical formula, then long-range diffusion and solid-state reactions occur.[49]

In a solution in equilibrium with the metastable solid and supersaturated with respect to stable phase, the solvent-mediated transformation initiates by the appearance of the nuclei of the stable phase. The driving force for the nuclei formation, ΔG_f, originates from the supersaturation in the system:

$$\Delta G_f = -\upsilon R_g T ln S \tag{2.33}$$

As these nuclei grow, solution becomes undersaturated with respect to the metastable phase. Thus, the metastable solid dissolves and produces supersaturation for the continuing growth of the stable phase. This dissolution-growth process continues until metastable phase disappears and the transformation is complete.[48] In other words, the difference between the driving forces of formation of both phases constitutes the thermodynamic driving force for the transformation reaction:[50]

$$\Delta G_{trs} = \Delta G_{f,stable\, phase} - \Delta G_{f,metastable\, phase} \tag{2.34}$$

Combining Equation 2.33 and 2.34 reveals that, the driving force for the transformation of one phase to another originates from the difference in their solubility at defined conditions.

The overall rate of a transformation reaction depends on the relative kinetics of dissolution and growth reactions which in turn determines the supersaturation profile of the solution. If the growth of the stable phase is too slow compared to dissolution, then the transformation rate is growth limited. In that case, dissolution of the metastable phase can maintain the supersaturation of the solution close to its initial value (Figure 2.8A). On the contrary, when the transformation is dissolution-limited, the consumption of supersaturation proceeds faster due to fast growth (Figure 2.8B).

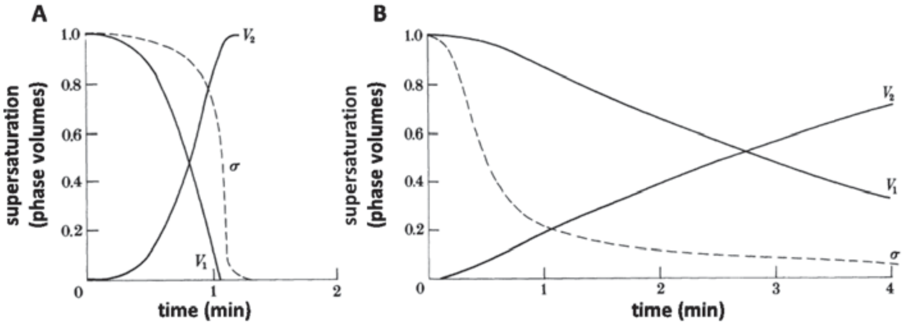

Figure 2.8. The change in volume fraction of each phase and the supersaturation for (A) growth-controlled, and (B) dissolution-controlled transformation with a parabolic growth law.[48]

The rates of both dissolution and growth reactions can be expressed with regards to the rate law:

$$R_d = -k_d(\sigma_i - \sigma) \tag{2.35}$$

$$R_g = k_g\sigma \tag{2.36}$$

where σ is the relative supersaturation in solution with respect to the growing phase and σ_i is the driving force at the start of the transformation process resulting from the solubility difference of two phases. In the cases when two responsible reactions for transformation reach comparable kinetics, a plateau supersaturation, σ_p, can be obtained that represents the point at which the mass dissolution and growth rates are balanced:

$$-\frac{dM_d}{dt} = \frac{dM_g}{dt} \tag{2.37}$$

Combining Equation 2.37 with the rate law expressions at plateau supersaturation enables expressing the equilibrium condition:

$$\alpha_1 k_d A_1 (\sigma_i - \sigma_p) = \alpha_2 k_g A_2 \sigma_p \tag{2.38}$$

where α and A are the shape factor and the total surface area of the dissolving and growing phases. As can be seen from Equation 2.38, the value of plateau supersaturation depends on the kinetic constants and the relative surface areas of two phases and it can be detected as a shoulder in the desupersaturation profile.

2.2.2.8 Determination of Transformation Rates

Transformation rates can be studied with microscopic, spectrometric and thermal methods via quantifying the extent of transformation during the course of reaction.[50,51] However these methods do not give a mechanistic insight on the process.

Solvent-mediated phase transformations consist of two subsequent processes as dissolution and growth. Whether the overall reaction rate would be dissolution or growth controlled depends on the kinetic coefficients of these reactions and the relative surface areas of the individual phases as stated above. By monitoring the changes in supersaturation profile of the reaction solution different regions in the transformation process and the corresponding controlling mechanisms can be detected as well as the equilibrium state between dissolution and reprecipitation reactions.

2.2.3 Non-Classical Theories of Crystallization

The well-established theories of classical nucleation and growth have been applied to many systems successfully. However, a number of phenomena associated with crystal formation, especially with *in vivo* mineralization of organisms, have been challenging to evaluate within the classical interpretations. As a result, alternative pathways for nucleation and growth of crystals from supersaturated solutions have been proposed.

In contrast to monomer attachment model proposed in classical nucleation theory (CNT), particle-based pathways for nucleation via aggregation of solution species have been proposed in an increasing number of studies during the last decade. Generally referred as prenucleation clusters, the aggregates are reported to comprise of ion complexes or multi-ion clusters and have been assigned either stable or metastable nature with respect to the monomers in solution.[52] It is important to note here, the very nature of these clusters defines whether the proposed hypothesis contradicts to the CNT or propose supplementing ideas to classical approach by taking free energy landscapes and kinetic contributions into account. For example in their study of CaP crystallization Habraken *et al.* explained the formation of amorphous phase at conditions that could not be reconciled with classical theory by the existence of prenucleation clusters that form due to resulting in a local free energy minimum in the system but are still metastable with respect to the monomers. Defined as multi-ion complexes here, these prenucleation clusters lowered the nucleation barrier for the amorphous phase so that the observed non-classical route for amorphous CaP formation could be explained using classical theory.[53] On the other hand, the prenucleation clusters proposed by Gebauer *et al.* are claimed to be stable solutes without a phase interface which defines a clearly contradicting thermodynamic landscape to CNT. Their formation was suggested to be energetically favorable due to entropic contributions without an energy barrier to overcome.[54] However, this concept is highly debatable and experimental evidence associated with this hypothesis has been argued by subsequent studies mentioning their applicability to a classical point of view.[33]

Whether the nucleation occurs through monomer addition or particle aggregation, the first phase to form might be of amorphous nature or consist of a different crystal phase than the stable final product. In accordance, two-step nucleation mechanisms (Figure 2.9), including precursor phases different from as predicted by CNT, have been proposed such as dense liquid precursors (DLP) and amorphous states.[32,55] The distinguishing point of these mechanisms that classifies them as non-classical is that the crystalline phase nucleates directly from the early precursors.[56] These studies propose pathways where the energy barrier for nucleation is overcome via a stepwise manner.

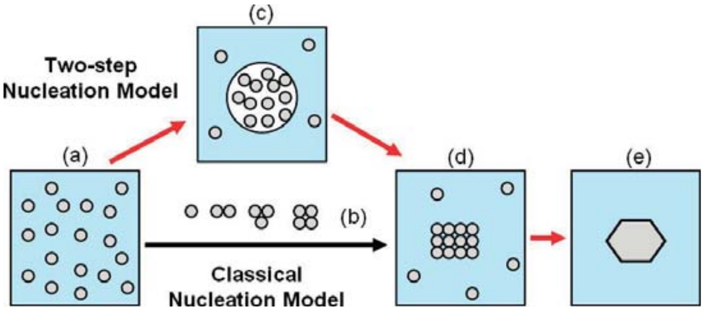

Figure 2.9. Alternative pathways of crystal formation in solution; (a) supersaturated solution, (b) ordered subcritical clusters of solute molecules as proposed by CNT, (c) liquid-like clusters of solute molecules as dense precursors proposed by two-step nucleation theory, (d) ordered crystalline nuclei, and (e) crystal.[55]

Alternative theories to classical growth mechanisms have also been proposed employing the particle aggregation models such as oriented attachment and mesocrystal formation (Figure 2.10). According to classical approach, growth by agglomeration can only occur when crystal particles in solution approach each other closely and grow during in contact. Hence it is a rather rare process.[57] Recent non-classical hypotheses suggest aggregation as a growth mechanism that can lead to formation of poly- or monocrystalline structures by the assembly of nanosized units. It should be noted that no general quantitative background have been established for these mechanisms yet, opposed to well defined rate expressions of classical growth mechanisms.

According to oriented attachment mechanism supersaturation is eliminated during initial formation of primary nanoparticles, and these nanoparticles then unite together to form single crystals by spontaneous self-organization (Figure 2.10b).[58] The crystallographic orientation of the particles with respect to each other is proposed to be determined by the minimization of the free energy. Oriented attachment has been demonstrated for some systems involving the assembly of up to hundreds of particles.[59] However, it should be emphasized that assignment of similar mechanism for the formation of micron-size crystals requires much higher numbers of primary particles and highly efficient assembly mechanisms.[57] Mesocrystals are also defined as colloidal crystals composed of individual nanocrystals that are aligned via self-assembly. It is proposed that they form in two phase systems one phase being the nanoparticles (other can be polymer etc) and as nanoparticles are aligned crystal fusion is thermodynamically favored under displacement of the polymers, eventually forming a single crystal.[60] They have been shown to exhibit scattering properties similar to single crystals, however, this theory is also highly debated and recently criticized for misinterpretation of XRD data.[61]

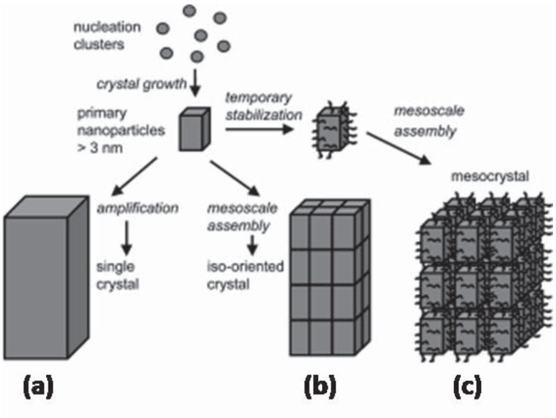

Figure 2.10. Schematic representation of proposed pathways for crystal growth; (a) classical pathway, (b) oriented attachment, and (c) mesocrystal formation.[60]

2.3 Effects of Additives on Crystallization

Any substance in the reaction medium other than the material being crystallized is considered as an additive or impurity in the precipitating system.[16] Additives can have profound effects on crystallization kinetics, and on the composition, structure and morphology of the resultant crystal.

On nucleation, additives show both promoting and inhibitory effects depending on the acting mechanism based on CNT. As shown in Equation 2.16, the free energy barrier for nucleation is highly affected by the temperature, supersaturation and the interfacial energy. Promoted nucleation rates can be observed if the presence of additives decreases the activation energy barrier to form stable nuclei via creating heterogeneous nucleation sites and reducing the interfacial energy parameter.[62-64] On the other hand, the presence of an additive might interfere with the kinetic factors of nucleation that are expressed in the pre-exponential factor, A, in the nucleation rate equation (Equation 2.17). In the cases where additives cause repulsion forces, interfere with the incoming flux of monomers to the nuclei surface or block the nucleation sites, their presence can lead to decreased nucleation rates.[65]

Non-classical pathways suggested for nucleation cast different roles on additives where they are effective on nucleation rates via altering mechanisms. Gower et al. proposed that in the presence of polymers as additives, a liquid-liquid phase separation can be induced in solution which aids in nucleation.[66] These "droplets" are defined as a highly hydrated amorphous precursor phase that behaves as a liquid and named as Polymer Induced Liquid Precursor (PILP). After their formation, it is stated that these droplets coalesce and start to crystallize while excluding the polymeric impurity. Also recently, prolonging effects of additives on crystal nucleation times have been associated with the stabilization of precursor phases. Studies on both calcium carbonate and calcium phosphate systems suggested the formation of amorphous precursors prior to crystallization and although different mechanisms for crystal formation were proposed in these studies, longer induction times were related to the increased life time of the unstable precursor phase with the presence of additives.[67-69]

Additives have been shown to inhibit or promote crystal growth process in accordance with the varying mechanisms they evoke. In general, evaluated within the framework of classical theory, inhibition of crystal growth is caused by adsorption of additives to the active growth sites of crystals (Figure 2.11) and promotion of growth is either a result of formation of a less soluble compound than that formed in the absence of additive, or the lowering of edge free energy that promote crystal growth, in particular at low supersaturation.

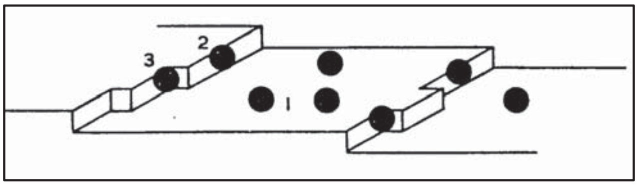

Figure 2.11. Sites for impurity adsorption on a crystal surface based on Kossel model; (1) face, (2) step, (3) kink.[70]

To create a gain in the free energy of adsorption for a surface-additive pair, most prominent contributors are:[13]

- direct Coulombic interactions
- dipole-dipole interactions
- Van der Waals forces, directional polarization forces

- specific chemical interactions such as metal-ligand interactions or hydrogen bonding
- solvation forces, entropy changes by solvent interactions

The reason behind the drastic influence of polar molecules, polyelectrolytes and chemically similar additives on adsorbent surface lies in corresponding contribution. Therefore, efficacy of the adsorption of an additive can be evaluated in such terms.

There are four well-distinguished mechanisms where ions or molecules alter the growth kinetics by changing the step velocity or the step free energy through adsorption:[37]

- step pinning
- incorporation
- kink blocking
- step edge adsorption

In *step-pinning* mechanism, additives are adsorbed on the step edges and the step can only advance by growing around those blocked sites. As the spacing between the impurities get smaller (e.g. due to increase in additive concentration), the growth is suppressed or even inhibited completely. *Incorporation* occurs when impurities are captured by the advancing steps or kink sites and become a part of the growing crystal. This results in distorted crystal structure and thereby an increase in the internal energy of the solid. Consequently, the solubility of the solid increases, and in turn, the effective supersaturation and the growth rate decreases. However, it is important to note that incorporation mechanism does not have to result in lowered growth rates always. At sufficiently low additive concentrations, the increase in the entropy of the solid due to distortion may stabilize the structure and decrease the solubility instead. *Kink blocking* is an effective growth inhibition mechanism. When impurities adsorb to the kink sites, even without incorporation, they decrease the kink site density and reduce the rate of growth via a kinetic contribution. The additives that lower the interfacial energy by adsorbing to the surfaces are called *surfactants*. They modify the growth kinetics by lowering the step edge energy.

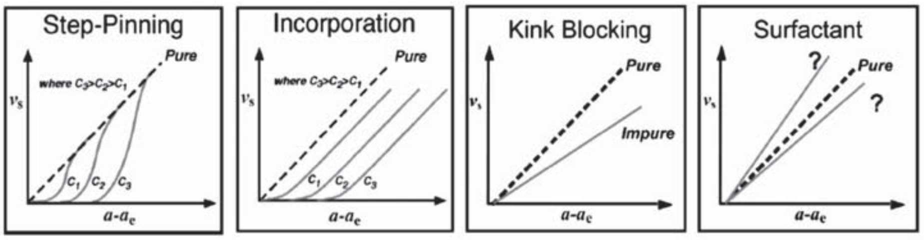

Figure 2.12. The mechanisms of impurity effects on growth kinetics; ‘c’ represents the concentration of impurity, ‘v_s’ is the step velocity and ‘a-a_e’ is the activity based supersaturation.[37]

Crystals can have different growth rates at individual faces, and the relative growth rates determine their final morphology where slow growing faces dominate on the final shape. When additives show selective interaction to certain faces depending on the molecular packing of the crystals, changes in morphology is observed and can be used as an indication of specific interfacial interaction. As an example, the study of Jongen *et al.* clearly demonstrated the selective adsorption of hydroxyl propyl methylcellulose (HPMC) additive on copper oxalate, that in turn resulted in more profound morphological changes with increasing additive concentration (Figure 2.13).[71]

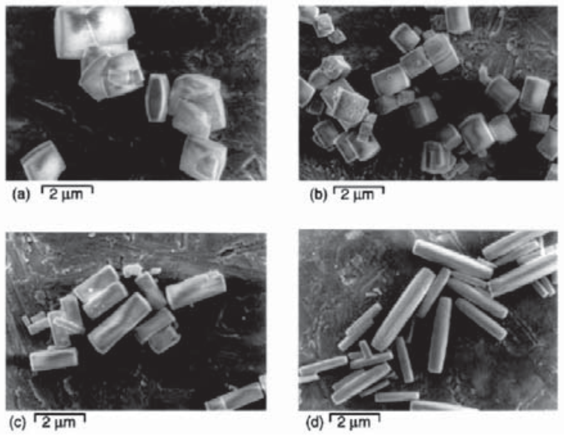

Figure 2.13. SEM images of copper oxalate precipitated (a) without the additive and with the additive concentration of (b) 0.005 g/L (c) 0.0195 g/L and (d) 0.156 g/L.[71]

2.4 Calcium Phosphates

Calcium phosphate (CaP) mineralization has been under extensive research mostly due to their relevance in medical issues as they constitute the main mineral content in human bone and teeth. A lot has been highlighted on the formation mechanism of CaP minerals and yet as many aspects are to be explored.

Table (2.1). Chemical formulas, Ca:P ratios and solubility products at 25 °C of some CaP minerals [9]

Compound	**Chemical formula**	**Ca:P ratio**	**-log(K_{sp})**
Amorphous CaP (ACP)	$Ca_xH_y(PO_4)_z.\ nH_2O$	1.20-2.20	23.9-28.3
Brushite (DCPD)	$CaHPO_4.\ 2H_2O$	1.00	6.59
Monetite (DCPA)	$CaHPO_4$	1.00	6.90
Octacalcium phosphate (OCP)	$Ca_8(HPO_4)_2(PO_4)_4.\ 5H_2O$	1.33	96.6
α- tricalcium phosphate (α-TCP)	α-$Ca_3(PO_4)_2$	1.5	25.5
β- tricalcium phosphate (β -TCP)	β -$Ca_3(PO_4)_2$	1.5	28.9
Hydroxyapatite (HA)	$Ca_{10}(PO_4)_6(OH)_2$	1.67	116.8

Due to the existence of several CaP phases with variations in their chemical formula and solubility (Table 2.1), CaP formation is a highly complex and dynamic process. During precipitation from solution, multiple phases can form simultaneously and undergo transformation where the end product(s) of any precipitating system is governed by both thermodynamic and kinetic factors. As can be seen from Figure 2.14A, HA is thermodynamically the most stable phase at any pH value higher than 4, however, different and multiple CaPs commonly form from a supersaturated solution through sequential precipitation of phases in accordance with Ostwald's rule of stages due to kinetic preference.[9] Thus, control over final products can be attained via manipulating variables that affect either of these elements.[72] In CaP precipitation from solution, the supersaturation level and pH of the reaction medium are the two most influential factors on the final products.[73] The supersaturation in solution with respect to individual phases depends on their relative solubility and constitutes the main thermodynamic component. The high dependence of the CaP system on pH is linked to the triprotic phosphate equilibria (Figure 2.14B). The variations in pH value alter the relative activities of the deprotonated forms of phosphoric acid, and thus affect the supersaturation with respect to individual phases. Another factor to be considered during controlled precipitation of CaPs is the ratio of calcium to phosphate ions in solution that has been shown to exert a secondary effect on the precipitation product via effecting the solution speciation and the kinetics of incorporation due to the differences in activation barriers for calcium and phosphate ions.[74,75]

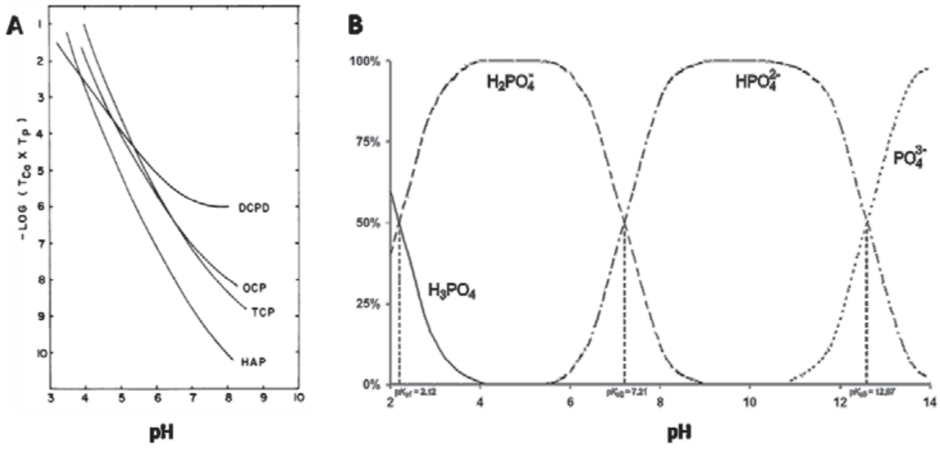

Figure 2.14. Solubility isotherms of CaP minerals at 37°C (A) and the dissociation of phosphate species with respect to pH (B).[76]

2.4.1. Biologically Related Calcium Phosphate Phases

Amorphous calcium phosphate (ACP) is one of the most frequent forms of CaP minerals observed in biological organisms, and the intermediate phase during formation of several CaPs both *in vivo* and *in vitro* conditions.[77] The chemical composition of ACP shows strong dependence on the reaction conditions where Ca:P ratio can change between 1.20-2.20 mainly with respect to pH of the reaction medium, and consequently results in variations in the solubility product.[9] In alkaline media, the most commonly found ACP has the formula of $Ca_3(PO_4)_2 . nH_2O$, with a Ca:P ratio of 1.5. In more acidic solutions, the content of HPO_4^{2-} ions increases and leads to lower Ca:P ratios.[78] ACP phases with Ca:P ratios higher than 1.5, can also be obtained in the presence of foreign ions such as carbonate and oxide. In general, ACP is a highly unstable phase and readily hydrolyzes to crystalline CaPs, where the final phase depends strongly on pH and the lifetime of ACP in solution has been shown to be a function of pH, ionic strength, temperature and presence of additive molecules or ions.[79] In highly alkaline solutions, transformation dominantly results in HA formation whereas mild alkaline and more acidic conditions lead to OCP and brushite formation, respectively.[78] The formation mechanism of ACP has been under extensive research and different hypotheses have been suggested. Posner's clusters, $Ca_9(PO_4)_6$, have been initially proposed as the building blocks for ACP, and samples from both synthetic and biological systems have been shown to contain these ion clusters.[80] However, further studies also suggested other pre-nucleation species and ACP phases that vary in structure and chemical composition depending on the reaction conditions.[78] Different hypotheses on ACP formation have suggested; stable prenucleation clusters which aggregate and form ACP [81], presence of soluble ion-complexes that lead to ACP precipitation by aggregating and taking up extra calcium ions from solution [53], and two-step formation that includes formation of an initial ACP phase via ion-complexes that later transforms into a second ACP phase through densification.[82] In the presence of polymeric additives, PILP mechanism is also suggested where liquid phase separation leads to a pseudo phase which then precipitates to form solid ACP.[83]

Brushite, also commonly referred as dicalcium phosphate dihydrate (DCPD), is the predominant crystalline phase during precipitation from solution at pH values below 6.5. It consists of calcium-phosphate chains and water bilayers in its lattice structure. *In vivo*, brushite might occur under pathological conditions and is found in urinary stones, and also has been suggested as one of the precursor phases prior to apatite formation.[84,85] Due to its high resorbability among CAPs, it has been suggested as a good candidate for bone tissue engineering composites and a coating material for implants since it would allow ready remodeling to apatite. The incongruent dissolution of brushite and its ready transformation leads to formation of Ca-deficient HA. Recent studies have shown, monetite, the anhydrous form of brushite, can also be employed as a successful precursor for biomimetic HA synthesis. The similarity between the crystal structures of monetite and HA promotes the direct phase transition and formation of HA with a closer resemblance to its biological counterpart.[86,87] Monetite can be obtained by precipitation from solution at similar pH range to brushite at temperatures above 80 °C, or by dehydration of brushite through thermal treatment.[88]

In aqueous solutions with pH values above 6.5, octacalcium phosphate (OCP) becomes the dominant precipitating phase. *In vivo*, OCP is one of the stable phases found in human dental and urinary calculi.[89] In addition, it is generally accepted that OCP is a precursor to bone apatite formation *in vivo*, which has been supported by the observations of a central OCP inclusion (also known as "central dark line") by high resolution electron microscopy in many biological apatites and in synthetically precipitated Ca-deficient HA.[90] OCP exerts a triclinic structure, separated by hydrated layers, which shows high structural similarity to HA and thus, epitaxial growth of these phases can be observed.

HA is thermodynamically the most stable phase among CaP minerals however due to the slow nucleation kinetics associated with its high interfacial energy, it usually forms through the stepwise transformation of less stable precursor phases in accordance with the Ostwald's rule of stages. Formation of HA without the initial precipitation of other CaPs can be achieved in solutions supersaturated only with respect to HA.[9] Apart from that condition, in acidic and neutral media, initial formation of kinetically favorable brushite or OCP is observed. In basic conditions the initial precipitation of these acidic CaP phases can be ruled out, and ACP formation is observed prior to HA.[91] Stoichiometric HA has a Ca:P ratio of 1.67, however both synthetic and biological forms deviate from stoichiometry and can exert Ca:P ratios between 1.50-1.67 due to the susceptibility of this crystal phase to ion substitutions. The formation mechanism of biological apatites has not been fully understood yet due to the high complexity of *in vivo* systems, however, investigations of *in situ* HA formation shed a light on this process. Most of these studies indicate a precursor-mediated pathway where ACP is a frequently suggested precursor.[79,92]

2.4.2. Phase Transformations of Calcium Phosphate Phases

Phase transformation processes are significantly relevant in CaP precipitation due to the existence of several phases with different solubility products. The course of reaction and the final products are dynamically dependent on both thermodynamic and kinetic factors. In this work, the formation of HA through phase transformation reactions of brushite and ACP are studied in detail, therefore, relevant literature is summarized below.

There is a general agreement that brushite transformation to more stable CaPs (such as OCP and HA) proceed via a dissolution-reprecipitation pathway in solution (hydrolysis) where new nuclei form after dissolution of brushite and brushite surface can act as a heterogeneous growth site.[93] Investigations on brushite hydrolysis revealed multiple variables that can act on the transformation reaction such as modifying brushite, altering reaction conditions and incorporating additives in the reaction medium. Modification of brushite via substitution of different cations affected both the transformation kinetics and the end product of hydrolysis.[94,95] In their study, Kumar *et al.* suggested that the morphology of potassium substituted brushite with a lattice strain and higher internal energy resulted in increased rates of transformation.[94] On the other hand, Madsen related both promoting and inhibiting effects of different cation substitutions on brushite hydrolysis to the effects of additives on the nucleation of the stable phase.[95] Presence of amino acids and polymers are also shown to have profound effects on brushite transformation through different mechanisms depending on the nature of interactions between the additive and the mineral phases. In their detailed study on brushite hydrolysis in the presence of amino acids, Tang *et al.* showed that amino acids can modify the interfacial energy barrier between brushite and HA, thus, affect the transformation kinetics via acting on the kinetics of heterogeneous nucleation.[96] Same group documented similar acting mechanism with citrate on induced transformation of brushite to HA in its presence.[97] In contrast, Chan *et al.* pointed out that glutamic acid facilitated the transformation of brushite to first OCP and then to HA by the disruption of the water layer bound on the crystal surface.[98]

Transformation of ACP into more stable phases has been under widespread research since ACP is now generally accepted as a precursor phase in *in vivo* bone formation.[80] However, the exact mechanism of this transformation is still under debate. Along with the experimental difficulties associated with ACP instability, effects of biomolecules on the crystallization process *in vivo* introduce additional complexity into this system. Classical routes have been proposed for ACP transformation which are directed by the chemical potential difference (supersaturation) between ACP and stable phases, and proceed via either dissolution-precipitation pathway in solution, or solid state transformation.[99] In addition, nonclassical pathways have also been suggested where transformation is independent of supersaturation in the system. In their studies, Tang *et al.* proposed a solution mediated surface nucleation process where HA heterogeneously nucleates on ACP via a polymorph transformation and kinetics of this reaction is a function of the amount of ACP in the system and the activity of calcium ions to be uptaken during formation of HA.[67,100-102] Nancollas *et al.* and Wang *et al.* proposed a different internal rearrangement mechanism where HA nucleation takes place within the ACP precursor through a solid-solid transformation.[82,91] Depending on the proposed transformation mechanism, additives have been given different roles for how they act on the transformation reaction. Presence of additives can directly affect the nucleation rate of HA, or the solubility of the ACP phase, which consequently reflects on the solution supersaturation and thus, the nucleation rate of HA, from a classical point of view. In contrast, if the phase transformation is independent of supersaturation as proposed by some studies, additives gain the role of stabilizing the ACP phase through surface interactions either by interfering with the surface nucleation of HA or limiting the mass transfer between the solid and solution.

2.5 Alginate

Polysaccharides perform a variety of functions in living organisms and have recently emerged to be important in the regulation of biomineral formation.[103,104] As a member of the polysaccharide family, alginate has been conveniently used in biomimetic mineralization studies as well as drug delivery and tissue engineering applications in the form of hydrogels, scaffolds, beads and etc.[105]

Alginate is a linear copolymer, derived from brown sea algae and composed of 1-4 linked β-D-mannuronic acid (M) and α-L-guluronic acid (G) residues with an alternating or block structure. The pKa values of M- and G- repeating units are 3.38 and 3.65, respectively and the pKa value of alginate polymer differs only slightly from its monomers. The viscosity of the alginate solutions increases with decreasing pH and reaches a maximum around pH $\approx$ 3-3.50 as carboxylate groups in the backbone become protonated and form hydrogen bonds. The M- and G- units of alginate differ in the orientation of carboxyl groups that in turn highly affects their functionality. Divalent ions show specific affinity towards the outward carboxyl groups of the G- units of alginate and can bind to G-blocks and alternating blocks of the polymer but not to M-blocks. This is achieved through cooperative binding of functional negatively charged carboxyl groups of G units to divalent cations. As a result, the physical properties of alginate and how it regulates mineralization become highly dependent on its chemical composition, sequential structure of the repeating units and molecular weight.

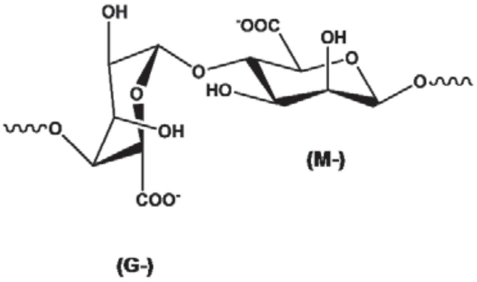

Figure 2.12. The chemical structure of M- and G- building blocks of alginate.

Effects of alginate on the crystallization process of minerals have been studied by our group and others previously. Salgado *et al.* reported that the presence of alginate in the reaction medium resulted in changing the morphology of calcite crystals via specific interactions with certain crystal faces.[106] Olderøy *et al.* showed stronger growth inhibition on vaterite and aragonite compared to calcite and possible polymorph switching by the presence of alginate additives in the reaction medium.[107,108] It was reported by Lakhstanov *et al.* that although presence of alginate decreases the growth rate of calcite, it induces heterogeneous nucleation of new crystals on existing ones.[109] In the case of precipitation from solution, on the other hand, alginate was reported to prolong induction times for nucleation.[69]

Although alginate-calcium phosphate composite materials are greatly studied due for their high potential towards tissue engineering applications, few studies have investigated the interactions between the polymer and mineral phases in detail in terms of the crystallization fundamentals. Few studies focused on the effects of alginate on hydroxyapatite crystallization. Malkaj *et al.* reported decreased growth rates for hydroxyapatite in the presence of alginate.[110] Through precipitation of HA in the varying concentrations of alginate matrix, Son *et al.* concluded alginate promotes nucleation via specific interactions between the calcium ions and carboxyl groups.[111]

CHAPTER 3

EXPERIMENTAL METHODS

3.1 Solution Speciation and Calculation of Supersaturation

The chemical speciation in solution and activity based supersaturation were determined by using thermodynamic calculation programs Minteq 3.0 and PHREEQC Interactive 3.1, both using Minteq v4 database.

For the calculation of activity coefficients, γ, the Davies equation was used:

$$log\gamma_i = -Az_i^2\left(\frac{\sqrt{I}}{1+\sqrt{I}} - 0.3I\right) \tag{3.1}$$

where z_i is the valence of ion i, I is the ionic strength and A is a parameter that can be calculated and depends on temperature and dielectric constant. Ionic strength is defined as:

$$I = \frac{1}{2}\sum_i z_i^2\, c_i \tag{3.2}$$

where c is the concentration and z is the charge of ion *i*. Davies equation was chosen due to its applicability in solutions with $I \leq 0.5$ M.

In order to calculate the chemical speciation and activity of each species, all possible equilibria in solution (i.e. dissociation, ion complexations, phosphate equilibria) were taken into account, by using the corresponding equilibrium constants and activity coefficients. Activity based supersaturation with respect to different CaP phases were then calculated according to Equation 2.7, by dividing the activity product of ions to the corresponding solubility products from the database, as given in Table (3.1).

Table 3.1. Calculation of supersaturation for different CaP phases

Compound	Supersaturation
Amorphous calcium phosphate	$S_{ACP} = \left(\frac{\{Ca^{2+}\}^3\{PO_4^{3-}\}^2}{K_{sp,ACP}}\right)^{1/5}$
Brushite	$S_{brs} = \left(\frac{\{Ca^{2+}\}\{HPO_4^{2-}\}}{K_{sp,brs}}\right)^{1/2}$
Monetite	$S_{DCPA} = \left(\frac{\{Ca^{2+}\}\{HPO_4^{2-}\}}{K_{sp,DCPA}}\right)^{1/2}$
Octacalcium phosphate	$S_{OCP} = \left(\frac{\{Ca^{2+}\}^4\{PO_4^{3-}\}^3\{H^+\}}{K_{sp,OCP}}\right)^{1/8}$
Hydroxyapatite	$S_{HA} = \left(\frac{\{Ca^{2+}\}^5\{PO_4^{3-}\}^3\{OH^-\}}{K_{sp,HA}}\right)^{1/9}$

3.2 Experimental Setup

All experiments were performed in double-walled glass reactors of 0.5 or 1.0 L, connected to a water bath to keep the temperature constant. Nitrogen, presaturated with water, was bubbled into all working solutions prior to and during the experiments to exclude atmospheric carbon dioxide.

3.3 Automated Titrators

The automated titrator systems (Titrando 902/907, Metrohm) are equipped with a high sensitivity pH electrode, a calcium ion specific electrode and four dosing units controlled with Tiamo software. Case-specific measuring or titration methods can be programmed for multiple purposes such as constant pH and constant composition experiments, potentiometric titration, controlled dosing of solutions into the reaction medium or recording of measurable quantities in specified time intervals. The pH and calcium measurements can be used either separately (Titrando 902) or in conjunction (Titrando 907) for monitoring solution composition or as signaling parameters to activate dynamic titration processes where the rate of titrant addition is adjusted automatically in accordance with the variations in the reference signal.

3.4 Determination of Induction Times

Induction times of corresponding CaPs were determined from the spontaneous batch experiments to evaluate the effects of additives on nucleation kinetics. For this purpose, stable supersaturated solutions of the regarding phases were prepared and the pH was monitored continuously. The abrupt drop in the pH was associated with spontaneous CaP precipitation due to the release of hydrogen ions as a result of crystallization. The induction times were then determined as the intersection point of two tangent lines on the pH curve.

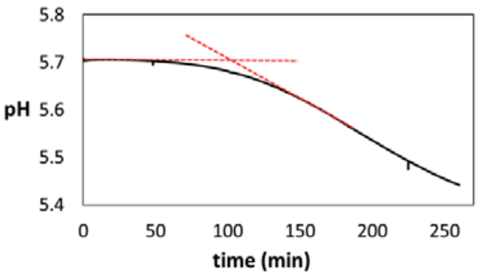

Figure 3.1. The pH curve of a solution supersaturated with respect to brushite that shows stable pH initially and then a fast drop due to the precipitation of brushite.

3.5 Determination of Growth Rates

In this study, overall growth rates were determined in terms of the total moles of precipitation per unit time per unit area, and contributions from individual faces were not quantified. The method for growth rate determinations, either batch or constant composition experiments, was chosen for each crystal phase according to the supersaturation range of reaction solutions and growth kinetics. Seeded batch experiments were performed and shown to be applicable for determination of brushite growth rate at moderate supersaturation. Constant composition method provides better accuracy, reproducibility and control particularly over the kinetic studies of slow growing minerals at low supersaturation range since it enables growth rate determinations at well-defined conditions. Therefore, the growth rate of HA and brushite at low supersaturation were determined by seeded constant composition experiments.

3.5.1. Seeded Batch Experiments

The growth rate of brushite was quantified with seeded batch experiments at an initial supersaturation of 2.34 with respect to brushite in the reaction medium. Stable (~15 min), moderately supersaturated solutions of brushite were prepared and well-characterized brushite seeds were added immediately. Seed amount was determined to ensure the supersaturation was consumed only by the growth of the seeds without additional nucleation. The pH of the solution was recorded continuously and the calcium ion concentration was measured at arbitrary time points after the seed addition. The depletion in calcium ion concentration as a function of time was fitted to a simple exponential function (Figure 3.2A) and its first derivative (dC/dt) was used to obtain the overall growth rate (R) as defined in Equation 2.26. The relative supersaturation at arbitrary time points was calculated with the software PHREEQC by using the measured calcium concentration and pH values (Figure 3.2B). Momentary phosphate concentration was calculated in relation to the consumed calcium amount by the assumption that only brushite growth took place in the reaction medium. Combining the growth rate function with data points of momentary supersaturation, the growth rate was represented as a function of relative supersaturation (σ) so that the rate constant (k) and apparent growth order (g) values were obtained (Fig 3.2C) in accordance with Equation 2.24.

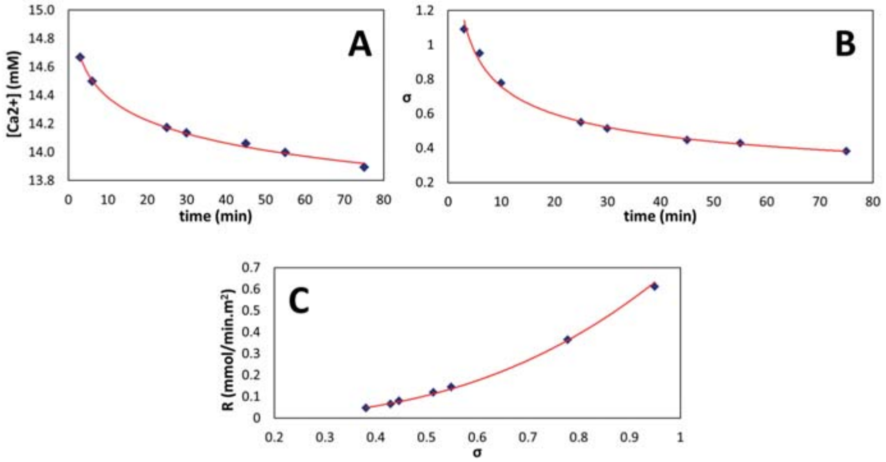

Figure 3.2. Procedure for the determination of growth rates from batch experiments. (A) Measured calcium ion concentration was modeled by a simple exponential function which was used for calculation of growth rate (R), (B) Momentary values of relative supersaturation was calculated by using pH and calcium concentration values by PHREEQC software and (C) Crystal growth rate (R) was plotted as a function of relative supersaturation to obtain k and g values.

3.5.2. Seeded Constant Composition Experiments

Constant composition experiments were used for quantification of the growth rates of HA and brushite at low supersaturation range (S_{HA}= 4.08-6.31, S_{brs}= 0.20-0.55). After preparation of supersaturated solutions and immediate addition of seeds, pH was monitored as an indicator for the course of the growth reactions and any change in pH prompted the simultaneous addition of titrant solutions. The schematic description of the constant composition experimental setup is given in Figure 3.3. Compositions of titrant solutions were adjusted for each working solution to maintain a constant thermodynamic driving force during the crystal growth by compensating for consumed ions in solid phase, changing ionic strength and alkalinity in the reaction media.[112] The chemical composition of the precipitating phase was represented in titrant composition by maintaining lattice ion ratios equal. The rate of precipitation which relates to the level of supersaturation and total surface area of inoculating seed crystals were also regarded to provide appropriate feed to the system. Titrant solutions including calcium and phosphate ions were added from coupled dosing units to ensure simultaneous addition and from opposite positions in the reactor to prevent local high supersaturation. Growth rates were quantified by using the titrant addition curves (Equation 2.27) where the effective concentration (C_{eff}) denotes number of moles precipitated per liter of titrant addition and dV/dt is the titrant curve gradient. Titrant addition curves were normalized to the changing surface area (A) of the seeds with proceeding growth by a factor of $\{(w_f/w_i)^{2/3}\}$ assuming 3D growth, where w_i and w_f represent initial and final masses of growing seeds respectively. Experiments were conducted at multiple supersaturation values and results were used to obtain k and g values (Equation 2.24).

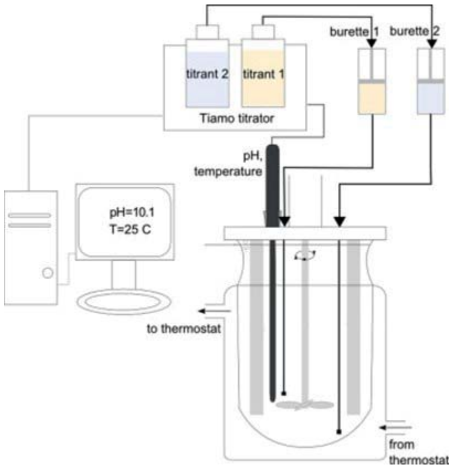

Figure3.3. Schematic description of the instrumental setup used in constant composition experiments.[112]

3.6 Determination of Transformation Rates

Solvent-mediated phase transformations were studied by the investigation of supersaturation profiles. The supersaturation profiles were followed via accompanying changes in pH relating to dissolution and growth reactions that activated the automated titration to maintain the pH at the initially chosen value. By this method, the extent of transformation was monitored from the titrant addition curves and the course of transformation was dictated through the formation of desired phase by the adjustment of pH as a primary control factor on CaP system. In addition, calcium and phosphate ion concentrations were determined at arbitrary time points to support the desupersaturation profiles obtained by pH data and to quantify values of the momentary supersaturation. The changes in the concentration profiles of the precursor ions were used to detect the proceeding reactions in the media. The transformation experiments were conducted under both seeded and unseeded conditions because this method enables to extract further information on the nucleation stage indirectly.

3.7 Characterization of Precipitates

In order to characterize CaP precipitates and to well distinguish between different phases solid precipitates were characterized by powder X-ray diffraction (XRD) (D8 Advance DaVinci, Bruker AXS GmBH) and Fourier Transform Infrared spectrometry (FTIR) (Tensor, Bruker). Scanning electron microscopy (SEM) (Hitachi S-3400N) was used to investigate the morphology of the precipitates. The specific surface area (A) of the seeds was determined by multiple point BET nitrogen adsorption method (Tristar II, Micromeritics) and an average of minimum three measurements was used. The size and number distribution of particles were determined by a Coulter Counter Multisizer (Beckman Coulter). For size determinations an average of three measurements was used in which approximately 10^4 particles were counted during each run.

3.8 Analysis of Solution Species

Calcium ion concentration in solution was determined either by online monitoring in the reaction vessel via the use of calcium ion specific electrode with 902/907 titrators or by the offline titration of filtered samples with EDTA. Samples (2-5 mL) to be analyzed via EDTA titration were kept overnight after addition of 3 mL of 0.1M HCl and dilution to 20 mL with water to dissociate ion complexes of calcium. Before titration, samples were further diluted to 40 mL and 1 mL of 4M KCl was added for ionic strength adjustment. Finally 1 mL of pH 10 NH_3^+/NH_4 buffer were added to maximize the binding capacity of EDTA. Standard calcium solutions were measured for calibration in both methods.

Phosphate ion concentration in solution was determined spectrophotometrically by formation of its molybdate complex and measuring the absorbance by UV-vis spectrometry [113]. For this purpose, a mixed reagent consisting of ammonium molybdate, potassium antimonyl tartrate, sulfuric acid and ascorbic acid was prepared freshly and added in 2 mL portions to the samples of 10 mL in volume. A new calibration curve was established for each preparation of the mixed reagent in the concentration range of 0.02-0.1 mM with regression values of above 0.99 (Figure 3.4). After incubation of samples at room temperature in dark bottles for 30 min, the absorbance was measured at 835 nm.

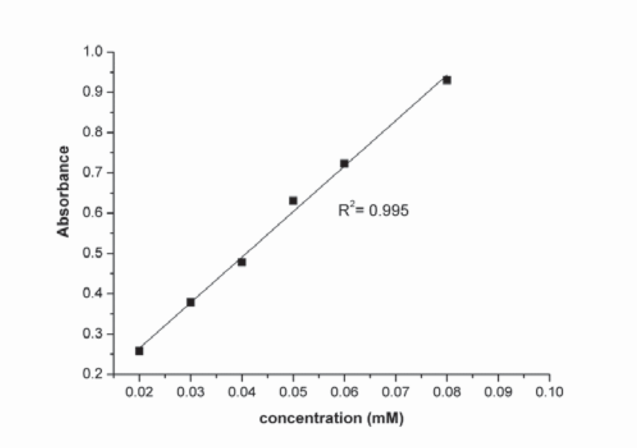

Figure 3.4. Calibration curve for the spectrophotometric determination of phosphorous concentration.

CHAPTER 4

SUMMARY AND DISCUSSION OF PAPERS

4.1 SUMMARY OF PAPERS

Paper I

Nucleation and Growth of Brushite in the Presence of Alginate

Brushite crystallization and the effects of alginate additives on this process were investigated by coupling seeded growth and unseeded batch experiments so that information on both the growth kinetics and mechanism and the nucleation stage could be deduced.

Growth experiments showed that the presence of alginate additives reduce the overall growth rates up to varying extents and change the growth mechanism of brushite differently. Polymer additives affect the growth process via molecular interactions with the crystal surface; thus, by using alginate additives with divergent characteristics (i.e. molecular weight, functionality) their operating mechanisms on brushite growth was investigated.

Oligomers resulted in lower growth rates than high molecular weight alginate and G-blocks were the most influential additives in decreasing the overall growth rate of brushite. In the light of previous research and results obtained in this study, the inhibitory effect of additives on brushite growth was attributed to the molecular adsorption mechanisms. Further inhibition with increasing additive concentration and effective G-units supported the hypothesis that high affinity functional groups can result in more effective adsorption to active growth sites and thus lower the growth rate. Possible mechanistic models of growth were also evaluated by using the apparent order of growth (g) from the growth rate expression (Equation 2.24). According to the evaluations based on the apparent growth order, at high initial supersaturation (S= 2.34) brushite growth in the absence of additives proceeded via a diffusion-controlled mechanism (g=1). High initial supersaturation used in the batch experiments can promote high surface nucleation rates and fast integration kinetics so that the supply of growth units to the active sites becomes the limiting factor on growth. Moreover, since most of the growth takes place under this high driving force, diffusion control is expressed as the overall dominant mechanism. Investigating the brushite growth at a lower supersaturation range (S=0.2-0.55) to evaluate the dependence of growth mechanism on supersaturation, revealed a combined mechanism of surface integration and surface nucleation (g=2.40).

When additives were introduced in the growth media at high supersaturation, higher values of apparent growth order was observed. In the presence of alginate and G-block additives, surface nucleation was the dominant growth mechanism ($g > 2$), whereas with M-blocks surface integration was indicated ($g \approx 2$). Additives containing G-block in their structure show specific affinity towards calcium ions and thus can cause an effective reduction in the active sites by adsorption. New growth sites can be generated by 2D nucleation when the driving force is high enough. This also explains the growth behavior observed in the presence of these additives, where especially with the G-blocks growth was almost completely inhibited as the lower levels of supersaturation were reached. M-blocks on the other hand, do not exhibit a specific affinity towards calcium, and surface nucleation did not occur. However, nonspecific interactions are still likely to occur via ionic interactions and hydrogen bonding and it is evident from the growth rates that presence of M-block oligomers lowered the rates of incorporation by affecting the accessibility of the growth sites. As a result, a change of growth mechanism from diffusion-controlled to surface integration controlled growth was observed and growth still continued at even at low supersaturation region.

Unseeded batch experiments revealed the effects of alginate additives on spontaneous precipitation of brushite. Presence of additives retarded the course of reaction in an increasing order of high molecular weight alginate, M-block oligomers and G-block oligomers. Samples collected at initial and final states of reactions at comparable supersaturation levels showed that the crystals precipitated in the presence of alginate were larger in size than their additive-free counterparts. Since seeded experiments showed reduced growth rates with alginate presence, larger particles at same levels of supersaturation illustrate the reduced nucleation rate and a lower number of particles consuming the supersaturation for growth. In the presence of M-block additives high supersaturation levels were maintained for longer times that can uphold the high nucleation rates. Combined with its growth-reducing effect, the presence of M-blocks led to the precipitation of small size particles high in numbers. In the case of G-blocks with the same upholding effect on nucleation and lower growth rates, even smaller particles would be expected, however, the opposite was observed as in the case of alginate presence. Thus, a retardation effect on nucleation was suggested and it was strongly related to the presence of G-units that is present on both additives.

Morphological investigation of the final crystallization products from batch experiments also indicated the differences in interaction of additives with the brushite crystals. The typical platelet-like morphology of brushite observed in the additive-free experiments is composed of prominent (010) faces of bilayers of structural water molecules and lateral faces (h0l) that express a mixed ionic nature with exposed calcium and phosphate ions. In the presence of alginate, this plate-like morphology was maintained with rough edges. In that case it can be assumed that sterically hindered macromolecules of alginate mainly adsorbed on the dominant faces. In contrast, presence of small M-block oligomers resulted in noticeably thicker particles, which can be interpreted as their preferential adsorption on lateral sites primarily due to ionic interactions. When G-block oligomers were added in the medium smooth dominant (010) faces were no longer retained, demonstrating that the specific affinity of G-units towards calcium is more operational than size and charge effects.

Paper II

Transformation of Brushite to Hydroxyapatite and Effects of Alginate Additives

In this study, the transformation of brushite to HA in solution was investigated by following the solution chemistry because this method enables to do detailed kinetic analysis of the transformation process. Experiments were conducted by monitoring the pH of the medium and keeping it at its initial value through base titration. The changes in solution pH were directly related to the dissolution of brushite followed by HA nucleation and growth, and thus titrant addition curves represented the course of transformation analogously.

The transformation kinetics were evaluated first by adding varying amounts of HA seeds in the medium to change the initial surface area ratio of brushite and hydroxyapatite in the absence of additives to evaluate the controlling mechanism. Titration curves showed an initial linear rate of titrant addition followed by a slightly inclined plateau and a final regime with a logarithmic addition rate. Linear rate of titrant addition was associated with constant transformation rate which indicated a constant driving force (ΔG_{tr}) for the reaction. The calculations of momentary supersaturation, and ΔG_{tr} supported this hypothesis. In the presence of varying amounts of HA seeds, equal transformation rates were obtained when titration curves were normalized to the surface area of the added seeds. Therefore, it was concluded that the rate of transformation was controlled by the rate of HA growth and the dissolution rate of brushite was not a limiting factor in the specified system. The plateau region that represented the establishment of equilibrium between dissolution and growth reactions were attained at the point of almost completed brushite dissolution. After brushite was completely consumed, the supersaturation profile of the solution was determined by HA growth where the final logarithmic part of the titration curves represented the desupersaturation of solutions until the solubility limit of HA was reached. Observation of the plateau and maxima of all curves at equal titrant volumes in experiments with varying amounts of HA seeds also supported this hypothesis since those values were determined by the initial constant brushite amount in all experiments. When additives were introduced, their effects on hydrolysis were studied both by seeded and unseeded experiments. HA seeded experiments showed that during the growth-controlled region of transformation reactions, additives were not highly influential in decreasing the rate of conversion and the differences in conversion rates between the sample groups developed as the transformation reactions proceeded. The retarding effect of alginate and other molecules with carboxyl functionality on HA growth is reported both in literature and in our studies; however, these studies were conducted at low supersaturation ranges (S_{HA}≈1.0-5.4). The supersaturation in the current transformation experiments ($S_{HA} \approx 36$) were high enough to promote high surface nucleation rates, resulting in fast surface integration kinetics and to further lead to a diffusion-controlled process. Thus the retardation effect of additives on growth, resulting from their blockage of active sites on crystal surfaces, might have lost their influence at low additive concentration and high supersaturation during the growth dominated region of transformation. At the plateau region where the rates of dissolution and growth reactions were balanced, supersaturation with respect to both phases reached its lowest value before the transformation reactions were complete. The decreasing supersaturation would lead to decreased growth rates for HA. The plateau region also represented the point of almost complete consumption of brushite which in turn could be associated with its size-dependent dissolution suppression. Therefore it was concluded that the retardation of transformation observed approaching and during the plateau region were resultant of these two outcomes in a synergistic fashion and the effects of additives were expressed more strongly in this region.

In the unseeded transformation experiments, increasing supersaturation due to brushite dissolution resulted in nucleation and subsequent growth. The titrant addition curves displayed an S-shape representative of that process, followed by a plateau and final logarithmic region. The CaP phases present in the medium during the course of transformation were characterized by FTIR, XRD and SEM analyses. Final products of transformation reactions were low crystalline HA in all experiments. During the initial region of the curves before the plateau, gradual dissolution of brushite and formation of the new phase was observed, and when the end of the plateau region was reached, brushite was no longer detected in the medium. XRD spectra of the samples collected at the plateau region did not show any strong diffraction peaks which might be due to the small crystallite size or low crystallinity of the sample below the detection limit. XRD analyses conducted at low angle ($2\theta = 4°-10°$) did not show distinguishable peaks of OCP in any of the samples meaning that the transformation reaction in the specified experimental conditions did not involve OCP as an intermediate phase. When titration curves were represented in terms of percent conversion, it was observed that low conversion percentages were maintained for longer in the presence of additives before reaching the growth dominated region represented by the steepest gradient. Titrant addition curves showed similar steep gradients in the presence of additives, but the time required to generate the critical surface area before crystal growth could dominate the reaction kinetics were effectively prolonged. Therefore by coupling the seeded and unseeded experiments it can be deduced that the alginate additives interfere in the nucleation period of HA and the most effective nucleation retardation was observed in the presence of G-block oligomers.

Paper III

Transformation of Amorphous Calcium Phosphate to Hydroxyapatite in the Presence of Alginate Additives

This study was designed to investigate ACP-mediated HA formation and the effects of alginate additives on this process. The supersaturation level for the experiments was defined to ensure the two-step formation mechanism where ACP formation was observed first and followed by the formation of HA in the system. The course of mineralization was followed by monitoring of pH and calcium ion activity which showed the distinct stages of reaction and coupling of these stages with characterization of precipitates revealed that each stage represented the occurrence of a separate phase in the system. Detailed analysis of additive-free system showed indications of the presence of assembled complex structures prior to phase separation of ACP. Then the first nucleation point marked the precipitation of ACP and the second nucleation point showed the appearance of crystalline nuclei in the system. After the distinct stages of the reaction and the corresponding chemical and structural progression of precipitates were well-defined, the effects of alginate based additives on the course of reaction were investigated. In the presence of additives, the time needed for ACP formation was prolonged where the initial driving force was constant but retardation effect scaled with the efficacy of functional groups of additives. This result led to the assumption that ACP formation can be mediated by the prenucleation complexes where additives interfere with their aggregation/ dehydration/ complexation mechanisms through electrostatic interactions. Alginate and M-block additives were effective also on the kinetics of HA formation and longer induction times were observed in their presence. Evaluation of induction times by considering the contribution of changing growth rates of HA showed that both additives were nucleation retardants and high molecular weight alginate was more effective at equal concentration. Previous studies of ACP-mediated HA formation suggested that the additives can induce such an effect by interfering with the heterogeneous nucleation of HA on the ACP surface. The stronger retardation of nucleation observed with the more G-block containing additives, which can better interact with the surface, can indicate the possibility of this hypothesis in the corresponding system also. In the presence of G-block oligomers, a change was induced in the crystallizing phase after ACP formation and the final precipitates were a mixture of OCP and HA. Considering the stronger effect of alginate observed in decreasing the nucleation rate of HA compared to M-block oligomers, a higher content of G-blocks might further hold down the HA nucleation. In addition growth rate studies revealed that G-block oligomers were highly effective in blocking the active sites on HA crystal surface. Therefore, we concluded OCP mineralization was kinetically favored in the system as a result of effective suppression of HA nucleation and growth.

4.2 DISCUSSION

Naturally derived composite tissues have been a rich source of inspiration for the design of synthetic biomaterials to achieve the requisite physicochemical and biological properties for hard tissue engineering applications.[114,115] Although it is currently not possible to exactly reproduce such materials by synthetic means, extensive research in this field ensures continuous progress towards better replicates. In order to design successful composites, it is essential to understand the interactions between the organic and inorganic building units and develop regulatory strategies for the mineralization process accordingly. The high level of complexity associated with the organic matrix assisted mineral formation requires studies conducted under controlled conditions where the effects of individual variables can be investigated systematically. Accordingly, the work in this thesis has been focused on detailed analyses of mineralization events in a specific composite system of alginate matrix with CaP mineral content that has been designed and investigated in our group as a potential scaffold material for bone tissue engineering applications.

Paper I deals with the fundamental interactions between alginate and brushite since brushite was the target CaP phase to be formed in the hydrogels and precipitation within the alginate matrix showed drastic differences from brushite precipitation in aqueous medium. The results of this study showed that alginate has an inhibitory effect on both nucleation and growth of brushite crystals. Investigating the effects of compositional variations of alginate on crystallization process revealed that the additives affected the brushite growth rates and mechanisms through their adsorption on the active growth sites, and in the presence of G-units, and low molecular weight additives, the adsorption phenomenon was more pronounced. These observations improved our understanding on intermolecular interactions between the mineral phase and the matrix molecule. After its precipitation in alginate hydrogels, brushite transformed to HA upon aging or incubation in SBF. For a bone tissue engineering construct, formation of apatitic mineral is a required functionality as it determines the success of the composite material under *in vivo* conditions. Therefore, in paper II, the transformation of brushite and the effects of alginate additives on this process were investigated by following the supersaturation profiles. This method allowed detailed kinetic interpretations of the transformation reaction. Seeded experiments showed that the rate determining step in transformation reaction was the growth of HA until the rates of dissolution and growth reactions become comparable due to changing surface area ratios and size-dependent dissolution suppression of brushite. Growth-controlled transformation kinetics supports the observation of earlier HA formation on the outer edges of brushite seeded alginate beads where the supersaturation gradient is higher compared to inner parts of the gel and results in faster nucleation kinetics. Unseeded transformation experiments revealed strong variations in the nucleation kinetics of HA in the presence of alginate additives and brought up new questions on the possible nucleation pathways of HA and the acting mechanism of the additives. In addition, ACP was observed as the prior metastable phase in the model system and its possible presence was indicated during transformation studies. ACP-mediated HA nucleation has been a debated topic recently also in terms of crystallization fundamentals where different mechanisms have been suggested. Thus, paper III concerns the ACP-mediated HA formation and how alginate additives affect this process in order to both highlight the role of ACP phase during the formation of HA in the model system and to contribute to the discussions on the fundamental background. By the combination of solution chemistry monitoring and several characterization methods, stepwise HA formation was followed. The results of this study showed the significant effects of alginate additives on the reaction kinetics and pathway of ACP-mediated HA formation where they caused effective retardation of HA formation in the presence of alginate and M-block oligomers, and a change of the final product by further repressing HA in the presence of G-block oligomers.

The work in this thesis deals specifically with the effects of alginate additives on different stages of CaP mineralization, however, the aim has been to contribute to the more general discussions on mineral formation in biological and synthetic systems. Investigating the effects of alginate additives with varying functionality and molecular weight has revealed practical information on the intermolecular interactions of the additives with CaP phases. These observations can give a reference for the behavior of additives with similar structure and functionality such as other polysaccharides that are known to have regulatory roles in biomineral formation.[104] Another point of focus in this work has been on the formation mechanisms of CaP crystals. In these studies potentiometric measurements (pH and/or Ca ion concentration) were combined with characterization methods (XRD, FTIR, SEM, TEM) so that a complete spectrum of chemical, structural and morphological data could be acquired.[116] Investigation of the early stages of crystallization reactions has been a challenging task in both *in vivo* and *in vitro* model systems and there are many questions yet to be answered. However, by using complementary methods a wide scale of information were deduced from solution crystallization.

CHAPTER 5

CONCLUSIONS AND OUTLOOK

This thesis covers the investigation of the effects of alginate additives on calcium phosphate mineralization processes simulated from a model system of mineralized alginate hydrogel. The crystallization phenomena within an organic matrix are highly influenced by the interactions between the organic and inorganic phases, thus, the motivation for this work has been to gain more insight on the roles of the alginate molecules on mineralization reactions which in turn enables a higher level of control on the model system. The methods used in this work have provided quantitative data on reaction kinetics as well as a qualitative understanding on the acting mechanisms of alginate additives via a systematic evaluation of the intermolecular interactions between the alginate molecules and inorganic phases. Observations on the active roles of the functional groups and the size effects of the alginate additives during crystallization phenomena can contribute to the evaluation of other molecules with similar characteristics also. The data obtained from these studies provides useful information to better control the mineral content in the chosen organic matrix in terms of the final forming phase, amount of mineralization, particle size and morphology which contributes vastly to the final features of a synthetic composite material.

Nature uses the interplay between the organic and inorganic constituents to form composite structures with remarkable levels of complexity and hierarchy which determine their superior physical properties and functionality. Accordingly, understanding the roles of macromolecules in different stages of mineralization is the key to have better control and tailoring ability on the final properties of the designed materials. Thus, a subsistent step in the field of biomineralization studies has been the use of extended knowledge on organic matrix-mineral interactions to design smart materials with well-defined, function-oriented structures. For example, by using the specific nucleation and growth of inorganic phases controlled by selective organic matrices a template-directed synthesis method can be followed to produce smart materials with mechanical, optical, and magnetic properties. Similar approaches can be employed for enhanced mineral coating strategies for biomedical applications. Along with the practical applications, the research in this field contributes to the understanding of crystallization process itself from a fundamental aspect. CaP crystallization is a complex and dynamic system and there are many questions yet to be answered specially on the *in vivo* formation mechanisms of apatitic minerals. Systematic studies on crystallization pathways and kinetics will provide the insight to solve the mysterious ways of Nature which paves the way for ultimate design strategies for synthetic biomaterials.

BIBLIOGRAPHY

(1) Meldrum, F. C.; Cölfen, H. *Chemical Reviews* **2008**, *108*, 4332.

(2) Cusack, M.; Freer, A. *Chemical Reviews* **2008**, *108*, 4433.

(3) Gorna, K.; Muñoz-Espí, R.; Gröhn, F.; Wegner, G. *Macromolecular Bioscience* **2007**, *7*, 163.

(4) Langer, R.; Vacanti, J. *Science* **1993**, *260*, 920.

(5) Hu, Q.; Nielsen, M. H.; Freeman, C. L.; Hamm, L. M.; Tao, J.; Lee, J. R. I.; Han, T. Y. J.; Becker, U.; Harding, J. H.; Dove, P. M.; De Yoreo, J. J. *Faraday Discussions* **2012**, *159*, 509.

(6) Habraken, W.; Habibovic, P.; Epple, M.; Bohner, M. *Materials Today* **2016**, *19*, 69.

(7) López-Ruiz, E.; Jiménez, G.; García, M. Á.; Antich, C.; Boulaiz, H.; Marchal, J. A.; Perán, M. *Expert Opinion on Therapeutic Patents* **2016**, *26*, 877.

(8) Montastruc, L.; Azzaro-Pantel, C.; Biscans, B.; Cabassud, M.; Domenech, S. *Chemical Engineering Journal* **2003**, *94*, 41.

(9) Wang, L.; Nancollas, G. H. *Chemical Reviews* **2008**, *108*, 4628.

(10) Bjørnøy, S. H.; Bassett, D. C.; Ucar, S.; Andreassen, J. P.; Sikorski, P. *Biomedical Materials (Bristol)* **2016**, *11*.

(11) Bjørnøy, S. H.; Bassett, D. C.; Ucar, S.; Strand, B. L.; Andreassen, J.-P.; Sikorski, P. *Acta Biomaterialia* **2016**, *44*, 254.

(12) Bjørnøy, S. H.; Mandaric, S.; Bassett, D. C.; Åslund, A. K. O.; Ucar, S.; Andreassen, J.-P.; Strand, B. L.; Sikorski, P. *Acta Biomaterialia* **2016**, *44*, 243.

(13) Mann, S. *Biomineralization: Principles and Concepts in Bioinorganic Materials Chemistry*; Oxford University Press, 2001.

(14) Mann, S. *Nature* **1988**, *332*, 119.

(15) Estroff, L. A. *Chemical Reviews* **2008**, *108*, 4329.

(16) Mullin, J. W. *Crystallization*; Butterworth-Heinemann, 1997.

(17) Milchev, A. *Journal of Solid State Electrochemistry* **2011**, *15*, 1401.

(18) Kashchiev, D.; van Rosmalen, G. M. *Crystal Research and Technology* **2003**, *38*, 555.

(19) Kostov, R. I. *Cambridge (Cambridge University Press) 2005. xii + 295 pp. Hardcover, Price £55.00.* **2006**, *70*, 606.

(20) Myerson, A. S. *Faraday Discussions* **2015**, *179*, 543.

(21) ter Horst, J. H.; Schmidt, C.; Ulrich, J. In *Handbook of Crystal Growth (Second Edition)*; Elsevier: Boston, 2015, p 1317.

(22) Roelands, C. P. M.; ter Horst, J. H.; Kramer, H. J. M.; Jansens, P. J. *Crystal Growth & Design* **2006**, *6*, 1380.

(23) Threlfall, T. L.; Coles, S. J. *CrystEngComm* **2016**, *18*, 369.

(24) Myerson, A. S.; Ginde, R. In *Handbook of Industrial Crystallization (Second Edition)*; Butterworth-Heinemann: Woburn, 2002, p 33.

(25) Agrawal, S. G.; Paterson, A. H. J. *Chemical Engineering Communications* **2015**, *202*, 698.

(26) Shiau, L. D.; Wang, H. P. *Journal of Crystal Growth* **2016**, *442*, 47.

(27) Woehl, T. J.; Evans, J. E.; Arslan, I.; Ristenpart, W. D.; Browning, N. D. *ACS Nano* **2012**, *6*, 8599.

(28) Verdoes, D.; Kashchiev, D.; van Rosmalen, G. M. *Journal of Crystal Growth* **1992**, *118*, 401.

(29) Nývlt, J. *Crystal Research and Technology* **1995**, *30*, 443.

(30) Zhao, J.; Liu, Y.; Sun, W.-b.; Yang, X. *Journal of Dental Sciences* **2012**, *7*, 316.

(31) Tsuji, T.; Onuma, K.; Yamamoto, A.; Iijima, M.; Shiba, K. *Proceedings of the National Academy of Sciences of the United States of America* **2008**, *105*, 16866.

(32) Wolf, S. E.; Leiterer, J.; Kappl, M.; Emmerling, F.; Tremel, W. *Journal of the American Chemical Society* **2008**, *130*, 12342.

(33) Wallace, A. F.; Hedges, L. O.; Fernandez-Martinez, A.; Raiteri, P.; Gale, J. D.; Waychunas, G. A.; Whitelam, S.; Banfield, J. F.; De Yoreo, J. J. *Science* **2013**, *341*, 885.

(34) Thompson, D. W. *On growth and form*; Cambridge Univ. Press, 1942.

(35) Bahrig, L.; Hickey, S. G.; Eychmuller, A. *CrystEngComm* **2014**, *16*, 9408.

(36) Nielsen, A. E. *Journal of Crystal Growth* **1984**, *67*, 289.

(37) De Yoreo, J. J.; Vekilov, P. G. *Reviews in Mineralogy and Geochemistry* **2003**, *54*, 57.

(38) Frank, F. *Discuss. Faraday Soc.* **1949**, *5*, 48.

(39) Uwaha, M. *Progress in Crystal Growth and Characterization of Materials* **2016**, *62*, 58.

(40) Teng, H. H.; Dove, P. M.; De Yoreo, J. J. *Geochimica et Cosmochimica Acta* **2000**, *64*, 2255.

(41) Nielsen, A. E.; Christoffersen, J. In *Biological Mineralization and Demineralization: Report of the Dahlem Workshop on Biological Mineralization and Demineralization Berlin 1981, October 18–23*; Nancollas, G. H., Ed.; Springer Berlin Heidelberg: Berlin, Heidelberg, 1982, p 37.

(42) Zhang, J.; Nancollas, G. H. *Journal of Crystal Growth* **1992**, *125*, 251.

(43) Zhang, J.; Nancollas, G. H. *Journal of Crystal Growth* **1992**, *123*, 59.

(44) Tang, R.; Nancollas, G. H.; Orme, C. A. *Journal of the American Chemical Society* **2001**, *123*, 5437.

(45) Lasaga, A. C.; Luttge, A. *Science* **2001**, *291*, 2400.

(46) Tang, R.; Orme, C. A.; Nancollas, G. H. *Journal of Physical Chemistry B* **2003**, *107*, 10653.

(47) Jeurgens, L. P. H.; Wang, Z.; Mittemeijer, E. J. *International Journal of Materials Research* **2009**, *100*, 1281.

(48) Cardew, P. T.; Davey, R. J. *Proceedings of the Royal Society of London A: Mathematical, Physical and Engineering Sciences* **1985**, *398*, 415.

(49) In *Ceramic Materials: Science and Engineering*; Springer New York: New York, NY, 2007, p 444.

(50) Spanos, N.; Koutsoukos, P. G. *Journal of Crystal Growth* **1998**, *191*, 783.

(51) Fulmer, M. T.; Brown, P. W. *Journal of Materials Science: Materials in Medicine* **1998**, *9*, 197.

(52) De Yoreo, J. J.; Sommerdijk, N. A. J. M.; Dove, P. M. In *New Perspectives on Mineral Nucleation and Growth: From Solution Precursors to Solid Materials*; Van Driessche, A. E. S., Kellermeier, M., Benning, L. G., Gebauer, D., Eds.; Springer International Publishing: Cham, 2017, p 1.

(53) Habraken, W. J. E. M.; Tao, J.; Brylka, L. J.; Friedrich, H.; Bertinetti, L.; Schenk, A. S.; Verch, A.; Dmitrovic, V.; Bomans, P. H. H.; Frederik, P. M.; Laven, J.; van der Schoot, P.; Aichmayer, B.; de With, G.; DeYoreo, J. J.; Sommerdijk, N. A. J. M. *Nature Communications* **2013**, *4*, 1507.

(54) Gebauer, D.; Cölfen, H. *Nano Today* **2011**, *6*, 564.

(55) Erdemir, D.; Lee, A. Y.; Myerson, A. S. *Accounts of Chemical Research* **2009**, *42*, 621.
(56) Nielsen, M. H.; Aloni, S.; De Yoreo, J. J. *Science* **2014**, *345*, 1158.
(57) Andreassen, J.-P.; Lewis, A. E. In *New Perspectives on Mineral Nucleation and Growth: From Solution Precursors to Solid Materials*; Van Driessche, A. E. S., Kellermeier, M., Benning, L. G., Gebauer, D., Eds.; Springer International Publishing: Cham, 2017, p 137.
(58) Ivanov, V. K.; Fedorov, P. P.; Baranchikov, A. Y.; Osiko, V. V. *Russian Chemical Reviews* **2014**, *83*, 1204.
(59) Yuwono, V. M.; Burrows, N. D.; Soltis, J. A.; Penn, R. L. *Journal of the American Chemical Society* **2010**, *132*, 2163.
(60) Niederberger, M.; Cölfen, H. *Physical Chemistry Chemical Physics* **2006**, *8*, 3271.
(61) Kim, Y. Y.; Schenk, A. S.; Ihli, J.; Kulak, A. N.; Hetherington, N. B. J.; Tang, C. C.; Schmahl, W. W.; Griesshaber, E.; Hyett, G.; Meldrum, F. C. *Nature Communications* **2014**, *5*.
(62) Ruiz-Agudo, E.; Putnis, C. V.; Pel, L.; Rodriguez-Navarro, C. *Crystal Growth & Design* **2013**, *13*, 40.
(63) Wada, N.; Horiuchi, N.; Nakamura, M.; Nozaki, K.; Hiyama, T.; Nagai, A.; Yamashita, K. *Journal of Crystal Growth* **2015**, *415*, 7.
(64) Saw, M. H.; Hishamuddin, E.; Chong, C. L.; Yeoh, C. B.; Lim, W. H. *Food Chemistry* **2017**, *214*, 277.
(65) Westin, K. J.; Rasmuson, Å. C. *Journal of Colloid and Interface Science* **2005**, *282*, 370.
(66) Gower, L. B.; Odom, D. J. *Journal of Crystal Growth* **2000**, *210*, 719.
(67) Ding, H.; Pan, H.; Xu, X.; Tang, R. *Crystal Growth & Design* **2014**, *14*, 763.
(68) Selmani, A.; Coha, I.; Magdic, K.; Colovic, B.; Jokanovic, V.; Segota, S.; Gajovic, S.; Gajovic, A.; Jurasin, D.; Dutour Sikiric, M. *CrystEngComm* **2015**, *17*, 8529.
(69) Rao, A.; Vásquez-Quitral, P.; Fernández, M. S.; Berg, J. K.; Sánchez, M.; Drechsler, M.; Neira-Carrillo, A.; Arias, J. L.; Gebauer, D.; Cölfen, H. *Crystal Growth & Design* **2016**, *16*, 1349.
(70) Davey, R. J.; Mullin, J. W. *Journal of Crystal Growth* **1974**, *23*, 89.
(71) Jongen, N.; Bowen, P.; Lemaître, J.; Valmalette, J.-C.; Hofmann, H. *Journal of Colloid and Interface Science* **2000**, *226*, 189.
(72) Lu, X.; Leng, Y. *Biomaterials* **2005**, *26*, 1097.
(73) Ferńndez, E.; Gil, F. J.; Ginebra, M. P.; Driessens, F. C. M.; Planell, J. A.; Best, S. M. *Journal of Materials Science: Materials in Medicine* **1999**, *10*, 169.
(74) Cheng, P.-T.; Pritzker, K. P. H. *Calcified Tissue International* **1983**, *35*, 596.
(75) Kannan, S.; Rocha, J. H. G.; Ventura, J. M. G.; Lemos, A. F.; Ferreira, J. M. F. *Scripta Materialia* **2005**, *53*, 1259.
(76) Johnsson, M. S.-A.; Nancollas, G. H. *Critical Reviews in Oral Biology & Medicine* **1992**, *3*, 61.
(77) Eanes, E. D. In *Calcium Phosphates in Biological and Industrial Systems*; Amjad, Z., Ed.; Springer US: Boston, MA, 1998, p 21.
(78) Combes, C.; Rey, C. *Acta Biomaterialia* **2010**, *6*, 3362.
(79) Termine, J. D.; Peckauskas, R. A.; Posner, A. S. *Archives of Biochemistry and Biophysics* **1970**, *140*, 318.

(80) Weiner, S.; Mahamid, J.; Politi, Y.; Ma, Y.; Addadi, L. *Frontiers of Materials Science in China* **2009**, *3*, 104.

(81) Dey, A.; Bomans, P. H. H.; Müller, F. A.; Will, J.; Frederik, P. M.; de With, G.; Sommerdijk, N. A. J. M. *Nat Mater* **2010**, *9*, 1010.

(82) Xie, B.; Halter, T. J.; Borah, B. M.; Nancollas, G. H. *Crystal Growth & Design* **2014**, *14*, 1659.

(83) Ibsen, C. J. S.; Gebauer, D.; Birkedal, H. *Chemistry of Materials* **2016**, *28*, 8550.

(84) LeGeros, R. Z. *Zeitschrift für Kardiologie* **2001**, *90*, 116.

(85) O'Neill, W. C. *Kidney International* **2007**, *72*, 792.

(86) Zou, Z.; Liu, X.; Chen, L.; Lin, K.; Chang, J. *Journal of Materials Chemistry* **2012**, *22*, 22637.

(87) Wang, M.; Gao, J.; Shi, C.; Zhu, Y.; Zeng, Y.; Wang, D. *Crystal Growth and Design* **2014**, *14*, 6459.

(88) Tamimi, F.; Sheikh, Z.; Barralet, J. *Acta Biomaterialia* **2012**, *8*, 474.

(89) Kakei, M.; Sakae, T.; Yoshikawa, M. *Journal of Electron Microscopy* **2009**, *58*, 393.

(90) Nelson, D. G. A.; Barry, J. C. *The Anatomical Record* **1989**, *224*, 265.

(91) Wang, C.-G.; Liao, J.-W.; Gou, B.-D.; Huang, J.; Tang, R.-K.; Tao, J.-H.; Zhang, T.-L.; Wang, K. *Crystal Growth & Design* **2009**, *9*, 2620.

(92) Mahamid, J.; Sharir, A.; Addadi, L.; Weiner, S. *Proceedings of the National Academy of Sciences* **2008**, *105*, 12748.

(93) Kanzaki, N.; Onuma, K.; Treboux, G.; Ito, A. *Journal of Crystal Growth* **2002**, *235*, 465.

(94) Kumar, M.; Xie, J.; Chittur, K.; Riley, C. *Biomaterials* **1999**, *20*, 1389.

(95) Lundager Madsen, H. E. *Journal of Crystal Growth* **2008**, *310*, 2602.

(96) Chu, X.; Jiang, W.; Zhang, Z.; Yan, Y.; Pan, H.; Xu, X.; Tang, R. *Journal of Physical Chemistry B* **2011**, *115*, 1151.

(97) Jiang, W.; Chu, X.; Wang, B.; Pan, H.; Xu, X.; Tang, R. *Journal of Physical Chemistry B* **2009**, *113*, 10838.

(98) Tsai, T. W. T.; Chen, W. Y.; Tseng, Y. H.; Chan, J. C. C. *Canadian Journal of Chemistry* **2011**, *89*, 885.

(99) Boskey, A. L.; Posner, A. S. *The Journal of Physical Chemistry* **1973**, *77*, 2313.

(100) Jiang, S.; Chen, Y.; Pan, H.; Zhang, Y.-J.; Tang, R. *Physical Chemistry Chemical Physics* **2013**, *15*, 12530.

(101) Chen, Y.; Gu, W.; Pan, H.; Jiang, S.; Tang, R. *CrystEngComm* **2014**, *16*, 1864.

(102) Jiang, S.; Pan, H.; Chen, Y.; Xu, X.; Tang, R. *Faraday Discussions* **2015**, *179*, 451.

(103) Reid, D. G.; Duer, M. J.; Murray, R. C.; Wise, E. R. *Chemistry of Materials* **2008**, *20*, 3549.

(104) Arias, J. L.; Fernández, M. S. *Chemical Reviews* **2008**, *108*, 4475.

(105) Venkatesan, J.; Bhatnagar, I.; Manivasagan, P.; Kang, K. H.; Kim, S. K. *International Journal of Biological Macromolecules* **2015**, *72*, 269.

(106) Salgado, L. T.; Amado Filho, G. M.; Fernandez, M. S.; Arias, J. L.; Farina, M. *Journal of Crystal Growth* **2011**, *321*, 65.

(107) Olderøy, M. Ø.; Xie, M.; Strand, B. L.; Flaten, E. M.; Sikorski, P.; Andreassen, J. P. *Crystal Growth and Design* **2009**, *9*, 5176.

(108) Olderøy, M. Ø.; Xie, M.; Strand, B. L.; Draget, K. I.; Sikorski, P.; Andreassen, J. P. *Crystal Growth and Design* **2011**, *11*, 520.
(109) Lakshtanov, L. Z.; Belova, D. A.; Okhrimenko, D. V.; Stipp, S. L. S. *Crystal Growth & Design* **2015**, *15*, 419.
(110) Malkaj, P.; Pierri, E.; Dalas, E. *Journal of Materials Science: Materials in Medicine* **2005**, *16*, 733.
(111) Son, K. D.; Yang, D. J.; Kim, M. S.; Kang, I.-K.; Kim, S. Y.; Kim, Y.-J. *Materials Chemistry and Physics* **2012**, *132*, 1041.
(112) Beck, R.; Seiersten, M.; Andreassen, J. P. *Journal of Crystal Growth* **2013**, *380*, 187.
(113) Murphy, J.; Riley, J. P. *Analytica Chimica Acta* **1962**, *27*, 31.
(114) Zan, G.; Wu, Q. *Advanced Materials* **2016**, *28*, 2099.
(115) Chen, F. M.; Liu, X. *Progress in Polymer Science* **2016**, *53*, 86.
(116) Habraken, W. J. E. M. In *Methods in Enzymology*; James, J. D. Y., Ed.; Academic Press: 2013; Vol. Volume 532, p 25.

Papers

Paper I

CRYSTAL GROWTH & DESIGN
Article
pubs.acs.org/crystal

Nucleation and Growth of Brushite in the Presence of Alginate

Seniz Ucar,[†] Sindre H. Bjørnøy,[‡] David C. Bassett,[‡] Berit L. Strand,[§] Pawel Sikorski,[‡] and Jens-Petter Andreassen*,[†]

[†]Department of Chemical Engineering, [‡]Department of Physics, and [§]Department of Biotechnology, Norwegian University of Science and Technology, Trondheim, Norway

Ⓢ *Supporting Information*

ABSTRACT: Biomineral formation *in vivo* is a complex process regulated by functional molecules. Highlighting the mechanisms underlying biomineralization is necessary for a better understanding of *in vivo* processes and for enhanced *in vitro* model systems. Here, the effect of alginate and its well-defined oligomers with M- or G-block structure on brushite nucleation and growth is investigated by seeded and unseeded experiments. Growth kinetics were studied by seeded experiments, and it was shown that molecular weight and functionality of alginate additives affect the crystal growth rates and the growth mechanisms. Growth retardation was most prominent when G-block additives were present. Growth proceeded by surface nucleation when alginate and G-block oligomers were added in the crystallization medium, whereas in the presence of M-block oligomers parabolic rate laws were obtained. By decoupling the seeded and unseeded experiments, information was deduced on the effects of additives on brushite nucleation. In the presence of alginate and G-block oligomers, nucleation was inhibited; however, M-blocks did not show a similar effect. Possible modes of interactions between the mineral and polymer additives are discussed by the evaluation of final crystal morphologies.

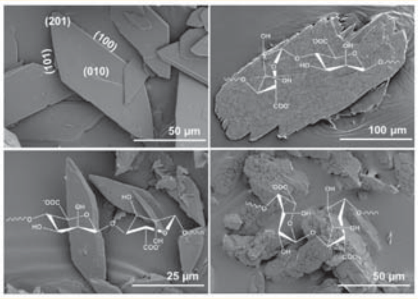

INTRODUCTION

The formation of inorganic minerals via a biological process (biomineralization) is a complex process involving the constructive interaction between organic and inorganic phases to result in composite tissues with intricate structures which give rise to unusual and often exceptional biological and physical properties.[1] Such structures are difficult to reproduce synthetically in the laboratory; nevertheless, natural biomineralization processes may offer a great source of inspiration to design synthetic bottom-up formation processes to tailor biomaterials in an attempt to mimic or reproduce the structures and hence the properties of natural hard tissues.[2] Both naturally and synthetically derived polymers, peptides and small molecules, and ions may be used for this purpose either as mineralization templates or modifying agents. In the case of polymeric additives, concentration, molecular weight, functional groups, and polymer block structure have been shown to impart significant influence over inorganic mineralization in terms of crystallinity, resulting crystal phase and crystal morphology, nucleation, and growth rates.[3,4] The role of macromolecules in controlling crystallization *in vivo* and *in vitro* model systems has been at the center of comprehensive research and continues to be an advancing field.

Polysaccharides are recognized as a strongly influential group of polymers acting upon calcium phosphate and calcium carbonate mineralization that are important classes of minerals in vertebrate and marine hard tissues, respectively.[5−9] Alginate is a linear polysaccharide copolymer, derived from brown sea algae and composed of 1−4 linked β-D-mannuronic acid (M) and α-L-guluronic acid (G) residues with an alternating or block structure. The M- and G-units of alginate differ in the orientation of carboxyl groups that in turn highly affects their functionalty. The pK_a values of M- and G-repeating units are 3.38 and 3.65, respectively, and the pK_a value of alginate polymer differs only slightly from its monomers. Calcium ions show specific affinity toward the outward carboxyl groups of the G-units of alginate and bind to G-blocks and alternating blocks of the polymer but not to M-blocks.[10] Therefore, the physical properties of alginate and how it regulates mineralization are highly dependent on its chemical composition, sequential structure of the repeating units and molecular weight. Our group recently conducted detailed investigations on the nucleation and growth of calcium carbonate in the presence of alginate and well-defined M- and G-block oligomers.[11,12] G-block oligomers were shown to have prominent effects on nucleation characteristics, polymorph switching, and resultant crystal morphology. Malkaj et al. investigated the effects of alginate on hydroxyapatite crystallization. They showed the inhibitory effect of alginate on crystal growth rate and attributed it to adsorption of polymer on the active growth sites.[13] A reduction in hydroxyapatite growth rate in the presence of alginate was also observed by Coleman et al., and further investigations in this study indicated varying effects of anionic polymers on crystal growth and morphology depending

Received: July 20, 2015
Revised: September 30, 2015
Published: October 5, 2015

DOI: 10.1021/acs.cgd.5b01032
Cryst. Growth Des. 2015, 15, 5397−5405

on chemical structure of polymer and subsequent changes in interaction mode with the crystal particles.[14] To our knowledge, there are no similar studies in the literature that have investigated the brushite−alginate system.

Alginate has been studied for many biomedical applications due to it being nontoxic, biocompatible, and biodegradable, and its ability to form hydrogels. Alginate hydrogels can be prepared under mild conditions by ionic cross-linking, and they show structural similarity to extracellular matrices of living tissues, which in turn allows for many applications in bioactive agent delivery, wound healing, and tissue engineering.[15] A recent study conducted in our group showed alginate hydrogels mineralized with brushite were potential candidates for bone tissue engineering applications.[16] Incorporation of bioceramics in alginate hydrogels enhances both the mechanical properties and the bioactivity of the polymer network. Brushite was chosen as the mineral phase due to its high solubility among calcium phosphates under physiological conditions, which enables ready transformation and bone remodeling by providing necessary space and ion source for bone-like mineral formation *in vivo*.[17] However, in the complexity of a hydrogel environment control over the mineral phase becomes more challenging due to varying effects of the polymer over the course of crystallization. When alginate solutions containing phosphate precursor were gelled and mineralized spontaneously in calcium containing gelling baths, multiple phases of calcium phosphates were precipitated, even at conditions which should favor formation of brushite. On the other hand, when brushite formation in the hydrogels was directed using small, crystalline seeds, mineral formation in the alginate network could be controlled to a much greater extent, and the hydrogel was mineralized with pure brushite. Interestingly, growth of seed crystals, as well as nucleation of new brushite crystals, was observed. These observations raised a number of interesting questions which are difficult to study in a gel system and which need to be investigated under more controlled conditions, including polymer concentration, composition, and a control of supersaturation.

In this study, the effect of alginate on brushite crystallization was investigated by both seeded and unseeded experiments. Alginates differing in molecular weight and block composition were used as additives, and the effects of compositional variations of the polymer on nucleation and growth of brushite were examined. In the first part, brushite growth was studied by seeded desupersaturation experiments which best represents the model system of seeded alginate hydrogels. To our knowledge, no previous studies have reported brushite growth kinetics studied by this method. The constant composition method was also included for detailed investigation of brushite growth mechanism in the absence of additives. In the second part, unseeded batch experiments were conducted to show the effects of alginate additives on nucleation and growth stages. By evaluating the results of seeded and unseeded experiments together, information was deduced on the effects of additives on the nucleation stage. Finally crystal morphologies were also examined to discuss the possible modes of interactions between the mineral and polymer phases.

■ EXPERIMENTAL SECTION

Materials. All chemical reagents were purchased from Sigma-Aldrich unless stated otherwise. Deionized water (DIW) was used for all purposes. Alginate with molecular mass of 274 kDa and 68% G, isolated from *Laminaria hyperborea* stipe, was obtained from FMC Biopolymer. Two different oligomers of alginate, denoted as G- and M-blocks, consisted of 90% and 5% G, respectively, with the degree of polymerization ≈ 20 for both. The G-blocks were produced from alginate from *L. hyp* stipe by acid degradation and fractionation as described previously.[18] The M-blocks were produced from alginate from *Ascophyllum nodosum* by acid degradation and calcium fractioning as described elsewhere.[19]

Methods. All experiments were carried out in a 1 L double-walled glass reactor, stirred with a Teflon coated three-bladed impeller of propeller type controlled by a digital stirrer engine (IKA), and two baffles were attached to the lid. Temperature was controlled by a water bath at a temperature of 25 °C for all experiments. Nitrogen, presaturated with water, was constantly bubbled into solutions throughout the precipitation reactions to prevent intrusion of atmospheric carbon dioxide. The chemical speciation and activity based supersaturation were determined by thermodynamic calculation program PHREEQC Interactive 3.1, using Minteq v4 database. The equilibrium constants used for solution speciation are given in Supporting Information (Table S1). The pH was recorded constantly by means of a combined glass electrode with KCl reference electrolyte connected to Tiamo software (Metrohm), and calibrations were carried out weekly.

Calcium ion concentration in the vessel was monitored by offline titration (Mettler Toledo DL 53) of samples with 10 mM EDTA. For this purpose, 2 mL samples were withdrawn and filtered through a 0.22 μm syringe filter (Millipore) to remove solid crystals. Samples were kept overnight after addition of 3 mL of 0.1 M HCl and dilution to 20 mL with water. Before analysis, samples were further diluted to 40 mL, and 1 mL of 4 M KCl and 1 mL of pH 10 NH_3^+/NH_4 buffer were added.

Characterization of solid phases were conducted via powder X-ray diffraction (XRD) (D8 Advance DaVinci, Bruker AXS GmBH) in the range of 5−75° with a step size of 0.013° and a step time of 0.67 s. SEM analyses (Hitachi S-3400N) were performed at an accelerating voltage of 5 kV, where samples were placed on carbon tape and sputter coated with gold.

Seed Preparation. Brushite seeds were prepared by mixing equimolar amounts of $Ca(NO_3)_2 \cdot 4H_2O$ and KH_2PO_4 to a total volume of 1 L under nitrogen environment and constant stirring at 800 rpm. Precipitates were aged in their saturated solution for at least 2 h after completion of reaction and observation of stable pH. Crystals were then filtered and washed with DIW and ethanol prior to drying at room temperature. Phase purity of seeds was verified by XRD and scanning electron microscopy (SEM) analyses. Specific surface area (SSA) was determined to be 0.646 ± 0.023 m^2/g by multiple point BET nitrogen adsorption method (Tristar II, Micromeritics), and volume distribution showed a mean diameter of 24.17 μm of an equivalent sphere with CV 40.3%, characterized by a Coulter Counter Multisizer (Beckman Coulter). For size determinations, an average of three measurements was used in which approximately 1×10^4 seeds were counted during each run. Seeds were stored for up to one month in their dry state prior to use.

Preparation of Solutions for Desupersaturation Experiments. Solutions of calcium and phosphate precursors were prepared separately from their stock solutions of $CaCl_2 \cdot 2H_2O$ and KH_2PO_4 (250 mmol/kg). An appropriate amount of KCl salt was added in calcium solution to ensure a final ionic strength of 0.15 M, whereas 1.0 M KOH was added to phosphate solution for adjustment of desired pH. In the case of experiments incorporating alginate, a corresponding amount of filtered polymer solution was added into the phosphate containing solution and stirred overnight prior to experiments. Alginate additives are fully deprotonated in the pH range of the growth experiments which was above the pK_a values of the repeating units of alginate. Supersaturated solutions were prepared by the addition of calcium-containing solution to phosphate-containing solution while stirring at 300 rpm to give the final concentrations of calcium and phosphate equal to 15 mM. Final pH was carefully adjusted to 5.700 ± 0.002 by dropwise addition of 0.1 M KOH. Supersaturation with respect to brushite was calculated to be $S = 2.34$ at initial conditions, and the solution was stable up to 15 min.

Supersaturation calculations were repeated in the presence of additives assuming all G-blocks present in solution bind to calcium ions. The low molar concentration of G-blocks with respect to the total calcium ion concentration at any experimental condition did not cause any significant decrease in free ion concentration to affect the supersaturation.

Seeded Desupersaturation Growth Experiments. For brushite seeded experiments, 100 mg of seeds with well-known surface area (A) was added to the vessel as a suspension immediately after preparation of supersaturated solutions to initiate growth reactions. Samples were withdrawn for calcium analysis during the course of growth. At the end of each experiment, the vessel content was filtered, washed, and dried for characterization by XRD and SEM.

Depletion in calcium ion concentration was measured by offline titration at arbitrary time points and fit to a simple exponential function later used to obtain an overall growth rate equation as a function of time (eq 1). Also, using measured calcium concentration and pH, momentary supersaturation values were calculated by PHREEQC software. Changes in phosphate concentration were assumed equal to depletion in calcium since ion consumption proceeds only via brushite growth in solution. Spectroscopic methods could not be used efficiently for phosphate determination at these experimental conditions due to small changes in ion concentration with respect to high initial values. Combining the growth rate function with data points of momentary supersaturation, the growth rate was represented as a function of relative supersaturation (σ) (eq 2). The predicted models of growth rates showed good fit with the experimental data and are shown in Supporting Information (Figure S1).

$$R = = \frac{1}{A}\frac{\mathrm{d}C}{\mathrm{d}t} \tag{1}$$

$$R = k\sigma^{g} \tag{2}$$

The relative supersaturation is defined as given in eq 3, where IAP denotes ion activity product and K_{sp} is the solubility product of brushite.

$$\sigma = S - 1 = \left(\frac{\mathrm{IAP}}{K_{\mathrm{sp}}}\right)^{1/2} - 1 \tag{3}$$

Each experiment was repeated in multiple runs, and the growth rate law was then used to obtain the growth rate constant, k, and the apparent order of growth, g.

Seeded Constant Composition Growth Experiments. Desupersaturation experiments are difficult to conduct at low supersaturation regions where crystal growth proceeds slowly and ion consumptions are too low to collect sufficiently reliable data. In order to overcome this drawback, constant composition experiments were performed in the relative supersaturation range of 0.20−0.55. Initially stable supersaturated solutions at pH 5.70 were prepared, and 50 mg of seeds in suspension was added in the vessel to initiate growth, as described above. A decrease in pH of more than 0.002 units associated with brushite growth triggered the addition of titrant solutions from two mechanically coupled titrant burets (902 Titrando, Metrohm) to maintain a constant supersaturation.

Compositions of titrant solutions were adjusted for each working solution to maintain a constant thermodynamic driving force during the brushite growth by compensating for ion consumption, changing ionic strength and alkalinity in the reaction media. Detailed preparation of titrant solutions has been previously given for calcium carbonate by our group.[20] In this study, the same methodology was used with the modifications for brushite growth. For this purpose, first the effect of the extent of brushite crystallization on total alkalinity and ion consumption was computed in moles (n) according to the equations given below:

$$n_{\mathrm{Ca}^{2+}} = n_{\mathrm{Ca}^{2+},i} - n_{\mathrm{Ca}^{2+},\mathrm{cryst}} \tag{4}$$

$$n_{\mathrm{PO}_4{}^{3-}} = n_{\mathrm{PO}_4{}^{3-},i} - n_{\mathrm{PO}_4{}^{3-},\mathrm{cryst}} \tag{5}$$

$$n_{\mathrm{H}^+} = n_{\mathrm{H}^+,i} - n_{\mathrm{H}^+,\mathrm{cryst}} \tag{6}$$

$$n_{\mathrm{alk}} = n_{\mathrm{alk,i}} - n_{\mathrm{alk,cryst}} \tag{7}$$

$$n_{\mathrm{alk,cryst}} = 3n_{\mathrm{PO}_4{}^{3-},\mathrm{cryst}} - n_{\mathrm{H}^+,\mathrm{cryst}} \tag{8}$$

In order to compensate for the calcium ion consumption by crystallization, an arbitrary concentration (c) was determined for the calcium to be added to the reaction medium from buret 1. The calcium concentration in buret 1 should be higher than the concentration in the working solution and should be adjusted according to the growth kinetics. Next, the composition of titrant solution 2 was calculated, in accordance with the titrant solution 1 and the total volume of titrant solutions to be added, to fulfill eqs 9−14. The adjustment for the ionic strength was also ensured with buret 2 in order to keep constant ionic activity coefficients used in the calculation of activity based supersaturation.

$$c_{\mathrm{Ca}^{2+}} = c_{\mathrm{Ca}^{2+},i} \tag{9}$$

$$c_{\mathrm{PO}_4{}^{3-}} = c_{\mathrm{PO}_4{}^{3-},i} \tag{10}$$

$$c_{\mathrm{H}^+} = c_{\mathrm{H}^+,i} \tag{11}$$

$$c_{\mathrm{K}^+} = c_{\mathrm{K}^+,i} \tag{12}$$

$$c_{\mathrm{Cl}^-} = c_{\mathrm{Cl}^-,i} \tag{13}$$

$$c_{\mathrm{alk}} = c_{\mathrm{alk,i}} \tag{14}$$

Note that the calculated composition in buret 2 is only valid for the chosen initial working solution and the determined calcium concentration in buret 1.

By the addition of titrant solutions, pH was controlled at a constant value with an overshoot to a maximum of 0.004 units only at the initial growth period. Constancy of supersaturation was confirmed with calcium analyses at arbitrary time points that showed less than 1% deviation in concentration during titrant addition.

The growth rate of brushite was calculated at each supersaturation value by using titrant addition curves (eq 15), where the effective concentration (C_{eff}) denotes number of moles precipitated per liter of titrant addition and $\mathrm{d}V/\mathrm{d}t$ is the titrant curve gradient. Titrant addition curves were normalized to an increasing surface area of the seeds with proceeding growth. For this purpose, the mass change of brushite was calculated from the volume of titrant added and related to the change in surface area by a factor of $[(w_i/w)^{2/3}]$, where w_i is the weight of seed crystals added initially and w is the weight of crystals present at time t, assuming three-dimensional growth with a constant shape factor.[21,22] Obtained results were then used to calculate the growth rate constant, k, and the apparent order of growth, g (eq 2).

$$R = \frac{1}{A}C_{\mathrm{eff}}\frac{\mathrm{d}V_{\mathrm{titr}}}{\mathrm{d}t} \tag{15}$$

Unseeded Batch Experiments. Supersaturated solutions were prepared as described above for desupersaturation experiments, and spontaneous precipitation was allowed to occur at constant stirring speed and temperature, under a nitrogen environment. Solution pH was recorded continuously, and samples were withdrawn at arbitrary time points for calcium analysis after the first detectable drop in pH. Reactions were continued until $S \approx 1.0$ for the additive free system and $S \approx 1.5$ for all others. At the end of each experiment, precipitates were filtered, washed, and air-dried for characterization by XRD and SEM.

■ RESULTS AND DISCUSSION

Seeded Growth Experiments. Seeded batch experiments were conducted in order to investigate and quantify the effects of different alginates on brushite growth. Initial experimental conditions were determined in accordance with preliminary experiments to give solutions supersaturated with respect to brushite and stable for up to 15 min. Brushite seeds were well characterized prior to usage in terms of phase purity and

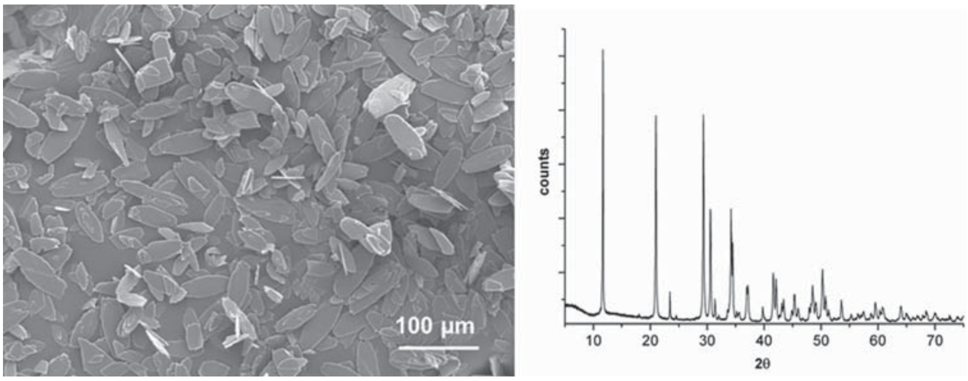

Figure 1. SEM image and XRD spectrum of brushite seeds.

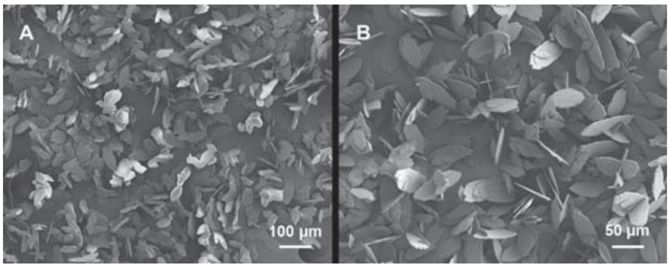

Figure 2. (A, B) SEM images of samples collected at the end of seeded experiments where $S \leq 1.5$ in the presence of 10 ppm M-blocks at different magnifications.

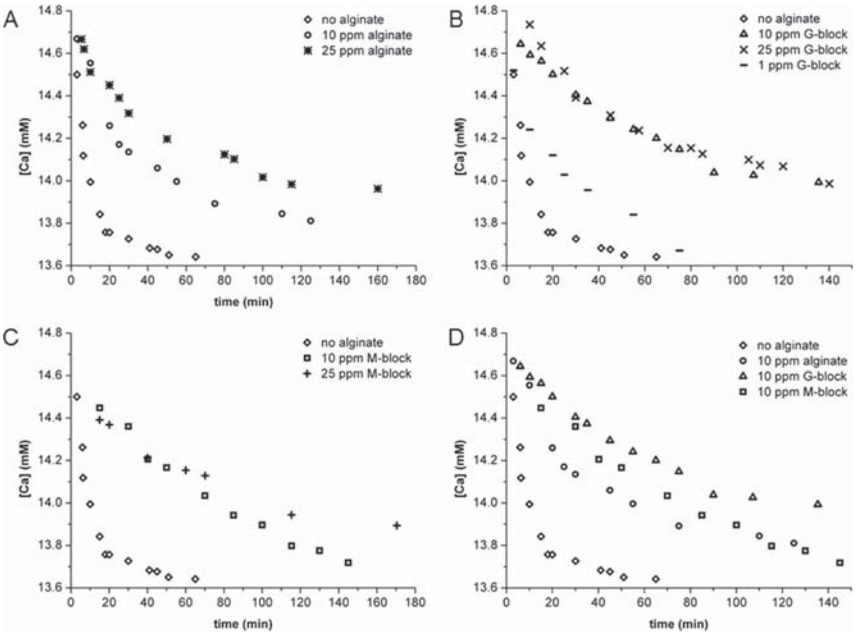

Figure 3. Calcium consumption with respect to time in the presence of different additives with 10 and 25 ppm concentrations (A−C). Comparison of additives at equal concentration is given separately for 10 ppm addition (D). The additive free system is included in all graphs. Note the different time scales.

morphology (Figure 1). The surface area of seeds was determined by multiple point BET as 0.646 ± 0.023 m^2/g.

Upon addition of seeds into the reaction medium, the pH started to drop immediately, which was accompanied by a simultaneous decrease in calcium ion concentration. To ensure ions were only consumed by the growing seeds, Coulter counter measurements were taken during growth experiments of brushite in the absence of alginate. Analysis of samples withdrawn during the course of the reaction showed steady numbers of crystals with increasing average size. In experiments including alginate additives, reliable data could not be obtained from size measurements due to aggregation of the crystals. However, SEM images of end products indicated that a non-nucleating environment was achieved as no new particles smaller than the original seeds were observed (Figure 2).

There was a significant change both in calcium consumption (Figure 3) and pH drop rates (not shown) when different types of alginate were added in the reaction vessel. By using the obtained calcium and pH depletion curves, growth rate constants (k) were calculated to quantify the effects of additives on the overall growth rate (Table 1). In the absence of alginate, a fast growth process was observed, and the reaction was almost complete within 50 min. After that point, calcium depletion curves and pH showed constant values that indicated the end of the reactions. Calculations of supersaturation with the momentary inputs of pH and ion concentrations at those time points resulted in $S \approx 1.00$ that supports the accuracy of thermodynamic calculations used. The growth rate constant was calculated to be 1.063 mmol/min·m^2 in the absence of any additive from the desupersaturation experiments. Addition of high molecular weight alginate resulted in a decrease in the rate of calcium consumption and pH drop starting from the initial stages of growth and continuing throughout the reaction. This retarding effect was observed to be highly dependent on additive concentration. When G-block oligomers of alginate were used at the same concentration as the alginate polymer, the concentration effect was less pronounced between 10 and 25 ppm additive concentrations, and growth rate constants obtained at those two G-block concentrations were very similar. Among all types of alginate additives, G-blocks resulted in the strongest inhibition on the overall course of growth. Calcium ion depletion slowed down even further with decreasing supersaturation in the vessel and was inhibited almost completely after consumption of 50% of available calcium (Figure 3B). In the presence of M-block oligomers, a reduced rate of calcium consumption was observed when compared to additive free systems; however, growth proceeded further when compared to both alginate and G-block counterparts (Figure 3C).

Table 1. Values of Growth Rate Constants (k) and Apparent Growth Orders (g)

	k (mmol/min·m^2)	g
no alginate	1.063 ± 0.128	1.091 ± 0.086
no alginate[a]	0.962 ± 0.155	2.402 ± 0.148
10 ppm alginate	0.743 ± 0.016	2.779 ± 0.030
25 ppm alginate	0.193 ± 0.022	3.964 ± 0.441
10 ppm G-block	0.116 ± 0.006	3.996 ± 0.083
25 ppm G-block	0.115 ± 0.003	3.395 ± 0.008
10 ppm M-block	0.210 ± 0.024	2.126 ± 0.095
25 ppm M-block	0.096 ± 0.005	2.134 ± 0.079

[a] Values given are calculated from constant composition experiments.

Crystal growth inhibition in the presence of polymeric additives has mostly been attributed to the adsorption of additives on active growth sites on the crystal surfaces. Previously, we and others have reported reduced growth rates for calcium carbonate and hydroxyapatite with addition of alginate, where the growth retarding effect was related to the high affinity of carboxyl groups in alginate toward calcium and subsequent blocking of growth sites.[11,13] Similarly, polyelectrolytes other than alginate with carboxyl and hydroxyl functionality showed an inhibitory effect on hydroxyapatite and calcium fluoride growth, and the adsorption hypothesis was confirmed by fitting of experimental results to Langmuir type adsorption curves.[23,24] In the present study, alginate and its oligomers are fully deprotonated in the pH range of growth experiments that in turn allows for ionic interactions with calcium ions. Therefore, by reference to the previous studies on calcium phosphate and calcium carbonate systems with alginate and other polyelectrolytes and the similar chemistry in solution, the inhibitory effect of alginate on brushite growth can be related to molecular adsorption mechanisms. Further inhibition by increasing polymer concentration and effective G units in parallel supports the hypothesis that high affinity functional groups can result in more effective adsorption to active growth sites and thus lower the growth rate. The magnitude of inhibition is increasing with additive concentration but can reach a maximum beyond which growth inhibition becomes less significant.[25] Comparable growth rates observed at two different concentrations of G-block oligomers indicate saturation of the active sites after which the extent of growth inhibition becomes less dependent on the additive concentration. A G-block concentration of 10 ppm can maximally yield ∼13 molecules per nm^2 of brushite seeds, which is high enough for an efficient surface coverage that inhibits growth. An additional experiment performed with 1 ppm G-block oligomers showed that inhibition follows a concentration-dependent manner before reaching saturation (Figure 3B).

The apparent order of growth (g) was determined from the rate expression (eq 2) and used to discuss possible mechanistic models of crystal growth. Although it is not possible to directly relate changes in solution chemistry to microscopic growth processes occurring at the crystal surface or distinguish between individual faces without support from direct methods such as AFM, general deductions can be made regarding overall growth mechanisms from indirect bulk measurements.[26]

The growth mechanism of a crystal depends highly upon supersaturation, and it is possible to obtain different and multiple mechanisms dominating at different regions of the supersaturation range.[27] In the case of brushite growth without additives, seeded desupersaturation experiments resulted in an average g value close to 1, which indicates a diffusion-controlled growth mechanism. High initial supersaturation ($S = 2.34$) used in the batch experiments can promote high surface nucleation rates resulting in fast surface integration kinetics and hence a diffusion-controlled process with a linear dependence on supersaturation. In order to gain more insight into the growth mechanism at low supersaturation, constant composition experiments were conducted, and the value of apparent growth order was calculated as 2.40 at the determined range from the slope of the logarithmic R vs σ curve (Figure 4). The values of the apparent growth orders demonstrated varying growth mechanisms for brushite under two different conditions that

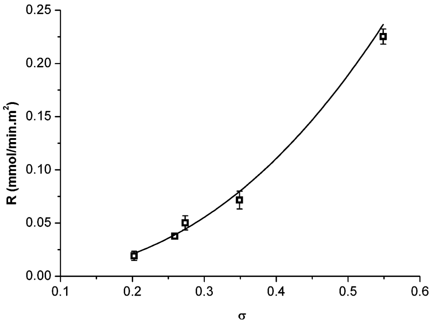

Figure 4. Plot of rate vs relative supersaturation obtained from constant composition experiments.

correlate with the dependence of the dominating growth mechanism on supersaturation. In desupersaturation experiments most of the growth took place at a high supersaturation range where a diffusion-controlled process becomes rate determining. The constant composition experiments were conducted at lower values of supersaturation. Spiral growth has been stated as the most dominant growth mechanism for sparingly soluble salts at low to moderate supersaturation range, and previous studies of brushite growth showed parabolic rate laws ($g \approx 2$).[21,28−30] Surface nucleation might accompany growth when supersaturation is sufficiently high to create new step edges. Therefore, the value of 2.40 can imply a combined mechanism of spiral growth ($g \approx 2$) and surface nucleation ($g > 2$), which has been previously observed for brushite growth.[21]

Experiments with alginate and G-block oligomers resulted in even higher apparent growth orders, indicating a surface nucleation mechanism. In the presence of additives which cause an effective reduction in active growth sites by adsorption, growth may proceed via surface nucleation to generate new growth sites when the driving force is high enough.[31] Thus, the transition in the growth mechanism might result from specific interactions between the additive and active sites on the crystal surface. When M-block oligomers were used as additives, g values were close to 2, which might be interpreted as growth is still proceeding via spiral growth and the mechanism is not changed. Carboxyl groups of M-blocks do not exhibit a specific affinity toward calcium ions; however, nonspecific interactions with the crystal surface are likely to occur via ionic interactions or H-bonding.[10] Oligomer chains might be nonspecifically adsorbed onto the crystal surface without significant blockage of active sites, and therefore the growth mechanism is not altered. However, their presence is effective in decreasing the rate of incorporation as seen evidently from the growth rates. Thus, it can be concluded that the presence of M-blocks affects the accessibility of the active sites in a concentration-dependent manner and retards the growth.

The changes in g values and proposed mechanisms for brushite growth in the presence of additives also shed light on the differences in growth behavior at low supersaturation range. In the presence of alginate and G-block additives almost complete inhibition of growth was observed at low supersaturation because a certain driving force is needed to continue growth via surface nucleation. However, in the presence of M-blocks crystal growth continued even at low supersaturation range with the spiral growth mechanism.

Unseeded Batch Experiments. Unseeded experiments were conducted to evaluate the effects of alginate-based additives on spontaneous crystallization of brushite. Although other calcium phosphate phases were observed within the gel matrix in our model system, all experiments in solution yielded phase pure brushite as the final product, but differences were observed in the progression of the reactions and morphology of the final particles.

Calcium depletion curves for unseeded experiments are given in Figure 5. In the absence of any additive, calcium consumption was fast, and the precipitation reaction was complete after approximately 100 min. When high molecular weight alginate was added in the reaction vessel, calcium depletion slowed down in proportion to the polymer concentration. In the presence of oligomers the retardation effect was most prominent. Addition of 10 ppm M-blocks in the reaction medium resulted in a prolonged time interval where calcium concentration and pH changes were very small, and this time lapse was followed by a faster consumption region at a rate comparable to high molecular weight alginate at the same concentration. In the case of G-blocks, the course of precipitation slowed down substantially compared to any other additives (Figure 5 inset).

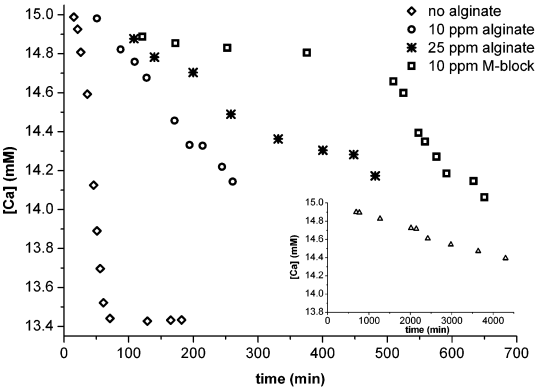

Figure 5. Calcium consumption curves of unseeded experiments with no additive, with alginate and M-blocks at indicated concentrations. Inset shows the calcium consumption curve in the presence of 10 ppm G-block. Note different time scales.

Samples were collected at initial and final reaction time points and at comparable levels of supersaturation from each batch for morphological evaluation by SEM. Appropriate time points were determined by calculations of supersaturation that is dominantly depending on pH. Since all experiments were conducted under nitrogen atmosphere, pH values are sufficient input data in order to calculate momentary supersaturation values. Early samples were collected at $S \approx 2.00$ revealing the effects of the various additives on initial stage of the precipitation reactions, whereas final samples were collected at $S \approx 1.0$ for additive free reactions and $S \leq 1.50$ for all others, by which point most of the available calcium had been consumed. In the early stages brushite crystals were observed to precipitate with a well-defined, platelet-like morphology in additive free experiments (Figure 6A). Crystals precipitated in the presence of 10 ppm alginate were larger initially (Figure 6B), and more prominent size differences were observed for the final products of the reactions (Figure 7B). Since seeded

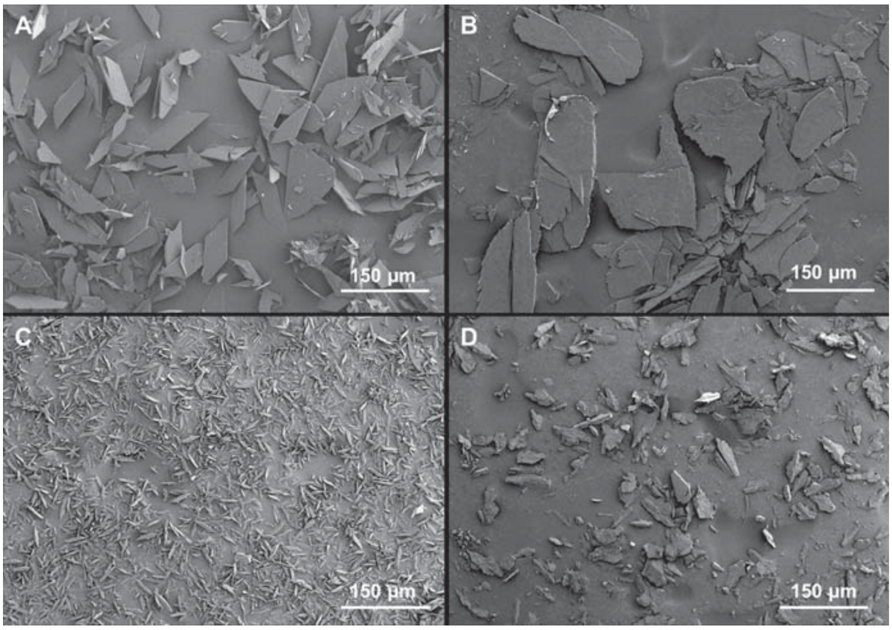

Figure 6. SEM images of samples collected at $S \approx 2.0$ during unseeded batch experiments with no additive (A), 10 ppm alginate (B), 10 ppm M-block (C), and 10 ppm G-block (D).

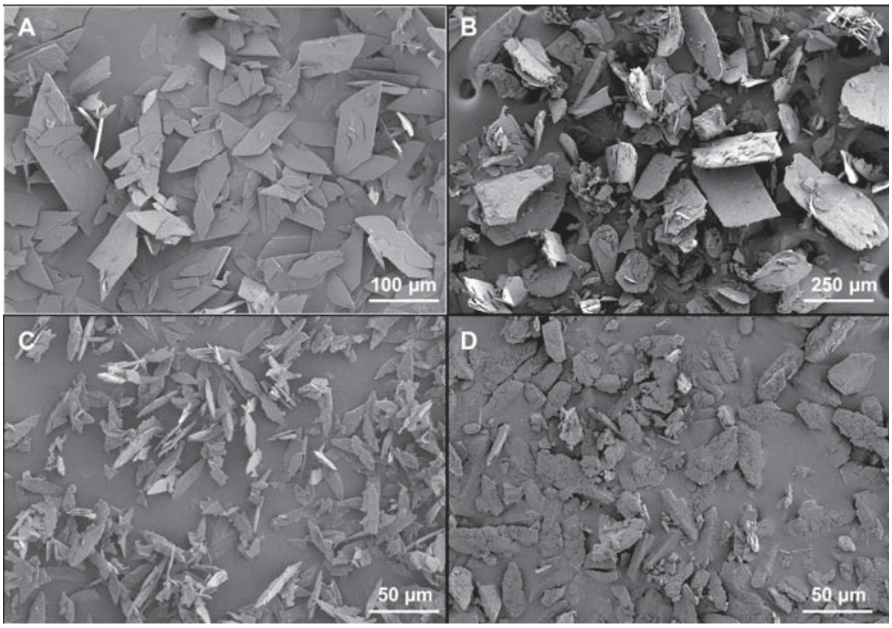

Figure 7. SEM images of final precipitation products from unseeded batch experiments with no additive (A), 10 ppm alginate (B), 10 ppm M-block (C), and 10 ppm G-block (D). Note the different scale bars.

experiments showed that the growth rate was reduced with the addition of alginate, large-sized particles observed at same levels of supersaturation illustrate that the nucleation rate was reduced and resulted in a lower number of particles consuming supersaturation for growth. This effect was even more pronounced at the final stages of the reactions. The brushite crystals precipitated in the presence of alginate were much larger than additive-free counterparts despite the lower growth

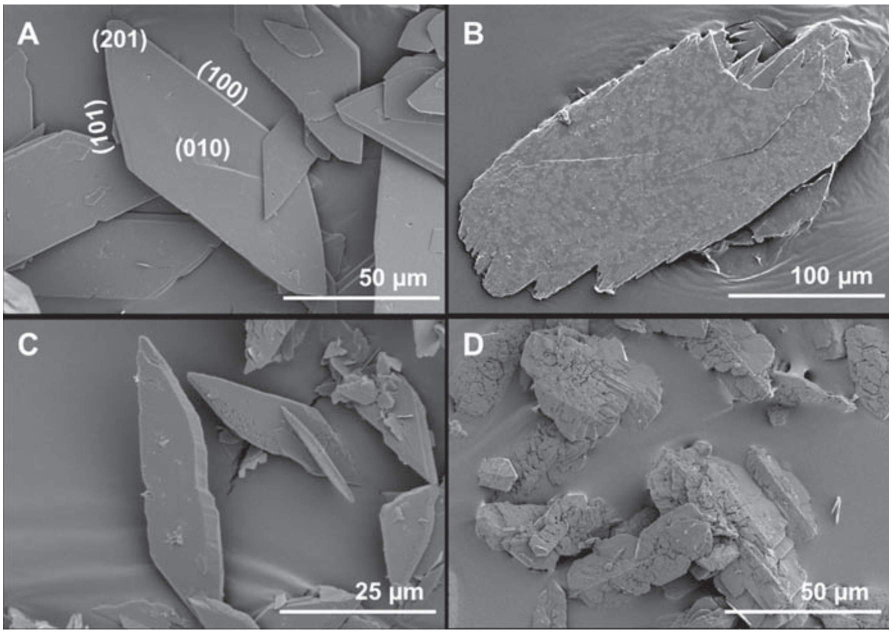

Figure 8. SEM images of final crystals from unseeded batch experiments with no additive (A), 10 ppm alginate (B), 10 ppm M-block (C), and 10 ppm G-block (D). Note the different scale bars.

rates and higher supersaturation at the end point of reactions. M-blocks did not show a retardation effect on nucleation (Figure 6C). As seen in the calcium and pH depletion curves (Figure 5), high supersaturation levels were maintained for prolonged times in the presence of oligomers, which can result in upholding high nucleation rates. Simultaneously reduced growth rates in the presence of M-block oligomers consequently led to precipitation of small size brushite particles (Figure 7C). In precipitation experiments including G-block oligomers, with the same upholding effect on supersaturation for much longer time and lower growth rates, even smaller particles would be expected, but the opposite was observed as in the case of alginate (Figures 6D and 7D). These results suggest a retardation effect on nucleation by the G-blocks that are present in both additives; however, further explanations cannot be offered within the experimental data of this study.

The morphology of a crystal is determined by the relative growth rates of its individual faces. When additives are adsorbed preferentially to a certain face, its relative growth rate decreases and that face is expressed more in the final morphology. Therefore, observation of the final morphologies may reveal the interactions of alginate based additives with brushite.

In additive-free experiments, brushite was precipitated with a typical platelet-like morphology with prominent (010) and lateral (*h*0*l*) faces (Figure 8A). In aqueous solution, it is assumed that the dominant (010) face of brushite crystal is composed of bilayers of structural water molecules, and lateral faces express a mixed ionic nature with exposed calcium and phosphate ions.[32] When alginate was added in the reaction medium, large crystals with the same platelet shape were obtained (Figure 8B). In that case, it can be assumed that sterically hindered macromolecules of alginate mostly adsorb on the dominant faces. In contrast, addition of small M-block oligomers with functional groups resulted in particles with a noticeable increase in thickness, which can be interpreted as they were preferentially adsorbed on the lateral faces of brushite crystals primarily due to electrostatic interactions (Figure 8C). In their study of additive interactions with brushite, Sikiric et al. presented similar findings where small molecules with sufficient charge density through functional groups preferentially interacted with lateral faces, whereas macromolecules and molecules with hindered structures specifically adsorbed on the dominant (010) face.[33] The most prominent morphological changes were observed in the presence of G-block oligomers where smooth (010) faces were no longer retained. In the presence of G-block oligomers, the specific affinity of the additives toward calcium ions might be more operational than size and charge effects (Figure 8D). This drastic change in morphology was also reflected in the XRD data. The most intense peaks of brushite are found at 2θ = 11.68°, 20.93°, 29.26°, 30.50°, and 34.15° that correspond to X-ray diffractions from {020}, {021}, {041}, $\{\bar{2}21\}$, and {220} planes, respectively. The plate-like structure and dominant (010) face of brushite leads to preferential orientation of the crystals and affects the diffraction pattern by enhancing the intensity of {020} reflection at 11.68°.[34] Although this effect was eliminated to some extent by grinding the samples, it could not be completely removed. Figure 9 shows the comparison of diffraction patterns of the precipitates with ideal isotropic XRD data of brushite at the five highest intensity peaks. As the preferential orientation due to the plate like structure of brushite was disturbed with the presence of G-block oligomers, relative peak intensities showed a closer fit to the ideal case.

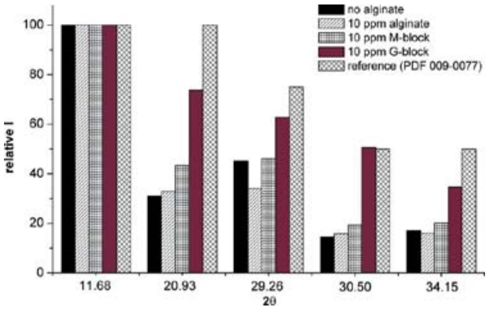

Figure 9. Relative intensities of XRD peaks of brushite precipitates.

CONCLUSION

Investigations of brushite crystallization in the presence of alginate additives revealed significant effects of compositional variations of alginate on the nucleation and growth processes. Growth kinetics in the presence of additives was studied by seeded desupersaturation experiments, and this method was shown to be applicable for brushite growth under specified experimental conditions. Although the constant composition method provides better accuracy and control particularly over the kinetic studies of slow growing minerals at low supersaturation range, for a fast growing mineral like brushite, growth kinetics can be efficiently studied at desupersaturation conditions and a relatively high level of supersaturation. Growth experiments showed decreased growth rates in the presence of all additives, but the extent of reduction and proposed growth mechanisms varied between the different types of alginates used. In the presence of alginate and G-block oligomers, specific affinity of G-blocks toward calcium ions resulted in a growth mechanism more dominated by surface nucleation possibly by blocking the active growth sites on the crystal surface. On the other hand, nonspecific interactions of M-block oligomers caused a reduction in growth rates and a parabolic dependence of growth on relative supersaturation, which is indicative of a spiral growth mechanism. Differences in growth mechanisms led to changing growth profiles at the low supersaturation region where spiral growth could proceed further, but growth via surface nucleation was almost completely inhibited with decreasing driving force. Unseeded batch experiments showed the effects of additives on the initial stages of precipitation. By decoupling the results of seeded and unseeded experiments, information was deduced regarding the nucleation stage where comparing particle sizes with the knowledge of relative growth rates suggested a retardation effect on brushite nucleation by additives with G-units.

ASSOCIATED CONTENT

Ⓢ Supporting Information

The Supporting Information is available free of charge on the ACS Publications website at DOI: 10.1021/acs.cgd.5b01032.

> The reactions and their corresponding equilibrium constants used for calculations of solution speciation by the thermodynamic software PHREEQC Interactive 3.1, representation of growth curves as a function of relative supersaturation including both the predicted growth models and the experimental data points (PDF)

AUTHOR INFORMATION

Corresponding Author

*E-mail: jens-petter.andreassen@ntnu.no.

Funding

We gratefully acknowledge financial support provided by the Research Council of Norway (FRINATEK Project 214607).

Notes

The authors declare no competing financial interest.

REFERENCES

(1) Alivisatos, A. P. *Science* **2000**, *289*, 736.

(2) Zhang, C. Y.; Zhang, W.; Yao, H. B.; Zhu, H. Z.; Mao, L. B.; Yu, S. H. *Cryst. Growth Des.* **2013**, *13*, 3505.

(3) Chrissanthopoulos, A.; Malkaj, P.; Dalas, E. *Mater. Lett.* **2006**, *60*, 3874.

(4) Butler, M. F.; Glaser, N.; Weaver, A. C.; Kirkland, M.; Heppenstall-Butler, M. *Cryst. Growth Des.* **2006**, *6*, 781.

(5) Aimoli, C. G.; de Lima, D. O.; Beppu, M. M. *Mater. Sci. Eng., C* **2008**, *28*, 1565.

(6) de Lima, D. O.; Aimoli, C. G.; Beppu, M. M. *Mater. Sci. Eng., C* **2009**, *29*, 1109.

(7) Kumar, R.; Prakash, K. H.; Cheang, P.; Gower, L.; Khor, K. A. *J. R. Soc., Interface* **2008**, *5*, 427.

(8) Fried, R.; Mastai, Y. *J. Cryst. Growth* **2012**, *338*, 147.

(9) Wang, T.; Leng, B.; Che, R.; Shao, Z. *Langmuir* **2010**, *26*, 13385.

(10) Mørch, Ý. A.; Donati, I.; Strand, B. L. *Biomacromolecules* **2006**, *7*, 1471.

(11) Olderøy, M. Ø.; Xie, M.; Strand, B. L.; Flaten, E. M.; Sikorski, P.; Andreassen, J. P. *Cryst. Growth Des.* **2009**, *9*, 5176.

(12) Olderøy, M. Ø.; Xie, M.; Strand, B. L.; Draget, K. I.; Sikorski, P.; Andreassen, J. P. *Cryst. Growth Des.* **2011**, *11*, 520.

(13) Malkaj, P.; Pierri, E.; Dalas, E. *J. Mater. Sci.: Mater. Med.* **2005**, *16*, 733.

(14) Coleman, R. J.; Jack, K. S.; Perrier, S.; Grøndahl, L. *Cryst. Growth Des.* **2013**, *13*, 4252.

(15) Lee, K. Y.; Mooney, D. J. *Prog. Polym. Sci.* **2012**, *37*, 106.

(16) Bjørnøy, S. H. Bassett, D. C. Ucar, S. Andreassen, J. P. Sikorski, P. *Biomed. Mater.* **2015**, under review.

(17) Theiss, F.; Apelt, D.; Brand, B.; Kutter, A.; Zlinszky, K.; Bohner, M.; Matter, S.; Frei, C.; Auer, J. A.; von Rechenberg, B. *Biomaterials* **2005**, *26*, 4383.

(18) Haug, A.; Larsen, B.; Smidsrod, O. *Acta Chem. Scand.* **1966**, *20*, 183.

(19) Skjakbraek, G.; Larsen, B. *Carbohydr. Res.* **1985**, *139*, 273.

(20) Beck, R.; Seiersten, M.; Andreassen, J. P. *J. Cryst. Growth* **2013**, *380*, 187.

(21) Marshall, R. W.; Nancollas, G. H. *J. Phys. Chem.* **1969**, *73*, 3838.

(22) Salimi, M. H.; Heughebaert, J. C.; Nancollas, G. H. *Langmuir* **1985**, *1*, 119.

(23) Öner, M.; Doğan, Ö. *Prog. Cryst. Growth Charact. Mater.* **2005**, *50*, 39.

(24) Amjad, Z. *Langmuir* **1991**, *7*, 2405.

(25) Xie, S.; Poornachary, S. K.; Chow, P. S.; Tan, R. B. H. *Cryst. Growth Des.* **2010**, *10*, 3363.

(26) Teng, H. H.; Dove, P. M.; De Yoreo, J. J. *Geochim. Cosmochim. Acta* **2000**, *64*, 2255.

(27) Nielsen, A. E. *J. Cryst. Growth* **1984**, *67*, 289.

(28) Nancollas, G. H.; Wefel, J. S. *J. Cryst. Growth* **1974**, *23*, 169.

(29) Hohl, H.; Koutsoukos, P. G.; Nancollas, G. H. *J. Cryst. Growth* **1982**, *57*, 325.

(30) Combes, C.; Freche, M.; Rey, C. *J. Mater. Sci.: Mater. Med.* **1995**, *6*, 699.

(31) Reynolds, R. C. *Limnol. Oceanogr.* **1978**, *23*, 585.

(32) Hanein, D.; Geiger, B.; Addadi, L. *Langmuir* **1993**, *9*, 1058.

(33) Sikirić, M.; Babić-Ivančić, V.; Milat, O.; Sarig, S.; Füredi-Milhofer, H. *Langmuir* **2000**, *16*, 9261.

(34) Lee, D.; Sfeir, C.; Kumta, P. N. *Mater. Sci. Eng., C* **2009**, *29*, 69.

SUPPORTING INFORMATION

Nucleation and Growth of Brushite in the Presence of Alginate

Seniz Ucar,[a] *Sindre H. Bjørnøy,*[b] *David C. Bassett,*[b] *Berit L. Strand,*[c] *Pawel Sikorski,*[b] *and Jens-Petter Andreassen**[, a]

Table S1. The reactions and their corresponding equilibrium constants (-log K) used to calculate the solution speciation at 25 °C

$H_2O \leftrightarrow H^+ + OH^-$	13.997
$Ca^{2+} + H_2O \leftrightarrow CaOH^+ + H^+$	12.697
$H_3PO_4 \leftrightarrow 3H^+ + PO_4^{3-}$	21.721
H_2PO_4- $\leftrightarrow 2H^+ + PO_4^{3-}$	19.573
$HPO_4^{2-} \leftrightarrow H^+ + PO_4^{3-}$	12.375
$CaH_2PO_4^+ \leftrightarrow Ca^{2+} + 2H^+ + PO_4^{3-}$	20.923
$CaHPO_4 \leftrightarrow Ca^{2+} + H^+ + PO_4^{3-}$	15.035
$CaPO_4^- \leftrightarrow Ca^{2+} + PO_4^{3-}$	6.46
$CaHPO_4.2H_20$ (s) $\leftrightarrow Ca^{2+} + H^+ + PO_4^{3-} + 2H_2O$	18.995

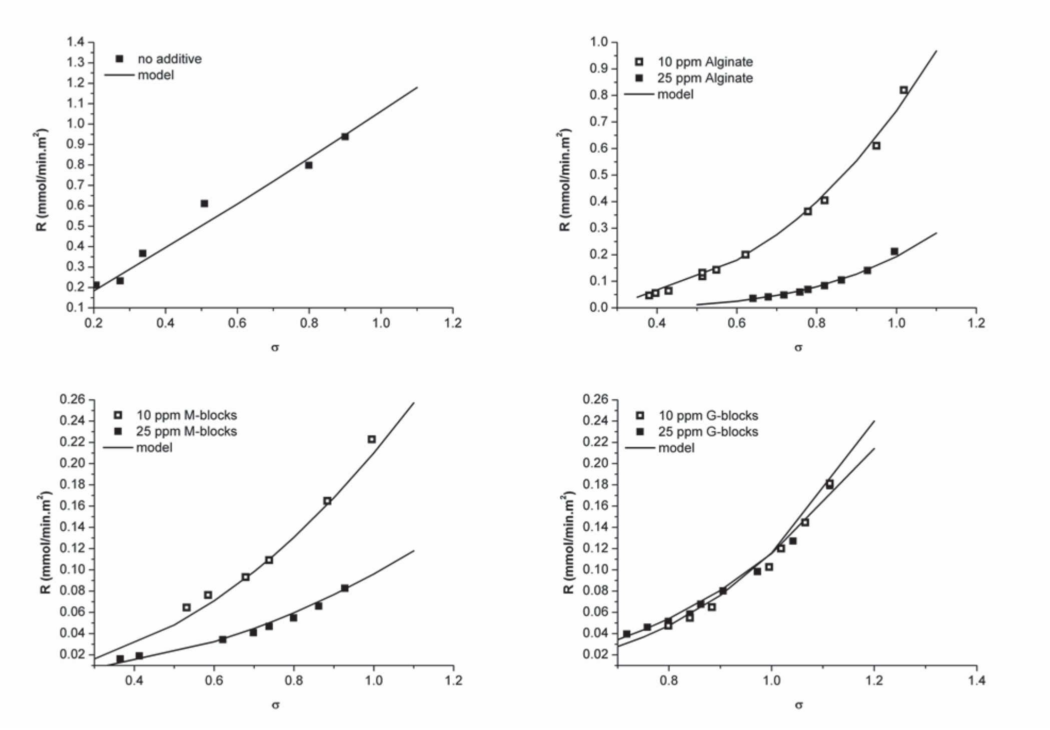

Figure S1. Representation of growth rates as a function of relative supersaturation. Solid lines show predicted models and markers show experimental data points.

Paper II

Journal of Crystal Growth 468 (2017) 774–780

Contents lists available at ScienceDirect

Journal of Crystal Growth

journal homepage: www.elsevier.com/locate/crysgro

Transformation of brushite to hydroxyapatite and effects of alginate additives

Seniz Ucar[a], Sindre H. Bjørnøy[b], David C. Bassett[b], Berit L. Strand[c], Pawel Sikorski[b], Jens-Petter Andreassen[a,*]

[a] *Department of Chemical Engineering, Norwegian University of Science and Technology, Trondheim, Norway*
[b] *Department of Physics, Norwegian University of Science and Technology, Trondheim, Norway*
[c] *Department of Biotechnology, Norwegian University of Science and Technology, Trondheim, Norway*

ARTICLE INFO

Communicated by Christian Kloc

Keywords:
Biocrystallization
Nucleation
Calcium compounds
Minerals

ABSTRACT

Phase transformations are important processes during mineral formation in both *in vivo* and *in vitro* model systems and macromolecules are influential in regulating the mineralization processes. Calcium phosphate mineralized alginate hydrogels are potential candidates for hard tissue engineering applications and transformation of the resorbable calcium phosphate phases to apatitic bone mineral *in vivo* enhances the success of these composite materials. Here, the transformation of brushite to hydroxyapatite (HA) and the effects of alginate additives on this process are studied by the investigation of supersaturation profiles with HA-seeded and unseeded experiments. This experimental design allows for detailed kinetic interpretation of the transformation reactions and deduction of information on the nucleation stage of HA by evaluating the results of seeded and unseeded experiments together. In the experimental conditions of this work, transformation was controlled by HA growth until the point of near complete brushite dissolution where the growth and dissolution rates were balanced. The presence of alginate additives at low concentration were not highly influential on transformation rates during the growth dominated region but their retardant effect became more pronounced as the dissolution and growth rates reached an equilibrium where both reactions were effective on transformation kinetics. Decoupling of seeded and unseeded transformation experiments suggested that alginate additives retard HA nucleation and this was most evident in the presence of G-block oligomers.

1. Introduction

The formation of inorganic minerals *via* a biological process (biomineralization) involves the constructive interaction between organic and inorganic phases to result in composite tissues with exceptional biological and physical properties [1]. Although it is currently not possible to exactly reproduce such materials by synthetic means, naturally derived composite tissues have been a rich source of inspiration for the design of synthetic biomaterials for hard tissue engineering applications [2,3]. Calcium phosphates (CaP) are an important class of minerals in this regard since hydroxyapatite (HA) is the dominant mineral phase in the calcified tissues of mammals. The *in vivo* mineralization mechanism of HA has been proposed to have multiple steps that include the initial precipitation of transient phases followed by their transformation [4,5]. Based on *in vitro* studies, amorphous calcium phosphate (ACP), brushite and octacalcium phosphate (OCP) have all been suggested as precursor phases for bone mineral formation *in vivo* [6].

In a recent study, our group investigated alginate hydrogels mineralized with brushite as potential candidates for bone tissue engineering applications and gelation and mineralization kinetics of this composite system were studied in detail [7,8]. Brushite is well suited to this purpose due to its higher solubility that leads to ready hydrolysis and therefore enables remodeling and transformation to bone-like mineral *in vivo* by providing the necessary space and ions [9]. Alginate has been extensively studied and clinically applied for many biomedical applications since it is non-toxic, biodegradable and is tolerated well *in vivo*, also it can form hydrogels under mild and physiologically compatible conditions. Alginate is a polysaccharide composed of 1–4 linked β-D-mannuronic acid (M) and α-L-guluronic acid (G) residues with an alternating or block structure. G- units show a specific affinity towards certain cations including calcium ions through their outward carboxyl groups so that calcium can selectively bind to G-blocks and alternating blocks of the polymer but not to M-blocks [10].

---

[*] Corresponding author.
E-mail address: jens-petter.andreassen@ntnu.no (J.-P. Andreassen).

http://dx.doi.org/10.1016/j.jcrysgro.2016.11.019

Therefore, its chemical composition, sequential structure of the repeating units and molecular weight are highly deterministic on how alginate regulates CaP mineralization [8]. Our model system showed that when seeded hydrogels were kept in their gelling bath at room temperature brushite minerals started to transform into HA after 24 h.

The driving force for solvent mediated transformation of brushite to HA originates from the large difference between the solubility products of these two phases (−log K_{sp} 18.99 and 44.33 for brushite and HA, respectively at 25 °C) [11]. Investigations on the hydrolysis of brushite to HA revealed multiple variables that can act on the transformation kinetics such as altering reaction conditions [12,13], modifying brushite [14,15] and incorporating additives in the reaction medium [16–18]. Previous studies of brushite to HA transformation showed that organic molecules can mediate the transformation reaction through different mechanisms depending on the nature of interactions between the additive and the mineral phases. Xie et al. showed that albumin has a retarding effect on brushite transformation *via* two mechanisms: binding of protein to calcium ions and electrostatic interactions between the protein and the CaP surface that restricts the dissolution and subsequent reprecipitation processes [16]. In contrast Tang et al. showed that the transformation of brushite to HA was promoted in the presence of citrate and acidic amino acids (aspartate and glutamate) *via* reducing the interfacial energy barrier between the two mineral phases [17,18].

In the present study, we investigate the transformation of brushite to HA and the effects of alginate additives on this process by a detailed investigation of reaction kinetics *via* supersaturation profiles to obtain more insight and control on our model system. According to the kinetic model of solvent mediated transformation postulated by Davey et al. the overall transformation can be either dissolution or growth controlled, depending on the ratio of kinetic constants of these reactions and the relative surface areas of two phases; where different control mechanisms give rise to different desupersaturation profiles during hydrolysis [19]. Although conversion data obtained by microscopic, spectrometric and thermal methods are used quite often to explore phase transformations of CaPs, mechanistic insight on transformation kinetics can be best obtained by investigation of the supersaturation profiles.

The transformation kinetics were evaluated first by changing the initial surface area ratio of brushite and hydroxyapatite in the absence of additives to evaluate the controlling mechanism. When additives were introduced, their effects on hydrolysis were studied both by seeded and unseeded experiments.

2. Experimental

2.1. Materials

All chemical reagents were purchased from Sigma-Aldrich unless stated otherwise. Deionized water (DI water) was used to prepare all aqueous solutions. Alginate with a molecular mass of 274 kDa and 68% G, isolated from Laminaria hyperborea *(L. hyp)* stipe, was obtained from FMC Biopolymer (Norway). Two different oligomers of alginate, denoted as G- and M-blocks, consisted of 90% and 5% G monomer, respectively, with the degree of polymerization ≈20 for both. The G-blocks were produced from alginate from *(L. hyp)* stipe by acid degradation and fractionation [20]. The M-blocks were produced from alginate from *Ascophyllum nodosum* by acid degradation and calcium fractioning as described elsewhere [21].

2.2. Methods

All experiments were carried out in a magnetically stirred 1 L double-walled glass reactor, with two baffles attached to the lid. Temperature was controlled by a water bath at 25 °C for all experiments. Nitrogen, presaturated with water, was constantly bubbled into solutions 2 h prior to and during the experiments to exclude atmospheric carbon dioxide. The chemical speciation and supersaturation was determined by thermodynamic calculation program PHREEQC Interactive 3.1, using Minteq v4 database. The equilibrium constants used for solution speciation are given in the supplementary information (Table S1) and the activity based supersaturation (S) is defined as given in Eq. (1) where IAP is the ion activity product, K_{sp} is the solubility product and υ is the number of ions in the unit formula of the corresponding phase (see Eqs. S1 and S2).

$$S=\left(\frac{\{IAP\}}{\{K_{sp}\}}\right)^{1/\upsilon} \tag{1}$$

The pH was recorded continuously by means of a combined glass electrode with KCl reference electrolyte connected to Tiamo software (Metrohm) and calibrations were carried out before each experiment. Calcium ion concentration in the vessel was monitored by either online recording of the calcium electrode potential in the vessel *via* Tiamo software or offline titration (Mettler Toledo DL 53) of samples with 10 mM EDTA as explained elsewhere [8]. Phosphate concentration was determined spectrophotometrically by formation of its molybdate complex and measuring absorbance at 835 nm [22].

Characterization of solid phases were conducted *via* powder XRD (D8 Advance, DaVinci, Bruker AXS GmbH) in the range of 4–75° with a step size of 0.013° and a step time of 0.67 s. FTIR (Tensor, Bruker) spectra of powder samples were also collected between 4000 and 550 cm^{-1}. SEM analyses (S-3400N, Hitachi) were performed at an accelerating voltage of 5 kV, where samples were placed on carbon tape and sputter coated with gold.

2.3. Seed preparation

Brushite seeds were prepared as described elsewhere [8]. Briefly, equimolar amounts of $Ca(NO_3)_2{\cdot}4H_2O$ and KH_2PO_4 solutions were mixed to a total volume of 1 L under nitrogen environment and constant stirring at 800 rpm at 25 °C. Precipitates were aged in their saturated solution for at least 2 h after completion of the reaction as indicated by stable pH. The crystals were then filtered, washed with DIW and ethanol prior to drying at room temperature. HA seeds were prepared by the method previously described by Nancollas and Mohan [23]. Briefly, 0.5 M of $Ca(NO_3)_2{\cdot}4H_2O$ solution was added slowly to a 0.3 M KH_2PO_4 solution under nitrogen environment and constant stirring at 800 rpm. During the precipitation reaction the pH of the solution was maintained between 8.5 and 10 by addition of KOH and temperature was kept at 70 °C. The precipitate was refluxed at 70 °C overnight. Crystals were then washed with DIW by repeated centrifugation and dried at 80 °C. Phase purity of seeds was verified by XRD and FTIR analyses. Specific surface area (SSA) was determined by multiple point BET nitrogen adsorption method (Tristar II, Micromeritics) and found to be $0.646 \pm 0.023\ m^2/g$ and $62.518 \pm 0.142\ m^2/g$ for brushite and HA seeds respectively. Seeds were stored for up to one month in their dry state prior to use.

2.4. Transformation experiments

Solvent mediated transformation of brushite was investigated by desupersaturation profiles. For this purpose, the solution pH was monitored as the primary variable as this reflects changes in the supersaturation profile during dissolution and precipitation. In addition, calcium and phosphate ion concentrations were determined at arbitrary time points to support the desupersaturation profiles obtained by pH data and to quantify values of the momentary supersaturation.

Transformation reactions were initiated by addition of 250 mg of brushite seeds dispersed in 1 mL of DI water in 0.5 L aqueous alkaline solution (Ionic strength=0.15 M, pH~8.30) under N_2 bubbling and constant stirring at 750 rpm. Subsequent fast dissolution of brushite seeds in this undersaturated solution resulted in an increase in the pH up to 8.60 ± 0.05 where a plateau was observed. Automated burettes were activated when a stable pH was attained to keep the value constant by titrating with 0.01 M NaOH throughout the experiments.

In the aqueous alkaline media (pH=8.60 ± 0.05) with NaOH addition, the phase transformation of brushite to HA occurs by subsequent dissolution and reprecipitation reactions resulting in the overall reaction given below (Eq. (2)) [24,25].

$$10\ CaHPO_4{\cdot}2H_2O+8\ OH^- \rightarrow Ca_{10}(PO_4)_6(OH)_2 + 4HPO_4^{2-}+26\ H_2O \quad (2)$$

By using the constant pH titration, the changes in pH were recorded with high precision and the course of transformation was evaluated by using the titrant addition curves. In addition, pH was kept at its initial high value chosen to eliminate possible OCP formation and make HA the favorable phase throughout the transformation reactions [11].

In the absence of additives, varying amounts of HA seeds (50, 75, 100 and 125 mg) were added in the reactor immediately after the titration was activated to evaluate the transformation kinetics. In order to investigate the effect of additives on transformation, corresponding amounts of alginate additives were included in the solution and experiments were carried out both with and without the addition of HA seeds.

3. Results and discussion

When brushite seeds were added to aqueous alkaline solutions (point 1, Fig. 1) pH values first showed a sharp decrease from pH ~8.40 to 8.00 due to the lower pH of the suspending solution (DI water, pH ≈7.00) followed by a more gradual increase up to 8.60 ± 0.05 due to brushite dissolution at which point the pH remained stable and the constant pH mode was activated (point 2, Fig. 1). Since brushite dissolution provided the necessary ions to build up the supersaturation in solution, the pH started to drop after this point either because of growth in the HA seeded experiments or spontaneous precipitation in the unseeded experiments, and it was maintained by automatic base titration.

3.1. Seeded transformation experiments

Transformation kinetics of brushite were initially investigated with the addition of HA seeds in the reaction medium immediately after a stable pH was observed and titration was activated. In the first set of seeded experiments, the amount of HA seeds was varied (75, 100 and 125 mg) in the absence of additives. Fig. 2 shows the rate of base addition with respect to time for different seed amounts. Titration curves showed an initial linear rate of titrant addition followed by a slightly inclined plateau and a final regime with a logarithmic addition rate.

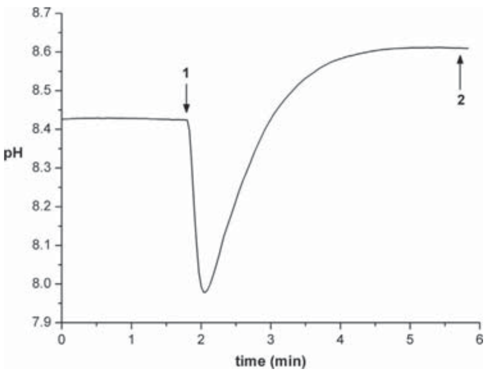

Fig. 1. The pH curve with respect to time where point 1 shows the addition of brushite seeds and point 2 shows the activation of titration to maintain the stable pH. The initial drop of the pH observed with seed addition is caused by the solution used to disperse brushite seeds.

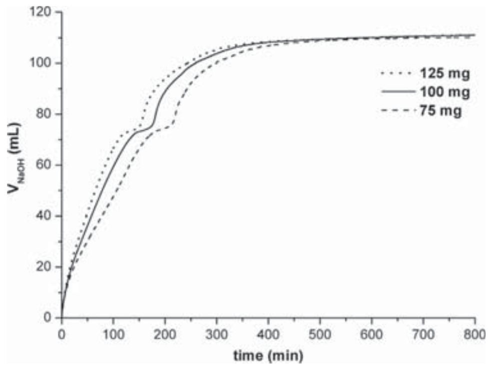

Fig. 2. Titrant addition curves of HA seeded transformation experiments in additive-free solution with three different seed amounts.

The linear rate of base titration until the plateau indicates a constant rate of transformation (R_{tr}) according to Eq. (2) which can be associated with a constant driving force for the transformation of brushite to HA (ΔG_{tr}) that can be given by;

$$\Delta G_{tr}=\Delta G_{HA}-\Delta G_{brs} \quad (3)$$

where the ΔG_{HA} is the driving force for the formation of HA and ΔG_{brs} is the driving force for the formation and hence the stability of brushite. In addition, the driving force for the formation of a CaP phase can be defined in dependence of its activity based supersaturation, S_{CaP} (Eq. (1)), where R_g is the gas constant and T is the absolute temperature (Eq. (4)).

$$\Delta G_{CaP}=-\upsilon R_g T \ln S_{CaP} \quad (4)$$

In order to examine the changes in solution supersaturation, samples were collected and analyzed for calcium and phosphate ion concentrations, and momentary supersaturation values were calculated with respect to both brushite and HA at the start of titration, during the linear region of the titration curves and in the plateau region (Fig. 3). Initially the solution was highly supersaturated with respect to HA (S_{HA}≈36) and slightly undersaturated with respect to brushite (S_{brs}≈0.84). Therefore, at the experimental conditions where both HA-seeded and unseeded transformation reactions were initiated, brushite was thermodynamically unstable ($\Delta G_{brs} > 0$) whereas HA

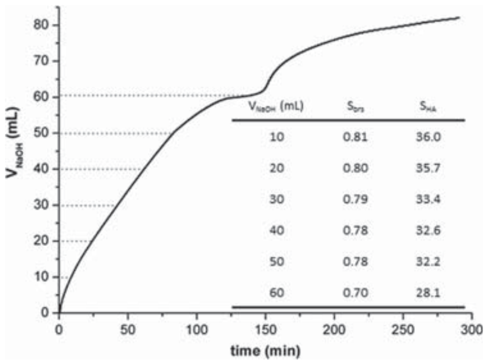

V_{NaOH} (mL)	S_{brs}	S_{HA}
10	0.81	36.0
20	0.80	35.7
30	0.79	33.4
40	0.78	32.6
50	0.78	32.2
60	0.70	28.1

Fig. 3. The data points of sample collection for ion concentration analyses and calculated values of momentary supersaturation with respect to brushite and HA during the transformation reaction.

growth was favorable ($\Delta G_{HA} < 0$) and ΔG_{tr} had an overall negative value. Results of ion analyses during the linear region of titrant addition showed decreasing calcium concentration and increasing phosphate concentration in the solution due to the difference in the stoichiometry of the two minerals (Eq. (2)). The changes in ion concentrations resulted in decreasing supersaturation for both brushite and HA but the calculation of ΔG_{tr} by use of the momentary S values showed the overall driving force for transformation was kept within less than 2.5% deviation as indicated by the constant rate of base consumption.

The decrease in the supersaturation values of both phases might indicate that the supersaturation consumption due to the HA growth was not effectively compensated by the brushite dissolution. Although there is a three orders of magnitude difference between the rate constants of the dissolution and growth reactions ($k_{d,\ brushite}$~10^{-5} [26,27] and $k_{g,\ HA}$~10^{-8} [28,29]), the overall rates of the dissolution and growth and so the controlling mechanism during the transformation reaction is highly dependent on the supersaturation of the reaction medium and the relative surface areas of both phases. When the transformation experiments were conducted in the presence of varying amounts of HA seeds, equal transformation rates were obtained when rates were normalized to the surface area of the seeds used. Therefore, it can be concluded that the rate of transformation was closely dependent and controlled by the rate of HA growth and the dissolution rate of brushite was not a limiting factor in the specified system.

In the plateau region the changes in pH were minimized which indicates reaching the plateau supersaturation where the equilibrium between two reactions was established and the mass dissolution and growth rates were balanced. Due to the large difference between the rate constants, this equilibrium can only be reached at critically low amounts of brushite attained at the point of almost complete dissolution. The end point of the plateau region thus corresponds to the point of complete consumption of the brushite crystals and completion of the transformation reactions. After brushite was completely consumed, the supersaturation profile of the solution is determined by HA growth only. The final logarithmic part of the titration curve represents desupersaturation of the solution by the growth of HA until the solubility limit was reached and calculation of the supersaturation at the final points of the experiments gave values of S_{HA}≈1.0. Observation of the plateau and maxima of all curves at equal volumes of base addition in all experiments and drastic decrease in both calcium and phosphate concentrations after the plateau region also supports this hypothesis.

In the second set of HA-seeded experiments, alginate additives were introduced and the mass of HA seeds was kept constant at 100 mg. Titrant addition curves showed the same three characteristic regions and here the data are presented in terms of the percentage of conversion to HA, assuming complete conversion at the end-point of the plateau where the solid brushite was completely consumed (Fig. 4).

The differences in conversion rates between the sample groups developed as the transformation proceeded and were more noticeably expressed towards the end of the reactions. The retarding effect of alginate and other molecules with carboxyl functionality on HA growth is previously reported in literature as an effect related to the adsorption of additives on the active growth sites on the crystal surfaces [28–30]. Growth experiments of HA in the presence of alginate and its oligomers were conducted in our group also and efficient growth retardation was observed that was in agreement with the literature (to be published). However, during the growth dominated region of the transformation rates, strong retardation in the presence of additives was not expressed as evident from the similar slopes of the curves. Both the studies by our group and documented in the literature were conducted at low supersaturation with respect to HA (S_{HA}≈1.0–5.4) where spiral growth is the controlling mechanism. However the high supersaturation in the current transformation experiments (S_{HA}≈36) can promote high surface nucleation rates, resulting in fast surface integration kinetics and can also further lead to a diffusion-controlled process. Thus the retardation effect of additives on growth, resulting from their blockage of active sites on crystal surfaces, may lose its influence at low additive concentration and high supersaturation during the growth dominated region of transformation.

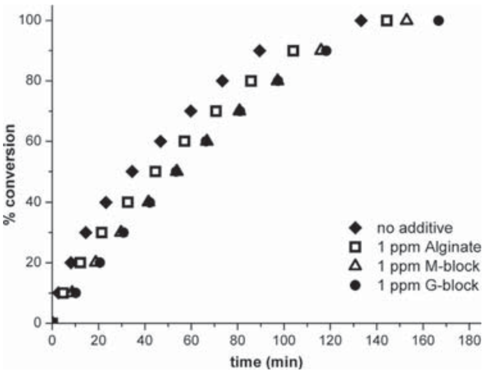

Fig. 4. The percentage conversion of brushite to HA in the seeded system (100 mg seeds) as a function of time in the absence and presence of indicated alginate additives.

The transformation rates decreased with time as the plateau regions were reached under all experimental conditions (between 80% and 100% conversion). It is important to note that the plateau region represents where the dissolution and growth rates were balanced so that transformation reactions were no longer growth-controlled. As the conversion proceeded, the supersaturation decreased slowly with respect to both phases, and reached its lowest value during the plateau before the completion of the transformation reactions. The decreasing supersaturation with respect to HA would lead to decreased growth rates, but the brushite dissolution rate would be expected to increase as the undersaturation level was increasing if evaluated analogously to growth in terms of driving force. However, previous studies of CaP dissolution showed the dissolution rates of CaPs markedly decreased with time even under constant undersaturation [31–34]. A detailed analysis of brushite dissolution by Nancollas et al. revealed that deceleration of dissolution is size dependent and as the crystallite size becomes close to the values for critical dissolution steps, the dissolution can be effectively suppressed or further inhibited, and the presence of additives could further delay dissolution by additional interference with the developing dissolution steps [35]. Therefore we can conclude that the retardation phenomena observed approaching and during the plateau region were a result of both the lowered rates of growth and size dependent dissolution suppression leading to decreased transformation rates in a synergistic fashion.

3.2. Unseeded transformation experiments

The second set of transformation experiments were conducted in the absence of HA seeds but in the presence of additives. When HA seeds were not present, increasing supersaturation due to brushite dissolution resulted in nucleation and subsequent growth. The titrant addition curves displayed a characteristic S-shape representative of that process instead of the linear region observed in the seeded experiments, followed by a similar plateau and a final logarithmic region (Fig. 5A).

In order to characterize the CaP phases present during the hydrolysis of brushite, samples were collected, washed and analyzed at different stages of transformation as shown in Fig. 5A. Both XRD and FTIR analyses showed the gradual disappearance of brushite until the plateau and subsequent formation of HA (Fig. 5B and C) [36,37]. The sample collected at point 1 showed the characteristic diffraction

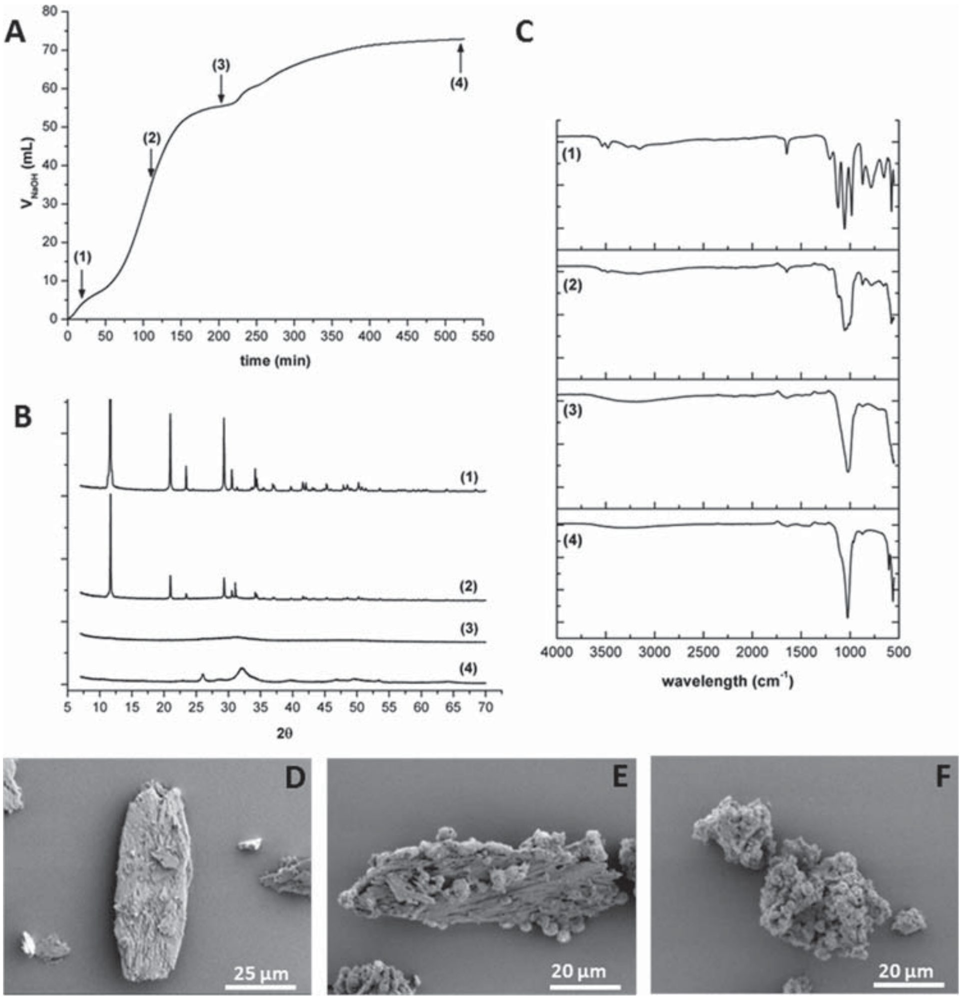

Fig. 5. The titrant addition curve for the transformation reaction of brushite in the absence of additives showing the time points of sample collection (A); XRD (B) and FTIR (C) spectra of the samples collected at the indicated reaction time points and associated SEM images of these samples taken at point 1 (D), point 2 (E) and point 3 (F).

pattern of brushite and the FTIR analysis also indicated its presence by the peaks observed at 3536 cm^{-1}, 3478 cm^{-1} 3265 cm^{-1} and 1647 cm^{-1} associated with the water molecules in the lattice and the peaks associated with the presence of HPO_4^{2-} ion at 1205, 1121, 1053, 984, 871 and 575 cm^{-1}. The SEM image of the sample also showed dissolving brushite particles (Fig. 5D). Brushite presence was still detected at point 2 and SEM images of samples taken at that point revealed the presence of dissolving brushite particles and a new phase forming on the dissolving platelets (Fig. 5E). Both XRD and FTIR spectra showed a decrease in the intensities of peaks associated with brushite and significant peak broadening was observed in FTIR. In addition a new FTIR peak at 1030 cm^{-1} attributable to PO_4^{3-} was observed indicating transformation and the presence of a new CaP phase. XRD spectra of the sample collected at the plateau region (point 3) did not show any strong diffraction peaks which might be due to the small crystallite size or low crystallinity of the sample below the detection limit. FTIR analysis revealed a broad band around 3200 cm^{-1} associated with OH^- ions and the PO_4^{3-} absorption band was observed at 1025 cm^{-1}. A representative SEM image of this precipitate is given in Fig. 5F. The brushite platelets are no longer present and the sample was dominated by the new phase formed. The analysis of the final sample with FTIR showed more intense absorption bands of PO_4^{3-} at 1025, 600 and 560 cm^{-1} and XRD spectra revealed the presence of poorly crystalline HA. XRD analyses conducted at low angle (2θ=4–10°) did not show distinguishable peaks of OCP in any of the samples. Therefore, it was concluded the transformation reaction in the specified experimental conditions did not involve an intermediate crystalline phase.

In order to evaluate the desupersaturation profile, the calcium electrode potential was monitored simultaneously with pH in the absence of additives (Fig. 6A). Data clearly demonstrated the dramatic increase in the calcium concentration due to brushite dissolution reaching a maximum at the point of activation of titration. Then, a slight decrease was observed with the proceeding transformation (up to ~200 min) and the calcium signal was almost stable during the plateau region of transformation (between ~200 and 320 min) indicating the equilibrium between dissolution and growth reactions. After the plateau, representing the completion of transformation and complete

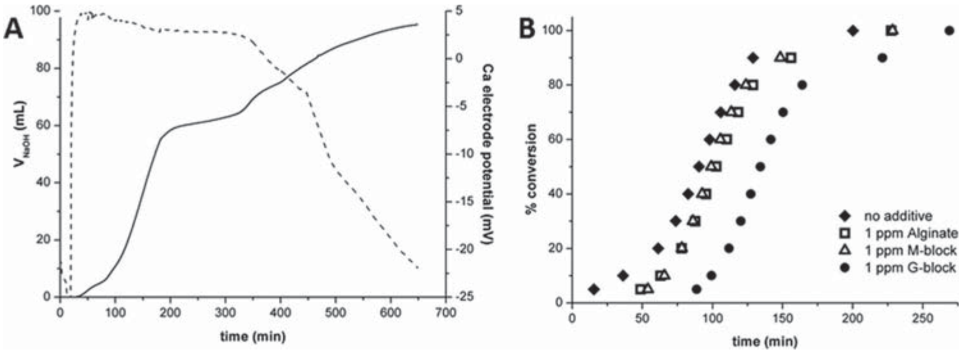

Fig. 6. Titrant addition (solid line) and calcium electrode potential (dotted line) with respect to time recorded during unseeded transformation of brushite in additive free medium (A), the percentage conversion of brushite to HA in the unseeded system as a function of time in the absence and presence of additives (B).

disappearance of solid brushite, a fast decrease in calcium signal was observed due to the consumption of ions by HA growth.

Representation of titration data in terms of percent conversion is given in Fig. 6B for all systems. We note that low conversion percentages were maintained for longer in the presence of additives before reaching the steepest gradient of the titrant addition curves that represents the growth dominated region. Seeded transformation experiments conducted at the same conditions showed additives were not highly influential in decreasing the rate of transformation during the growth dominated region of the transformation reactions. In the unseeded experiments, titrant addition curves showed similar steep gradients in the growth dominated region, but the presence of alginate additives effectively prolonged the time required to generate the critical surface area needed before crystal growth could dominate the reaction kinetics. Therefore by coupling the seeded and unseeded experiments it can be deduced that the alginate additives interfere in the nucleation period of HA and the most effective nucleation retardation was observed in the presence of G-block oligomers. The variations in nucleation kinetics under the same initial experimental conditions can result from the effective interactions of additives with the building units that can influence the nucleation rates *via* varying mechanisms such as affecting the interfacial energy of nuclei or chelating the ions. Adsorption of additives on crystal surfaces can result in changing the interfacial energy between two phases that would affect the kinetics of heterogeneous nucleation [38,39]. In addition, recent studies suggest formation of an amorphous phase prior to HA nucleation, even at low supersaturation, and relate the retardation effect of additives on HA nucleation to the stabilization of this precursor phase by surface adsorption of additives [40–42]. Future studies will be conducted to clarify the operating mechanism of additives on HA nucleation.

4. Conclusion

HA formation *via* the transformation of brushite under alkaline conditions was studied by determining the supersaturation profiles. This method allows for detailed kinetic analysis of hydrolysis that cannot be studied by conventional methods used for investigation of phase transformations such as microscopic or thermal analyses. It was shown that under specified experimental conditions transformation was growth-controlled until the dissolution and growth rates were balanced at the point of near complete brushite consumption. Transformation rates were reduced towards the end of reactions due to both a diminishing HA growth rate with decreasing supersaturation and size dependent suppression of brushite dissolution. The presence of alginate additives at low concentration was not highly influential on decreasing transformation rates during the growth dominated region. Their effect became more pronounced as the dissolution and growth rates reached equilibrium where both reactions were effective in governing transformation kinetics. Decoupling of seeded and unseeded transformation experiments suggested a retardant effect of alginate additives on HA nucleation and this was most evident in the presence of G-block oligomers.

Author contributions

The manuscript was written through contributions of all authors. All authors have given approval to the final version of the manuscript.

Acknowledgement

We gratefully acknowledge financial support provided by the Research Council of Norway (FRINATEK Project 214607).

Appendix A. Supplementary material

Supplementary data associated with this article can be found in the online version at http://dx.doi.org/10.1016/j.jcrysgro.2016.11.019.

References

[1] A.P. Alivisatos, Science 289 (2000) 736.
[2] G. Zan, Q. Wu, Adv. Mater. 28 (2016) 2099.
[3] F.M. Chen, X. Liu, Prog. Polym. Sci. 53 (2016) 86.
[4] H.A. Lowenstam, S. Weiner, Science 227 (1985) 51.
[5] Y.H. Tseng, C.Y. Mou, J.C.C. Chan, J. Am. Chem. Soc. 128 (2006) 6909.
[6] S.V. Dorozhkin, M. Epple, Angew. Chem. – Int. Ed. 41 (2002) 3130.
[7] S.H. Bjornoy, D.C. Bassett, S. Ucar, J.P. Andreassen, P. Sikorski, Biomed. Mater. 11 (2016) 1748.
[8] S. Ucar, S.H. Bjørnøy, D.C. Bassett, B.L. Strand, P. Sikorski, J.P. Andreassen, Cryst. Growth Des. 15 (2015) 5397.
[9] C. Drouet, Biomed. Res. Int. 2013 (2013) 12.
[10] Ý.A. Mørch, I. Donati, B.L. Strand, Biomacromolecules 7 (2006) 1471.
[11] L. Wang, G.H. Nancollas, Chem. Rev. 108 (2008) 4628.
[12] M.T. Fulmer, P.W. Brown, J. Mater. Sci.: Mater. Med. 9 (1998) 197.
[13] N. Kanzaki, K. Onuma, G. Treboux, A. Ito, J. Cryst. Growth 235 (2002) 465.
[14] M. Kumar, J. Xie, K. Chittur, C. Riley, Biomaterials 20 (1999) 1389.
[15] X. Zhang, F. Geng, X. Huang, M. Ma, J. Cryst. Growth 409 (2015) 44.
[16] J. Xie, C. Riley, K. Chittur, J. Biomed. Mater. Res. 57 (2001) 357.
[17] W. Jiang, X. Chu, B. Wang, H. Pan, X. Xu, R. Tang, J. Phys. Chem. B 113 (2009) 10838.
[18] X. Chu, W. Jiang, Z. Zhang, Y. Yan, H. Pan, X. Xu, R. Tang, J. Phys. Chem. B 115 (2011) 1151.
[19] P.T. Cardew, R. Davey, J. Proc. R. Soc. Lond. A: Math. Phys. Eng. Sci. 398 (1985) 415.
[20] A. Haug, B. Larsen, O. Smidsrod, Acta Chem. Scand. 20 (1966) 183.
[21] G. Skjakbraek, B. Larsen, Carbohydr. Res. 139 (1985) 273.
[22] J. Murphy, J.P. Riley, Anal. Chim. Acta 27 (1962) 31.
[23] G.H. Nancollas, M.S. Mohan, Arch. Oral Biol. 15 (1970) 731.
[24] J. Katić, M. Metikoš-Huković, S.D. Škapin, M. Petravić, M. Varašanec, Electrochim. Acta 127 (2014) 173.
[25] K. Furutaka, H. Monma, T. Okura, S. Takahashi, J. Eur. Ceram. Soc. 26 (2006) 543.
[26] R. Tang, M. Hass, W. Wu, S. Gulde, G.H. Nancollas, J. Colloid Interface Sci. 260

(2003) 379.
[27] J. Zhang, G.H. Nancollas, J. Phys. Chem. 98 (1994) 1689.
[28] P. Malkaj, E. Pierri, E. Dalas, J. Mater. Sci.: Mater. Med. 16 (2005) 733.
[29] S. Koutsopoulos, E. Dalas, J. Crystal Growth 217 (2000) 410.
[30] M. Öner, Ö. Doğan, Prog. Cryst. Growth Charact. Mater. 50 (2005) 39.
[31] J. Zhang, G.H. Nancollas, J. Cryst. Growth 123 (1992) 59.
[32] J. Zhang, G.H. Nancollas, J. Phys. Chem. 96 (1992) 5478.
[33] R. Tang, G.H. Nancollas, J. Cryst. Growth 212 (2000) 261.
[34] R. Tang, G.H. Nancollas, C.A. Orme, J. Am. Chem. Soc. 123 (2001) 5437.
[35] R. Tang, C.A. Orme, G.H. Nancollas, J. Phys. Chem. B 107 (2003) 10653.
[36] M. Wang, J. Gao, C. Shi, Y. Zhu, Y. Zeng, D. Wang, Cryst. Growth Des. 14 (2014) 6459.
[37] A. Hirsch, I. Azuri, L. Addadi, S. Weiner, K. Yang, S. Curtarolo, L. Kronik, Chem. Mater. 26 (2014) 2934.
[38] Y. Wang, Z. Sam, X. Zeng, C. Kui, Q. Min, W. Weng, Mater. Sci. Eng.: C 27 (2007) 244.
[39] M.T. Jahromi, G. Yao, M. Cerruti, J. R. Soc. Interface/R. Soc. 10 (2013) 20120906.
[40] Y. Chen, W. Gu, H. Pan, S. Jiang, R. Tang, CrystEngComm 16 (2014) 1864.
[41] B. Xie, T.J. Halter, B.M. Borah, G.H. Nancollas, Cryst. Growth Des. 14 (2014) 1659.
[42] K. Chatzipanagis, M. Iafisco, T. Roncal-Herrero, M. Bilton, A. Tampieri, R. Kroger, J.M. Delgado-Lopez, CrystEngComm 18 (2016) 3170.

SUPPLEMENTARY INFORMATION

Table S1. The reactions and their corresponding equilibrium constants (-log K) used to calculate the solution speciation at 25 °C

$H_2O \leftrightarrow H^+ + OH^-$	13.997
$Ca^{2+} + H_2O \leftrightarrow CaOH^+ + H^+$	12.697
$H_3PO_4 \leftrightarrow 3H^+ + PO_4^{3-}$	21.721
H_2PO_4- $\leftrightarrow 2H^+ + PO_4^{3-}$	19.573
$HPO_4^{2-} \leftrightarrow H^+ + PO_4^{3-}$	12.375
$CaH_2PO_4^+ \leftrightarrow Ca^{2+} + 2H^+ + PO_4^{3-}$	20.923
$CaHPO_4 \leftrightarrow Ca^{2+} + H^+ + PO_4^{3-}$	15.035
$CaPO_4^- \leftrightarrow Ca^{2+} + PO_4^{3-}$	6.46
$CaHPO_4.2H_20$ (s) $\leftrightarrow Ca^{2+} + H^+ + PO_4^{3-} + 2H_2O$	18.995
$Ca_5(PO_4)_3(OH) \leftrightarrow 5Ca^{2+} + OH^- + 3PO_4^{3-}$	44.33

$$S_{brs} = \left(\frac{\{Ca^{2+}\}\{H^+\}\{PO_4^{3-}\}}{K_{sp,brs}}\right)^{1/3} \quad \text{(Eq. S1)}$$

$$S_{HA} = \left(\frac{\{Ca^{2+}\}^5\{PO_4^{3-}\}^3\{OH^-\}}{K_{sp,HA}}\right)^{1/9} \quad \text{..(Eq. S2)}$$

Paper III

Transformation of Amorphous Calcium Phosphate to Hydroxyapatite in The Presence of Alginate Additives

Seniz Ucar,[a] *Sindre H. Bjørnøy,*[b] *David C. Bassett,*[b,c] *Berit L. Strand,*[d] *Pawel Sikorski,*[b] *and Jens-Petter Andreassen** [a]

[a] Department of Chemical Engineering, [b] Department of Physics and [d] Department of Biotechnology, Norwegian University of Science and Technology, Trondheim, Norway.

[c] Department of Chemical Engineering, University of Birmingham, Birmingham, UK.

ABSTRACT

Hydroxyapatite (HA) is the main mineral in vertebral tooth and bone tissue, thus, it is often incorporated into synthetic composite materials designed for hard tissue engineering applications. Investigating the formation mechanism of apatitic minerals and the effects of matrix molecules during mineralization is important for the development of better designed materials. This work is motivated by mineralization studies of an alginate hydrogel and explores the mechanism of HA formation via an amorphous calcium phosphate (ACP) precursor and the effects of alginate based additives on this process. In order to highlight the course of the formation reaction a combination of potentiometric measurements and characterization methods were used. Results indicated the presence of prenucleation complexes prior to ACP formation which was followed by HA crystallization. The effects of high molecular weight alginate and its well-defined oligomers with M- or G-block structure were investigated on HA formation and it was shown that alginate and M-block oligomers delayed HA formation by reducing both the nucleation and growth rates of HA. In the presence of G-block oligomers a phase change was induced and coexistence of octacalcium phosphate (OCP) and HA was detected. The information obtained in this study enabled further understanding of the mineralization reactions observed within the alginate hydrogels.

INTRODUCTION

Calcium phosphates (CaP) are an important class of biological minerals found in natural hard tissues; among them hydroxyapatite (HA) is the dominant mineral phase in mammalian calcified tissues. Consequently, composite biomaterials designed for bone tissue engineering applications often incorporate either HA or a precursor CaP phase that can transform to HA under *in vivo* conditions. Understanding the formation mechanisms of apatitic minerals and the effects of organic components on the crystallization process can inform the development of improved biomaterials,[1] *in vitro* model systems of biomineralization, [2] and may also inspire new synthetic syntheses of non-biogenic minerals.[3]

Extensive studies on the nucleation mechanism of biological HA agree that rather than forming directly from solution HA follows a crystallization pathway via an amorphous calcium phosphate (ACP) precursor.[4,5] However, there is an ongoing debate regarding how this ACP-mediated process is driven, from the initial formation of ACP to its transformation mechanism to HA.

Posner's clusters, $Ca_9(PO_4)_6$, were initially proposed as the building blocks for ACP, and samples from both synthetic and biological systems have been shown to contain these ion clusters.[5] However, further studies also proposed that other pre-nucleation species and ACP phases that vary in structure and chemical composition depending on the reaction conditions, may be present.[6] Several hypotheses regarding the mechanism of ACP formation have been suggested: stable prenucleation clusters which aggregate and form ACP [7], the presence of soluble ion-complexes that lead to ACP precipitation by aggregating and consuming extra calcium ions from solution [8], and a two-step formation that includes the formation of an initial ACP phase via ion-complexes that later transforms into a second ACP phase through densification.[9] In the presence of polymeric additives in the reaction medium, formation of ACP through a polymer induced liquid precursor (PILP) mechanism has also been suggested.[10]

The transformation mechanism of the ACP precursor to HA is also a subject of active debate and multiple mechanisms have been proposed. According to the classical theory, phase transformation is governed by the chemical potential difference between phases (i.e. activity based supersaturation), and can either follow a dissolution-reprecipitation pathway in solution or a solid state transformation which is particularly common at high temperature.[11,12] The solvent mediated phase transformation through dissolution- reprecipitation reactions can be governed either by dissolution of the metastable phase or nucleation and growth of the stable phase depending on the supersaturation and the relative kinetics of the individual reactions as modeled by Cardew and Davey.[13] In an attempt to describe phenomena occurring during transformation, various alternative or ‘nonclassical’ mechanisms have also been suggested. For example, Tang *et al.* proposed a solution mediated surface nucleation process where HA heterogeneously nucleates on ACP, but the transformation rate in these studies was stated to be a function of the amount of initial ACP formed and calcium activity in solution, rather than solution supersaturation.[14-17] Nancollas *et al.* and Wang *et al.* proposed an alternative mechanism whereby HA nucleation takes place within the ACP precursor through a solid-

solid transformation. In these theories the kinetics of transformation are also not directly linked to the solution supersaturation.[9,18]

Different proposed mechanisms of the ACP-mediated nucleation process consequently infer different roles of additives on HA nucleation kinetics. The presence of additives can directly affect the dissolution rate of ACP, the nucleation rate of HA, or the chemistry and the solubility of the ACP phase, which consequently reflects on the solution supersaturation and thus the nucleation rate of HA, from a classical point of view.[11] In contrast, if the phase transformation is independent of supersaturation as proposed by some studies, additives gain the role of stabilizing the ACP phase through surface interactions. This may occur either by interfering with the surface nucleation of HA or limiting the mass transfer between the solid and solution.[9,16]

Recent studies in our group focused on the composite biomaterials composed of alginate hydrogels with CaP mineral content. Alginate is a polysaccharide polymer which is composed of 1-4 linked β-D-mannuronic acid (M) and α-L-guluronic acid (G) residues with an alternating or block structure. The M- and G- units of alginate differ in the configuration of carboxyl groups that in turn highly affects their functionality. Calcium ions show specific affinity towards the outward carboxyl groups of the G- units of alginate, therefore, how alginate regulates mineralization is highly dependent on its chemical composition, sequential structure of the repeating units and molecular weight. Spatiotemporal analysis of the evolution of CaP phases within the hydrogel network showed precipitation of ACP as a metastable precursor phase and its transformation to more stable crystalline phases such as brushite, octacalcium phosphate (OCP) and HA depending on the reaction conditions.[19] Detailed investigations on the transformation phenomenon brought up new questions on the nucleation events of HA such as the nucleation mechanism, and the roles of ACP precursor and alginate additives on nucleation.[20] Thus, the present study aims to explore the mechanism underlying HA formation via the amorphous precursor in the presence of alginate additives. For this purpose, the effects of alginate additives with varying molecular weight and functionality have been investigated to shed a light on the operating mechanism of the chosen matrix molecule on HA formation.

EXPERIMENTAL SECTION

Materials

All chemical reagents were purchased from Sigma-Aldrich unless stated otherwise. Ultrapure deionized water (DIW) was used to prepare all aqueous solutions. Alginate, isolated from *Laminaria hyperborea (L.hyp)* stipe, was obtained from FMC Biopolymer (Norway) with a molecular mass of 274 kDa and 68% G content. Two different oligomers of alginate, denoted as G- and M-blocks, consisted of 90% and 5% G monomer, respectively, with the degree of polymerization ≈ 20 for both. The G-blocks were produced from *L. hyp* stipe alginate by acid degradation and fractionation.[21] The M-blocks were produced from alginate from *Ascophyllum nodosum* by acid degradation and calcium fractioning as described elsewhere.[22]

Methods

All experiments were carried out in a magnetically stirred 0.5 L double-walled glass reactor, and two baffels were attached to the lid. Temperature was controlled by a water bath at 25°C for all experiments. Nitrogen, presaturated with water, was constantly bubbled into solutions 2 h prior to and during the experiments to exclude atmospheric carbon dioxide. The chemical speciation and activity based supersaturation (S) was determined by the thermodynamic calculation program PHREEQC Interactive 3.1, using Minteq v4 database (Equation 1). The equilibrium constants used for solution speciation are given in the supplementary information (Table S1).

$$S = \left(\frac{IAP}{K_{sp}}\right)^{\frac{1}{\upsilon}} \qquad (1)$$

IAP represents the ionic activity product in solution, K_{sp} is the solubility product and υ is the number of ions in one mole of the corresponding compound.

The pH was recorded continuously by means of a combined glass electrode with a KCl reference electrolyte and calcium ion activity in the vessel was monitored online via a calcium ion specific electrode with Tiamo software (Metrohm). Phosphate concentration was determined spectrophotometrically following formation of its molybdate complex.[23]

Characterization of solid phases were conducted via powder X-ray Diffraction (XRD) (D8 Advance, Bruker AXS GmBH) in the range of 4-75°with a step size of 0.013° and a step time of 0.67 s. Fourier transform infrared (FTIR) (Bruker, Tensor) spectra of powder samples were also collected between 4000-550 cm^{-1}. Scanning electron microscopy (SEM) (Hitachi S-3400N) analyses were performed at an accelerating voltage of 5 kV, where samples were placed on carbon tape and sputter coated with gold. Transmission electron microscopy (TEM) (Jeol, JEM 2100, LaB6 camera) investigations of particles were conducted at an accelerating voltage of 200 kV by sampling via drop-casting at various time points. Diffraction patterns were analyzed using DiffTools in Digital Micrograph software (version 2.32, Gatan).

Hydroxyapatite Precipitation in Batch Experiments

Spontaneous precipitation of HA was achieved in batch experiments by preparing supersaturated solutions of HA (S_{HA}= 25.6) and allowing precipitation to occur under constant stirring (300 rpm). Supersaturation level of the working solution was defined by scanning through a range of values between S= 17.1- 34.0 in accordance with the previous studies of HA formation in our group, and choosing the supersaturation at which the two-step precipitation behavior was observed within reasonable time span. For this purpose, the phosphate solution (2.4 mM) containing KNO_3 for ionic strength adjustment and KOH to adjust the final solution pH to 7.40 ± 0.02, was prepared from its stock to a total volume of 250 mL and calcium solution (20 mL, 50 mM) was added in the reaction medium at a rate of 150 mL/min via an automated dosing unit (907 Titrando, Metrohm). In experiments with alginate additives, the corresponding amount of filtered polymer solution (1 mg/L) was added to the phosphate solution initially.

Seeded Constant Composition Growth Experiments

HA growth experiments were conducted by the constant composition method at: (i) a low supersaturation range (S= 4.1-6.3) to determine the effects of additives on surface-controlled growth of HA and (ii) the supersaturation value (S= 21.5) at which HA nuclei were first detected during the spontaneous precipitation reactions via ACP transformation. In order to examine the interactions of alginate-based additives with HA surface seeded growth experiments were conducted at four different supersaturation values in the absence and presence of additives and a minimum of three replicates were carried out at each experimental condition. The growth rate of HA at the single supersaturation value related to spontaneous precipitation experiments was determined in the absence and presence of additives with two replicates at each experimental condition. HA seeds were prepared by the method previously described by Nancollas and Mohan.[24] Briefly, 0.5 M of $Ca(NO_3)_2.4H_2O$ solution was added slowly to a 0.3 M KH_2PO_4 solution under nitrogen environment and constant stirring at 800 rpm. During the precipitation reaction the pH of the solution was maintained between 8.5-10.0 by addition of KOH and the temperature was kept at 70 °C. The precipitate was refluxed at 70 °C overnight. Crystals were then washed with DIW by repeated centrifugation and dried at 80 °C. Phase purity of seeds was verified by XRD and FTIR analyses. Specific surface area (SSA) of the seeds was determined by the multiple point BET nitrogen adsorption method (Tristar II, Micromeritics) and found to be 62.52 ± 0.14 m^2/g. For the seeded growth experiments solutions of calcium and phosphate precursors were prepared from their stock solutions of $Ca(NO_3)_2.4H_2O$ and KH_2PO_4 and working solutions were prepared at defined supersaturation levels including KNO_3 salt to adjust the ionic strength and KOH for pH adjustment (Table S2). All solutions were bubbled with presaturated nitrogen 2 h prior to and during the experiments. Carefully weighed amounts of HA seed crystals were added in phosphate precursor solution and allowed to thoroughly disperse for 45 min under stirring. Crystal growth was initiated by the addition of calcium solution to the reaction medium up to the desired concentration. In experiments with alginate additives, a corresponding amount of filtered polymer solution was added to the phosphate containing solution prior to addition of calcium. A decrease in pH of more than 0.002 units associated with HA growth triggered the addition of titrant solutions from two mechanically coupled titrant burettes (907 Titrando, Metrohm) to maintain a constant supersaturation.

Compositions of titrant solutions were adjusted for each working solution to compensate for ion consumption, changing ionic strength and alkalinity in the reaction media. A detailed study on the preparation of titrant solutions has been previously published by our group for the calcium carbonate system.[25] In this study, the same methodology was used with the modifications for HA growth as given in in the supplementary information (S1). Following the addition of titrant solutions, pH was maintained at a constant value with a maximum overshoot of 0.005 units which occurred only at the initial growth period. Constancy of supersaturation was confirmed by calcium and phosphate ion analyses at arbitrary time points and showed that concentrations deviated less than 4% during titrant addition.

The growth rate of HA *(R)* was calculated using titrant addition curves (Equation 2), where the effective concentration (C_{eff}) denotes number of moles precipitated per liter of titrant addition and dV_{titr}/dt is the titrant curve gradient. Titrant addition curves were normalized to the changing surface area (A) of the seeds with proceeding growth. The mass change of HA was calculated from the volume of titrant added and related to the change in surface area by a factor of $(w_i/w)^{2/3}$, where w_i is the weight of seed crystals added initially and w is the weight of crystals present at time t, assuming three dimensional growth with a constant shape factor.[26] The growth rate constant, k (mol/min.m^2), and the apparent order of growth, g were calculated by using the rates of reaction at different supersaturation values (Equation 3). The k values demonstrate the effects of additives on the kinetics of the reaction and g values are used to assess the growth mechanism of HA and the changes induced by the additives.

$$R = \frac{1}{A} C_{eff} \frac{dV_{titr}}{dt} \qquad (2)$$

$$R = k(S-1)^g \qquad (3)$$

RESULTS & DISCUSSION

Hydroxyapatite Growth Experiments at Low S

Crystal growth experiments in the presence of HA seeds were conducted under constant composition to quantify the effects of alginate additives on the growth kinetics of HA. The experiments conducted in the low supersaturation range ensured surface-controlled growth mechanisms in order to examine the interactions of additives with the crystal surface. The highest growth rates were obtained from additive-free experiments and the presence of alginate additives in the reaction medium resulted in substantially reduced rates of growth (Figure 1). The reduction in the overall growth rates (*R*) varied with different additives as a function of the growth rate constants, *k*, and the apparent growth orders, *g*, due to different intermolecular interactions between the crystals and each additive (Table 1).

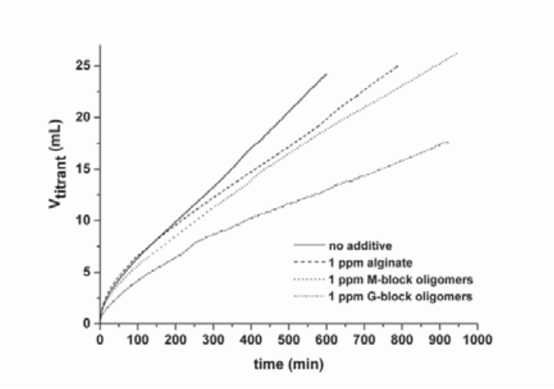

Figure 1. Titrant addition curves of HA seeded constant composition experiments at S= 6.3 in the additive-free medium and in the presence of indicated alginate additives (m_{seed}= 30 mg, C_{eff}= 0.5 mM).

Table 1. Values of the growth rate constants (*k*) and the apparent growth orders (*g*) obtained for HA seeded growth experiments under constant composition.

	k (10^{-10} mol / min.m^2)	g
no additive	3.45	1.99 ± 0.08
1 ppm alginate	1.47	2.30 ± 0.12
1 ppm M-block	2.29	1.96 ± 0.15
1 ppm G-block	0.63	2.52 ± 0.12

The presence of additives resulted in lowered *k* values up to different extents that scaled with the concentration of G-units. M-block oligomers and alginate resulted in ~34 % and 58 % reduction in *k* respectively, whereas the most prominent decrease (~82 %) was observed with the addition of G-block oligomers. Previous studies of HA growth in the presence of alginate associated its retardation effect with the high affinity of carboxyl groups of G-units in alginate towards calcium and subsequent blocking of growth sites.[27,28] Other polyelectrolytes and amino acids with carboxyl and hydroxyl functionality also led to growth retardation of HA in a similar manner, and the adsorption hypothesis was confirmed by fitting growth data to Langmuir type adsorption curves.[29-31] The increasing magnitude of reduction in *k* values with increasing concentration of G-units observed in this study also supports the hypothesis that high affinity functional groups result in more effective adsorption to active growth sites and thus lower the kinetics of growth more effectively. In the case of M-block oligomers where carboxyl groups do not exhibit specific affinity towards calcium ions, nonspecific interactions with the crystal surface are still likely to occur via ionic interactions and hydrogen bonding where nonspecific adsorption of the oligomer chains onto the crystal surface can affect the accessibility of the active sites.[32]

The apparent growth order, *g*, was determined from the rate expression (Equation 3) to infer possible mechanistic growth models and the effects of additives on the HA growth mechanism. It should be noted however, only general deductions on the overall growth mechanism can be made by using data obtained via indirect measurement methods such as ion concentration measurements.[33] In the absence of additives, the HA growth rate showed a parabolic dependence on the relative supersaturation. It has been frequently observed that the growth rates of sparingly soluble salts at low to moderate supersaturation are determined by the development of steps on the crystal surface and the kinetic order of this surface integration controlled mechanism is generally excepted as $g \approx 2$.[34] Previous studies conducted under similar experimental conditions and supersaturation also revealed parabolic rate laws for HA growth.[27,35,36] The growth order was not altered when M-block oligomers were present; however the presence of both alginate and G-block oligomers resulted in g values higher than 2 which indicates a change in the mechanism towards polynuclear growth. In the presence of additives which cause an effective reduction in active growth sites by adsorption, growth may proceed via surface nucleation to generate new growth sites when the driving force is high enough.[37] Thus, the additives with G-units can induce changes in the growth mechanism via their strong specific interactions with the active sites on the crystal surface. A g value slightly above 2 with the addition of alginate indicated a combined mechanism of surface integration and polynuclear growth.[38,39] In the presence of G-blocks the increase in g value was higher which showed a stronger contribution of surface nucleation mechanism on the overall growth process.

The stronger influence of G-block oligomers compared to alginate and M-block oligomers on both growth kinetics and mechanism can be associated with the higher G-unit content, however, molecular weight of these additives should also be considered as an effective parameter on the intermolecular interactions between the additive and the crystal surfaces. High molecular weight of alginate additive and consequent steric hindrance may interfere with the molecular adsorption mechanism on the crystal surface whereas in the case of short G-block oligomer chains adsorption on the surface would be more effective. Therefore, the strongest retardation effect and change of mechanism observed on growth in the presence of G-block oligomers can be assessed as a result of the synergistic effect of both functionality and size of the molecules. In the presence of M-block oligomers, although similar in size, such a change in the growth mechanism was not induced since nonspecifically adsorbed molecules do not cause a significant blockage of active sites.

Spontaneous Hydroxyapatite Formation

HA formation in the batch experiments was investigated by spontaneous precipitation from supersaturated solutions by addition of calcium ions to a phosphate solution. The pH and calcium electrode potential profiles were monitored during the reactions and same characteristic regions were observed in all systems as shown in Figure 2.

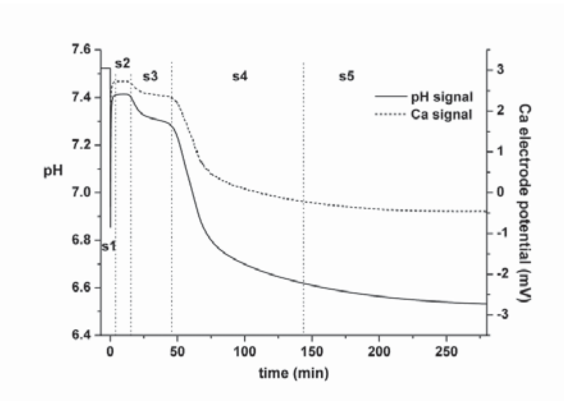

Figure 2. pH and calcium electrode potential monitored as a function of time during the spontaneous precipitation of HA in the absence of additives. Curves were sectioned in five stages (labeled s1-s5) in accordance with distinct changes in signal profiles.

In all systems, addition of calcium ions to the reaction medium resulted in an immediate drop in pH, shortly followed by a sharp rebound which was then followed by a more gradual increase and leveling off (stage 1). Since the pH of the system is a function of the speciation of phosphate, changes in pH can be interpreted in terms of their changing ratios.[18] Upon addition of calcium in the reaction medium, ion pairs can form between calcium and phosphate species. Under the specified experimental conditions, the dominant ion pairs were $[CaH_2PO_4]^+$ and $[CaHPO_4]^0$, and the formation of $[CaPO_4]^-$ could be neglected. Thermodynamic calculations showed the initial activity based ratio of $H_2PO_4^-$ / HPO_4^{2-} in solution before addition of calcium was 0.481, and the ratio of ion pairs $[CaH_2PO_4]^+$ / $[CaHPO_4]^0$ that would form with the addition of calcium was 0.0302. As the calculations demonstrated, ion pairs changed the ratio of free phosphate species towards a higher $H_2PO_4^-$ content and thus resulted in an overall decrease in pH. The fluctuations in pH before its stabilization has been attributed to possible formation of unstable clusters and solid due to high local supersaturation caused by the addition of high concentration calcium solution, which then dissociate immediately to establish the equilibrium.[18]

Following s1 the pH remained stable and this was accompanied by a stable signal for Ca^{2+} (stage 2). The first discernable drop in either signal was considered as evidence of the first nucleation event which indicated the appearance of the first new phase from the solution. This point determined the onset of stage 3. The second abrupt drop in the monitored signals was, in accordance, interpreted as a second nucleation event and the emergence of a second separate phase in the system. This point determined the onset of stage 4. Any units (clusters) formed in the solution before the first nucleation point, i.e. during stages 1 and 2, are termed as prenucleation species in this context. Reaction products were monitored to observe the structural and chemical evolution of species at different stages to illustrate the formation mechanism of final precipitates.

Detailed analyses were conducted on the additive-free experiments to identify the chemical and structural progression of precipitates that correspond to the distinct stages in pH and calcium electrode potential profiles. During stage 2, the pH and Ca signals were stable and there was no obvious indication of a phase separation in the system, however, poorly structured species were observed by TEM (Figure 4A) and the calcium electrode signal indicated lower calcium activity in solution (1.30 mM) then the thermodynamically calculated value (1.33 mM). In order to better determine the nature of these initial species replicate experiments were conducted whilst varying the rates of Ca^{2+} addition (Figure 3). If the prenucleation species formed during this stage are represented by a complex structure of $[Ca_x(HPO_4)_y(H_2PO_4)_z]^{2x-2y-z}$, equilibration of the pH and the calcium electrode signal at the same level under both conditions suggests that the composition of the species was not affected by the rate of Ca^{2+} addition.[8,9] The different pH profiles observed before the equilibrium point can be related to the slow dehydration rate of $Ca^{2+}$and thus the instability of the initially formed complexes.[9] Faster addition of Ca^{2+} can augment the formation of calcium-deficient and unstable complexes (resulting in the severe drop in pH) which then dissociate and release the extra phosphate species during the equilibration of the solution.

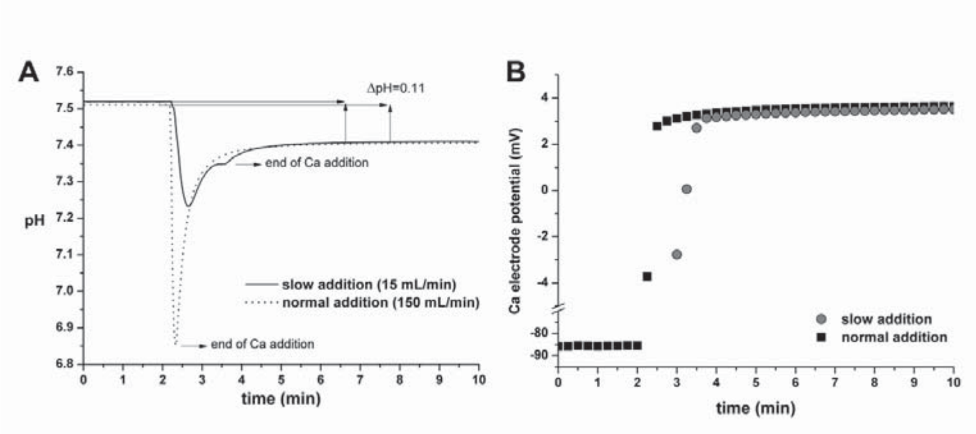

Figure 3. pH (A) and Ca electrode signal (B) profiles of additive-free phosphate solutions with the addition of Ca at the indicated rates.

Following stage 2, the first abrupt drop was detected in both pH and Ca signals, followed by a plateau region (stage 3). FTIR analysis of the first post-nucleation species collected at stage 3 revealed broad PO_4^{3-} bands around 1020 cm^{-1}, weak band at 875 cm^{-1} associated with HPO4^{2-} and water associated bands and peaks around 3300, 1630 and 640 cm-^{1} (Figure 5A). No XRD peaks were detected which, together with the FTIR results, indicate an amorphous nature or small crystallite size lower than the detection limit of the instrument (Figure 5B). TEM analysis of precipitates collected during stage 3 confirmed that during the initial part of the plateau, only spherical particles with an amorphous nature were present (Figure 4B). Near the end of the plateau region of stage 3, primary crystalline nuclei were also detected along with the previously observed amorphous phase and identified as HA (Figure 4C). The electron diffraction patterns indicated the (111) and (210) planes of HA with the d-spacing of 0.389 and 0.309 nm, respectively. Thus, it was concluded that the first discernable drop in the pH curve was associated with the formation of ACP and the second drop was due to the appearance of the crystalline phase.

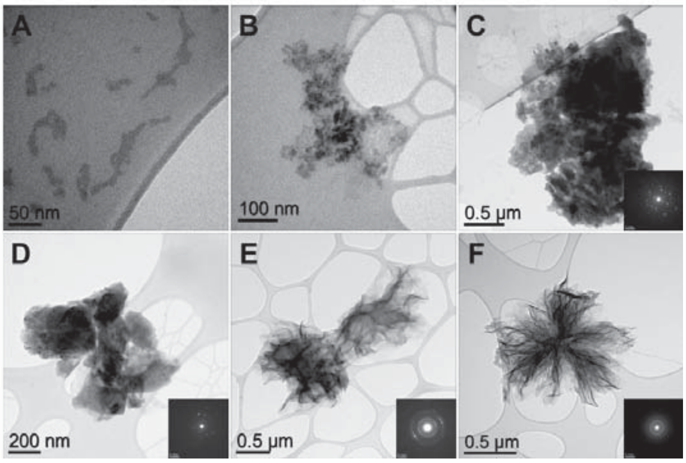

Figure 4. TEM micrographs and corresponding electron diffraction patterns of samples collected during the reaction in the absence of additives; (A) 3-10 min (s2), (B) 16-22 min (s3), (C) 33-38 min (s3), (D) 55-60 min (s4), (E) 85-90 min (s5) and (F) after 48 h of aging in the mother liquor.

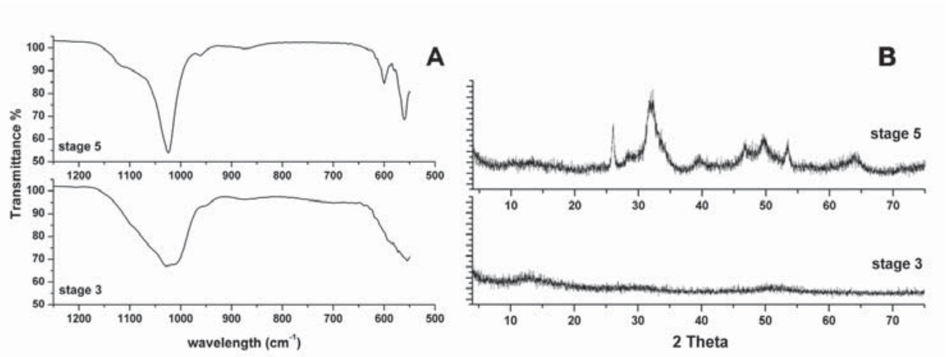

Figure 5. FTIR (A) and XRD (B) spectra of the intermediate and final products of the precipitation reaction collected at stage 3 and stage 5, respectively, in the additive-free medium.

Following the appereance of the crystalline phase, both pH and Ca signals showed a substantial decrease during stage 4, where ACP was completely transformed to HA. TEM analysis showed the co-existence of both amorphous and crystalline phases at the beginning of stage 4 (Figure 4D). When stage 5 was reached only HA was present in the solid phase and the prominent (002) and (112/211) planes were expressed in the diffraction data (Figure 4E). During stage 5, a continuous slow decrease was observed in both pH and Ca^{2+} signals up to 48 h (data not shown) which indicated further HA growth and maturation (Figure 4F). FTIR analysis of the precipitates collected at stage 5 showed sharp distinguishable peaks of PO_4^{3-} at 1025 and 962 cm^{-1}; and splitting of the v_4 bending of PO_4^{3-} at 600 and 560 cm^{-1} indicated HA crystallization (Figure 5A).[16] The weak band at 875 cm^{-1} was still present as an implication of non-stoichiometric composition. XRD spectrum revealed the characteristic HA peaks at this stage (Figure 5B).

Previous studies have reported intermediate phases such as a denser ACP phase, brushite and OCP during transformation of ACP to HA, as well as direct transformation to HA depending on the reaction conditions such as temperature, pH, reactant concentrations and presence of impurities.[40] Under the specified experimental conditions, no intermediate crystalline phase was detected prior to HA formation, however a morphological change was observed in the amorphous phase at subsequent stages that might indicate further structuring of ACP as shown in Figure 6. The structural evolution of particles followed by solution chemistry and observed in TEM micrographs was also evident in SEM images of precipitates collected at stage 3 and 5 which showed the change in particle morphology from spherical particles to thin flake-like particles, respectively (Figure 7).

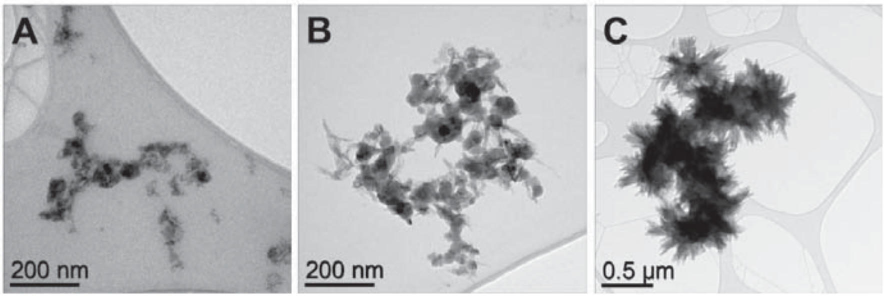

Figure 6. TEM micrographs of amorphous samples collected during the reaction in the absence of additives; (A) 16-22 min (s3), (B) 33-38 min (s3), (C) 55-60 min (s4).

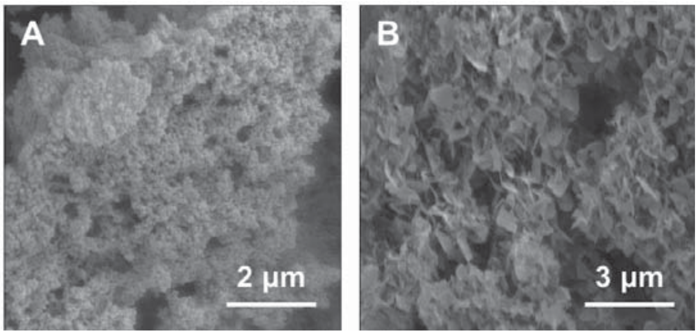

Figure 7. SEM images of the (A) intermediate amorphous (stage 3) and (B) final hydroxyapatite (stage 5) precipitates of the spontaneous precipitation reaction in the absence of additives.

The course of reactions was examined by means of pH signals (Figure 8) and characterization of precipitates when alginate based additives were introduced in the reaction media (Figure S 1-3). In the presence of M-block oligomers and high molecular weight alginate, pH curves displayed the same five characteristic regions as in the additive-free experiments (Figure 8) and characterization of intermediate (stage 3) and final products showed very similar features. Spherical aggregates with an amorphous structure were observed following the first nucleation point and the final products with a flake-like morphology showed XRD and FTIR spectra characteristic of HA. In the presence of G-block oligomers, the pH curve followed the same behavior until stage 4 and showed a slight difference at this stage compared to the continuous drop observed in the previous cases (Figure 8 inset). Characterization of precipitates by XRD and TEM revealed amorphous behavior after the first nucleation point whereas the final products were a mixture of OCP and HA.

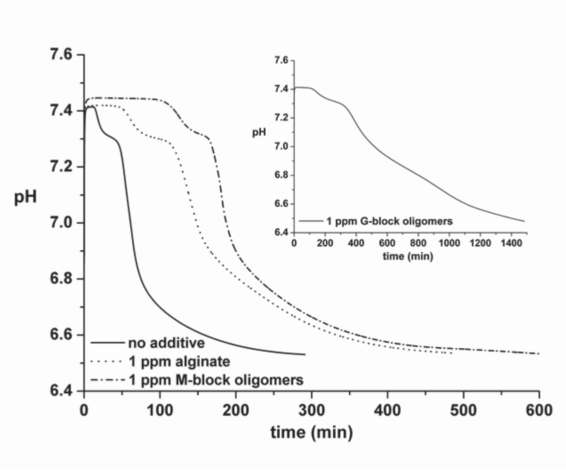

Figure 8. pH profiles of spontaneous precipitation experiments in the absence and presence of the indicated alginate based additives. Inset shows pH profile in the presence of G-block oligomers. Note the different time scales.

Although the characteristic regions of the pH curves and the forming phases indicated at subsequent stages remained unchanged in the presence of alginate and M-block oligomers, the duration of each stage was highly affected (Figure 8). In the presence of G-block oligomers, the mineralization kinetics were more substantially retarded, as given in Table 2. Note that the duration of s5 was not included since it was not possible to estimate accurately as the endpoint was difficult to discern and relatively arbitrary.

Table 2. The discrete time periods for the mineral formation stages in the absence and presence of alginate based additives.

	s_1 (min)	s_2 (min)	s_3 (min)	s_4 (min)
no additive	< 2	14±1	30±2	100±4
alginate	< 2	55±10	61±2	210±4
M-blocks	< 2	92±18	55±5	185±5
G-blocks	< 2	158±18	206±10	790±20

As can be seen from Table 2, the presence of additives had no influence on s1, however, they prolonged the time both for ACP nucleation (s2) and crystalline phase formation in the system (s3). Stage 4 was also prolonged which is the period when ACP transformation to crystalline phase is complete.

The induction time for ACP precipitation (s2) was prolonged in the presence of additives where short oligomer chains were found to be more effective inhibitors. It should be noted that the supersaturation calculations were repeated in the presence of additives assuming all G-blocks present in solution bind to calcium ions. The low molar concentration of G-blocks at any experimental condition with respect to the total calcium ion concentration did not cause any significant decrease in the free ion concentration to affect the initial solution supersaturation. Previous studies showed that the presence of additives can alter the ACP solubility and thus affect its induction time as a result of the changing supersaturation with respect to ACP.[11,41] However, calculation of supersaturation by using the momentary pH and ion concentrations showed that the plateau region was attained at the same supersaturation level for all experiments (S_{HA}=21.5 and $S_{ACP,1}$= 1.0) prior to observation of any crystalline particles. This indicates that the solubility of the precipitates, and thus the initial supersaturation was not affected due to the presence of additives. Thus, we concluded that the increase in induction times of ACP nucleation was not resulting from a decreasing driving force in the system under the specified experimental conditions.

The calcium activity at stage 2 was measured constant under all experimental conditions with a value lower than calculated by the thermodynamic software. In addition, the initial pH drop and equilibration between stage 1 and stage 2 was not affected by the presence of additives suggesting that the additives did not significantly affect the initial prenucleation complex formation (Figure S4). In light of the gathered information and elimination of the thermodynamic factors, the prolongation of induction times for ACP should have kinetic origins. If ACP forms via the prenucleation species, the presence of additives can suppress the reaction progression by being operative on aggregation/ dehydration/ complexation mechanisms through electrostatic interactions. In their study, Habraken *et al.* reported the presence of prenucleation complexes with similar characteristics that transforms to ACP via binding of calcium and loss of structural water, and their formation was stated to be a reaction-limited aggregation process involving hydrogen bonding.[8] The increasing effects of additives by the order of alginate, M-block oligomers and G-block oligomers supports that electrostatic interactions are dominantly effective on this process and G-block oligomers induce the strongest effect due to high concentration of hydroxyl groups and their specific interactions with calcium ions.

Stage 3 was also prolonged when the additives were present in the reaction medium. At the beginning of this stage, ACP growth continues with the accompanying drop in the pH until the plateau prior to the appearance of any crystalline nuclei. In the presence of alginate and M-block additives, the time spent until reaching the plateau were doubled with respect to the additive free experiments, and in the presence of G-block oligomers the effect was even more significant which showed the reduction in the rate of ACP growth in the presence of additives.

The plateau region of stage 3 was reached at the same supersaturation level in all experiments and this metastable state was maintained until appearance of the crystalline phase in the system expressed with the second nucleation point. Alginate and M-block oligomers did not induce any change on the reaction products and HA was the crystallizing phase in their presence (Figure S1). In order to observe the second nucleation point, there should be sufficient HA nucleation and growth to express an effective change on the pH and Ca signals. Therefore, any retardant effect of additives on the rate of HA nucleation, J, or growth results in the prolongation of stage 3. The contribution of growth rate on the experimentally determined induction time can be calculated when the method used for detection of induction time is based on the appearance of a certain volume (or mass) of many nucleating crystallites such as in the case of pH indication. For a primary nucleation event where particles have a 3-dimensional growth with a constant shape factor, α, the induction time, t_{ind}, can be given as;

$$t_{ind} = \sqrt[4]{\frac{\vartheta}{\alpha R^3 J}} \qquad (4)$$

where υ is the minimum detectable volume fraction of the new phase.[42] In order to determine the impact of growth rate on the induction time observed for HA formation, growth rate of HA was determined at the experimental conditions simulated from the plateau region (S_{HA}= 21.5) in the absence and presence of additives (Table 3).

Table 3. The growth rate *(R)* values of HA calculated from the seeded constant composition experiments at S_{HA}= 21.5 and the ratios of nucleation rates, J, of HA in presence of indicated additives to the additive-free nucleation rate, J_{NA}, calculated by using Equation 4. Induction times, t_{ind}, were defined as the time period from the start of the plateau region to the second nucleation point.

	R **(mol/min.m^2) x 10^{-6}**	**t_{ind} (min)**	**J/J_{NA}**
no additive	1.110 ± 0.035	16	
1 ppm alginate	0.755 ± 0.062	30	0.3
1 ppm M-block	0.748 ± 0.116	25	0.5

By using Equation 4, the effects of additives on the nucleation rates were determined by deducing the contribution of growth rates. It was shown in Table 3 that alginate and M-block additives resulted in prolonged induction times for HA via reducing both the nucleation and growth rates of this phase up to different extents. Determination of supersaturation showed that HA nucleation occurred under constant driving force at all experimental conditions, thus, the thermodynamic origins for the nucleation suppression were eliminated. Previous studies of ACP-mediated HA formation suggested that the additives can induce such an effect by interfering with the heterogeneous nucleation of HA on the ACP surface.[17,43] The stronger retardation of nucleation observed with the more G-block containing additives, which can better interact with the surface, can indicate the possibility of this hypothesis in the corresponding system also.

HA proceeds to grow and ACP completely transforms to HA at stage 4. Previous transformation studies held in our group showed that HA growth was the limiting reaction on the rate of transformation even at higher supersaturation with respect to HA and against the dissolution of brushite which has a lower solubility than ACP at constant temperature.[20] Thus, it was concluded that stage 4 was controlled by the HA growth where the presence of additives extended the time span via the growth inhibition.

In the presence of G-block oligomers, XRD spectra of precipitates collected at stage 5 showed a mixture of OCP and HA (Figure S1). Although the crystalline phase was formed at the same supersaturation level in all systems, the presence of G-block oligomers induced a change in the precipitating phase. TEM investigations also showed the coexistence of both crystalline phases where small HA crystals were observed together with large OCP plates (Figure 9) Considering the stronger effect of alginate observed in decreasing the nucleation rate of HA compared to M-block oligomers, a higher content of G-blocks might further hold down the HA nucleation. In addition growth rate studies revealed that G-block oligomers were highly effective in blocking the active sites on HA crystal surface. Therefore, OCP mineralization can be kinetically favored in the system as a result of effective suppression of HA formation.

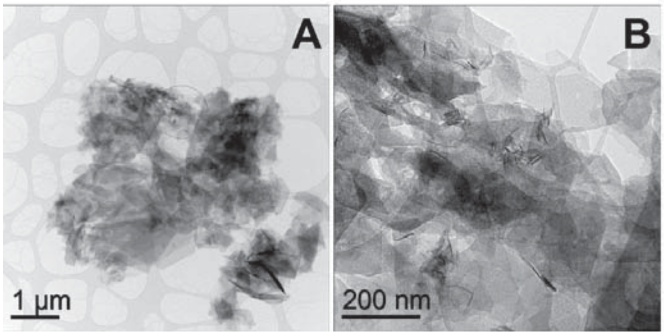

Figure 9. TEM micrographs of final products precipitated in the presence of 1 ppm G-block oligomers. The circled area in (A) is shown in higher magnification in (B).

CONCLUSION

HA formation via ACP precursor was investigated by combining potentiometric measurements of pH and calcium activity in solution with solid characterization techniques. The subsequent stages of the HA formation was determined from the pH and calcium signal curves and the characterization of precipitates at each stage showed that each step was associated with a separate phase with its own chemistry. Prenucleation complex species were suggested to form prior to ACP phase separation in the system which was followed by transformation of ACP to HA via a dissolution-reprecipitation pathway. The effects of alginate-based additives with varying functionality and size were examined on the course of reaction and it was shown that the presence of high molecular weight alginate and M-block oligomers affected the kinetics of HA formation whereas in the presence of G-block oligomers the final precipitating phase was a mixture of OCP and HA. Understanding the effects of alginate molecules on the formation of CaP minerals paves the way for gaining better control on the final properties of the composite materials designed for tissue engineering applications.

ASSOCIATED CONTENT

Supporting Information

The Supporting Information is available free of charge via the Internet at http://pubs.acs.org. The reactions and their corresponding equilibrium constants used for calculations of solution speciation by the thermodynamic software PHREEQC Interactive 3.1, experimental conditions and titrant solution preparation for HA seeded growth experiments, characterization of precipitation products by FTIR, XRD, SEM and TEM, initial pH profiles of spontaneous precipitation experiments in the absence and presence of additives (PDF)

AUTHOR INFORMATION

Corresponding Author

*Jens-Petter Andreassen

Department of Chemical Engineering, Norwegian University of Science and Technology, Trondheim, Norway

E-mail: jens-petter.andreassen@ntnu.no

Author Contributions

The manuscript was written through contributions of all authors. All authors have given approval to the final version of the manuscript.

Funding Sources

We gratefully acknowledge financial support provided by the Research Council of Norway (FRINATEK Project 214607).

ACKNOWLEDGMENT

The TEM work was carried out on the NORTEM (Jeol, JEM 2100, LaB6 camera), TEM Gemini Centre, Norwegian University of Science and Technology (NTNU), Norway.

REFERENCES

(1) Oyen, M. L. *MRS Bull.* **2008**, *33*, 49.

(2) Wang, Y.; Azaïs, T.; Robin, M.; Vallée, A.; Catania, C.; Legriel, P.; Pehau-Arnaudet, G.; Babonneau, F.; Giraud-Guille, M.-M.; Nassif, N. *Nat. Mater.* **2012**, *11*, 724.

(3) Bassett, D. C.; Grover, L. M.; Müller, F. A.; McKee, M. D.; Barralet, J. E. *Adv. Funct. Mater.* **2011**, *21*, 2968.

(4) Olszta, M. J.; Cheng, X.; Jee, S. S.; Kumar, R.; Kim, Y.-Y.; Kaufman, M. J.; Douglas, E. P.; Gower, L. B. *Mater. Sci. Eng. R* **2007**, *58*, 77.

(5) Weiner, S.; Mahamid, J.; Politi, Y.; Ma, Y.; Addadi, L. *Front. Mater. Sci. China* **2009**, *3*, 104.

(6) Combes, C.; Rey, C. *Acta Biomater.* **2010**, *6*, 3362.

(7) Dey, A.; Bomans, P. H. H.; Müller, F. A.; Will, J.; Frederik, P. M.; de With, G.; Sommerdijk, N. A. J. M. *Nat. Mater.* **2010**, *9*, 1010.

(8) Habraken, W. J. E. M.; Tao, J.; Brylka, L. J.; Friedrich, H.; Bertinetti, L.; Schenk, A. S.; Verch, A.; Dmitrovic, V.; Bomans, P. H. H.; Frederik, P. M.; Laven, J.; van der Schoot, P.; Aichmayer, B.; de With, G.; DeYoreo, J. J.; Sommerdijk, N. A. J. M. *Nat. Comm.* **2013**, *4*, 1507.

(9) Xie, B.; Halter, T. J.; Borah, B. M.; Nancollas, G. H. *Cryst. Growth Des.* **2014**, *14*, 1659.

(10) Ibsen, C. J. S.; Gebauer, D.; Birkedal, H. *Chem. Mater.* **2016**, *28*, 8550.

(11) Boskey, A. L.; Posner, A. S. *J. Phys. Chem.* **1973**, *77*, 2313.

(12) Mullin, J. W. *Crystallization*; Butterworth-Heinemann, **1997**.

(13) Cardew, P. T.; Davey, R. J. *Proc. Math. Phys. Eng. Sci.* **1985**, *398*, 415.

(14) Jiang, S.; Chen, Y.; Pan, H.; Zhang, Y.-J.; Tang, R. *Phys. Chem. Chem. Phys.* **2013**, *15*, 12530.

(15) Ding, H.; Pan, H.; Xu, X.; Tang, R. *Cryst. Growth Des.* **2014**, *14*, 763.

(16) Chen, Y.; Gu, W.; Pan, H.; Jiang, S.; Tang, R. *Cryst. Eng. Comm.* **2014**, *16*, 1864.

(17) Jiang, S.; Pan, H.; Chen, Y.; Xu, X.; Tang, R. *Faraday Discuss.* **2015**, *179*, 451.

(18) Wang, C.-G.; Liao, J.-W.; Gou, B.-D.; Huang, J.; Tang, R.-K.; Tao, J.-H.; Zhang, T.-L.; Wang, K. *Cryst. Growth Des.* **2009**, *9*, 2620.

(19) Bjørnøy, S. H.; Bassett, D. C.; Ucar, S.; Strand, B. L.; Andreassen, J.-P.; Sikorski, P. *Acta Biomater.* **2016**, *44*, 254.

(20) Ucar, S.; Bjørnøy, S. H.; Bassett, D. C.; Strand, B. L.; Sikorski, P.; Andreassen, J. P. *J Cryst. Growth* **2016**.

(21) Haug, A.; Larsen, B.; Smidsrod, O. *Acta Chem. Scand.* **1966**, *20*, 183.

(22) Skjakbraek, G.; Larsen, B. *Carbohyd. Res.* **1985**, *139*, 273.

(23) Murphy, J.; Riley, J. P. *Anal. Chim. Acta* **1962**, *27*, 31.

(24) Nancollas, G. H.; Mohan, M. S. *Arch. Oral Biol.* **1970**, *15*, 731.

(25) Beck, R.; Seiersten, M.; Andreassen, J. P. *J Cryst. Growth* **2013**, *380*, 187.

(26) Salimi, M. H.; Heughebaert, J. C.; Nancollas, G. H. *Langmuir* **1985**, *1*, 119.

(27) Malkaj, P.; Pierri, E.; Dalas, E. *J Mater. Sci. Mater. M* **2005**, *16*, 733.

(28) Coleman, R. J.; Jack, K. S.; Perrier, S.; Grøndahl, L. *Cryst. Growth Des.* **2013**, *13*, 4252.

(29) Öner, M.; Doğan, Ö. *Prog. Cryst. Growth Ch.* **2005**, *50*, 39.

(30) Mangood, A.; Malkaj, P.; Dalas, E. *J Cryst. Growth* **2006**, *290*, 565.

(31) Koutsopoulos, S.; Dalas, E. *J Cryst. Growth* **2000**, *217*, 410.

(32) Mørch, Ý. A.; Donati, I.; Strand, B. L. *Biomacromolecules* **2006**, *7*, 1471.

(33) Teng, H. H.; Dove, P. M.; De Yoreo, J. J. *Geochim. Cosmochim. Acta* **2000**, *64*, 2255.

(34) Nielsen, A. E. *J Cryst. Growth* **1984**, *67*, 289.

(35) Chrissanthopoulos, A.; Klouras, N.; Ntala, C.; Sevastos, D.; Dalas, E. *J. Mater. Sci. Mater. Med*. **2015**, *26*.

(36) Huang, S. p.; Zhou, K. c.; Li, Z. y. *T. Nonferr. Metal. Soc.* **2007**, *17*, 612.

(37) Reynolds, R. C. *Limnol. Oceanogr.* **1978**, *23*, 585.

(38) Christoffersen, M. R.; Christoffersen, J. *J Cryst. Growth* **1992**, *121*, 617.

(39) Onuma, K.; Ito, A.; Tateishi, T.; Kameyama, T. *J Cryst. Growth* **1995**, *154*, 118.

(40) Bar-Yosef Ofir, P.; Govrin-Lippman, R.; Garti, N.; Füredi-Milhofer, H. *Cryst. Growth Des.* **2004**, *4*, 177.

(41) Boskey, A. L.; Posner, A. S. *Mater. Res. Bull.* **1974**, *9*, 907.

(42) van der Leeden, M. C.; Kashchiev, D.; van Rosmalen, G. M. *J Cryst. Growth* **1993**, *130*, 221.

(43) Chatzipanagis, K.; Iafisco, M.; Roncal-Herrero, T.; Bilton, M.; Tampieri, A.; Kroger, R.; Delgado-Lopez, J. M. *Cryst. Eng. Comm.* **2016**, *18*, 3170.

SUPPLEMENTARY INFORMATION

Table S1. The reactions and their corresponding equilibrium constants (-log K) used to calculate the solution speciation at 25 °C.

$H_2O \leftrightarrow H^+ + OH^-$	13.997
$Ca^{2+} + H_2O \leftrightarrow CaOH^+ + H^+$	12.697
$H_3PO_4 \leftrightarrow 3H^+ + PO_4^{3-}$	21.721
$H_2PO_4- \leftrightarrow 2H^+ + PO_4^{3-}$	19.573
$HPO_4^{2-} \leftrightarrow H^+ + PO_4^{3-}$	12.375
$CaH_2PO_4^+ \leftrightarrow Ca^{2+} + 2H^+ + PO_4^{3-}$	20.923
$CaHPO_4 \leftrightarrow Ca^{2+} + H^+ + PO_4^{3-}$	15.035
$CaPO_4^- \leftrightarrow Ca^{2+} + PO_4^{3-}$	6.460
$Ca_5(PO_4)_3OH$ (s) $\leftrightarrow 5Ca^{2+} + 3PO_4^{3-} + H_2O - H^+$	44.333
$Ca_4H(PO_4)_3.3H_2O$ (s) $\leftrightarrow 4Ca^{2+} + 3PO_4^{3-} + 3H_2O + H^+$	47.95
$Ca_3(PO_4)_2 \leftrightarrow 3Ca^{2+} + 2PO_4^{3-}$ (amorphous 1)	25.500
$Ca_3(PO_4)_2 \leftrightarrow 3Ca^{2+} + 2PO_4^{3-}$ (amorphous 2)	28.250
$Ca_3(PO_4)_2 \leftrightarrow 3Ca^{2+} + 2PO_4^{3-}$ (beta)	28.920

Table S2. Experimental conditions for seeded constant composition growth experiments of HA at 25 °C (Ca/P= 1.67).

Ca^{2+} (mM)	**pH**	**S**	**C_{eff} (mM)**	**m_{seeds} (mg)**
0.60	7.40 ± 0.02	4.1	0.50	30
0.70	7.40 ± 0.02	4.7	0.50	30
0.80	7.40 ± 0.02	5.2	0.50	30
1.00	7.40 ± 0.02	6.3	0.50	30
3.48	7.30 ± 0.02	21.5	0.80	20

Preparation of Titrant Solutions for Constant Composition Growth Experiments

Compositions of titrant solutions were adjusted for each working solution to compensate for ion consumption, changing ionic strength and alkalinity in the reaction media. For this purpose, first, the effect of the extent of HA crystallization on total alkalinity and ion consumption were computed in moles (n) according to the equations given below:

$$n_{Ca^{2+}} = n_{Ca^{2+},i} - n_{Ca^{2+},cryst} \qquad (1)$$

$$n_{PO_4{}^{3-}} = n_{PO_4{}^{3-},i} - n_{PO_4{}^{3-},cryst} \qquad (2)$$

$$n_{OH^-} = n_{H^+,i} - n_{OH^-,cryst} \qquad (3)$$

$$n_{alk} = n_{alk,i} - n_{alk,cryst} \qquad (4)$$

$$n_{alk,cryst} = 3n_{PO_4{}^{3-},cryst} + n_{OH^-,cryst} \qquad (5)$$

Then, an arbitrary calcium concentration (c) was chosen to be added to the reaction medium from burette 1 in order to compensate for the calcium ion consumed by crystallization. The calcium concentration in burette 1 should be higher than the concentration in the working solution and should be adjusted according to the growth kinetics. Next, the composition of titrant solution 2 was calculated, according to the titrant solution 1 and the total volume of titrant solutions to be added, to fulfil Equations 6-11.

$$c_{Ca^{2+}} = c_{Ca^{2+},i} \qquad (6)$$

$$c_{PO_4{}^{3-}} = c_{PO_4{}^{3-},i} \qquad (7)$$

$$c_{H^+} = c_{H^+,i} \qquad (8)$$

$$c_{K^+} = c_{K^+,i} \qquad (9)$$

$$c_{NO_3^-} = c_{NO_3^-,i} \qquad (10)$$

$$c_{alk} = c_{alk,i} \qquad (11)$$

The adjustment for the ionic strength was also ensured with burette 2 to keep the ionic activity coefficients constant. The composition of burette 2 should be recalculated for each initial working solution and the calcium concentration in burette 1.

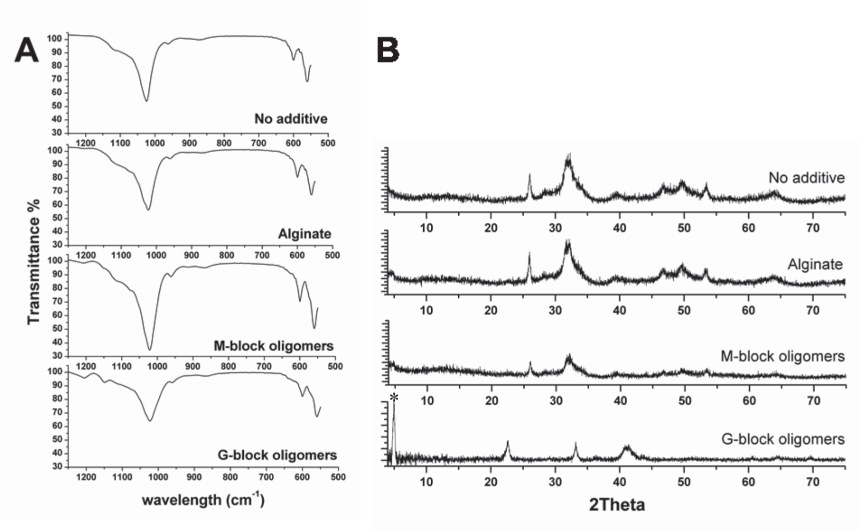

Figure S1. (A) FTIR and (B) XRD spectra of precipitates collected during stage 5 in the absence and presence of indicated additives. Asterisk marks the distinguishing XRD peak of OCP precipitated in the presence of G-block oligomers.

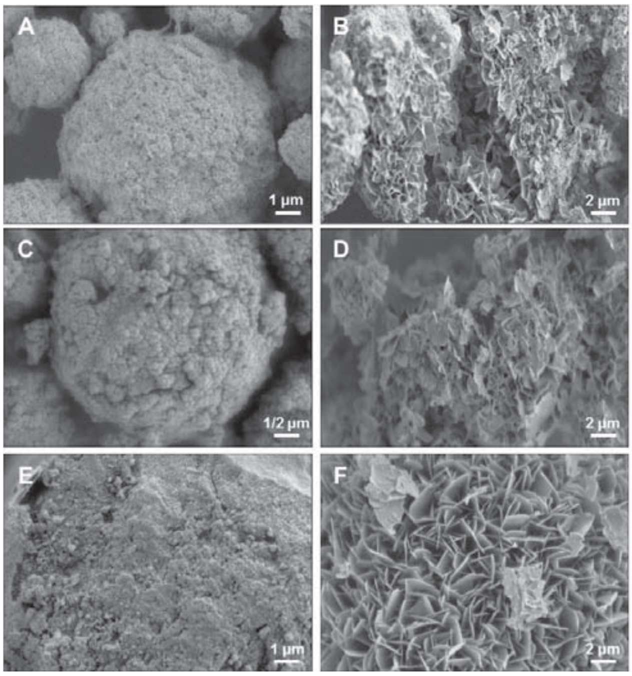

Figure S2. SEM images of the (A,C,E) intermediate (stage 3) and (B,D,F) final products (stage 5) of the spontaneous precipitation reactions in the presence of (A,B) alginate, (C,D) M-block oligomers and (E,F) G-block oligomers with the concentration of 1 ppm.

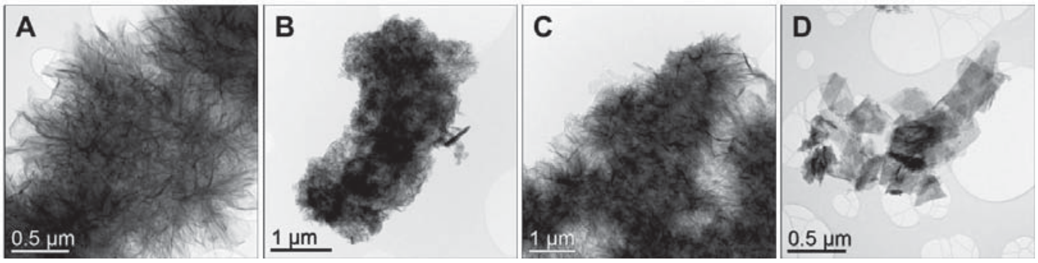

Figure S3. TEM micrographs of final products collected (A) in the absence of additives; and in the presence of (B) alginate; (C) M-block oligomers and (D) G-block oligomers with the concentration of 1 ppm.

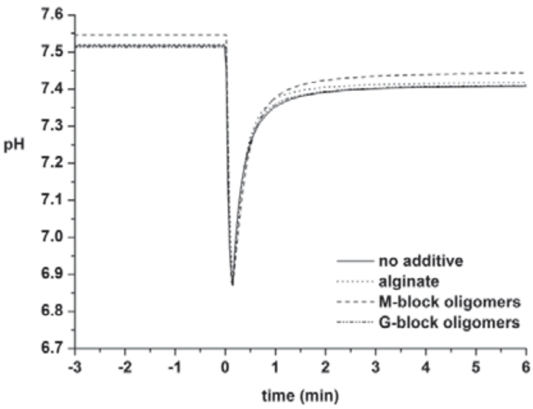

Figure S4. pH profiles of spontaneous precipitation experiments in the absence and presence of the indicated additives where t= 0 denotes the time point calcium solution was added in the reaction medium.

Supplementary Attachments

Controlled mineralisation and recrystallisation of brushite within alginate hydrogels

2016 Biomed. Mater. 11 015013

(http://iopscience.iop.org/1748-605X/11/1/015013)

IOP Publishing Biomed. Mater. 11 (2016) 015013 doi:10.1088/1748-6041/11/1/015013

Biomedical Materials

RECEIVED
16 July 2015

REVISED
16 October 2015

ACCEPTED FOR PUBLICATION
10 November 2015

PUBLISHED
2 February 2016

PAPER

Controlled mineralisation and recrystallisation of brushite within alginate hydrogels

Sindre H Bjørnøy[1], **David C Bassett**[1], **Seniz Ucar**[2], **Jens-Petter Andreassen**[2] **and Pawel Sikorski**[1]

[1] Department of Physics, Norwegian University of Science and Technology, 7491 Trondheim, Norway
[2] Department of Chemical Engineering, Norwegian University of Science and Technology, 7491 Trondheim, Norway

E-mail: pawel.sikorski@ntnu.no

Keywords: alginate, biomineralisation, hybrid materials, hydrogels, brushite

Online supplementary data available from online

Abstract

Due to high solubility and fast resorption behaviour under physiological conditions, brushite ($CaHPO_4{\cdot}2H_2O$, calcium monohydrogen phosphate dihydrate, dicalcium phosphate dihydrate) has great potential in bone regeneration applications, both in combination with scaffolds or as a component of calcium phosphate cements. The use of brushite in combination with hydrogels opens up possibilities for new cell-based tissue engineering applications of this promising material. However, published preparation methods of brushite composites, in which the mineral phase is precipitated within the hydrogel network, fail to offer the necessary degree of control over the mineral phase, content and distribution within the hydrogel matrix. The main focus of this study is to address these shortcomings by determining the precise fabrication parameters needed to prepare composites with controlled composition and properties. Composite alginate microbeads were prepared using a counter-diffusion technique, which allows for the simultaneous crosslinking of the hydrogel and precipitation of an inorganic mineral phase. Reliable nucleation of a desired mineral phase within the alginate network proved more challenging than simple aqueous precipitation. This was largely due to ion transport within the hydrogel producing concentration gradients that modified levels of supersaturation and favoured the nucleation of other phases such as hydroxyapatite and octacalcium phosphate, which would otherwise not form. To overcome this, the incorporation of brushite seed crystals resulted in good control during the mineral phase, and by adjusting the number of seeds and amount of precursor concentration, the amount of mineral could be tuned. The material was characterised with a range of physical techniques, including scanning electron microscopy, powder x-ray diffraction and Rietveld refinement, Fourier transform infrared spectroscopy, and thermogravimetric analysis, in order to assess the mineral morphology, phase and amount within the organic matrix. The mineral content of the composite material converted from brushite into hydroxyapatite when submerged in simulated body fluid, indicating possible bioactivity. Additionally, initial cell culture studies revealed that both the material and the synthesis procedure are compatible with cells relevant to bone tissue engineering.

1. Introduction

In cell-based tissue engineering (TE) there is a need for synthetic materials that can act as scaffolds for cells. These materials must be biocompatible, preferably biodegradable, and be able to provide an environment that ensures attachment, proliferation and sustained function of specific cell types [1, 2]. For bone TE, an ideal scaffold should have appropriate mechanical properties, provide an environment for nutrient and growth factor exchange and have a certain porosity for cell migration and vascularisation [3]. Hydrogels are a class of polymeric networks capable of retaining large amounts of water and have shown good promise as TE scaffolds [4, 5]. Their hydrated form allows for the diffusion of nutrients and the delivery of bioactive agents, but their high water content also means that hydrogels are inherently soft materials with low mechanical strength and are therefore more suitable for soft tissues [6]. However, hydrogel-based scaffolds do possess the potential to be non-invasive, injectable temporary scaffolds which can deliver cells, growth factors, drugs or combinations of these to a damaged site [7]. Hydrogels can also be used in combination with load-bearing structures in order to promote the growth of new healthy bone and to aid in overcoming some of the challenges of metal implants, i.e. corrosion or implant rejection [8, 9].

Human bone tissue consists mainly of hydroxyapatite (HAp) nanocrystals in an ordered collagen matrix. The interplay between the stiff, but brittle, inorganic phase and the soft, but tough, organic phase, combined with a hierarchical design provides the extraordinary mechanical strength of this natural composite [10]. Adding an inorganic phase, such as HAp, to a hydrogel is one approach to improve the mechanical properties of the biomaterial, although so far the level required for load-bearing applications has not been reached [11–16]. However, cell response to mechanical stimuli has gained attention lately and tuning the mechanical properties of a scaffold may hold great potential [17]. It has also been shown that alginate mineralised with HAp improves cell adhesion, and the mineral itself can act as an osteoconductive surface [18–20].

For many years HAp has been the calcium phosphate (CaP) phase of choice for application in bone augmentation procedures owing to its likeness to natural bone mineral and stability under physiological conditions. There are, however, several other CaP phases that may dissolve or transform *in vivo* to allow or encourage natural remodelling procedures, thereby creating a bioactive implant. Both brushite ($CaHPO_4 \cdot 2H_2O$) and octacalcium phosphate (OCP) have been suggested as natural precursor phases to HAp, although *in vivo* evidence of this is rarely found [21]. Brushite has, over the past two decades, received a great deal of attention as a potential bioceramic in the repair of osseous tissue [22, 23]. The solubility of brushite is higher than that of HAp and OCP (pK_{sp} of 6.6, 58.6 and 48.7, respectively, at 37 °C) [24] and it therefore transforms readily into these phases in physiological conditions. The increased solubility offers a considerable advantage over alternative calcium phosphate-based materials as it may provide the space and necessary ions for natural bone remodelling and regeneration [23]. It has also been shown that the resorption rate of brushite is higher than for HAp [25]. There are, however, some issues with the long-term fate of large volumes of implanted brushite, as it has been shown to transform into more stable phases like OCP and HAp [26, 27]. This effect seems to be site-specific and is likely related to the *in vivo* fluid exchange in the sample location [28, 29]. Such behaviour has implications for the choice of brushite to fill large bone lesions. Interest in brushite as a biomaterial is mounting, and while there are many examples of promising HAp-alginate composites, there is very little literature regarding brushite in combination with hydrogels. Brushite powder has been incorporated into an alginate matrix for fertiliser purposes and the recrystallisation of brushite in alginate at a cement-hydrogel interface has been studied by Raman-spectroscopy [30, 31]. A recent attempt was made by Amer *et al* to precipitate brushite *in situ* with alginate [32]. While mineral was formed within the hydrogel, little attention was paid to the reaction conditions or biocompatibility, which resulted in poorly defined composites and unstable gels. During preliminary experiments, we found that taking such an approach for the synthesis of a brushite alginate composite was unsatisfactory in terms of reaction control and reproducibility. Therefore, we sought to improve this synthesis by controlling the inherently dynamic reaction conditions of pH by using appropriate buffers and employed crystal seeds as a means to encourage the growth of phase pure brushite within the alginate matrix without recourse to use extreme reaction conditions that would be toxic to cells [33].

The driving force for the nucleation and growth of a specific phase in solution is supersaturation, i.e. the difference in chemical potential of a molecule in the solution and one in the crystal [34]. According to the literature, brushite is thermodynamically stable below approximately pH 4, but due to the nucleation and growth kinetics of different CaP phases, brushite can be precipitated at higher pH [35, 36]. However, it has been seen that for increasing precursor concentration, the pH at which brushite nucleates decreases [37, 38]. The pH affects the solubility and hence the supersaturation of the different phases in the $Ca(OH)_2$–H_3PO_4–H_2O system. The precipitation of CaP consumes, depending on the phase, either PO_4^{3-} or HPO_4^{2-}, which leads to a decrease in pH due to:

$$H_2PO_4^{-} \rightarrow HPO_4^{2-} + H^{+} \quad (1)$$

$$HPO_4^{2-} \rightarrow PO_4^{3-} + H^{+} \quad (2)$$

An indication of the bioactivity of a biomaterial for bone tissue engineering can be obtained by the formation of bone-like apatite on its surface when it is soaked in simulated body fluid (SBF) [39]. Despite the criticism and limitations of this technique [40–42], SBF has been regularly used to indicate the apatite-forming and bone-bonding abilities of biomaterials, and is generally accepted as a good initial test for *in vitro* behaviour. Here this technique was employed to study the transformation of brushite into HAp within an alginate–brushite composite, not to predict the *in vivo* behaviour of the material.

Our group has previously developed several strategies to mineralise alginate beads with HAp [14, 43].In this study we investigated the mineralisation of alginate in the pH range of 5–7 with the specific aim of creating a bioactive composite material of alginate and brushite with controllable phase and mineral content, where the synthesis and/or material itself is cell-compatible.

2. Materials and methods

2.1. Chemical reagents

All the chemical reagents were purchased from Sigma-Aldrich, Norway unless otherwise stated. De-ionized water (DIW with a resistivity of 10–15 MΩcm) was used in all of the experiments.

2.2. Preparation of brushite-seeds

The brushite crystals were synthesised as follows. 500 ml of 0.4 M $Ca(NO_3)_2 \cdot 4H_2O$ and 500 ml of 0.4 M KH_2PO_4 and 26 mM KOH were prepared and bubbled with nitrogen gas. The solutions were mixed and the pH was monitored. The precipitates formed were aged by stirring for 2 h after the changes in pH stopped, before they were filtered and washed with DIW and ethanol. The crystals were dried at room temperature and their size was measured using a Coulter Counter Multisizer 3 (Beckman Coulter).

2.3. Composite beads made by counter-diffusion precipitation

The beads were made in a similar way to that which we have previously described [43]. Briefly, alginate with a guluronic acid residue fraction of $F_G = 0.68$, corresponding to 68% (FMC Biopolymer) was dissolved in DI-water to a final concentration of 1.8 wt% containing 0.9 wt% sodium chloride. A mixture of $Na_2HPO_4 \cdot 7H_2O$ and $NaH_2PO_4 \cdot 2H_2O$ was added to a phosphate concentration of 300 mM, where the ratio was decided by the final pH (5–7). The solution was stirred for at least 1 h. A gelling solution was made by dissolving calcium chloride in DI-water to give a final concentration of 1 M. Tris(hydroxymethyl)aminomethane (TRIS) or sodium acetate (NaAc) was used to buffer the solution at pH 7, or 6 and 5, respectively. The alginate solution was drawn from a needle with the help of a syringe pump and an electrostatic potential between the needle tip and the gelling bath. The needle diameter was 400 μm and it was electrostatically charged at a potential of 7 kV to ensure a uniform bead diameter of $\sim$500 μm.

2.4. Composite beads made by counter-diffusion precipitation with brushite-seeds

For the seeded beads, brushite-powder was ground using an agate mortar and pestle to disrupt the aggregates formed during the drying process, and mixed with alginate solution (1.8% alginate, 0.9% NaCl, 300 mM PO_4^{3-}, pH 5) to a final concentration of 0.1 wt%, 1 wt% and 5 wt% of wet mass. The alginate solution was stirred for at least 1 h to ensure homogeneous mixing. Control beads with no phosphate precursor were made with the same seed concentration. The beads were made using the same technique described previously, however, only gelling bath with 1 M $CaCl_2$, 0.9 wt% NaCl, and 100 mM sodium acetate at pH 5 was used.

2.5. Incubation in SBF

Simulated body fluid (SBF) was made following the instructions given by Kokubo and Takadama [39]. Beads made from 4 ml alginate solution were added into plastic tubes filled with 50 ml SBF-solution and placed at 37 °C. Beads containing originally 0.1 wt%, 1 wt% and 5 wt% brushite-seeds were kept in SBF-solution for 24 h, 72 h and 168 h, respectively, before they were removed and characterised. Non-mineralised beads without seeds were kept for 168 h in SBF before characterisation as a control.

2.6. Material characterisation

The beads were optically imaged in the wet state using an inverted microscope (Eclipse TS100, Nikon, Japan).

SEM analysis (Hitachi S-5500 S(T)EM) was performed with an acceleration voltage of 1–10 kV. The sample beads were dehydrated in increasing concentrations of ethanol. The ethanol was then substituted with acetone before they were critical point dried (Emitech K850 critical point dryer). The beads were placed on SEM-stubs with carbon tape and sputter coated (Cressington 208 HR) with a 5–10 nm layer of platinum/palladium (80/20). The chosen beads were cut in the wet state by embedding them in an alginate cylinder, gelled with the *in situ* technique [44], or agarose cylinder, where a 2% agarose solution was heated on a hot plate and the beads were introduced before the gel had set. These cylinders were cut into 100 or 200 μm sections using a vibrating blade microtome (VT1000S, Leica Biosystems, Nussloch GmbH, Germany). These sections were then dried and mounted using the same procedure as for the whole beads.

Powder XRD (D8 Advance DaVinci, Bruker AXS GmBH, Germany) was performed in the range of 5–75° with a step size of 0.013° and a step time of 0.67 s. The alginate-CaP composites were air-dried and crushed with a mortar and pestle before they were analysed. Rietveld analysis (Topas4.2, Bruker) was performed in order to assess the relative number of mineral phases. The background parameters, sample displacement, scale factor, crystallite size and cell parameters were refined. In order to check the reliability of the Rietveld analysis on the samples, an analysis of mixes of pure mineral samples with known sample ratios was performed.

Thermogravimetric analysis (TGA) (Netzsch STA449C TGA, Netzsch-Gerätebau GmbH, Germany) was performed in the temperature range of 25–1000 °C at a heating rate of 20 °C min^{-1} under an air flow of 80 ml min^{-1}. A 20 min hold between 70–100 °C was performed in order to remove any adsorbed water. In order to estimate the mineral content in the beads, curves describing the sample residual mass $m(T)$ were modelled by adding a fraction *f* of the curve for the pure minerals to a fraction 1–*f* of the curve for pure alginate, where the fraction *f* denotes the assumed mineral content. For cases where there was more than one mineral phase the relative amount of the mineral, as found with Rietveld analysis, was used:

$$\Delta m(T) = f_H \Delta m_H(T) + f_B \Delta m_B(T) + (1 - f_H - f_B) \Delta m_{\mathrm{Alg}}(T) \qquad (3)$$

where $\Delta m_H(T)$ and $\Delta m_B(T)$ are the mass loss curve for pure HAp and brushite mineral phases, $\Delta m_{\mathrm{Alg}}(T)$ is the mass loss curve for the alginate gel, and f_H and f_B are the fractions of HAp and brushite. The total mineral fraction ($f_H + f_B$) was then fitted in order for the modelled TGA curves to match the experimental data at at 1000 °C. An example of this can be seen in figure S1 in the supplementary information (stacks.iop.org/BMM/11/015013/mmedia). The error was calculated based on the control samples.

Attenuated total reflection Fourier transform infrared (ATR-FTIR) spectroscopy (Nicolet 8700 ATR-FTIR spectrometer, ThermoFisher Scientific, USA) was performed in the range of 550–4000 cm^{-1} at room temperature. An average of 32 scans was taken.

2.7. Cell experiments

Murine calvarial pre-osteoblast cells, MC3T3-E1 subclone 4 (ATCC® CRL-2593™), were cultured to 80% confluency in α-MEM supplemented with 1 μg ml^{-1} gensumycin, 2 mM glutamine and 10% fetal calf serum, before trypsinising and mixing with alginate at a final concentration of 1×10^6 cells ml^{-1}. 300 mM PO_4 and 1 wt% brushite seeds were added to the alginate and 0.9% saline was added to give a final alginate concentration of 1.8 wt%. Alginate was also prepared in the same way without phosphate solution or brushite seeds. Microbeads containing cells were produced by electrostatic extrusion, as described previously [43]. The gelling solution used either 300 mM $CaCl_2$ or 1 M $CaCl_2$ containing 0.9% NaCl and was adjusted to pH 5 with 50 mM or 100 mM NaAc, respectively, or 50 mM $CaCl_2$ for non-mineralised control samples containing no phosphate or brushite seeds. 10 ml of alginate microbeads were left in the gelling solution for 10 min prior to washing with PBS and then culture media, and were then suspended in 10 ml of culture media and placed in an incubator. To assess the cell viability post-encapsulation a combination of a calcein-AM / ethidium homodimer-1 assay (LIVE/DEAD® Viability/Cytotoxicity Kit, L-3224, Molecular Probes®) and an AlamarBlue® viability assay (DAL1100, Molecular Probes®) were used. This combination of assays was used because of difficulties in accurately counting the cells stained using the LIVE/DEAD assay in the mineralised samples, which were much more optically dense than the non-mineralised controls. The AlamarBlue assay relies on optical measurements of the incubating media and is therefore not influenced by the optical properties of the samples. Viability was monitored at 1, 3, 10 and 15 d post-encapsulation on 6 repeat samples of known mass (between 0.4–0.6 g). At each point in time the live/dead cell count in the non-mineralised control samples was taken and AlamarBlue reduction was measured for all the samples (optical absorption at 570 and 590 nm, Perkin Elmer Victor 3). Comparing the results obtained by the AlamarBlue reduction assay allowed the % viability of the experimental samples to be normalised to the viability of the non-mineralised control samples measured by the live/dead assay. The viability of the control sample was normalised with respect to the total number of encapsulated cells at the start of the experiment.

3. Results and discussion

3.1. Investigating parameters for CaP precipitation within alginate microbeads

The alginate/CaP composite beads were prepared by the counter diffusion method, as described in section 2.3. This arrangement created a highly dynamic system in which the phosphate ions diffused out of the bead, Ca^{2+} diffused into the bead, and gelling of the alginate and precipitation of CaP happened simultaneously. Formation of the mineral consumed phosphate ions, which lowered the pH locally in the hydrogel, as can be seen from equations (1) and (2). As a result, a local pH-gradient within the alginate beads was formed, and the pH in the gelling bath decreased over time, see figure 1. Both the gelling and the mineral precipitation processes consumed calcium ions.

In the first instance, we investigated an approach to produce alginate/brushite composites similar to that proposed by Amer *et al* [32], although with a reversed Ca/P ratio and a smaller bead size. The reversed Ca/P ratio was needed to form stable alginate gels [43]. This is due to the fact that the affinity between phosphate ions and calcium ions is greater then that between alginate and calcium ions. Consequently, if the calcium concentration in the gelling bath is too low, the available Ca-ions are consumed by the forming mineral phase and a stable alginate gel is not formed.

Surprisingly, no evidence of monetite or brushite was found within the hydrogel network. Contrary to their observations, the mineral phase within the beads produced in this study was poorly crystalline HAp, as seen in the lower spectrum of figure 2. An optical image of a representative sample can be seen in figure 3(a). It was also observed that some of the phosphate precursor diffused out of the beads and formed brushite-precipitates in the gelling bath. It is not only the Ca/P ratio that plays a role in the formation of CaP-precipitates; the pH is a determining factor for the nucleation of the different phases [24]. Unfortunately, no information about pH is given in the work of Amer *et al*. In this work, the pH in the gelling bath was observed to change from an initial value of pH 7 to as low as pH 3 during bead formation. This large drop in pH can also contribute to destabilising the gel. The pK_a of alginate ranges from 3.4 to 4.4 depending on the type of alginate and the conditions [45]. At such a low pH the alginate can begin to lose its charge and hence affinity for Ca^{2+}. This effect in combination with the consumption of Ca^{2+} due to mineral formation can lead to destabilisation of the gel bead, seen as wrinkles in figure 3(b). Similar observations have been reported previously, although the charge neutralisation was then due to an oppositely charged polymer, not pH [46].

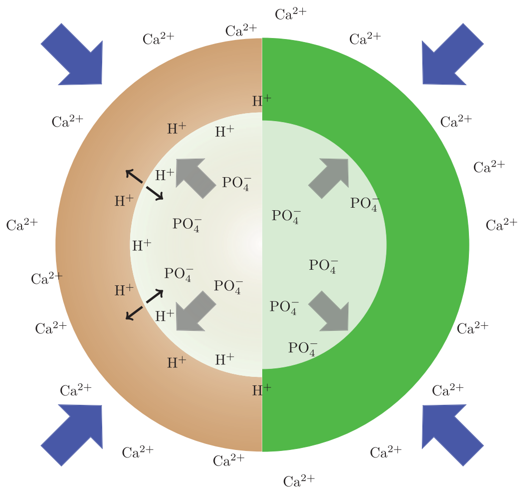

Figure 1. A schematic diagram illustrating the gelling and mineralising system. After the alginate drop has entered the gelling bath, Ca^{2+} diffuses inwards (blue arrows), the phosphate ions (PO$_4^-$) diffuse outwards (grey arrows), gelling and mineralising occurs at the front of the Ca^{2+} diffusion illustrated by a colour difference in the figure. On the right, the green colour indicates gelled alginate. On the left, the brown colour illustrates mineral formation and the associated local release of H$^+$, their diffusion being indicated by black arrows. The mineral front trails slightly behind the gelling front.

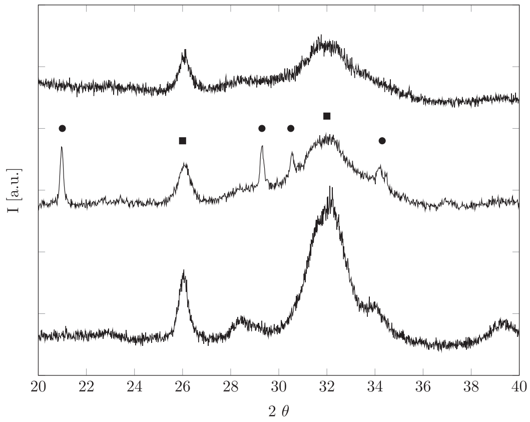

Figure 2. XRD-spectra for samples made with 300 mM phosphate in the alginate solution and 1 M calcium chloride in the gelling bath. Bottom: no buffer. Middle: a representative sample from the pH-study with a 50 mM NaAc buffer. Top: a sample with a 500 mM NaAc buffer. ● denotes brushite, ■ denotes HAp.

In order to investigate the role of pH on both the nucleation and growth of different CaP crystal phases, a series of experiments was performed where the initial pH in both the alginate solution and the gelling bath was systematically varied between pH 5 and pH 7 (a total of nine combinations) by the addition of a buffer (see Materials and methods). For a sample formed using a 50 mM buffer, upon inspection with optical microscopy (figure 3(b)), it was clear that the mineralisation was inhomogeneous in the sense that individual beads were mineralised differently. This sample was representative for most of the experiments. Note that this buffer concentration was not sufficient to keep the pH stable during bead formation. This time-dependent change in the pH-value was believed to be the cause of the inhomogeneity observed in figure 3. The XRD-results showed that the mineral formed was, in most cases, not pure phase, but a mixture of brushite and HAp, as can be seen in the top spectrum of figure 2, and in some cases minor amounts of OCP. The estimated amount of mineral for the different samples varied between 2–49 ± 3 weight percent of dry mass, corresponding to 0.1–1.8 ± 0.2 weight percent mineral content in the hydrated gel.

The buffer strength was increased to 100 and 500 mM in an attempt to stabilise the pH at pH 5. In

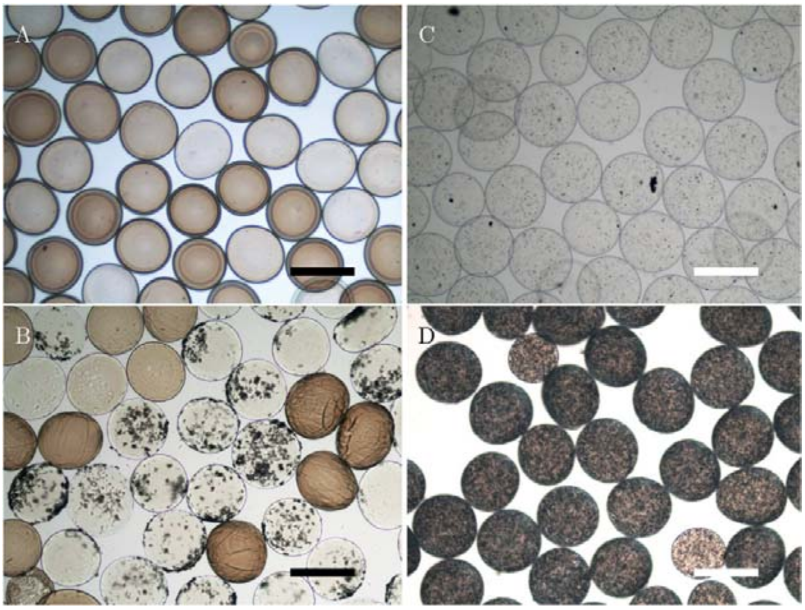

Figure 3. Optical images of (A): a sample gelled in an unbuffered bath. (B): a sample made with alginate solution at pH 7 and a gelling bath at pH 6 with 50 mM NaAc buffer. The brown beads are mineralised throughout, while the black spots are larger brushite crystals on the surface of the beads. (C): a sample with 0.1% brushite-seeds without phosphate precursor. (D): a sample with 0.1% brushite seeds with phosphate precursor and a gelling bath at pH 5 with a 100 mM NaAc buffer. The scale bars are 500 μm.

both cases the change in pH was lower, as expected, although these experiments resulted in phase pure HAp within the alginate composite as can be seen in figure 2 for a sample with a 500 mM buffer. A possible explanation for this is that the ideal pH for the formation of brushite is somewhere below pH 5, although if the pH within the microbead is too low, the phosphate precursor might diffuse out of the alginate network before any mineral is formed. Hence, at no buffering, HAp is formed initially and the pH drops quickly to a value where no new crystals are nucleated. For strong buffering the pH does not drop into the region where brushite formation is favoured. A lower concentration of buffer (50 mM) allowed for the formation of some brushite, but the process was poorly controlled. For further experiments an initial pH 5 in the gelling bath was chosen as a compromise between brushite formation and cell survival. The buffer concentration was also increased to 100 mM in order to ensure more stable conditions over time in the gelling bath.

The variation in mineral amount and the occurrence of several phases indicated a complex crystallisation process within the alginate microbeads, sensitive to the local supersaturation, pH, precursor concentration and precursor ratios, all of which changed during bead formation. A lack of control over the process was identified, as the resulting mineral phase and amount varied between experiments performed under the same conditions. However, a clear trend from these experiments was that a lower pH in the alginate solution led to a lower amount of mineral within the hydrogel beads, regardless of the initial pH in the gelling bath. A possible explanation for this is that the higher local pH within the gel network immediately after the droplet entered the gelling bath affected the local supersaturation and allowed for faster nucleation of the mineral. In cases where the initial pH within the beads was lower, more of the phosphate precursor diffused out into the gelling bath before precipitation occurred. The high initial pH is incompatible with the formation of brushite, at least in a controlled manner. To overcome this, brushite seed crystals were incorporated in the alginate solution in order to promote the early growth of brushite and to gain control over which phases nucleated in the sample.

3.2. Control of brushite formation within an alginate matrix using seed crystals

To promote the growth of brushite within the alginate network, brushite seeds were introduced into the alginate solution at three different concentrations: 0.1, 1 and 5 weight percent (hereby referred to as low, medium and high concentration of seeds). The seed crystals had a size range of approximately 30 μm, measured by a Coulter counter. The dried seeds were ground using a mortar and pestle prior to mixing with the alginate solution to distribute the seeds evenly and to avoid clogging the needle. The phase purity of the seeds was verified with XRD. The beads were then made with alginate solutions containing seeds and phosphate precursor. The pH of the gelling bath was kept at pH 5 with a 100 mM sodium acetate buffer and contained 1 M $CaCl_2$ and 0.9% NaCl.

Table 1. The results for seeded beads gelled in 1 M $CaCl_2$, 0.9 wt% NaCl, 100 mM NaAc.

Seed conc.	PO_4 mM	Final pH	Dry mass %	Wet mass %	Brushite %
0.1%	300	4.88	71 ± 3	4.5 ± 0.6	95
0.1%	0	5.00	0 ± 3	0.0 ± 0.1	100
1%	300	4.85	79 ± 3	6.9 ± 1.2	99
1%	0	5.00	32 ± 3	0.8 ± 0.2	100
5%	300	4.73	85 ± 3	10.6 ± 2.5	98
5%	0	5.00	72 ± 3	4.7 ± 0.5	100

Note: The mass percentage refers to the mineral content, while the last column refers to the brushite percentage of this mineral.

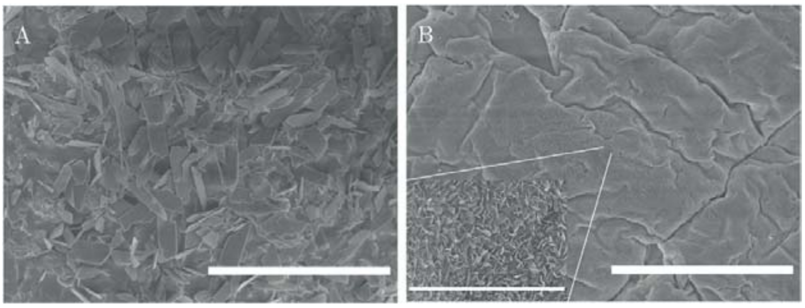

Figure 4. SEM micrograph of the surface an alginate microbead made with medium seed concentration and phosphate precursor. (A): before and (B): after 168 h in SBF. The scale bars are 30 μm and 2 μm for the inset.

Table 1 summarises the results obtained for the seeded experiments in the conditions described above. All the samples made with a phosphate precursor and brushite seeds contained close to pure phase brushite with 71 ± 3 to 86 ± 3% mineral amount (dry mass) corresponding to 4.5 ± 0.6 to 10.6 ± 2.5% wet mass. Figures 3(c) and (d) show optical images of low concentration seeded beads with and without a phosphate precursor. Comparing figures 3(a) and (b) to figure 3(d), the mineralisation of the beads was clearly more homogeneous when seed crystals were incorporated in the alginate solution. As can be seen from table 1, there was an increase in mineral content from the seeded control sample without a phosphate precursor to the beads with seeds and a phosphate precursor. Calculations based on the TGA-data indicated that similar amounts of new mineral were formed in all the samples. This increase can either arise from the growth of the seeds, the nucleation of new crystals or a combination of these.

Optical microscopy indicated the formation of new mineral crystals, as can be seen when comparing figures 3(c)–(d). This was confirmed by SEM images of the surface and cross-sections. Figure 4(a) shows the surface of a medium concentration seeded bead. A large number of crystals can be observed on the surface which were not observed for beads with brushite seeds, but without a phosphate precursor (figure S2 supplementary information (stacks.iop.org/BMM/11/015013/mmedia)). The SEM images from the cross-section of a low concentration seeded bead (figure 5) clearly show mineral crystals (white arrows) situated within the alginate network. These are much smaller in size than the seed crystals, which suggests that they were nucleated during bead fabrication.

Although the mineralisation was homogeneous between the beads, the mineral distribution inside the alginate network was not homogeneous. The mineral formed a denser shell on the outside, and the beads appeared less mineralised towards the centre. This was as expected from previous work with the counter-diffusion method at high supersaturation [14]. The difference in mineral content can be seen in figure 5, where images from the centre and the edge of a cross-section from a bead are shown. There is also an image (figure 5(c)) of a seed crystal showing the difference in size between the seeded crystals and nucleated crystals. Note the difference in size of the seed crystal and surface crystals compared to the crystals within the network (figure 4(a) versus figure 5(a)). The smaller crystals within the network suggested a different growth rate than for the crystals on the surface.

To assess the quality of the XRD analysis, control experiments were performed. Three samples of 33.3% brushite and 66.7% HAp were made individually and characterised. Rietveld analysis resulted in 38.8 ± 0.7 % brushite. For a series of six mixtures ranging from 0 to 100% brushite, the analysis consistently overestimated the amount of brushite by 3.2 ± 2.4 percentage points. These results indicate that the analysis had good precision, albeit with a systematic overestimation. One should note a large increase in the brushite signal between the control and 0 h sample in the XRD spectra shown in figure 6. The control sample contained only seeds (0.1%) and no mineral precursor while the 0 h

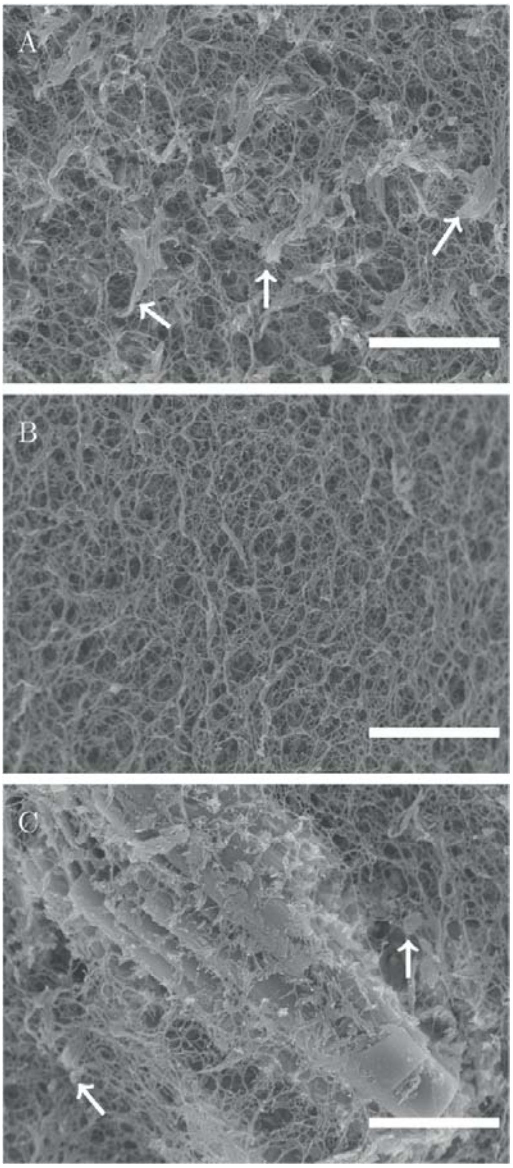

Figure 5. SEM micrographs of the cross-section of a low concentration seeded bead. (A): mineralised network in the outer region, (B): less mineralised network towards the centre. (C): the surroundings of a brushite seed. The white arrows indicate the selected mineral crystals. The scalebar is 1 μm.

sample was mineralised with 300 mM phosphate. There was a large increase in the brushite signal, indicating growth or the formation of new brushite crystals within the sample (also seen in figure 3(d)), at the same time no peaks associated with the HAp phase were present. These peaks appeared only after storage. From the control samples of pure HAp and brushite crystals mixed at a known ratio, the HAp peaks were easily detectable in a mix with 20% HAp and 80% brushite (data not shown). This indicates that a minimal amount HAp was formed initially.

For TGA-modelling, low, medium and high concentrations of seeds corresponding to dry mass percent of 5.3, 35.7 and 73.5, assuming only alginate and CaP remains after drying, were introduced into an alginate solution without phosphate precursor. The TGA of these samples resulted in a calculated dry mass percent of $0 \pm 3, 32 \pm 3$ and 72 ± 3. The expected ideal values are outside the uncertainties of the calculated values for the lower seed concentrations, although they show a similar increase in mass as would be expected, suggesting that the method is reliable although somewhat inaccurate.

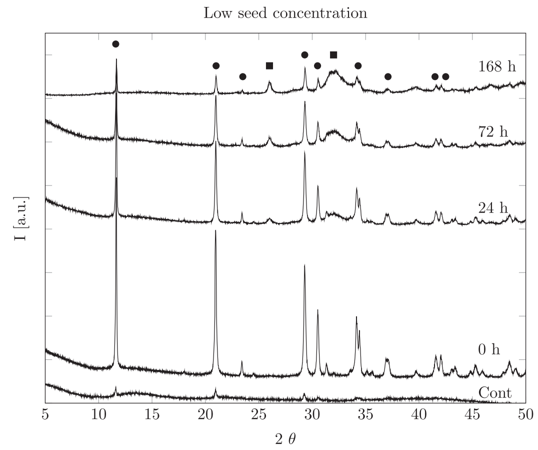

Figure 6. XRD-spectra for the different timepoints for a sample with low concentration brushite seeds with PO_4^{3-}. ● denotes brushite, ■ denotes HAp. The legend numbers indicate the number of hours in SBF and the control sample did not contain PO_4^{3-}-precursor.

For the pure alginate control there was a pronounced weight loss from 650–800 °C related to the decomposition of calcium carbonate into calcium oxide. This behaviour was not observed when the phosphate mineral was precipitated during gelling (see figure S1 and a short discussion given in the supplementary Information (stacks.iop.org/BMM/11/015013/mmedia)). Due to this change in decomposition behaviour and the overestimation of brushite from the Rietveld analysis, the TGA model overestimated the mineral content by about five percentage points dry mass for heavily mineralised samples. The values presented in figure 7 are midpoints between the original model and a model with 3% less brushite and five percentage points less estimated dry mass, with error bars reaching the two extremes.

The seeds introduced into the alginate solution affected the crystallisation conditions for the whole bead, not just in the immediate proximity of the seeds. As can be seen from figure 5, new crystals of brushite were nucleated within the alginate network. This could either result from a change in the conditions of the alginate solution, where a combination of pH and supersaturation favoured the nucleation of brushite or it may have been a secondary nucleation mechanism [47]. Nucleation occurs much more readily when solute crystals are already present in the medium due to a lowered energy barrier, where parent crystals act as catalysts for nucleation [48].

3.3. Bioactivity of alginate composites in SBF

In order to evaluate the potential bioactivity of these CaP mineral–alginate composite materials, the samples were incubated in SBF for 24, 72 and 168 h before they were characterised. Figure 6 shows the XRD results for the low seed concentration sample. The results clearly show a gradual increase of HAp and decrease of the brushite signal, which was observed for all the different seed concentrations. This data is summarised in figure 7, where a clear transformation of initial brushite into HAp is observed over time. An initial decrease in the total mineral content can also be seen. The image in figure 4(a) was taken before incubation in SBF, and the one in (b) was taken after 168 h incubation in SBF. For the composite containing a phosphate precursor there was, before incubation, a large number of brushite crystals on the surface. These appear to have dissolved and reprecipitated as smaller HAp crystals, seen in the inset in figure 4(b). This dissolution is presumably the cause of the decrease in the overall mineral content. These results also show that the lowest seed concentration transformed into HAp earlier than the other samples. As controls, alginate beads with seeds, but no phosphate precursor and alginate beads without seeds or phosphate precursor were also kept in SBF for 168 h. The seeded control showed no conversion into HAp (see figure S2 in supplementary information (stacks.iop.org/BMM/11/015013/mmedia)), while the pure alginate control showed no mineral formation.

This study was performed under static conditions and was therefore not a prediction of actual *in vivo* behaviour [49]. This was done in order to study the transformation behaviour of the mineral in a solution supersaturated with respect to HAp. The dissolution of brushite and the formation of HAp occurred under the same initial conditions in the different sample groups. Comparing these results with the work of Miller *et al* [50], who performed a study of brushite transformation in four different SBF solutions, including a TRIS-buffered solution similiar to the one used in this study, the behaviour is similar except for two main points. In this study, the initial brushite was not completely dissolved or transformed within 168 h. That is probably due to the fact that static conditions were used. A more

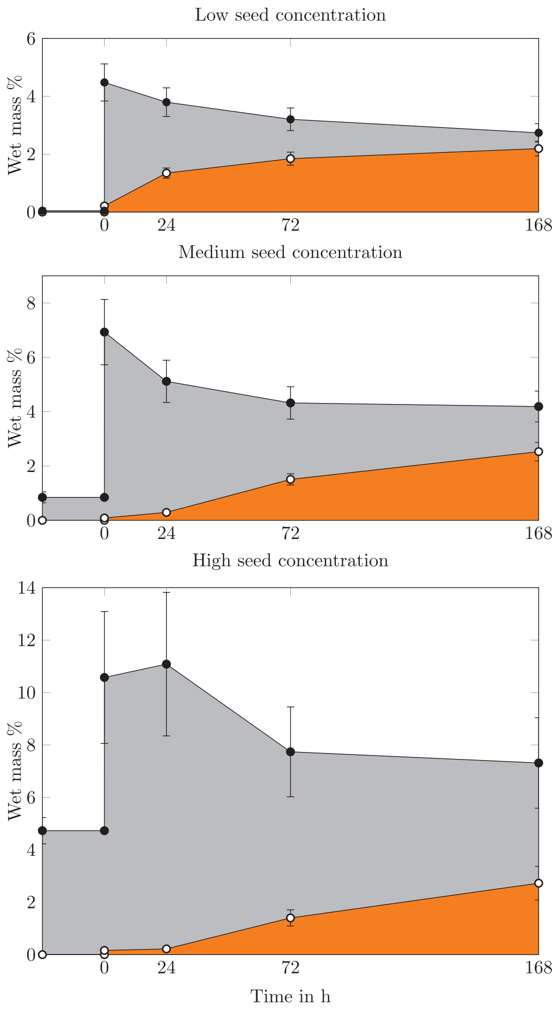

Figure 7. Graphs of the mineral evolution for the three different sample groups as estimated by XRD and TGA (equation (3)). Black points: total mineral content. White points and orange area: HAp content. Grey area: brushite content. The area before the 0 h point shows the amount of mineral introduced as seeds. The *y*-axis is scaled so the figures are directly comparable.

interesting observation is that no OCP was observed in this work. This can be seen in figure 6, where two distinct peaks of OCP (9.45° and 9.77°) are absent.

FTIR analysis, as shown in figure 8, confirmed the formation of brushite for all the samples seeded with brushite, with strong absorbance bands at 986 and 1005 cm^{-1} corresponding to the $\upsilon 2$ P–O symmetrical stretching mode and 1059, 1125 and 1137 cm^{-1} corresponding to the $\upsilon 6$ triply degenerated P–O stretching mode [51]. Changes in the FTIR spectrum occurred for all the samples exposed to SBF, which indicated a change from HPO_4^{2-} to PO_4^{3-}. This can be seen in the disappearance of the $\upsilon 3$ P–O(H) stretching mode at 875 cm^{-1} and the appearance of a strong adsorption at 1025 cm^{-1}. Changes also occurred in the $\upsilon 4$ O–P–O(H) bending mode, which is located at 578 cm^{-1} for brushite and 602 cm^{-1} for HAp [51, 52]. These changes occurred more rapidly for the samples formed with less initial seed material. After 168 h incubation, low concentration seeded composites had almost completely lost the vibrational modes associated with brushite and the resulting spectra resembled poorly crystalline HA; by comparison, the high concentration seeded samples, however, had only partially converted by this time.

The FTIR results largely reflect what was found by XRD analysis, as shown in figure 6, although the loss of intensity of the brushite signal appears earlier for FTIR. This could suggest a loss of protons and the formation of an intermediate amorphous phase, before reprecipitation to HAp. As XRD techniques rely on crystalline samples for a signal, amorphous phases would not be detected by XRD.

The accelerated transformation of brushite into HAp at a decreased seed concentration may derive from

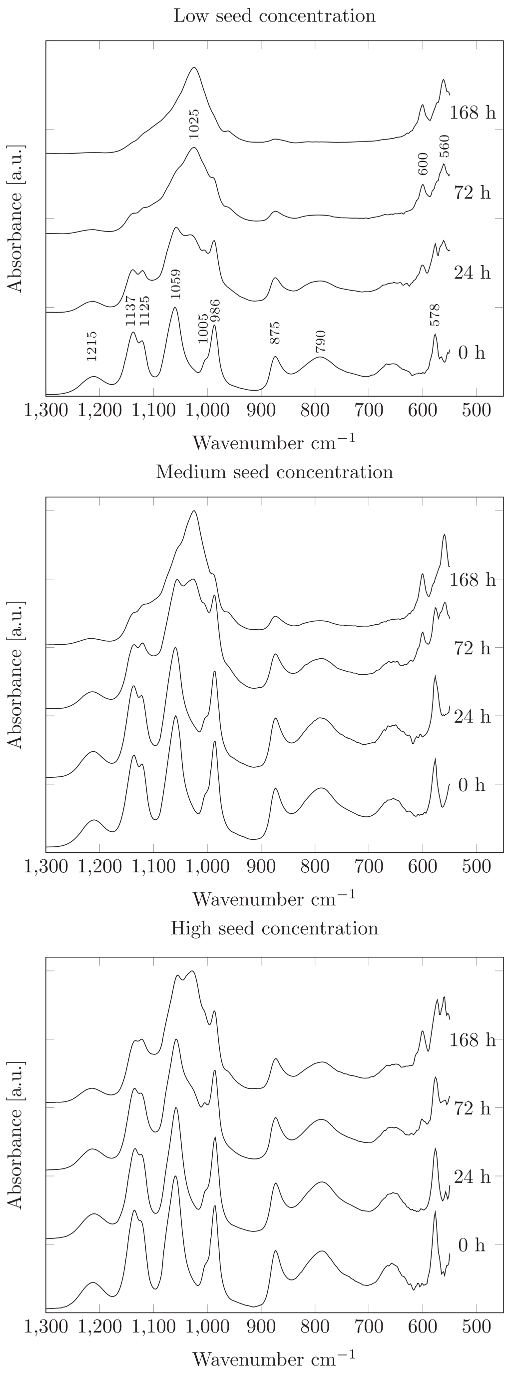

Figure 8. FTIR-spectra of the samples with 0.1%, 1% and 5% seed concentrations following the indicated periods of incubation in SBF.

the smaller size of the newly formed brushite crystals. For higher seed concentrations, a higher amount of the initial phosphate will be consumed in the crystal growth of these seeds. In the cases of higher seed loading, the consumption of ions by growth would likely have caused a decrease in the number of newly formed particles [48]. The smaller crystals had a higher surface area and therefore dissolved more readily. The increased bioactivity of smaller crystals is further corroborated by a control sample in which beads containing a medium seed

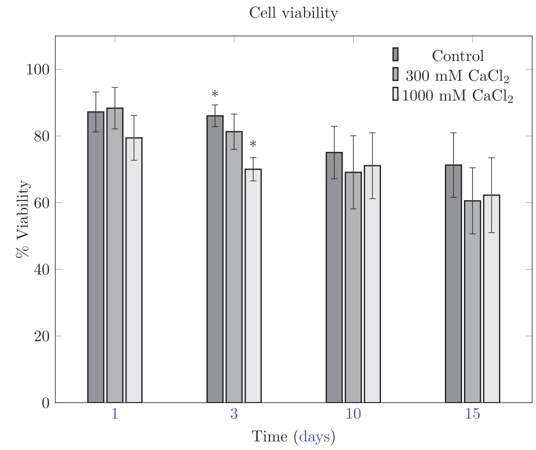

Figure 9. The cell viability in % at four different points in time for two different calcium concentrations compared to a non-mineralised control. The buffer concentrations were 50 mM NaAc for the control and 300 mM $CaCl_2$ sample and 100 mM NaAc for the 1000 mM $CaCl_2$ sample. The * marks the statistical significance ($p < 0.01$).

concentration without a phosphate precursor showed no conversion into HAp after 168 h in SBF solution.

3.4. Cell encapsulation and survival

Alginate hydrogels provide a good matrix for cell encapsulation; we have previously shown that cells can also be encapsulated and survive in alginate microbeads mineralised with HAp [53, 54]. Gryshkov *et al* have also shown that high voltage does not affect cell viability [55]. Previously, the mineralised alginate was synthesised under mild conditions of mineral precursor concentrations and near physiological pH. Here we used more acidic conditions to achieve the desired brushite mineral phase. Since cells cannot survive such a low pH, we tested the viability of pre-osteoblast cells post-encapsulation. Cells were encapsulated in alginate containing 1% brushite seeds, 300 mM PO_4 and gelled in 1 M $CaCl_2$ and 100 mM NaAc at pH 5 or 300 mM $CaCl_2$ and 50 mM NaAc and the viability of encapsulated cells was compared to non-mineralised control beads made with pure alginate and gelled in 50 mM $CaCl_2$ (see figure 9). Surprisingly there was little difference in cell viability 24 h after encapsulation between the controls and the mineralised beads gelled in 300 mM $CaCl_2$ (87.2 ± 6.0% versus 88.3 ± 6.2%). However, a lower viability for the mineralised samples gelled in 1 M $CaCl_2$ was recorded (79.4 ± 6.7%). The cell viability reduced gradually over the 15 d of the culture period for all the samples. After 15 d of culture the cell viability was 60.5 ± 9.9% and 62.2 ± 11.2% for the mineralised samples and 71.2 ± 9.7% for the non-mineralised controls. This gradual reduction was probably due to natural cell death without renewal since the cells appeared to not divide within the alginate matrix as very similar numbers of cells were observed within each bead at each point in time. Since the rate of cell death was very similar for all the samples it would appear that the mineral made in either condition had little influence on cell viability.

4. Conclusions

Building upon our previous work regarding the counter-diffusion synthesis of alginate-calcium phosphate (HAp) composite materials, here we have formulated robust methods to control the phase purity and amount of brushite formed within alginate hydrogels. These new materials may have a significant advantage over HAp containing alginates as bone tissue engineering constructs, since brushite is metastable under physiological conditions and will convert to HAp, as we have demonstrated in simulated body fluid, and may act as a reservoir for essential ions for bone remodelling. Reliable nucleation of the preferred brushite phase inside the alginate network proved more complicated than in aqueous solution in the absence of alginate, where control over the initial parameters of pH and stoichiometry was enough to predict the resulting phase. The incorporation of brushite seed crystals into the alginate solution prior to gelation resulted in improved control and reproducibility of the mineral phase and by adjusting the number of seeds and amount of precursor concentration, the amount of mineral could also be tuned. The bioactivity of the precipitated mineral was shown to be higher than that of mixtures of preformed mineral incorporated in an alginate matrix, likely due to the smaller crystal size of the mineral precipitated within the alginate matrix. Furthermore, we found that our synthesis method was well tolerated by pre-osteoblast cells, and cell viability was similar to the non-mineralised control samples post-encapsulation and survived well over a period of 15 d. This is significant for the intended use of these materials as support structures for cells in the context of bone tissue regeneration.

Acknowledgments

We acknowledge the Research Council of Norway for financial support (FRINATEK project 214607). We thank Dr O Sigurjonsson, Reykjavik University, Iceland for providing us with the cell line used in this study. We also thank Dr B L Strand for fruitful advice regarding alginate.

References

[1] Hollister S J 2009 *Adv. Mater.* **21** 3330–42

[2] Rokstad A M A, Lacík I, de Vos P and Strand B L 2014 *Adv. Drug Deliv. Rev.* **67–8** 111–30

[3] Place E S, Evans N D and Stevens M M 2009 *Nat. Mater.* **8** 457–70

[4] Hoffman A S 2002 *Adv. Drug Deliv. Rev.* **54** 3–12

[5] Dragan E S 2014 *Chem. Eng. J.* **243** 572–90

[6] Amini A R, Laurencin C T and Nukavarapu S P 2012 *Crit. Rev. Biomed. Eng.* **40** 363–408

[7] Drury J L and Mooney D J 2003 *Biomaterials* **24** 4337–51

[8] Kolambkar Y M, Dupont K M, Boerckel J D, Huebsch N, Mooney D J, Hutmacher D W and Guldberg R E 2011 *Biomaterials* **32** 65–74

[9] Cohen J 1998 *J. Bone Joint Surg. Am.* **80** 1554

[10] Rho J Y, Kuhn-Spearing L and Zioupos P 1998 *Med. Eng. Phys.* **20** 92–102

[11] Bernhardt A, Despang F, Lode A, Demmler A, Hanke T and Gelinsky M 2009 *J. Tissue Eng. Regen. Med.* **3** 54–62

[12] Yokoi T, Kawashita M, Kikuta K and Ohtsuki C 2010 *J. Cryst. Growth* **312** 2376–82

[13] Rajkumar M, Meenakshisundaram N and Rajendran V 2011 *Mater. Charact.* **62** 469–79

[14] Xie M, Olderoy M O, Zhang Z, Andreassen J P, Strand B L and Sikorski P 2012 *RSC Adv.* **2** 1457

[15] Li Z, Su Y, Xie B, Wang H, Wen T, He C, Shen H, Wu D and Wang D 2013 *J. Mater. Chem.* B **1** 1755

[16] Luo Y, Lode A, Sonntag F, Nies B and Gelinsky M 2013 *J. Mater. Chem.* B **1** 4088

[17] Zhu C, Bao G and Wang N 2000 *Annu. Rev. Biomed. Eng.* **2** 189–226

[18] Suárez-González D, Barnhart K, Saito E, Vanderby R, Hollister S J and Murphy W L 2010 *J. Biomed. Mater. Res.* A **95** 222–34

[19] Lin H R and Yeh Y J 2004 *J. Biomed. Mater. Res.* B **71** 52–65

[20] Albrektsson T and Johansson C 2001 *Eur. Spine J.* **10** S96–101

[21] Johnsson M S and Nancollas G H 1992 *Crit. Rev. Oral Biol. Med.* **3** 61–82 (PMID: 1730071)

[22] Mirtchi A, Lemaître J and Munting E 1989 *Biomaterials* **10** 634–8

[23] Tamimi F, Sheikh Z and Barralet J 2012 *Acta Biomater.* **8** 474–87

[24] Elliott J 1994 *Structure and Chemistry of the Apatites and Other Calcium Orthophosphates* (Amsterdam: Elsevier) (doi: 10.1016/B978-0-444-81582-8.50001-8)

[25] Apelt D, Theiss F, El-Warrak A, Zlinszky K, Bettschart-Wolfisberger R, Bohner M, Matter S, Auer J and von Rechenberg B 2004 *Biomaterials* **25** 1439–51

[26] Klammert U, Ignatius A, Wolfram U, Reuther T and Gbureck U 2011 *Acta Biomater.* **7** 3469–75

[27] Kanter B, Geffers M, Ignatius A and Gbureck U 2014 *Acta Biomater.* **10** 3279–87

[28] Habibovic P, Gbureck U, Doillon C, Bassett D, Vanblitterswijk C and Barralet J 2008 *Biomaterials* **29** 944–53

[29] Gbureck U, Hölzel T, Klammert U, Würzler K, Müller F A and Barralet J E 2007 *Adv. Funct. Mater.* **17** 3940–5

[30] Nanzyo M, Shibata Y and Wada N 2002 *Soil Sci. Plant Nutrition* **48** 847–53

[31] Koburger S, Bannerman A, Grover L M, Müller F A, Bowen J and Paxton J Z 2014 *Biomater. Sci.* **2** 41

[32] Amer W, Abdelouahdi K, Ramananarivo H R, Fihri A, El Achaby M, Zahouily M, Barakat A, Djessas K, Clark J and Solhy A 2014 *Mater. Sci. Eng.* C **35** 341–6

[33] Kelton K 1991 *Solid State Phys.* **45** 75–177

[34] Kashchiev D and van Rosmalen G M 2003 *Cryst. Res. Technol.* **38** 555–74

[35] Boistelle R and Lopez-Valero I 1990 *J. Cryst. Growth* **102** 609–17

[36] Wuthier R E, Rice I G S, Wallace J E B, Weaver R L, Legeros R Z and Eanes E D 1985 *Calcif. Tissue Int.* **37** 401–10

[37] Abbona F, Madsen H and Boistelle R 1986 *J. Cryst. Growth* **74** 581–90

[38] Abbona F, Christensson F, Angela M and Madsen H 1993 *J. Cryst. Growth* **131** 331–46

[39] Kokubo T and Takadama H 2006 *Biomaterials* **27** 2907–15

[40] Bohner M and Lemaitre J 2009 *Biomaterials* **30** 2175–9

[41] Rohanová D, Boccaccini A R, Yunos D M, Horkavcová D, Bezovská I and Helebrant A 2011 *Acta Biomater.* **7** 2623–30

[42] Mandel S and Tas A C 2010 *Mater. Sci. Eng.* C **30** 245–54

[43] Xie M, Olderøy M O, Andreassen J P, Selbach S M, Strand B L and Sikorski P 2010 *Acta Biomater.* **6** 3665–75

[44] Draget K I, Østgaard K and Smidsrød O 1989 *Appl. Microbiology Biotechnol.* **31** 79–83

[45] Haug A 1964 *Composition and Properties of Alginate* (Trondheim: N.T.H. Trykk)

[46] Strand B L, Gåserød O, Kulseng B, Espevik T and Skjåk Bræk G 2002 *J. Microencap.* **19** 615–30

[47] Garside J 1985 *Chem. Eng. Sci.* **40** 3–26

[48] Frawley P J, Mitchell N A, Ó'Ciardhá C T and Hutton K W 2012 *Chem. Eng. Sci.* **75** 183–97

[49] Rámila A and Vallet-Reg M 2001 *Biomaterials* **22** 2301–06

[50] Miller M A, Kendall M R, Jain M K, Larson P R, Madden A S and Tas A C 2012 *J. Am. Ceram. Soc.* **95** 2178–88

[51] Casciani F and Condrate R A 1979 *Spectrosc. Lett.* **12** 699–713

[52] Rehman I and Bonfield W 1997 *J. Mater. Sci.: Mater. Med.* **8** 1–4

[53] Westhrin M, Xie M, Olderøy M O, Sikorski P, Strand B L and Standal T 2015 *Plos One* **10** e0120374

[54] Olderøy M, Xie M, Westhrin M, Andreassen J P, Zhang Z, Strand B L, Standal T and Sikorski P 2012 *Eur. Cells Mater.* **23** 53

[55] Gryshkov O, Pogozhykh D, Zernetsch H, Hofmann N, Mueller T and Glasmacher B 2014 *Mater. Sci. Eng.* C **36** 77–83

Supplementary Information: Controlled mineralisation and recrystallisation of brushite within alginate hydrogels

Sindre H. Bjørnøy[1], **David Bassett**[1], **Seniz Ucar**[2], **Jens-Petter Andreassen**[2], **Pawel Sikorski**[1]

[1] Department of Physics, Norwegian University of Science and Technology, Trondheim, Norway
[2] Department of Chemical Engineering, Norwegian University of Science and Technology, Norway

E-mail: `pawel.sikorski@ntnu.no`

TGA and XRD analysis

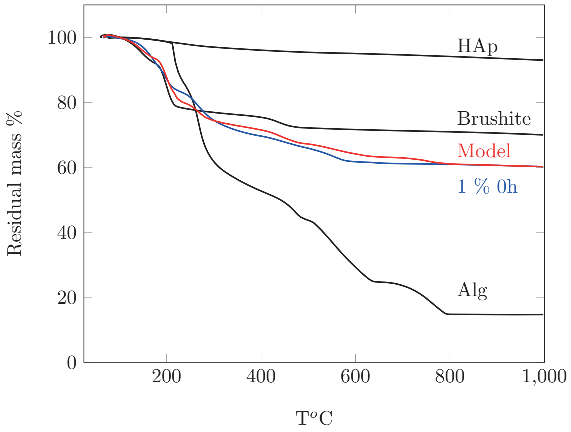

Figure S1 Illustration of the method used to determine mineral amount from TGA-data. Black curves: HAp, DCPD and alginate. Blue curve: 1 % seeds. Red curve: Model with f_D=0.82 and $f_H = 0$.

Figure S1 shows the principle of the method used to determine the mineral amount. The curves for control samples of pure alginate, pure brushite and pure HAp are added and fitted to the experimental curve. For samples with more than one mineral phase, the relative amount of each phase was found by Rietveld analysis. ICDD standards used for Rietveld analysis: Brushite: PDF# 04-013-3344[1] and HAp: PDF# 00-055-0592[2].

The reason for the discrepancy between the model and the experimental data in the range of circa 500-800^{o}C is not known. The pure alginate sample has a pronounced weight loss from 650-800^{o}C due to the decomposition of $CaCO_3$ into CaO. There are two possible explanations why this is not observed in the experiments. It could be that the presence of mineral influences the reaction where Ca reacts with the carbon from the burning alginate and prevents the formation of $CaCO_3$. Another explanation could be that the presence of mineral affects the temperature at which the $CaCO_3$ decomposes into CaO. Newkirk and Aliferis has shown that the temperature at which the decomposition of $NaCO_3$ occur can be altered due to its chemical environment.[3] They observed that simply by changing the cruicible material which the sample was kept in the decomposition temperature changed. Also by mixing silica grains with the $NaCO_3$, the decomposition temperature was reduced and this effect was increased for smaller grains providing a large surface area. We speculate that a similar effect might be present in this case, and the mineral present in our sample provides a large surface area due to the small crystal size. As the model is based on adding a fraction of the pure alginate curve and fractions of the mineral curves, it does not take into account changes in the thermal behaviour of the different compounds. We therefore chose to fit our model to match the final weight of the experimental sample rather than minimize the discrepancy between the curves.

Bioactivity

Figure S2 shows that seeded beads without phosphate precursor did not transform after 1 week in SBF.

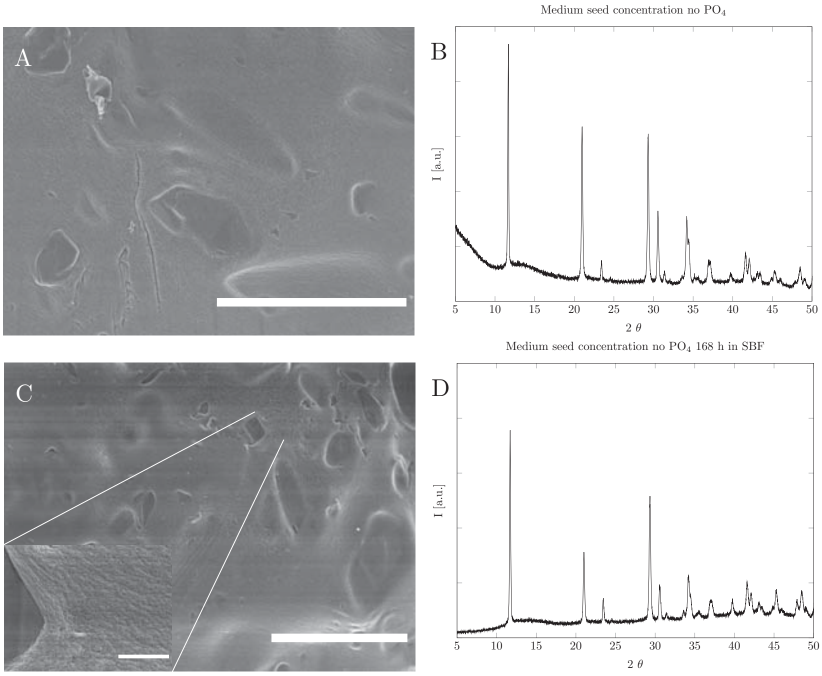

Figure S2 SEM micrograph of the surface of an alginate microbead (A) and a corresponding XRD-spectra (B) of a sample made with medium seed concentration and without phosphate precursor. **C** and **D:** data for the same samples collected after 168h incubation in SBF. No mineral formation is visible on the surface of the bead. The XRD-spectra show no indication of HAp formation. Scale bars are 30 µm and 2 µm for inset.

References

[1] Curry N A and Jones D W 1971 *J. Chem. Soc. A Inorganic, Phys. Theor.* 3725 ISSN 0022-4944 URL `http://pubs.rsc.org/en/content/articlehtml/1971/j1/j19710003725`

[2] Tas A C 2012 *Powder Diffr.* **16** 102–106 ISSN 0885-7156 URL `http://journals.cambridge.org/abstract_S0885715600005765`

[3] Newkirk A E and Aliferis I 1958 *Analytical Chemistry* **30** 982–984 ISSN 0003-2700 URL `http://dx.doi.org/10.1021/ac60137a031`

Acta Biomaterialia 44 (2016) 254–266

Contents lists available at ScienceDirect

Acta Biomaterialia

journal homepage: www.elsevier.com/locate/actabiomat

Full length article

A correlative spatiotemporal microscale study of calcium phosphate formation and transformation within an alginate hydrogel matrix

Sindre H. Bjørnøy [a], David C. Bassett [a], Seniz Ucar [b], Berit L. Strand [c], Jens-Petter Andreassen [b], Pawel Sikorski [a,*]

[a] Department of Physics, NTNU, Norwegian University of Science and Technology, 7491 Trondheim, Norway
[b] Department of Chemical Engineering, NTNU, Norwegian University of Science and Technology, 7491 Trondheim, Norway
[c] Department of Biotechnology, NTNU, Norwegian University of Science and Technology, 7491 Trondheim, Norway

ARTICLE INFO

Article history:
Received 28 May 2016
Received in revised form 16 August 2016
Accepted 19 August 2016
Available online 24 August 2016

Keywords:
Alginate
Hydrogel
Raman spectroscopy
Calcium phosphate

ABSTRACT

The modification of soft hydrogels with hard inorganic components is a method used to form composite materials with application in non-load-bearing bone tissue engineering. The inclusion of an inorganic component may provide mechanical enhancement, introduce osteoconductive or osteoinductive properties, or change other aspects of interactions between native or implanted cells and the material. A thorough understanding of the interactions between such components is needed to improve the rational design of such biomaterials. To achieve this goal, model systems which could allow study of the formation and transformation of mineral phases within a hydrogel network with a range of experimental methods and high spatial and time resolution are needed. Here, we report a detailed investigation of the formation and transformation process of calcium phosphate mineral within an alginate hydrogel matrix. A combination of optical microscopy, confocal Raman microspectroscopy and electron microscopy was used to investigate the spatial distribution, morphology and crystal phase of the calcium phosphate mineral, as well as to study transformation of the mineral phases during the hydrogel mineralization process and upon incubation in a simulated body fluid. It was found, that under the conditions used in this work, mineral initially formed as a metastable amorphous calcium phosphate phase (ACP). The ACP particles had a distinctive spherical morphology and transformed within minutes into brushite in the presence of brushite seed crystals or into octacalcium phosphate, when no seeds were present in the hydrogel matrix. Incubation of brushite–alginate composites in simulated body fluid resulted in formation of hydroxyapatite. The characterization strategy presented here allows for non-destructive, *in situ* observation of mineralization processes in optically transparent hydrogels with little to no sample preparation.

Statement of Significance

The precipitation and transformations of calcium phosphates (CaP) is a complex process, where both formation kinetics and the stability of different mineral phases control the outcome. This situation is even more complex if CaP is precipitated in a hydrogel matrix, where one can expect the organic matrix to modulate crystallization by introducing supersaturation gradients or changing the nucleation and growth kinetics of crystals. In this study we apply a range of characterization techniques to study the mineral formation and transformations of CaP within an alginate matrix with spatiotemporal resolution. It demonstrates how a detailed investigation of the mineral precipitation and transformations can aid in the future rational design of hydrogel-based materials for bone tissue engineering and studies of biomineralization processes.

1. Introduction

Hydrogels combined with inorganic materials are attractive candidates in the search for an injectable composite material for hard tissue regeneration. The hydrogel can be used as a carrier

---

* Corresponding author.
E-mail addresses: sindre.bjornoy@ntnu.no (S.H. Bjørnøy), david.bassett@ntnu.no (D.C. Bassett), seniz.ucar@ntnu.no (S. Ucar), berit.l.strand@ntnu.no (B.L. Strand), jens-petter.andreassen@ntnu.no (J.-P. Andreassen), pawel.sikorski@ntnu.no (P. Sikorski).

http://dx.doi.org/10.1016/j.actbio.2016.08.041
1742-7061/

material for cells, drugs or other bioactive molecules and also act as a scaffold for tissue formation [1]. The inorganic phase provides nucleation sites and the necessary ions for *in vivo* bone formation and also modifies the mechanical properties of the resulting composite material [2,3]. In cases where calcium phosphate (CaP) has been used as the inorganic phase, hydroxyapatite (HAp) has long been the material of choice due to its similarity to the mineral found in bone [4–6]. However, HAp is thermodynamically stable under *in vivo* conditions, and therefore will not readily dissolve and provide ions for bone formation. Therefore, in recent years, less stable CaP phases such as Octacalcium phosphate (OCP) and brushite (the abbreviation DCPD has been used in sample names and figure legends to indicate brushite) have attracted increasing interest in this regard [7]. These acidic phases are often present in the early stages of precipitation *in vitro*, even at mildly alkaline conditions, as they tend to nucleate more easily than HAp [8]. In the more complex *in vivo* environment, evidence of such precursors has been elusive. Whether this stems from the influence of templating molecules or is due to dehydration or other artifacts during sample preparation is not entirely clear. Peptide motifs from dentin matrix proteins have been shown to accelerate the formation of crystalline HAp *in vitro*, which supports the first scenario [9]. On the other hand, using *in situ* characterization techniques or minimal sample preparation there have been reports of several non-apatitic precursor phases during early mineralization, including amorphous phosphate (ACP) and OCP [10]. More recently, ACP has been shown to act as a precursor to HAp during osteogenesis within a ceramic tissue engineering scaffold loaded with bone marrow mesenchymal stem cells and implanted in a murine model [11]. Also, cellularly derived ACP nanospheres have been shown to transform into crystalline platelets of HA upon contact with the collagen matrix of continuously mineralizing fin bones of zebrafish [12]. Similar mineralization pathways have also been suggested for other types of biominerals, such as calcium carbonate found in sea urchins and mollusks [13].

Our group focuses on the formation of alginate–CaP composite materials by counter-diffusion in which mineral is precipitated simultaneously with hydrogel crosslinking. This approach allows control over the resulting CaP phase and has recently been investigated in particular for the formation of HAp and brushite [14,15]. In order to produce phase pure alginate–brushite composites, seed crystals were used to initiate nucleation, since conditions which normally produce brushite when precipitated in solution, resulted in HAp inside the gel network, irrespective of the precursor concentrations and initial pH [15]. Further investigation into this phenomena revealed an inhibitory effect of alginate on the growth and nucleation of brushite in the presence of small amounts of alginate [16].

A thorough understanding of CaP formation and transformation processes is essential for both fundamental studies of biomineralization and for the development of synthetic hard tissue engineering scaffold biomaterials. CaP mineralization, although dependent on reaction conditions such as pH and ionic strength, is often dictated by kinetics rather than thermodynamics. In addition, the crystallization process may be influenced by both (bio) organic molecules and spatial confinement [17–25]. This represents a particular scientific challenge, since it is difficult to precisely monitor mineralization processes *in situ*. We have recently presented a new approach that enables the correlative application of a range of characterization techniques to closely monitor crystallization processes within hydrogels [26]. Here we apply this toolbox to study the formation and transformation of CaP–mineral within an alginate matrix at low pH (approx. pH 5) and the influence of brushite seeds dispersed in the matrix under otherwise identical conditions. The non-destructive characterization techniques were also used to monitor the transformation behavior of minerals within alginate hydrogels during incubation in simulated body fluid (SBF), providing a means to measure the same samples over several time points. This resulted in a thorough spatiotemporal description of the gel and mineral formation, maturation and transformation pathways at the microscale in unprecedented detail.

2. Experimental

2.1. Flow cell samples

De-ionized water (DIW, with a resistivity of 10–15 MΩcm) was used in all of the experiments. Alginate solutions were prepared with 1.8 mass% alginate (LF200S, $M_w = 2.74 \times 10^5$ g mol^{-1}, $F_G = 0.68$, FMC Biopolymer, Sandvika, Norway), 0.9 mass% NaCl (27810.295, VWR, Philadelphia, PA, USA) and a mixture of $Na_2HPO_4 \cdot 7H_2O$ (206515000, Thermo Fisher Scientific, Oslo, Norway) and $NaH_2PO_4 \cdot 2H_2O$ (04269, Sigma Aldrich, Oslo, Norway) to a phosphate concentration of 100 mM or 300 mM at pH 7. A 1.5 μL droplet of alginate solution was placed between two glass slides separated by 140 μm in order to produce a disc. A 1 M $CaCl_2$ (C8106, Sigma Aldrich, Oslo, Norway) solution buffered either at pH 5 with sodium acetate (NaAc) (A6283, Sigma Aldrich, Oslo, Norway) or at pH 7 with tris(hydroxymethyl) aminomethane (TRIS) (252859, Sigma Aldrich, Oslo, Norway) was introduced into the flow cell initiating the gelling and mineralization process as the calcium diffused into the disc. The reaction occurs in a large excess of calcium ions to ensure proper gelation of the alginate. SBF was made according to Kokubo *et al.* [27]. Samples were placed in 50 mL of SBF and the solution was replenished with fresh SBF every 24 h.

2.2. Preparation of crystals for seeding and Raman analysis

Brushite seed crystals were made by mixing 500 mL of 0.4 M $Ca(NO_3)_2 \cdot 4H_2O$ (31218, Sigma Aldrich, Oslo, Norway) and 500 mL of 0.4 M KH_2PO_4 (P3786, Sigma Aldrich, Oslo, Norway) and 26 mM KOH (221473, Sigma Aldrich, Oslo, Norway). The resulting precipitate was aged for 2 h before they were washed and filtered with DIW and ethanol. The size of the crystals was measured using a Coulter Counter Multisizer 3 (Beckman Coulter, CA, USA). The seed crystals were ground using an agate pestle and mortar in order to disrupt any aggregation and 0.2 mass% were added to alginate solutions under stirring. The solutions were left stirring for 1 h to ensure uniform distribution of the seed crystals.

OCP and HAp were made according to methods described by Elliott [28]. Briefly, OCP was made by hydrolysis of brushite crystals in 0.5 M NaAc ($pH > 9$) at 37 °C for 1 week. The solution was replenished daily. HAp was made by slowly dripping a solution with 640 mM $Ca(NO_3)_2$ into an equal volume of 250 mM $(NH_4)_2HPO_4$ (215996, Sigma Aldrich, Oslo, Norway) under rapid stirring. Both solutions had an initial pH above 10 and NH_4OH (221228 Sigma Aldrich, Oslo, Norway) was used to maintain pH above 10. The resulting precipitate was aged over night.

The resulting crystals were in all cases washed and filtered using DIW and ethanol and crystalline phase purity was measured using powder XRD (D8 Advance DaVinci, Bruker AXS GmbH, Karlsruhe, Germany) prior to Raman measurements, see Figs. S1–S3 in the Supplementary Information.

2.3. Characterization

Dark-field and phase contrast images of alginate samples with varying phosphate content, see Table 1, were recorded using an optical microscope (Eclipse TS100, Nikon Instruments Europe BV, Amsterdam, Netherlands) through a 4× lens at 4 FPS for the first

Table 1
An overview of the composition of the different alginate samples studied. Alginate concentration was in all cases 1.8 mass%. AlgP0 and AlgP0DCPD were not buffered.

Sample	Phosphate conc. [mM]	Initial pH	DCPD seed conc. [mass %]
AlgP0	0	~7	–
AlgP100	100	7	–
AlgP300	300	7	–
AlgP0DCPD	0	~7	0.2
AlgP300DCPD	300	7	0.2

15 s and at 0.2 FPS during the remaining gelation process. The images were analyzed with MATLAB (2014b) in order to extract the velocity at which the gel front moved, briefly a series of images of the moving gel front was recorded and the position of the front was fitted with an ellipse. A gel front radius was calculated by averaging the two ellipse axis (in all cases the shape was close to circular) and the position of the front was plotted as a function of time. The approximately linear region of the resulting plot was used to calculate the gel front velocity, cf. Fig. S4. Further details of the analysis are given elsewhere [26].

Selected samples were critical point dried (Emitech K850 critical point dryer, Quorum Technologies Ltd, East Sussex, England), mounted on aluminum stubs using carbon tape and coated with 3–5 nm platinum/palladium (Cressington 208 HR, Cressington Scientific Instruments Ltd, Watford, England) before SEM-analysis (S-5500, Hitachi, Tokyo, Japan).

Raman microspectroscopy (InVia Reflex, Renishaw, Gloucestershire, England) was performed by making 120 measurements (integration time 1 s, 30 accumulations) at one spot directly after the gelling solution had been introduced. Line scans consisting of recorded spectra (integration time 1 s, 30 accumulations) from 50 points along the radius of mineralized alginate discs were also collected 1 h and 24 h after the gelling solution had been introduced. All measurements were performed with a 535 nm laser through a 10× lens. Confocality was reduced at the expense of spatial resolution in order to obtain an average signal from the whole thickness of the disc.

By adding 20 μM R6G-EDA (rhodamine 6G modified with ethylenediamine according to published methods [29,30]) and 5 μM sulforhodamine 101 (SR101, S7635, Sigma Aldrich, Oslo, Norway) pH measurements were performed using confocal laser scanning microscopy (TCS SP5, Leica Microsystems, Wetzlar, Germany). Images were recorded at 0.1 FPS for a duration of 33 min. Details of the measurements settings and analysis are presented elsewhere [26]. Briefly, the intensity ratio between a pH-sensitive and pH-insensitive dye was compared to a standard curve made using the same measurement conditions in order to calculate the pH in each pixel of the images.

3. Results and discussion

Previously we have shown that the velocity of the alginate gel front was limited by inwards diffusion of Ca^{2+} [26]. Tanaka *et al.* have shown that the diffusion of molecules with a molecular weight lower than 2×10^4 is the same in water, as it is in gels made with 2% or 4% alginate, indicating that viscosity does not affect the diffusion of small molecules in this system [31]. With the addition of phosphate to this system, there is a simultaneous consumption of calcium ions due to precipitation of a mineral phase within the gel network. Therefore it follows that the gel front velocity is likely to reduce. To investigate this experimentally we studied the gel front evolution in our flow cell with additional phosphate present in the hydrogel phase using optical microscopy. Fig. 1a–c shows a typical phosphate containing sample during the gelation process. Due to a difference in refractive indexes between gelled and ungelled alginate, the position of the gel front was clearly visible in phase contrast microscopy, see Fig. 1a. Using dark field microscopy, the mineralized gel was clearly visible due to the fact that it scattered more of the incoming illumination, seen in Fig. 1b and c. Fig. 1d shows a bar plot of the gel front velocities recorded for the different samples.

As expected, the gel front velocity was greatest for phosphate free samples and decreased with increasing phosphate concentration. Table 1 provides a summary of the conditions used for the different samples. An interesting characteristic of the mineralization process was observed in dark field microscopy: the leading edge of the mineralization zone contained a narrow region which scattered more light, indicated by asterisks in Fig. 1b and c. This region, appearing as a brighter band, moved inwards immediately behind the gel front as the mineralization progressed and was formed at the same time or just after influx of the Ca-ions and the resulting gelling of alginate (cf. Fig. 1b and c). This change of position indicated that the origin of this region was a metastable phase which transformed or dissolved after a relatively short time (~120 s as estimated from the images). The nature of this phase is investigated in detail below. In this geometry, supersaturation with respect to CaP was highest close to the gel front and would be quickly reduced once the mineral phase had formed. It is therefore likely that this transient zone was located close to the region with the highest supersaturation, and contained a metastable form of CaP.

We have previously shown the potent effect of brushite seed crystals on phase selection within alginate hydrogels and with the added benefit of our spatiotemporal characterization toolbox we further investigate this effect here [15]. It has previously been shown that alginate, and especially the guluronate residues (G-blocks) which have a high affinity for calcium, have an inhibitory effect on the nucleation (and growth) of calcium phosphate crystals [16]. Chelation of calcium ions is a likely explanation for the nucleation inhibition, while non-specific interactions between alginate and crystals and specific interactions between G-blocks and active growth sites are probable causes of growth inhibition. Considering this inhibitory effect of alginate on the nucleation (and growth) of calcium phosphate, as observed by us and others, we expected that the addition of seed crystals would increase the Ca^{2+} consumption rate, as it would not rely on nucleation of new crystals [16,32]. We tested this hypothesis by incorporating 0.2 mass% brushite seed crystals with an average size of 30 μm in alginate containing 300 mM phosphate precursor and monitored gel front velocity and crystal growth. For these samples, one might expect the gel front velocity to be reduced to a larger extent compared to samples without seed crystals, due to an increased consumption of Ca^{2+}. However, no significant difference was observed experimentally (Fig. 1d). A transient zone similar to the one observed for unseeded samples was also observed close to the mineral front for seeded samples, see Fig. 2. These observations indicate that a similar process was responsible for the initial reduction in the calcium and phosphate concentrations for both seeded and unseeded samples. For brevity, we term the three observed regions ungelled, transient and gelled; however, note that the transient zone has also been crosslinked and is to be considered a gelled region. Details of this transformation process focusing on phase composition, transformation kinetics and morphology of the formed mineral phases are described below.

To characterize the phase composition of the mineral formed in the experiments described above in real time, we used confocal Raman micro-spectroscopy (CRM) since this technique allows both spatial and temporal resolution of small sample volumes (typical sample volume was 1.5 μL). In addition CRM can be used, contrary

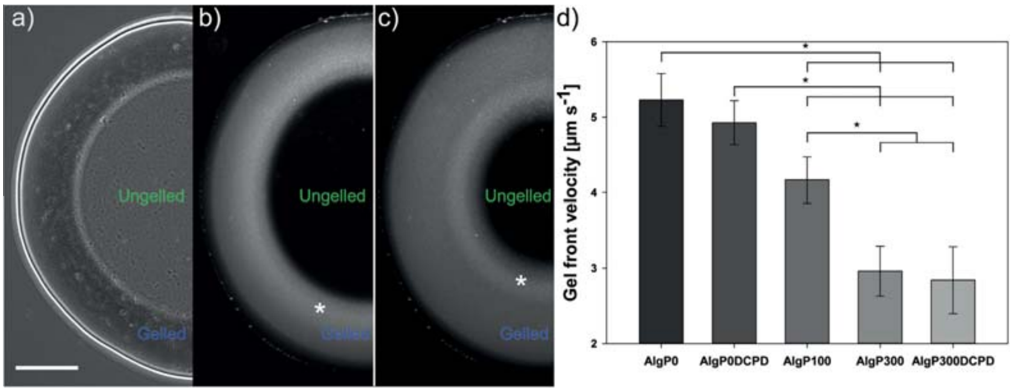

Fig. 1. (a) A phase contrast image of a partially gelled AlgP300 sample. The gel front is clearly visible between the gelled and the ungelled part. Scalebar: 500 µm. (b) A dark field micrograph showing the gelation and mineralization of an alginate disc after 150 s. (c) The same sample as in b after 300 s. A moving bright band of mineral is marked by an asterisk in b and c. (d) Bar plot of the gel front velocity as a function of phosphate concentration and the presence of brushite seeds. The asterisk marks statistically different values (One way ANOVA, $p < 0.05$).

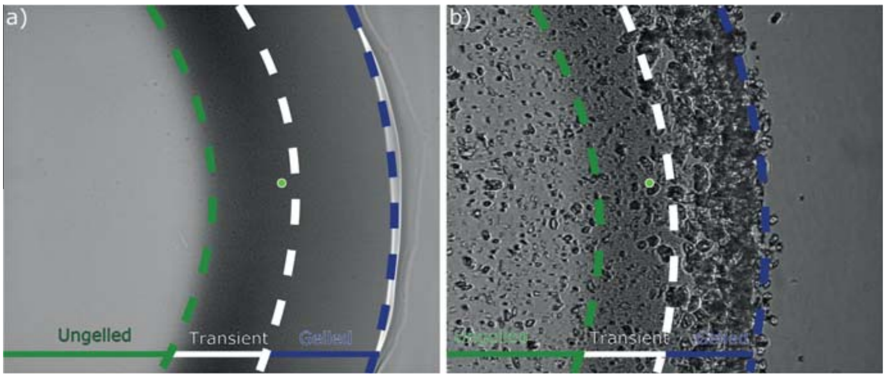

Fig. 2. Phase contrast microscopy images showing an AlgP300 (a) and an AlgP300DCPD (b) sample during the gelling process. Three regions are marked in the images: the ungelled region shown in green, the transient zone shown in white, and a gelled region shown in blue. The marker indicates the approximate position of the CRM time scan. The frame width of the images is 845 µm. (For interpretation of the references to colour in this figure legend, the reader is referred to the web version of this article.)

to IR-spectroscopy, to monitor hydrogels in their native hydrated state [33]. Initially, Raman spectra were collected from an area approximately 200 µm from the edge of the sample, as indicated in Fig. 2. 120 scans were recorded consecutively for one hour from the same location following the introduction of Ca^{2+} to allow observation of mineral evolution. Fig. 3a shows Raman spectra of an AlgP300 sample at the indicated time points. These spectra have not been normalized, and are scaled according to the measurement time. The spectrum denoted 0 s was recorded from the alginate droplet before the calcium solution had been introduced and contains four main peaks: the three peaks with highest intensity originate from the phosphate ions in the solution. The peaks at 879 cm^{-1} and 1078 cm^{-1} were assigned to symmetric stretching of P–$(OH)_2$ and P–O_2 respectively for $H_2PO_4^-$, while the peak at 990 cm^{-1} was due to symmetric stretching of P–O_3 in HPO_4^{2-} [34]. The weaker P–OH stretching from this ion was found by curve fitting at 852 cm^{-1} overlapping with the 879 cm^{-1} peak from $H_2PO_4^-$. The weak peak located around 810–816 cm^{-1} was assigned to the alginate polymer [35]. Alginate also has a peak located at 890–892 cm^{-1}, which overlaps with one of the $H_2PO_4^-$ peaks and could not be resolved. As calcium was introduced the HPO_4^{2-} peak intensity was quickly reduced, while the $H_2PO_4^-$ peak intensities were gradually reduced. We note that the transient zone did not give any strong Raman signal. However, a weak and broad peak located at 955 cm^{-1} which, over time, split into two overlapping peaks located at 946 cm^{-1} and 957 cm^{-1} was observed. The intensity of the 946 cm^{-1} peak was reduced while the 957 cm^{-1} peak increased in intensity, became sharper and shifted towards higher wavenumbers as time progressed, as shown in Fig. 3a. The appearance and reduction in intensity of this broad peak corresponded to the appearance and disappearance of the transient region observed in optical microscopy. Peak sharpening is indicative of increased crystallinity and the observed peak shift is indicative of mineral maturation similar to that which was previously observed in a bone tissue model [10]. Different literature sources report the Raman signal from amorphous calcium phosphate ACP to be a broad peak centered at 945–955 cm^{-1} [9,10,36]. Although the signal was weak, this was interpreted as an indication that the mineral in the transient region was amorphous. After 15 min a peak appeared around 928–935 which was assigned to the C–C stretching of acetate, which was due to the buffer diffusing into the hydrogel [37]. The same measurements were repeated on a similar sample infused with a TRIS-buffered Ca^{2+} solution at pH 7. The same weak ACP peak at 955 cm^{-1} was observed here without the

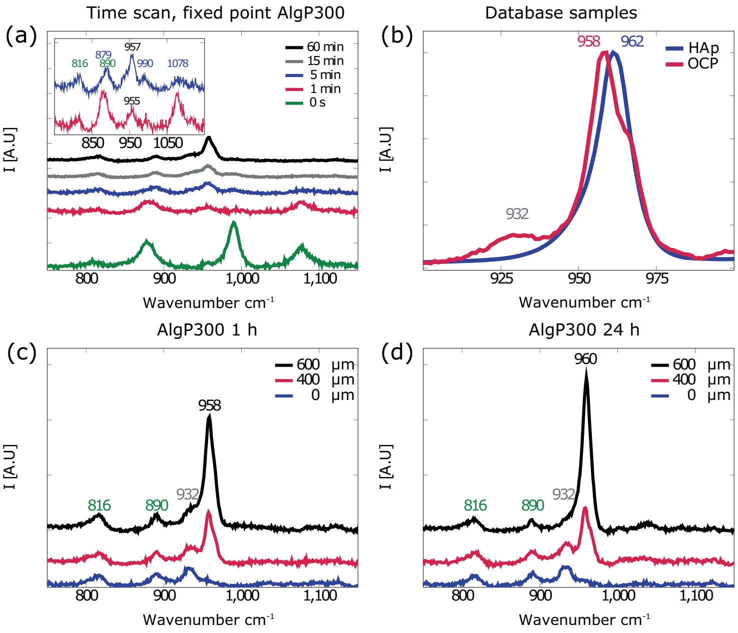

Fig. 3. (a) Raman spectra of an AlgP300 sample from a single spot at 5 time points. The inset shows the 1 min and 5 min spectra with a reduced *y*-axis range in order to accentuate the peaks. (b) Raman spectra from the main peak of pure phase samples of HAp, and OCP prepared in solution. Note the difference in peak shape between HAp and OCP. (c) and (d) Raman spectra from a line scan of an AlgP300 sample after 1 and 24 h respectively. The spectra names refer to distance from the center of the discs. The numbers in the graph specify peak positions in cm^{-1}.

interfering acetate peak at 932 cm^{-1}, see Supplementary Information Fig. S5b.

After 1 h, a line scan consisting of 50 points from the edge of the disc towards the center was recorded in order to investigate any spatial differences along the radius. The line scan was repeated over the same area after 24 h in the mother liquor. Fig. 3c and d shows Raman spectra recorded from three such points in an AlgP300 sample after 1 h and 24 h, respectively. The position of the spectra are given as a distance from the center. The phosphate in CaP-phases such as brushite, HA and tricalcium phosphate (TCP) have easily distinguishable Raman spectra [38]. However, it is more challenging to differentiate between HA and OCP. Crane *et al*. used a weak peak, arising from v_1 HPO_4 stretching, positioned around 1010 cm^{-1} to identify OCP [10]. As a result of the experimental design in this work, the 1010 cm^{-1} peak was almost at the same level as the background noise (cf. Supplementary Information Fig. S5a), and was not deemed suitable. Instead the peak shape and position of the main phosphate peak was used to determine the dominating phase. Fowler *et al*. have thoroughly assigned the different Raman bands of OCP and show a main peak situated around 956–959 cm^{-1} with a strong shoulder at 966–967 cm^{-1}, both arising from v_1 PO_4 stretching [39]. The v_1 PO_4 stretching of HAp is reported to be a single peak located at 959–962 cm^{-1} with a weak and broad shoulder at around 950 cm^{-1} leading to an asymmetric peak shape of the main phosphate peak of HAp [40]. The difference in peak shape between OCP and HAp are clearly visible in the spectra of pure phase samples shown in Fig. 3b. Therefore, fitting of the recorded spectra in a region between 920 and 980 cm^{-1} was used to determine the dominating crystal phase, shown in red (OCP) and blue (HAp) in Fig. 4. Fig. 4a and b shows micrographs of an AlgP300 sample after 1 h and 24 h incubation in the mother liquor. The line scans from the sample are visualized in Fig. 4c and d, where the intensity of the peak located at 958 cm^{-1} (the main phosphate peak in the spectra arising from v_1 PO_4 stretching [38]) has been plotted as a function of distance from the center for the two samples. The intensity at 987 cm^{-1}, corresponding to the main peak of brushite has also been plotted. The lines mark the position of the CRM line scans and the numbers refer to the position of SEM-images shown in Fig. 7. It was found that the mineral present in the hydrogel after 1 h was mainly OCP, although a narrow band towards the edge of the disc was predominantly HAp, see Fig. 4c. After storage for 24 h in the gelling solution, a more heavily mineralized band was seen in optical microscopy along the edge of the disc, see Fig. 4b. The Raman intensity in the outer region of the disc and the width of the HAp dominated region had both increased compared to the 1 h sample, as shown in Fig. 4d. No brushite was observed within the alginate network in these experiments, the small rise in the black curve is due to background noise.

The same set of CRM measurements was repeated for samples containing 0.2 mass% brushite seeds mixed into the alginate solution with 300 mM phosphate, denoted AlgP300DCPD. A weak broad peak located at 955 cm^{-1} was also seen for these samples, however instead of shifting towards higher wavenumbers, it disappeared as the brushite peak at 987 cm^{-1} increased in intensity, as seen in the inset of Fig. 5a. The initial peak at 955 cm^{-1} was present for less than a minute, which corresponds to the appearance of the transient region observed by optical microscopy. Fig. 5b shows the Raman spectrum for a pure phase brushite sample. After 1 h and 24 h, line scans were performed. Three spectra from chosen positions at both time points are shown in Fig. 5c and d. Micrographs of this sample after 1 h and 24 h incubation in the mother liquor are shown in Fig. 6a and b. The intensity at 960 cm^{-1} and 987 cm^{-1} have been plotted as a function of distance from the center in Fig. 6c and d. In contrast to the line scan for unseeded samples, which was relatively smooth with the Raman signal intensity

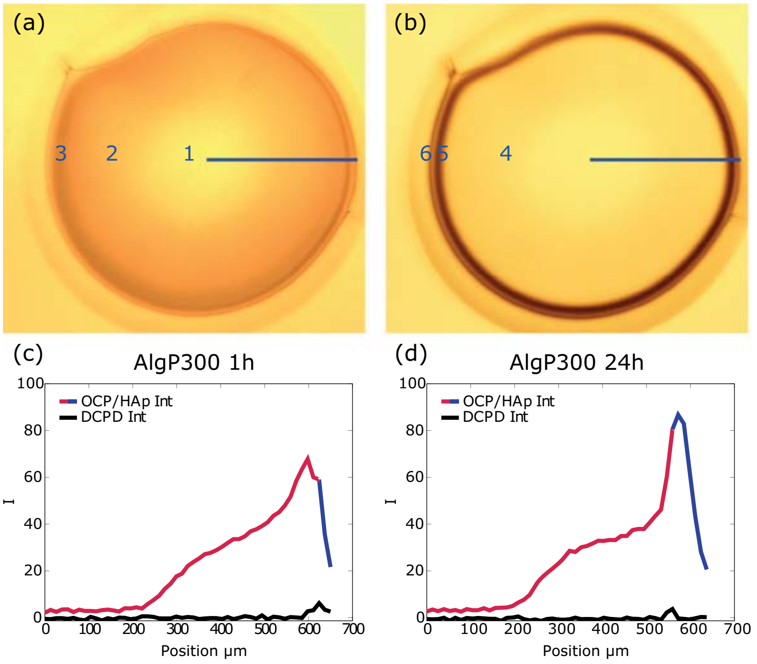

Fig. 4. Optical images and Raman data for an unseeded hydrogel disc (ø ≈ 1.3 mm) with 300 mM phosphate gelled and mineralized in a 1 M calcium solution at pH 5. (a) After 1 h in the gelling solution. (b) After 24 h in the gelling solution. The numbers correspond to positions of the SEM-images shown in Fig. 7. (c) A line scan (shown by the blue line in (a)) showing the intensity of the 958 cm^{-1} peak, corresponding to the dominant phase as determined by curve fitting, either OCP in red and HAp in blue. The intensity of the 987 cm^{-1} peak, corresponding to DCPD, is shown in black. (d) A line scan (blue line in (b)) over the same area of the same sample after 24 h in the gelling solution. (For interpretation of the references to colour in this figure legend, the reader is referred to the web version of this article.)

highest at the edge of the disc and gradually decreasing towards the center, the seeded samples resulted in a more jagged signal which persisted into the center of the disc. This was interpreted as a result of the larger brushite crystals present in the hydrogel. These crystals were larger than the laser beam spot size and more dispersed within the hydrogel network. As a result the Raman signal originating from the mineral crystals appear more discrete along the line scan for the AlgP300DCPD samples. For the AlgP300 samples, the crystals were much smaller than the spot size and a more averaged signal from both mineral and hydrogel was obtained in every point spectrum. Both optical images and CRM measurements indicated that there was less mineral towards the center, but nevertheless growth of the seeds occurred throughout the sample. A micrograph of the sample before $CaCl_2$ was introduced can be seen in the Supplementary Information (Fig. S6). A line scan was repeated in the same area following 24 h incubation in the mother liquor, seen in Fig. 6d. The brushite peak at 987 cm^{-1} disappeared towards the edge of the disc and was replaced by a peak located at 960 cm^{-1}, indicating conversion of brushite to HAp. There was no evidence in the Raman data that OCP was part of the transformation pathway when brushite had precipitated first.

To determine the crystal morphology and distribution of the mineral within the hydrogel network, selected samples were prepared for SEM-analysis. Fig. 7 shows images recorded for an AlgP300 sample kept in the gelling solution for 1 h (a–c) and for 24 h (d–f). Their corresponding positions (1 = a, 2 = b etc.) are shown in Fig. 4. Fig. 7a shows an image recorded from the center of a disc. No mineral could be seen in this area corroborating the CRM and optical microscopy results. The images in Fig. 7b and c shows a combination of nodules intertwined with alginate fibers (black arrowheads) and flaky plate-like crystals (white arrowheads). These crystals were more numerous in Fig. 7c which was recorded at a position closer to the edge of the disc. Following storage for 24 h in the gelling solution, mineral located in the same region as Fig. 7b had grown considerably and appeared more plate-like (Fig. 7d). The Raman signal from the same region did not increase in intensity and showed no sign of peak sharpening which indicates that the amount of mineral or degree of crystallinity did not change. The larger crystals seen in Fig. 7d as compared to Fig. 7b are then likely the result of Ostwald ripening, where larger crystals have grown at the expense of smaller crystals without changing the total amount of mineral within this region. Peak fitting of the OCP dual-peak revealed that the center of the two peaks was shifted from 957 to 958 cm^{-1} and 965 to 966 cm^{-1}, respectively. The exact origin of this shift is not known, however it could be a similar maturation process as previously described for HAp [10]. The images in Fig. 7e and f, show an abundance of well formed crystals. Within the hydrogel, large platelets with feathered edges were found (Fig. 7e), contrasting to well defined acicular crystals at the outermost region of the disc (Fig. 7f). See Fig. S7 in the Supplementary Information which shows a lower magnification overview to confirm the uniform mineral distribution over the different regions. Raman spectra from these regions revealed that the mineral in Fig. 7b–d was OCP while the mineral in e and f was HAp.

Fig. 8 shows an AlgP300DCPD sample prepared at pH 5 and kept in the gelling solution for 1 h (a–c) and 24 h (d–f). For samples stored for 1 h, large brushite crystals were observed throughout the alginate matrix, as shown in Fig. 8a and b. The size of these

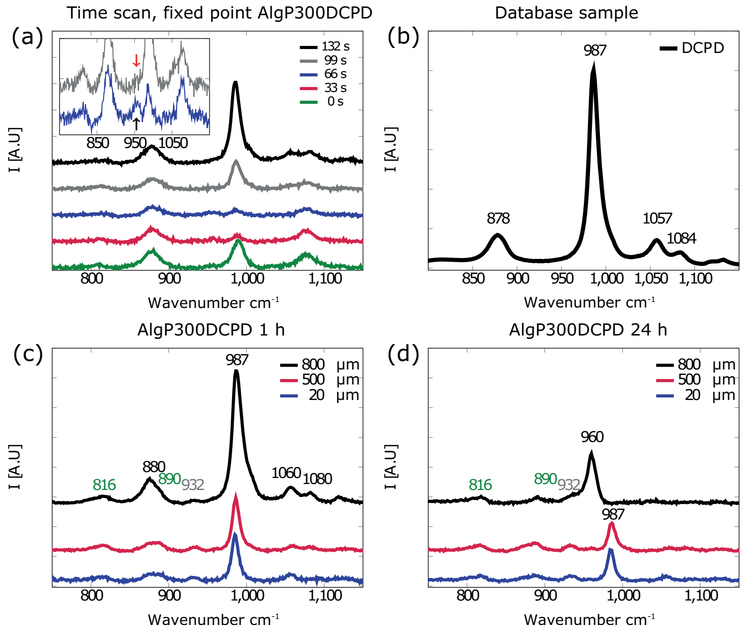

Fig. 5. (a) Raman spectra of an AlgP300DCPD sample from a single spot at 5 time points. The inset shows a close up of the 66 s and 99 s plots where a peak located at 955 cm^{-1} is visible after 66 s (black arrow) and gone after 99 s (red arrow). (b) Raman spectra of phase pure DCPD prepared in solution. (c) and (d) Raman spectra from a line scan of an AlgP300DCPD sample after 1 and 24 h respectively. (For interpretation of the references to colour in this figure legend, the reader is referred to the web version of this article.)

brushite crystals, and the absence of smaller crystals, indicated that nucleation of new crystals did not occur within the hydrogel network. This was further supported by observations described below, where the mineralization process was visualized immediately after precipitation of the mineral phase. No evidence of small brushite crystals was found and dissolution of ACP which was consumed by growth of brushite seeds was observed (cf. Fig. 9e). In addition, a dense layer of crystals on the outer surface of the disc was also present. This layer, shown in Fig. 8c was probably a result of the high supersaturation in this region, in combination with uninhibited growth into the surrounding solution. After 24 h, this surface layer was not present and the crystal structure close to the surface of the disc had changed from large brushite platelets to acicular HAp crystals similar to those observed in the same region of the AlgP300 samples, (cf. Figs. 8f and 7f). This sample fractured during mounting and the surface to the left in Fig. 8d shows a cross-section of the disc. A magnified image of this section, shown in Fig. 8e, reveals that the crystals were also needle-like further into the alginate network in contrast to unseeded samples which had platelets in the same region. This also confirms that the crystals were present throughout the thickness of the disc. CRM analysis of this region showed that these crystals were HAp.

Both optical microscopy and CRM showed that a metastable phase was present in the early stages of mineralization in the alginate discs. Based on observations from optical microscopy we estimate that, once formed, this phase was stable for no more than 120 s. In order to study the morphology of this phase, samples were kept in the gelling solution until the gel formed approximately halfway through the disc, after which they were flushed with DIW. This was immediately followed by opening the flow cells and plunging the hydrogel discs into 96% ethanol in order to prevent any dissolution or transformation of precipitated CaP phases. The samples were exposed to the gelling solution for approximately 3 min, leaving three distinct regions corresponding to the regions shown in Fig. 2. Fig. 9a–c shows an AlgP300 sample prepared at pH 5 and arrested after 3 min reaction time. In the overview image (Fig. 9a) the gelled region, transient region and ungelled region are marked with the same colors as in Fig. 2. The image in Fig. 9b was recorded within the gelled region, nodules and flaky crystals similar to the ones observed for 1 h samples were present (cf. Fig. 7b). The transient region, shown in Fig. 9c contained spherical particles with a size range between 30 and 400 nm. These particles were uniformly distributed within the alginate network. Several nodules, intimately connected with alginate fibers, were also observed in this region. These nodules were larger and less numerous than the spherical particles which suggests that the transformation of the spherical particles into nodules and later flaky platelets is solution based and not a solid state transformation.

Fig. 9d–f shows an AlgP300DCPD sample prepared at pH 5 and arrested after 3 min reaction time. Spherical particles were also observed for this sample in the transient zone (marked white in Fig. 9d). 9e shows a brushite seed crystal located in the transient zone. The spherical particles were not observed in the immediate vicinity of this seed, shown at higher magnification in Fig. 9f. In the gelled region, (marked blue in Fig. 9d), no spherical particles were observed and an abundance of brushite crystals (size range 20–80 µm) could be seen within the hydrogel, similar to those observed by optical microscopy. The absence of spherical particles in the gelled region, and the consumption of these particles around the brushite seeds indicated that they consisted of a metastable phase which appeared to reprecipitate into growing DCPD crystals. This is consistent with CRM observations. The SEM observations are strong indications that this transformation happens via a dissolution–recrystallization process.

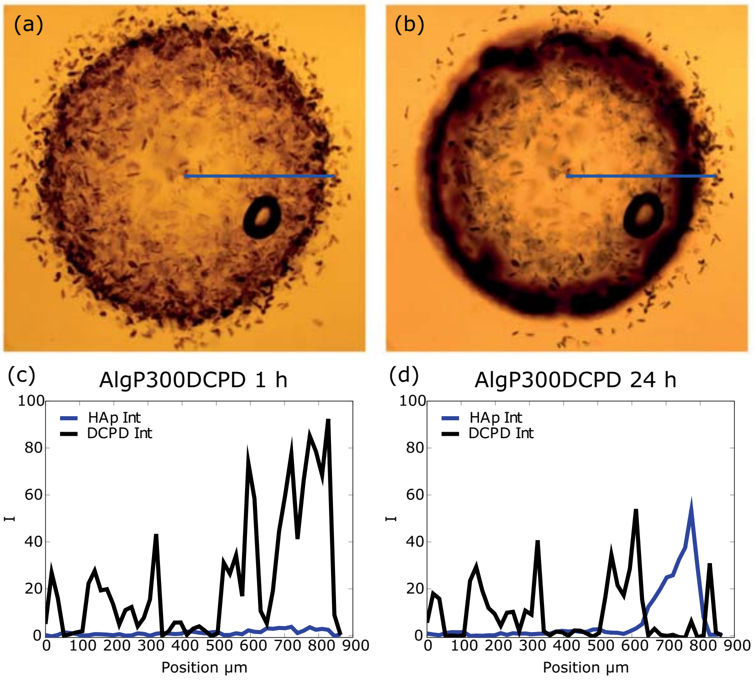

Fig. 6. Optical images and Raman data for an AlgP300DCPD hydrogel disc (ø ≈ 1.6 mm) gelled and mineralized in a 1 M calcium solution at pH 5. (a) After 1 h in the gelling solution. (b) After 24 h in the gelling solution. (c) A line scan (shown by the blue line in (a)) with the intensity of the 960 cm^{-1} peak corresponding to HAp shown in blue and the intensity of the 987 cm^{-1} peak, corresponding to DCPD, is shown in black. (d) A line scan of the same sample after 24 h in the gelling solution. (For interpretation of the references to colour in this figure legend, the reader is referred to the web version of this article.)

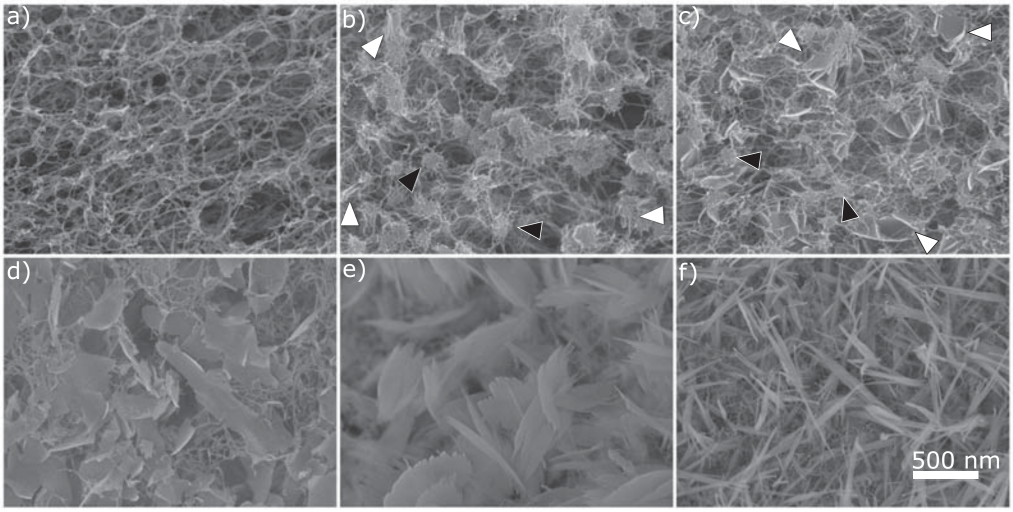

Fig. 7. SEM-images of an AlgP300 sample gelled and mineralized in a 1 M CaCl$_2$ solution at pH 5. (a), (b) and (c) are recorded from a sample incubated in the gelling solution for 1 h, while (d), (e) and (f) are recorded from a sample incubated in the gelling solution for 24 h. Black arrowheads indicate to selected alginate/mineral nodules. White arrowheads indicate selected flaky plate like crystals. The scale bar applies to all of the images in this figure.

Fig. 9g–i shows magnified images of spherical particles found in the transient region of an AlgP300DCPD sample prepared at pH 5 (g), an AlgP300 sample prepared at pH 5 (h) and an AlgP300 sample prepared at pH 7 (i). The spherical particles had a non-uniform diameter ranging from 30 to 400 nm and appeared identical regardless of the initial conditions in which they were made. Elliott

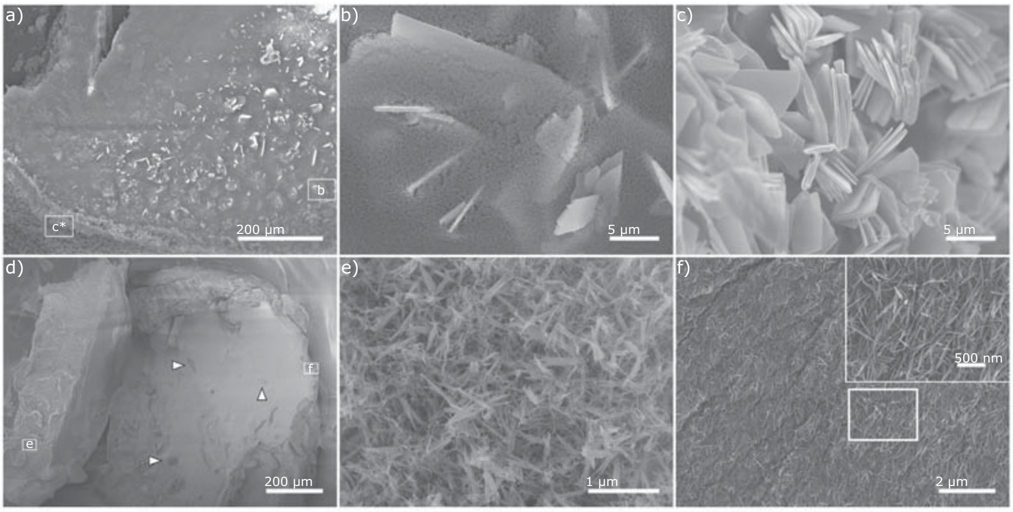

Fig. 8. SEM-images of an AlgP300DCPD sample gelled and mineralized in a 1 M calcium solution at pH 5. The sample shown in (a), (b) and (c) was incubated in the gelling solution for 1 h and shows large brushite crystals within the alginate network and a dense layer of crystals at the surface, seen in (c). The sample shown in (d) (this images is a collage of two separate images), (e) and (f) was incubated in the gelling solution for 24 h and shows a few remaining brushite crystals marked with white arrowheads and acicular HAp crystals within the alginate network. White boxes show the position of higher magnification images. The asterisk denotes the image was from a similar region in the sample geometry.

reports that ACP is often present as spherical particles in the range of 20–120 nm, which fits well with our conclusion that these particles are ACP [28]. The SEM analysis in combination with CRM suggests that ACP was formed initially which then rapidly transformed into OCP or HAp for unseeded samples and into brushite for samples seeded with brushite crystals. In both cases transformation into the more stable HAp phase occurred gradually and all transformations were likely to have taken place via a dissolution–reprecipitation process.

pH is an important factor in determining nucleation and growth of different CaP-phases [41]. In solution, ions diffuse readily and the pH can be expected to be uniform throughout the sample volume. The situation was somewhat more complex within the system studied in this work. The alginate was initially buffered at pH 7, and the gelling solution was buffered at pH 5 or pH 7 and as CaP precipitated, H^+ was released locally. In order to gain information regarding the dynamics of the pH in the system, optical measurements with a pH-sensitive dye were performed. We have previously shown this method to be highly sensitive to changes in pH between 4 and 6.5 [26]. Fig. 10a shows the pH value for three different samples averaged from a 121 × 121 µm area in the center of the alginate discs as a function of time from when the gelling solution was introduced. The measurements show a local generation of H^+ at the mineralization front which consequently diffused inwards to the center of the disc and outwards into the surrounding solution. This can be seen in Fig. 10b and c where a reduction in pH was observed both in the center of the discs and in the surrounding solution. In the sample subjected to a calcium solution of pH 5, part of the decrease in pH is due to the inwards diffusion of the acidic calcium solution. However, the similarity in the shape of the curves in Fig. 10a indicates that the generation of H^+ is the main reason for the change in pH regardless of the initial pH in the gelling solution. In addition, careful examination of the curve denoted AlgP300 pH5 edge in Fig. 10b reveals a slight u-shape. This u-shape is more clear in Fig. 10c, where both the alginate solution and the calcium solution was initially pH 7. In this case, the only source of H^+ was the precipitation of CaP. This shape indicates the outward diffusion of H^+ generated from the mineral formation. It can be seen that the surrounding calcium solution experienced a reduction in pH as the local generation of H^+ exceeded the buffering capacity. A subsequent increase in pH occurred as the solution regained its buffering capacity due to its comparatively larger volume. In both cases the pH in the center and at the halfway point are expected, with time, to reach the same pH-value of the surrounding solution.

As seen in Fig. 10a, the pH in the center of the discs changed most within 150–350 s after the introduction of the gelling solution. The results from the SEM and CRM analysis show that ACP is the dominant mineral phase within this time frame. This suggests that formation of ACP is the main cause of H^+ release. The subsequent transformation into OCP or brushite appear to have occurred under similar conditions, i.e. pH < 5, for all sample types as can be seen from the similar shape of the curves in Fig. 10a. In cases were brushite seeds were present, the amorphous phase was then consumed due to growth of brushite crystals, likely via a dissolution–reprecipitation pathway. For unseeded samples, consumption of the amorphous phase occurred via nucleation and growth of OCP at the same pH-conditions as for the seeded samples. It is likely that the alginate inhibited the nucleation of brushite, as one would expect this phase to nucleate at a pH-value less than 5 [16,41]. As some of the phosphate was consumed in the mineralization process, the buffering capacity of the alginate solution was reduced. Due to the local generation and fast diffusion of H^+, the central region of the disc experienced the lowest recorded pH, as can be observed in Fig. 10b and c. Due to a lower concentration of buffer in the surrounding solution, the diffusion of the buffer was slower than the mineral front, leading to a prolonged duration of reduced pH in the center of the discs, see Fig. S10 in the Supplementary Information for a brief discussion of this effect. We speculate that not only the consumption of the available phosphate in the sample, but also a reduction in pH led to the unmineralized zone in the center of gelled discs. This is because pH is an effective variable on supersaturation and reduced pH would lead to lower supersaturation which in turn results in reduced

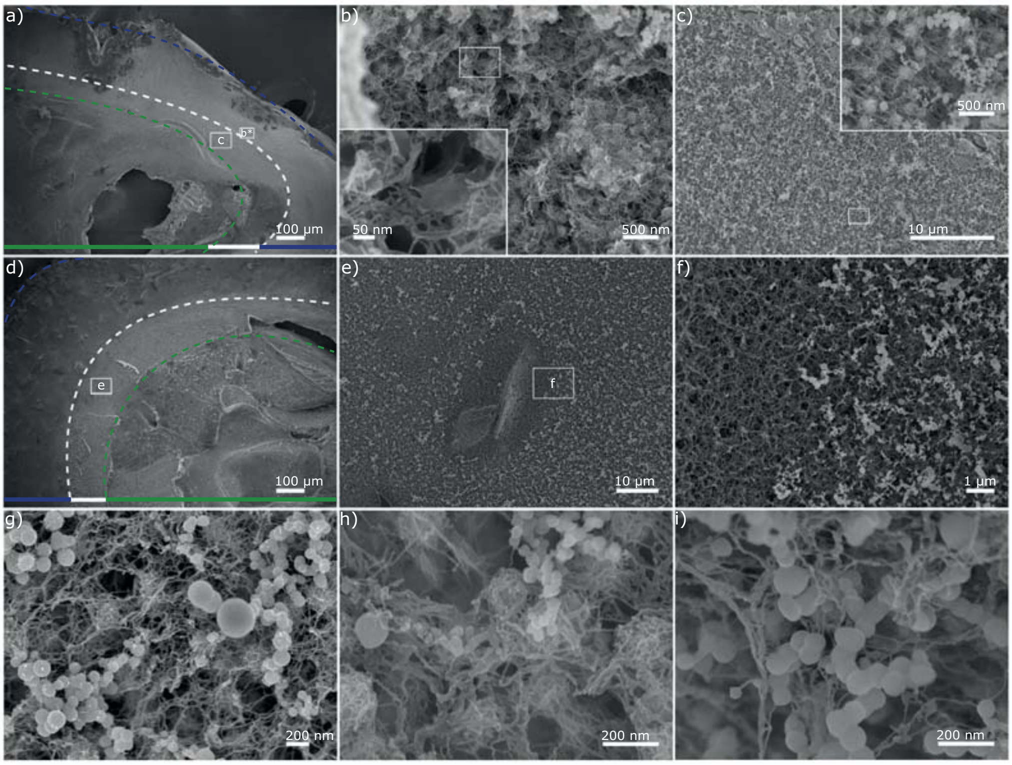

Fig. 9. SEM images of an AlgP300 sample ((a), (b), (c), (h) and (i)) and an AlgP300DCPD sample ((d), (e), (f) and (g)) gelled at pH 5 and arrested after 3 min reaction time. The image in (a) shows a low magnification overview with the gelled, transient and ungelled regions marked with blue, white and green respectively. (b) and (c) are higher magnification images from the gelled and transient regions respectively. (d) is a low magnification overview of a seeded sample with similar regions marked as in (a). (e) and (f) are magnified images of an area surrounding a seed, showing how the metastable phase has been consumed by the crystal seed. Images (g) (AlgP300DCPD made at pH 5), (h) (AlgP300 made at pH5) and (i) (AlgP300 made at pH7) show similar morphologies of particles found in the transient zone of samples made under different conditions. White boxes show the position of higher magnification images. The asterisk denotes the image was from a similar region in the sample geometry. (For interpretation of the references to colour in this figure legend, the reader is referred to the web version of this article.)

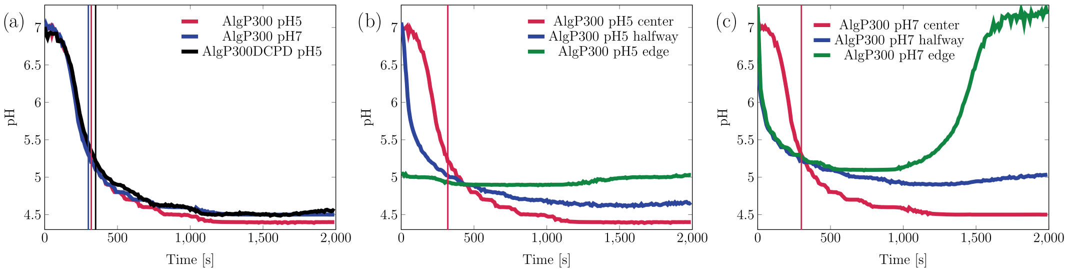

Fig. 10. (a) pH-data gathered from a 121 × 121 µm square in the center of discs produced under three different conditions (given in the legend). The vertical lines mark the time point at which the samples were gelled, as determined by optical microscopy. The graphs in (b) and (c) show AlgP300 samples subjected to gelling solution of pH 5 and pH7 respectively. The pH value was recorded (also 121 × 121 µm area averages) over time from 3 positions; at the edge close to the surrounding solution, at a point halfway into the disc and from the center. It can be seen in both conditions that the surrounding solution experiences a drop in pH followed by an increase back to the initial buffered pH. This phenomenon is more obvious in (c).

nucleation of new crystals. This may also explain why in seeded samples crystals grew throughout the geometry (cf. Figs. 6 and S9) since this process was not dependent on nucleation.

Incubating materials in simulated body fluid (SBF) has previously been used to indicate the ability of samples to nucleate HAp in physiological conditions [27]. The relevance of this incubation to predict *in vivo* behavior is a matter of debate [42]. In particular, there have been investigations with both false positives and false negatives, leaving no definitive trend [43]. However, the method is also often used to form an apatite layer on synthetic scaffold which is believed to enhance the bone bonding ability of the implant [2,44–46,21]. In this work, it was used to study how the incorporation of CaP in the alginate matrix affected the formation of HAp, and demonstrate the ability to monitor this transformation with spatiotemporal resolution, not to predict an *in vivo* response. AlgP300DCPD samples were examined with CRM (shown in Supplementary Information, Fig. S9) and SEM as prepared (Fig. 11a–c) and following 24 h (Fig. 11d–f) and 168 h (Fig. 11g–i) incubation in SBF. As a control, alginate samples which contained brushite seeds, but no phosphate precursor, were also incubated and analyzed with CRM. For the mineralized samples, a large number of brushite crystals were observed to be protruding out from the hydrogel surface initially, as shown in Fig. 11a. Fig. 11b shows a region close to the edge of the sample where a shell of large brushite crystals could be observed along the edge and individual crystals were also observed embedded in the alginate network. Fig. 11c shows brushite crystals from a region nearer the center of the disc, revealing that large crystals were also present in this region, in contrast to the unseeded samples (cf. Fig. 7a). Following 24 h incubation in SBF there was a reduction in the abundance of large brushite crystals in all areas of the sample (Fig. 11d). A dense band of small plate like aggregated crystals had formed from the edge and 100–200 μm towards the center of the disc (Fig. 11e). As shown in Fig. 11f, some of the individual brushite crystals had these new crystals encrusted directly on their surfaces. The new crystalline phase was confirmed to be HAp with CRM (see Fig. S9 in Supplementary Information). The dense layer of brushite crystals at the periphery of the sample had completely transformed into HAp, however the micro-scale morphology of these crystals was still intact (see Fig. S8). Following one week storage in SBF, all of the large brushite crystals within the alginate network had dissolved (Fig. 11g) and a dense shell of HAp had formed along the edge of the disc (Fig. 11h). This shell extended ca. 200 μm towards the center of the disc (Fig. 11g), and the alginate network was heavily mineralized throughout the thickness of the disc (observed from samples which fractured during preparation). Fig. 11h and i clearly demonstrates that HAp formed uniformly along the edge of the disc and non-uniformly at the location of brushite crystals further into the disc. This indicated that the source of HAp formation was driven by both dissolution of brushite crystals and inwards diffusion of the SBF-solution along the edge while further into the disc, the primary source for HAp nucleation and growth was the dissolution of the resident brushite crystals. The non-mineralized control samples did not show any HAp formation within the alginate network, however after 1 week of incubation, some HAp had formed on the interface between the hydrogel and the surrounding solution (see Fig. S9). This shows that the mineralized hydrogel promotes the formation of HAp at

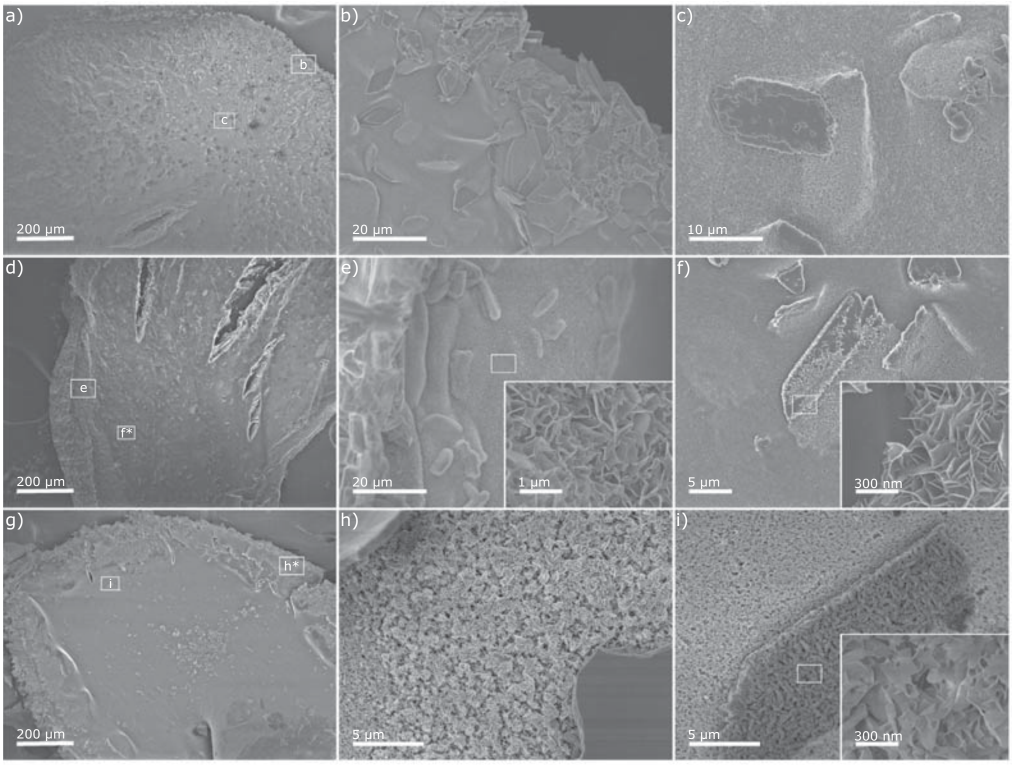

Fig. 11. SEM images of an AlgP300DCPD sample after 0 h (a–c), 24 h (d–f) and 168 h (g–i) incubation in SBF. (a), (d) and (g) show a low magnification overview images at the different time points. White boxes show the position of higher magnification images. The asterisk denotes the image was from a similar region in the sample geometry. (b) shows the extensive growth of brushite crystals along the edge of a disc. (c) shows a higher magnification image of brushite crystals present further into the disc. (e) shows a region close to the edge of a disc where a uniform region of flaky HAp crystals (a high magnification image can be seen in the inset) is visible as well as areas where the morphology of previous brushite crystals that have been converted into HAp. (f) shows the nucleation of HAp (seen as flaky crystals in the high magnification inset) close to and on the surface of a brushite crystal after 24 h incubation. (h) shows a region close to edge after 168 h incubation where a uniform band of flaky HAp crystals could be seen. (i) shows nanocrystals which have assumed the morphology of an initial brushite crystal.

physiological pH, probably due to an increased, localized supersaturation provided by the dissolution of brushite.

4. Conclusion

In summary, we have shown that by combining a simple experimental design with several correlative advanced characterization techniques, new insight into the mineralization processes within hydrogels can be obtained. Simultaneous gelling and mineralization of an alginate hydrogel was performed and spatiotemporally monitored using a thin disc geometry that was particularly convenient for optical based *in situ* characterization techniques. At high supersaturation, crystal seeds do not affect the initial nucleation of ACP, but merely directs the reprecipitation as the ACP dissolves in the dynamic system, i.e. reduced pH as shown by measurements and reduced supersaturation due to consumption of precursors. We have also conclusively discriminated between HAp and OCP via peak fitting of the $\nu1$ PO_4 stretch in the Raman spectrum, and shown that this can be monitored *in situ* in the hydrogel matrix used herein. Transformation of brushite into HAp following incubation in SBF was also monitored, thereby demonstrating utility of this characterization toolbox for non-destructive, *in situ* evaluation of hydrogel based hard tissue scaffold biomaterials.

Acknowledgement

The authors thank the Research Council of Norway for financial support (FRINATEK project 214607).

Appendix A. Supplementary data

Supplementary data associated with this article can be found, in the online version, at http://dx.doi.org/10.1016/j.actbio.2016.08.041.

References

[1] S. Van Vlierberghe, P. Dubruel, E. Schacht, Biopolymer-based hydrogels as scaffolds for tissue engineering applications: a review, Biomacromolecules 12 (5) (2011) 1387–1408, http://dx.doi.org/10.1021/bm200083n.
[2] K. Gkioni, S.C. Leeuwenburgh, T.E. Douglas, A.G. Mikos, J.A. Jansen, Mineralization of hydrogels for bone regeneration, Tissue Eng. B Rev. 16 (6) (2010) 577–585, http://dx.doi.org/10.1089/ten.teb.2010.0462.
[3] A.K. Gaharwar, N.A. Peppas, A. Khademhosseini, Nanocomposite hydrogels for biomedical applications, Biotechnol. Bioeng. 111 (3) (2014) 441–453, http://dx.doi.org/10.1002/bit.25160.
[4] H.-R. Lin, Y.-J. Yeh, Porous alginate/hydroxyapatite composite scaffolds for bone tissue engineering: preparation, characterization, and in vitro studies, J. Biomed. Mater. Res. B Appl. Biomater. 71 (1) (2004) 52–65, http://dx.doi.org/10.1002/jbm.b.30065.
[5] M. Rajkumar, N. Meenakshisundaram, V. Rajendran, Development of nanocomposites based on hydroxyapatite/sodium alginate: synthesis and characterisation, Mater. Characterizat. 62 (5) (2011) 469–479, http://dx.doi.org/10.1016/j.matchar.2011.02.008.
[6] Z. Li, Y. Su, B. Xie, H. Wang, T. Wen, C. He, H. Shen, D. Wu, D. Wang, A tough hydrogelhydroxyapatite bone-like composite fabricated in situ by the electrophoresis approach, J. Mater. Chem. B 1 (12) (2013) 1755, http://dx.doi.org/10.1039/c3tb00246b.
[7] M.S. Johnsson, G.H. Nancollas, The role of brushite and octacalcium phosphate in apatite formation, Crit. Rev. Oral Biol. Med. 3 (1) (1992) 61–82, http://dx.doi.org/10.1177/10454411920030010601.
[8] R. Boistelle, I. Lopez-Valero, Growth units and nucleation: the case of calcium phosphates, J. Cryst. Growth 102 (3) (1990) 609–617, http://dx.doi.org/10.1016/0022-0248(90)90420-P.
[9] T. Tsuji, K. Onuma, A. Yamamoto, M. Iijima, K. Shiba, Direct transformation from amorphous to crystalline calcium phosphate facilitated by motif-programmed artificial proteins, Proc. Natl. Acad. Sci. U.S.A. 105 (44) (2008) 16866–16870, http://dx.doi.org/10.1073/pnas.0804277105.
[10] N.J. Crane, V. Popescu, M.D. Morris, P. Steenhuis, M.A. Ignelzi, Raman spectroscopic evidence for octacalcium phosphate and other transient mineral species deposited during intramembranous mineralization, Bone 39 (3) (2006) 434–442, http://dx.doi.org/10.1016/j.bone.2006.02.059.
[11] G. Campi, A. Ricci, A. Guagliardi, C. Giannini, S. Lagomarsino, R. Cancedda, M. Mastrogiacomo, A. Cedola, Early stage mineralization in tissue engineering mapped by high resolution X-ray microdiffraction, Acta biomater. 8 (9) (2012) 3411–3418, http://dx.doi.org/10.1016/j.actbio.2012.05.034.
[12] J. Mahamid, B. Aichmayer, E. Shimoni, R. Ziblat, C. Li, S. Siegel, O. Paris, P. Fratzl, S. Weiner, L. Addadi, Mapping amorphous calcium phosphate transformation into crystalline mineral from the cell to the bone in zebrafish fin rays, Proc. Natl. Acad. Sci. U.S.A. 107 (14) (2010) 6316–6321, http://dx.doi.org/10.1073/pnas.0914218107.
[13] L.B. Gower, Biomimetic model systems for investigating the amorphous precursor pathway and its role in biomineralization, Chem. Rev. 108 (11) (2008) 4551–4627, http://dx.doi.org/10.1021/cr800443h.
[14] M. Xie, M.Ø. Olderøy, J.P. Andreassen, S.M. Selbach, B.L. Strand, P. Sikorski, Alginate-controlled formation of nanoscale calcium carbonate and hydroxyapatite mineral phase within hydrogel networks, Acta Biomater. 6 (9) (2010) 3665–3675, http://dx.doi.org/10.1016/j.actbio.2010.03.034.
[15] S.H. Bjørnøy, D.C. Bassett, S. Ucar, J.-P. Andreassen, P. Sikorski, Controlled mineralisation and recrystallisation of brushite within alginate hydrogels, Biomed. Mater. (2016) 015013, http://dx.doi.org/10.1088/1748-6041/11/1/015013.
[16] S. Ucar, S.H. Bjørnøy, D.C. Bassett, B.L. Strand, P. Sikorski, J.-P. Andreassen, Nucleation and growth of brushite in the presence of alginate, Cryst. Growth Des. (2015), http://dx.doi.org/10.1021/acs.cgd.5b01032.
[17] L. Gower, D. Tirrell, Calcium carbonate films and helices grown in solutions of poly(aspartate), J. Cryst. Growth 191 (1–2) (1998) 153–160, http://dx.doi.org/10.1016/S0022-0248(98)00002-5.
[18] H. Cölfen, S. Mann, Higher-order organization by mesoscale self-assembly and transformation of hybrid nanostructures, Angew. Chem. Int. Ed. 42 (21) (2003) 2350–2365, http://dx.doi.org/10.1002/anie.200200562.
[19] F.C. Meldrum, H. Colfen, Controlling mineral morphologies and structures in biological and synthetic systems, Chem. Rev. 108 (11) (2008) 4332–4432, http://dx.doi.org/10.1021/cr8002856.
[20] F. Nudelman, K. Pieterse, A. George, P.H.H. Bomans, H. Friedrich, L.J. Brylka, P.A.J. Hilbers, G. de With, N.A.J.M. Sommerdijk, The role of collagen in bone apatite formation in the presence of hydroxyapatite nucleation inhibitors, Nat. Mater. 9 (12) (2010) 1004–1009, http://dx.doi.org/10.1038/nmat2875.
[21] K. Bleek, A. Taubert, New developments in polymer-controlled, bioinspired calcium phosphate mineralization from aqueous solution, Acta Biomater. 9 (5) (2013) 6283–6321, http://dx.doi.org/10.1016/j.actbio.2012.12.027.
[22] H. Ping, H. Xie, B.-L. Su, Y.-B. Cheng, W. Wang, H. Wang, Y. Wang, J. Zhang, F. Zhang, Z. Fu, Organized intrafibrillar mineralization, directed by a rationally designed multi-functional protein, J. Mater. Chem. B 3 (2015) 4496–4502, http://dx.doi.org/10.1039/C5TB00386E.
[23] B. Cantaert, E. Beniash, F.C. Meldrum, Nanoscale confinement controls the crystallization of calcium phosphate: relevance to bone formation, Chemistry (Weinheim an der Bergstrasse, Germany) 19 (44) (2013) 14918–14924, http://dx.doi.org/10.1002/chem.201302835.
[24] Y.-W. Wang, H.K. Christenson, F.C. Meldrum, Confinement increases the lifetimes of hydroxyapatite precursors, Chem. Mater. 26 (20) (2014) 5830–5838, http://dx.doi.org/10.1021/cm501770r.
[25] A.K. Rajasekharan, M. Andersson, Role of Nanoscale confinement on calcium phosphate formation at high supersaturation, Cryst. Growth Des. 15 (6) (2015) 2775–2780, http://dx.doi.org/10.1021/acs.cgd.5b00139.
[26] S.H. Bjørnøy, S. Mandaric, D.C. Bassett, A.K.O. Åslund, S. Ucar, J.-P. Andreassen, B.L. Strand, P. Sikorski, Gelling kinetics and *in situ* mineralization of alginate hydrogels: A correlative spatiotemporal characterization toolbox, Acta Biomater. 44 (2016) 243–253, http://dx.doi.org/10.1016/j.actbio.2016.07.046.
[27] T. Kokubo, H. Takadama, How useful is SBF in predicting in vivo bone bioactivity?, Biomaterials 27 (15) (2006) 2907–2915, http://dxdoi.org/10.1016/j.biomaterials.2006.01.017.
[28] J. Elliott, Structure and Chemistry of the Apatites and Other Calcium Orthophosphates, Elsevier B.V., 1994, http://dx.doi.org/10.1016/B978-0-444-81582-8.50001-8.
[29] J.-S. Wu, I.-C. Hwang, K.S. Kim, J.S. Kim, Rhodamine-based Hg^{2+}-selective chemodosimeter in aqueous solution: fluorescent OFF-ON, Org. Lett. 9 (5) (2007) 907–910, http://dx.doi.org/10.1021/ol070109c.
[30] Z. Li, S. Wu, J. Han, S. Han, Imaging of intracellular acidic compartments with a sensitive rhodamine based fluorogenic pH sensor, The Analyst 136 (2011) 3698–3706, http://dx.doi.org/10.1039/c1an15108h.
[31] H. Tanaka, M. Matsumura, I.A. Veliky, Diffusion characteristics of substrates in Ca-alginate gel beads, Biotechnol. Bioeng. 26 (1) (1984) 53–58, http://dx.doi.org/10.1002/bit.260260111.
[32] P. Malkaj, E. Pierri, E. Dalas, The crystallization of hydroxyapatite in the presence of sodium alginate, J. Mater. Sci. Mater. Med. 16 (8) (2005) 733–737, http://dx.doi.org/10.1007/s10856-005-2610-9.
[33] S. Koburger, A. Bannerman, L.M. Grover, F.A. Müller, J. Bowen, J.Z. Paxton, A novel method for monitoring mineralisation in hydrogels at the engineered hardsoft tissue interface, Biomat. Sci. 2 (1) (2014) 41, http://dx.doi.org/10.1039/c3bm60102a.
[34] W.L. Marshall, G.M. Begun, Raman spectroscopy of aqueous phosphate solutions at temperatures up to 450 °C Two liquid phases, supercritical fluids, and pyro- to ortho-phosphate conversions, J. Chem. Soc. Faraday Trans. 2 85 (12) (1989) 1963, http://dx.doi.org/10.1039/f29898501963.
[35] M.M. Campos-Vallette, N.P. Chandía, E. Clavijo, D. Leal, B. Matsuhiro, I.O. Osorio-Román, S. Torres, Characterization of sodium alginate and its block fractions by surface-enhanced Raman spectroscopy, J. Raman Spectrosc. (2009), http://dx.doi.org/10.1002/jrs.2517.

[36] G.R. Sauer, W.B. Zunic, J.R. Durig, R.E. Wuthier, Fourier transform raman spectroscopy of synthetic and biological calcium phosphates, Calcified Tissue Int. 54 (5) (1994) 414–420, http://dx.doi.org/10.1007/BF00305529.

[37] W.W. Rudolph, D. Fischer, G. Irmer, Vibrational spectroscopic studies and DFT calculations on $NaCH_3CO_2$ (aq) and CH_3COOH (aq), Dalton Trans. 43 (8) (2014) 3174–3185, http://dx.doi.org/10.1039/C3DT52580E.

[38] S. Koutsopoulos, Synthesis and characterization of hydroxyapatite crystals: a review study on the analytical methods, J. Biomed. Mater. Res. 62 (4) (2002) 600–612, http://dx.doi.org/10.1002/jbm.10280.

[39] B.O. Fowler, M. Markovic, W.E. Brown, Octacalcium phosphate. 3. Infrared and Raman vibrational spectra, Chem. Mater. 5 (10) (1993) 1417–1423, http://dx.doi.org/10.1021/cm00034a009.

[40] G. Penel, G. Leroy, C. Rey, E. Bres, MicroRaman spectral study of the PO_4 and CO_3 vibrational modes in synthetic and biological apatites, Calcified Tissue Int. 63 (6) (1998) 475–481, http://dx.doi.org/10.1007/s002239900561.

[41] F. Abbona, H. Madsen, R. Boistelle, The initial phases of calcium and magnesium phosphates precipitated from solutions of high to medium concentrations, J. Cryst. Growth 74 (3) (1986) 581–590, http://dx.doi.org/10.1016/0022-0248(86)90205-8.

[42] M. Bohner, J. Lemaitre, Can bioactivity be tested in vitro with SBF solution?, Biomaterials 30 (12) (2009) 2175–2179, http://dxdoi.org/10.1016/j.biomaterials.2009.01.008.

[43] A.A. Zadpoor, Relationship between in vitro apatite-forming ability measured using simulated body fluid and in vivo bioactivity of biomaterials, Mater. Sci. Eng. C Mater. Biol. Appl. 35 (2014) 134–143, http://dx.doi.org/10.1016/j.mSection.10.026.

[44] L. Jongpaiboonkit, T. Franklin-Ford, W.L. Murphy, Growth of hydroxyapatite coatings on biodegradable polymer microspheres, ACS Appl. Mater. Interfaces 1 (7) (2009) 1504–1511, http://dx.doi.org/10.1021/am9001716.

[45] I. Hofmann, L. Müller, P. Greil, F.A. Müller, Calcium phosphate nucleation on cellulose fabrics, Surf. Coatings Technol. 201 (6) (2006) 2392–2398, http://dx.doi.org/10.1016/j.surfcoat.2006.04.007.

[46] K. Rodríguez, S. Renneckar, P. Gatenholm, Biomimetic calcium phosphate crystal mineralization on electrospun cellulose-based scaffolds, ACS Appl. Mater. Interfaces 3 (3) (2011) 681–689, http://dx.doi.org/10.1021/am100972r.

Supplementary Information for: A correlative spatiotemporal microscale study of calcium phosphate formation and transformation within an alginate hydrogel matrix

---

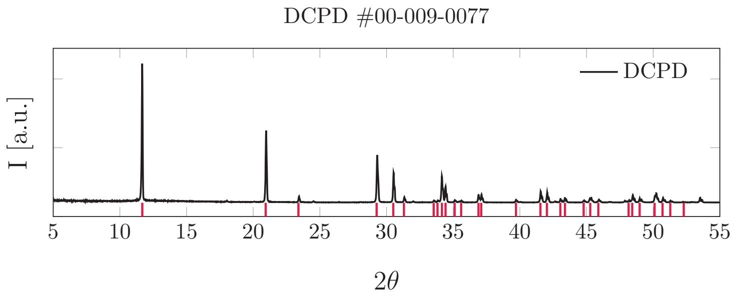
DCPD #00-009-0077

Figure S.1: The XRD-spectrum of the brushite crystals used for seeding and Raman database sample. ICDD pdf-card 00-009-0077 has been used to identify the crystal structure (shown in red lines). Reflections with less than 3 % relative intensity has been removed for clarity.

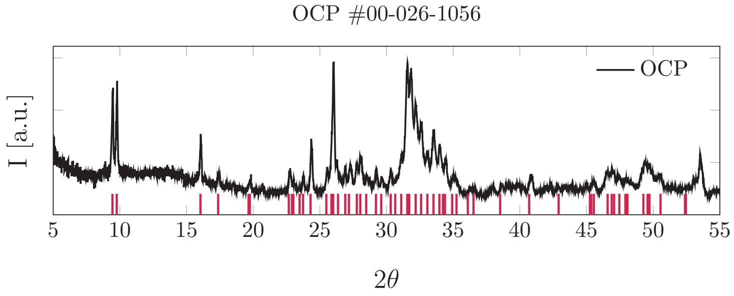
OCP #00-026-1056

Figure S.2: The XRD-spectrum of the OCP crystals used for Raman database sample. ICDD pdf-card 00-026-1056 has been used to identify the crystal structure (shown in red lines). Reflections with less than 3 % relative intensity has been removed for clarity

Preprint submitted to Elsevier *August 15, 2016*

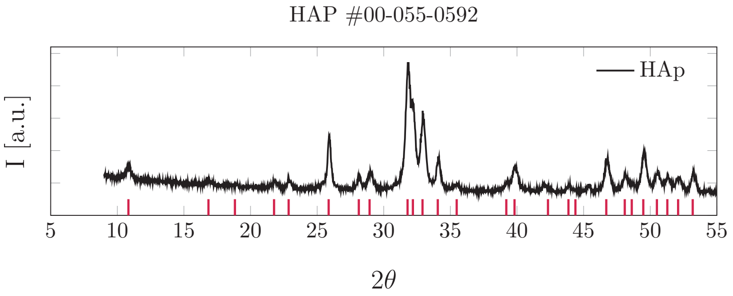

Figure S.3: The XRD-spectrum of the HAp crystals used for Raman database sample. ICDD pdf-card 00-055-0592 has been used to identify the crystal structure (shown in red lines). Reflections with less than 3 % relative intensity has been removed for clarity

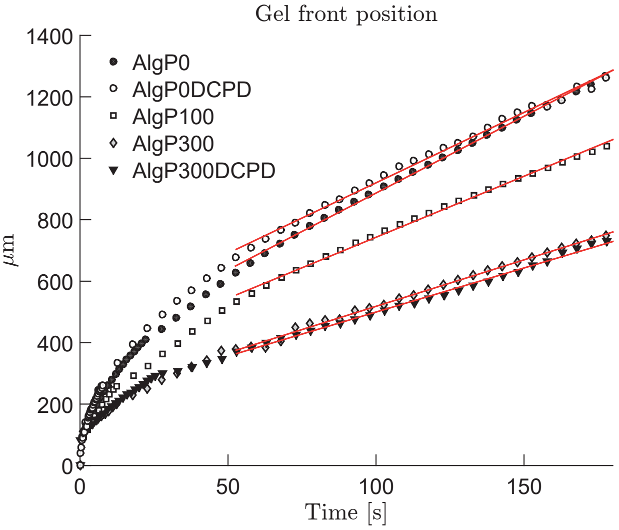

Figure S.4: Plots of typical gel front measurements at different conditions. All samples were subjected to a 1 M $CaCl_2$ solution at pH 5. The gel front velocity was calculated by fitting the approximately linear region of the plots. Linear fits fitted from the 50 s point are shown in red.

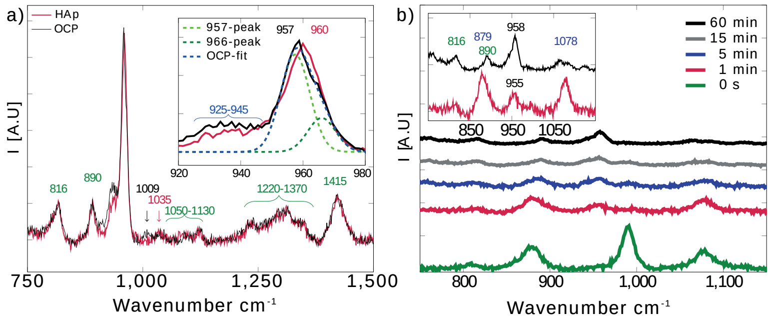

Figure S.5: **a)** A comparison of the Raman spectra of alginate with OCP and alginate with HAp. Peak designations in red and black correspond to HAp and OCP respectively. Note the HPO_4-peak located at 1009 cm^{-1}. Peak designation in green indicate peaks arising from the alginate, while that in blue is a broad peak assigned to the acetate buffer.The inset shows details of the main peak shape. The OCP peak is shifted slightly to a lower wavenumber, and has a shoulder at 966 cm^{-1} as compared to the HAp-peak. An example of a two-peak Gaussian curve-fitting of the OCP-peak is shown. **b)** A Raman time scan for a sample gelled at pH 7. This procedure also had an initial peak around 955 cm^{-1}, however, there was a delayed appearance of the main crystalline phosphate peak as compared to samples prepared at pH 5. The inset shows details of the spectra recorded at 1 min and 60 min, highlighting the difference in the peak shape of the peak located at 955-960 cm^{-1} over time.

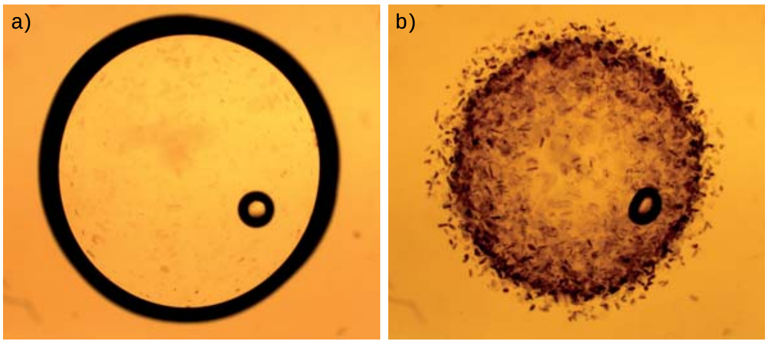

Figure S.6: An AlgP300DCPD sample (⊘ ≈1.6 mm) shown before (**a)**) and 1 h after (**b)**) the introduction of $CaCl_2$. Note that the brushite crystals in **a)** are barely visible as compared to **b)**. This indicated the growth of crystals across the entire sample, although it is more pronounced towards the edge of the disc.

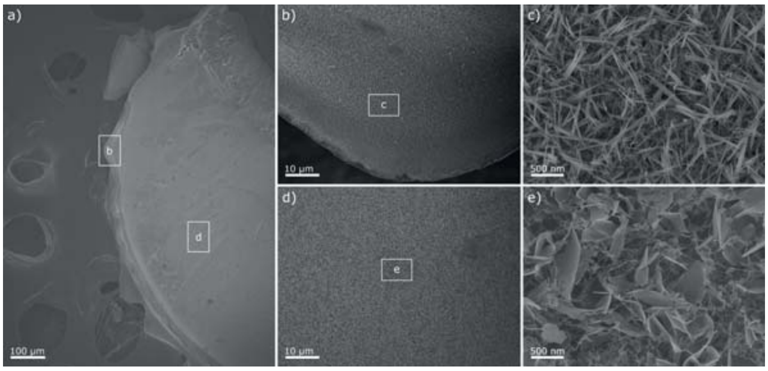

Figure S.7: **a)** shows a low magnification overview image of an AlgP300 sample stored in the mother liquor for 24 h. **b)** and **d)** are higher magnification images of the regions marked in **a)** showing the uniformity of the mineral in the respective areas. **c)** and **e)** show a more detailed crystal morphology of areas marked in the previous images.

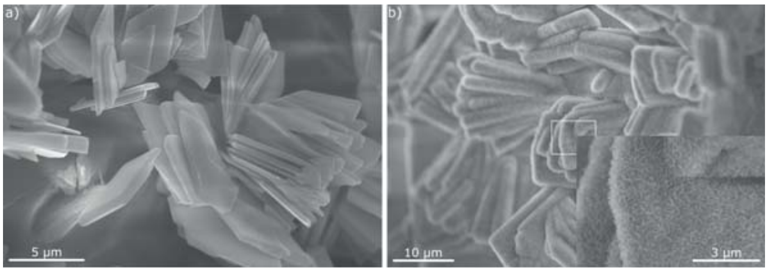

Figure S.8: A comparison of mineral located on the outer surface of an AlgP300DCPD disc prior to (**a)**) and after (**b)**) storage in SBF. The mineral has changed phase during incubation in SBF, but the large scale morphology remained intact, in contrast to what was observed when the discs were kept in the original gelling solution (cf. Figure 8). The inset in **b)** shows a higher magnification image of the marked region, here nanoscale HAp is evident as the *de novo* crystalline phase.

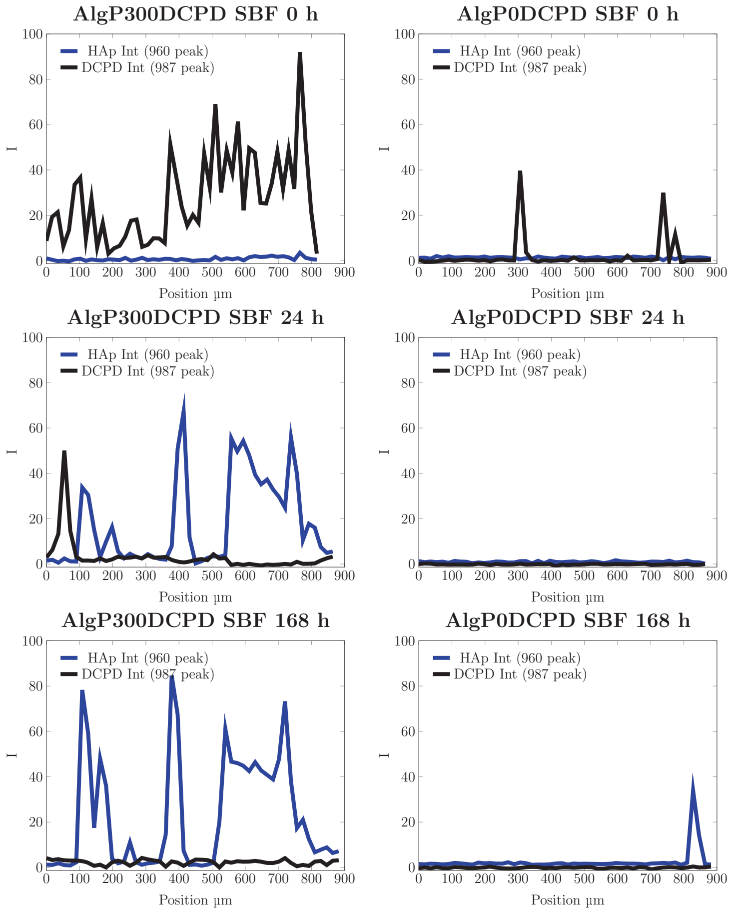

Figure S.9: A comparison of AlgP300DCPD and AlgP0DCPD (no phosphate precursor, otherwise identical) upon incubation in SBF over time. The phosphate containing sample quickly formed a broad HAp band, while there was no formation of HAp in the sample containing only brushite seeds after 24 h. After 1 week in SBF, there was complete transformation of brushite to HAp for AlgP300DCPD samples and there was a minor formation of HAp on the interface between the gelled disc and the surrounding solution for AlgP0DCPD samples.

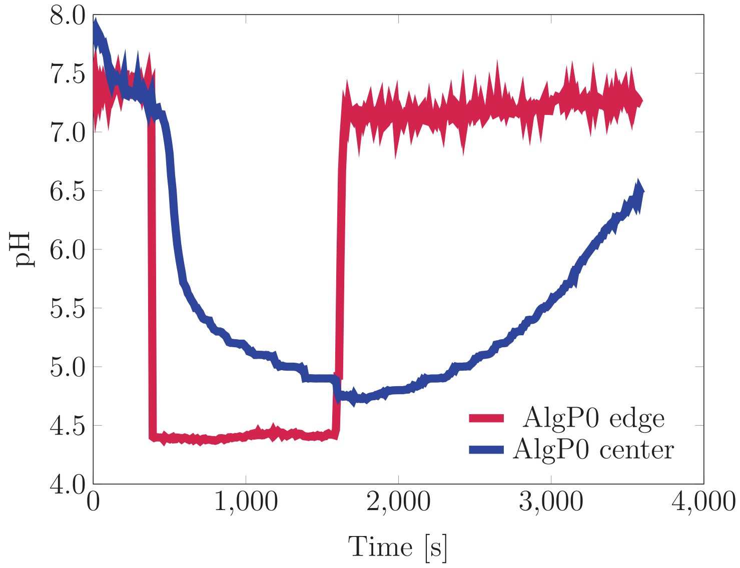

Figure S.10: A graph showing pH as a function of time at two locations for an AlgP0 sample gelled with a pH ∼ 7 $CaCl_2$ solution and subsequently flushed with a pH ∼ 4.5 solution after 400 s and a pH ∼ 7 solution after1600 s to show the rate at which the pH change as the buffers diffuse into the hydrogel. The buffers and concentrations used were the same as in the experiments in the manuscript. As the hydrogel discs were mineralized the initial formation of either amorphous CaP, OCP or brushite lead to an initial decrease in pH. One could speculate that the later transformation into the more stable HAp would sustain this lower pH, as during the transformation of OCP into HAp there is a consumption of OH^- and as brushite transforms into HAp there is also a release of H^+. However, as the graph shows, the diffusion of buffers at this concentration into non-mineralized hydrogel discs were slow and this is probably the main cause for the sustained pH gradient between the surrounding solution and the center of the hydrogel discs, seen in Figure 10.